Towards Improved Therapies, Model Systems and Understanding of Spinocerebellar Ataxia Type 3

by

Lauren R. Moore

A dissertation submitted in partial fulfillment
of the requirements for the degree of
Doctor of Philosophy
(Neuroscience)
in the University of Michigan
2019

Doctoral Committee:

Professor Henry L. Paulson, Chair
Professor Andrew Lieberman
Professor Jack M. Parent
Professor Vikram Shakkottai
Professor Gary D. Smith

Lauren R. Moore

lrmo@umich.edu

ORCID iD: 0000-0001-7644-9179

Acknowledgements

I would first like to thank my thesis committee chair, Dr. Henry Paulson, for his dedicated and enthusiastic mentorship throughout my graduate thesis work. Dr. Paulson is an outstanding educator and supportive mentor, and has been instrumental in developing my confidence, knowledge and skills as a neuroscientist. I thank my thesis committee members, Dr. Andrew Lieberman, Dr. Jack Parent, Dr. Vikram Shakkottai, and Dr. Gary Smith, for their valuable support and guidance during and outside of committee meetings. The many insightful discussions I've had with each of them over the last five years has immeasurably improved both my studies and my ability to think as a scientist. I thank Dr. Shakkottai and current and past members of the Shakkottai lab, Dr. Dave Bushart and Dr. Ravi Chopra, for their scientific contributions to multiple collaborative projects. I thank Dr. Gary Smith and the MStem Laboratory senior lab technician, Laura Keller, for the significant time, training, space, and resources that they contributed towards the development and characterization of the SCA3 disease-specific human embryonic stem cell line. I thank the many members of the Paulson lab that have made my graduate experience so educational and enjoyable. I particularly want to thank Dr. Hayley McLoughlin who has been a significant mentor, teacher, and collaborator in the lab throughout my entire graduate experience. I recognize past and current Paulson lab members who have contributed to this dissertation work: Dr. Maria do Carmo Costa, Rob Komlo, Kate Blumenstein, Annie Zalon, Svetlana Fischer, and Dr. Gautam Rajpal. I also acknowledge contributions made by the many undergraduate research students that I've had the privilege to mentor: Rodrigo Delatorre, Dorcas Li, Maurice Tohme, Zaid Haque, Ian Dillingham, and Hannah Perlstein. I would also like to thank several additional Faculty who have helped shape my dissertation work through thoughtful discussion and guidance: Dr. Sami Barmada, Dr. Peter Todd, and Dr. Bill Dauer. Additional collaborators and funding sources are acknowledged throughout the dissertation.

Table of Contents

List of Figures

Abstract

Spinocerebellar ataxia type 3 (SCA3) is a progressive neurodegenerative disorder and the most common dominantly inherited ataxia worldwide. The genetic cause of SCA3 was first identified over 25 years ago, yet there remains no effective therapies to slow or alter progression of this debilitating and ultimately fatal disorder. One of nine polyglutamine diseases, SCA3 is caused by a *CAG* trinucleotide repeat expansion in the *ATXN3* gene leading to an extended polyglutamine sequence in the encoded disease protein. Polyglutamine-expanded mutant ATXN3 (mutATXN3) acts through a presumed dominant toxic mechanism that requires its sequestration into neuronal nuclei, but the underlying processes that contribute to neuronal toxicity in SCA3 are still poorly understood. This dissertation aims to address key gaps in our understanding of SCA3 disease mechanisms, and develop new tools and therapies to advance the field towards the ultimate goal of a disease-modifying therapy for SCA3 patients. Chapter 1 reviews SCA3 disease mechanisms, model systems, and progress towards oligonucleotide-based therapies for SCA3. In Chapters 2 and 3, I assess a gene silencing therapeutic approach for SCA3 in multiple cellular and mouse transgenic models of disease. I first perform a short-term proof-of-concept study assessing safety and target engagement of several candidate antisense oligonucleotides (ASO) targeting *ATXN3* in two transgenic mouse models of SCA3. Next, I demonstrate in a longitudinal preclinical study that an anti-*ATXN3* ASO can lead to sustained reduction in mutATXN3 protein and prevent molecular, neuropathological, electrophysiological and behavioral features of the disease in SCA3 transgenic mice. Together, these two preclinical studies establish efficacy of *ATXN3*-targeted ASOs as a disease-modifying therapeutic strategy for SCA3, and support further efforts to develop ASOs for human clinical trials in SCA3. In Chapter 4, I perform the first characterization of a novel SCA3 disease-specific human embryonic stem cell (SCA3-hESC) line, and identify disease-relevant phenotypes in SCA3-hESCs and differentiated cortical neurons. Robust ATXN3

aggregation and formation of aggresomes, two SCA3 phenotypes not observed in any other cell line expressing physiological levels of mutATXN3 protein, were completely rescued following ASO transfection into SCA3-hESCs. These studies validate the SCA3-hESC line as a unique and highly relevant human disease model that holds strong potential to advance understanding of SCA3 disease mechanisms and facilitate the evaluation of possible SCA3 therapies. Finally, Chapter 5 addresses key gaps in our understanding of SCA3, such as why is mutATXN3 transported into neuronal nuclei in SCA3 and how does this lead to neuronal toxicity. Using cellular and mouse models of SCA3, I reveal the first descriptive evidence of generalized impairments in nuclear trafficking as indicated by mislocalization of key proteins regulating nucleocytoplasmic transport (NCT) and formation of cytoplasmic puncta enriched in key NCT proteins. Furthermore, I demonstrate that ASO knockdown of mutATXN3 rescues abnormal subcellular localization of the master nuclear trafficking GTPase RAs-related Nuclear protein (Ran) and improves genomic integrity of neurons in disease-vulnerable brain regions of SCA3 mice. Together, this dissertation demonstrates the significant promise of ASO therapies for SCA3, establishes the utility of SCA3-hESCs for disease modeling and translational studies, and provides evidence for a novel disease mechanism that may contribute to aberrant mutATXN3 behavior and toxicity in SCA3.

CHAPTER 1.
Introduction

Spinocerebellar ataxia type 3 (SCA3), also known as Machado-Joseph Disease (MJD), is an autosomal dominant neurodegenerative disorder caused by a *CAG* trinucleotide repeat expansion in the *ATXN3* gene encoding the deubiquitinase ATXN3[1]. Despite over 25 years of research since identification of the causative genetic mutation, there remains limited understanding of the underlying causes of neuronal dysfunction and degeneration in SCA3 and no effective therapies to slow this progressive and inevitably fatal disorder. This dissertation combines basic and translational approaches with the aim to advance our understanding of disease mechanisms, identify effective therapies, and develop improved *in vitro* disease models for SCA3. In this introductory Chapter, I review the clinical and neuropathological features of SCA3 and what is known regarding the normal function and dysfunction of ATXN3 in disease. I also discuss recently identified roles for nucleocytoplasmic trafficking dysfunction in neurodegenerative processes. Next, I make a case for the potential of gene silencing therapies for the treatment of SCA3. Finally, I discuss current human pluripotent stem cell models of SCA3, including their potential to improve translational studies and some limitations of existing model systems. This overview aims to bring into context the work that will be presented in subsequent chapters of this dissertation.

1.1 Spinocerebellar Ataxia Type 3 (SCA3)

1.1.1 Proteinopathies, microsatellite repeats, and the polyglutamine diseases

The average lifespan has increased from <50 years of age in 1900 to ~80 years in 2010 thanks to major advancements in our understanding, early diagnosis, and treatment of previously untreatable diseases like microbial diseases, cancers and cardiovascular disease[2]. However, the escalating number of elderly persons alive today that have benefitted from decreased morbidity of the aforementioned disorders has made clear the next greatest threat to public health: neurological diseases for which the

overall greatest risk factor is age[3]. In 2011, an estimated 100 million Americans were afflicted with one of over a thousand neurological disorders, the most common of which include Alzheimer's disease (AD) and related dementias, pain-associated disorders, epilepsy, Parkinson's disease (PD), traumatic brain injury, and multiple sclerosis[4]. There are also over 360 neurological diseases classified as rare disorders meaning they affect <200,000 Americans in a given year[4]. The associated societal costs of neurological diseases, such as years of healthy life/employment lost to death or disability and costs of patient care, are estimated to be significantly higher for neurological diseases than for any other class of disorders[5]. Unfortunately, advancements towards development of effective therapies for neurological diseases have not kept pace with those in cancer and cardiovascular treatment. Thus, significant research and funding efforts are urgently needed to combat the growing health crisis presented by these diverse, debilitating, and increasingly common disorders.

Many neurodegenerative diseases including AD, PD, and rare neurological diseases fit into a heterogeneous group of disorders called proteinopathies[6]. Neurodegenerative proteinopathies share a common neuropathological feature – the accumulation of misfolded protein aggregates in affected brain tissues[6,7]. Many, but not all, of these diseases present in adulthood and progress in severity with age[7]. They affect diverse and often multiple brain regions that may extend to peripheral tissue. They present with a range of co-morbidities and associated cognitive, behavioral, and motor impairments[7]. In addition, the underlying misfolded protein seeding aggregation, aggregate characteristics, and their spatial distribution are similarly heterogeneous across the different neurodegenerative proteinopathies[7].

Though all proteinopathies share age as a significant risk factor[3,8], many environmental and genetic risk factors are associated with or directly cause neurodegenerative proteinopathies. Environmental risk factors like pesticides, stress, injury, diet, and smoking increase the risk of diseases like PD, AD, and amyotrophic lateral sclerosis (ALS)[8-10]. Genome-wide association studies have identified genetic risk variants that increase an individual's likelihood of developing a neurodegenerative proteinopathy[11,12]. Many neurodegenerative proteinopathies are also directly caused by heritable or *de novo* genetic mutations[13].

Microsatellite repeat disorders, which include over 20 neurological diseases, are one such family of inheritable neurodegenerative proteinopathies[14]. These disorders are linked to genetic variation in unstable sections of genomic DNA called microsatellite repeats. Microsatellite repeats consist of short DNA motifs, usually 1-6 nucleotides in length, consecutively repeated usually without interruption[14]. More than a thousand microsatellite repeat sequences comprising about 3% of the human genome have been identified throughout both coding and non-coding regions of the human genome[15-17]. Microsatellites in non-coding DNA regions (i.e. within upstream promoter and 5'UTR sequences of genes) may play a role in transcriptional regulation. Many non-coding microsatellites have no identified function, but have been incredibly useful for understanding evolutionary biology and DNA fingerprinting[18]. In addition, ~20-40% of human proteins contain sequences of repetitive amino acids that are encoded from microsatellites within exonic regions of coding genes[17].

The repetitive nature of microsatellite repeats greatly increases their genomic instability, resulting in high mutation rates and genetic diversity in these DNA loci[19,20]. Microsatellite repeats exhibit a propensity to increase or decrease in repeat length generationally and within somatic cells leading to mosaicism in somatic tissue[17,21]. The mutation rate of microsatellite repeats generally increases with increasing repeat length, and is particularly high for microsatellites enriched in the nucleotides guanine and cytosine[19]. Genetic variation in microsatellite length can have little or no significant biological consequences for an individual. However, severe biological consequences occur when the number of tandem repeats increases above thresholds for a select number of loci. Over two-dozen inherited neurodegenerative or neuromuscular disorders called microsatellite diseases or repeat expansion disorders are directly linked to expanded microsatellite repeats[22]. These diseases can be caused by repeat expansions in non-coding DNA (i.e. within promoter sequences, 3'UTR, 5'UTR, or introns) or within coding DNA leading to translation into repetitive amino acid sequences[14]. A number of repeat expansion diseases and their genetic loci are summarized in **Fig. 1.1**.

The source of toxicity in microsatellite diseases depends on the location and length of the repeat expansion. For example, a *CGG* repeat expansion upstream of the

FMR1 gene triggers extensive methylation of its promoter leading to transcriptional suppression and loss-of-function of the encoded protein FMRP[23]. Pathogenic repeat expansions within the exon of a gene can be translated into repetitive polypeptide sequences that alter protein structure and activity, inducing loss-of-function and/or gain-of-function toxic effects[16]. The most well studied toxic gain-of-function mechanism in microsatellite disorders is the deposition of misfolded protein aggregates containing the repeat expanded protein[24]. *In vitro* studies have shown that tandem amino acid repeats encoded by microsatellite repeats have a high propensity to misfold and form protein aggregates, and in general, increased repeat length positively correlates with increased aggregation efficiency of the encoded protein[24]. The RNA itself that is transcribed from microsatellites can also aberrantly interact with nucleic acid-binding partners to form toxic RNA foci[25]. Often not one, but multiple of these toxic mechanisms simultaneously occur within a single disorder, leading to complex changes in gene expression, RNA structure and behavior, and protein function.

Spinocerebellar ataxia type 3 (SCA3), the focus of this dissertation, is one of a group of nine microsatellite disorders called polyglutamine (polyQ) diseases. As the title suggests, polyQ diseases are caused by a *CAG* trinucleotide repeat expansion within coding DNA that is translated into abnormally long, repetitive polyQ tracts in the disease protein[26]. The nine disorders that make up the polyQ diseases include Huntington's disease (HD), Dentatorubral–pallidoluysian atrophy (DRPLA), spinal bulbar muscular atrophy (SBMA), and six distinct spinocerebellar ataxias (SCAs) including SCA1, SCA2, SCA3, SCA6, SCA7, and SCA17[26]. Genetic and clinical characteristics of the polyQ diseases are summarized in **Table 1.1.** The most prevalent polyQ disease is HD followed by SCA3[22,26]. The polyQ diseases share several key features. They are all: (1) autosomal dominant disorders, with the exception of SBMA which is X-linked and sex limited; (2) affect multiple neural and peripheral tissues predominantly spanning the CNS and neuromuscular systems; (3) typically present in adulthood and exhibit a slow progression in symptoms and pathology; (4) display neuropathological accumulation of protein aggregates containing the polyQ-expanded disease protein; and (5) unfortunately, are fatal disorders with no approved treatments to alter disease course[26].

Beyond these similarities, the polyQ diseases are nine diverse disorders, both in terms of pathology and clinical presentation[26]. The drastically different etiologies of polyQ diseases result from the unique protein contexts in which the polyQ expansions occur in each of these nine diseases. Though these disorders are clearly distinct, insights into one polyQ disease or identification of commonly shared polyQ disease mechanisms may advance our understanding of polyQ diseases and neurodegenerative proteinopathies in general leading to new therapeutic targets for these fatal disorders.

1.1.2 Genetic, clinical, and neuropathological features of SCA3

The genetic neurodegenerative disorder now designated SCA3 was first recognized in the 1970s in several families of Azorean descent as a heritable "ataxia-plus" disorder with overlapping clinical and pathological characteristics[27]. Two of the identified families presenting with this dominant ataxia were descended from William Machado and Antone Joseph leading to the disease designation Machado-Joseph Disease (MJD), a label still regionally used today particularly in Portuguese-speaking countries. In 1993, the genetic mutation causing SCA3 was mapped to chromosome 14q32.1 by two separate groups: one group studying the Azorean-linked MJD lineages and another group which designated the disease SCA3 after discovering that the genetic locus in families exhibiting similar symptoms to SCA1 and SCA2 was distinct from these two previously identified diseases[28]. In 1994, cloning of the SCA3 and MJD genetic loci, which showed they were the same, led to convergence of these diseases into a single disorder that will be referred to here as SCA3[29].

SCA3 is caused by a polyQ-encoding *CAG* trinucleotide expansion in the disease gene now identified as *ATXN3*[28,29]. Unaffected individuals exhibit normal genetic variation in *ATXN3* repeat lengths ranging from 12-44 *CAG* repeats, whereas SCA3 occurs when the repeat length of at least one *ATXN3* allele extends past a threshold of 55 extending as high as 86 in SCA3 patients[30-33]. Like all polyQ diseases, SCA3 patients exhibit a strong positive correlation between *CAG* repeat length in the disease gene and disease severity: patients with longer repeats exhibit earlier onset, faster progression, and greater severity of symptoms than those with repeats closer to the disease threshold[31-33]. SCA3 also exhibits anticipation in the number of *ATXN3 CAG* repeats, a phenomenon shared across the polyQ diseases[31,32]. Anticipation describes

the tendency for expanded microsatellite repeats (e.g. the expanded *CAG* repeat in mutant *ATXN3* in the case of SCA3) to become increasingly longer in subsequent generations particularly when passed from the paternal parent to offspring[33]. When anticipation occurs, it typically leads to more severe disease in offspring.

SCA3 is the most common dominantly inherited form of ataxia worldwide, with an estimated prevalence between 1:50,000 to 1:100,000[22,34]. Significant regional and ethnic differences in SCA3 prevalence have been reported, with the greatest prevalence reported in East Asian countries including China, Japan and Taiwan, as well as Portugal and Brazil[35]. Symptom onset in SCA3 typically begins in adulthood between the third to fifth decade of life and progresses slowly with age[36]. SCA3 patients exhibit a wide range of progressive motor impairments, including prominent cerebellar ataxia with abnormal gait, impaired balance, limb incoordination, dystonia, spasticity, dysarthria, dysphagia, and oculomotor abnormalities[26,36]. Parkinsonism with or without tremors also occurs in a subset of severe SCA3 patients[37]. Though severity and rate of decline is variable across patients, SCA3 brainstem-associated failures usually culminate in death within 10-15 years of symptom onset[38].

Progressive motor impairments observed in SCA3 patients are the result of neuronal dysfunction and loss in somatosensory and motor nuclei spanning the brainstem, cerebellum, midbrain, spinal cord, striatum, and diencephalon[36]. A prominent gross anatomical feature in SCA3 patients is enlargement of the fourth ventricle resulting from atrophy of neurons within the basilar pons, deep cerebellar nuclei, and loss of pontocerebellar fibers and spinocerebellar tracts[33,36]. Post-mortem SCA3 patient brains exhibit significant degeneration of dopaminergic neurons of the substantia nigra and vestibular nuclei[33,36,39]. SCA3 also leads to degeneration of motor neurons of the cranial nerve nuclei, red nucleus, subthalamic nucleus, globus pallidus, and some thalamic nuclei[36,40]. Spinal cord atrophy can also occur in anterior horn, dorsal root ganglia, and dorsal nuclei[41]. Unlike most other SCAs, olivary nuclei and the cerebellar cortex including Purkinje cells are relatively spared in SCA3[36].

The cerebral cortex is also affected in SCA3 patients, although to a lesser extent than brainstem and cerebellar nuclei[42]. Magnetic resonance spectroscopy (MRS) studies of SCA3 patients have identified metabolic abnormalities in white matter tracts

beginning in premanifest SCA3[43]. SCA3 patients exhibit reduced gray matter volume throughout temporal, frontal, parietal and insular areas[44]. Symptomatic SCA3 patients display mild cognitive impairments in executive function and memory, likely reflecting cerebral involvement in disease and/or disruptions to cerebellar-cerebral circuitry[44]. Sleep disorders are also common amongst patients, including REM sleep behavior disorder and restless leg disorder[45,46]. SCA3 pathology is also not limited to the central nervous system (CNS), with patients exhibiting progressive peripheral neuropathy particularly in distal limbs leading to muscle atrophy and areflexia[47,48].

Accumulation of ubiquitinated protein aggregates or inclusions containing the mutant polyQ-expanded ATXN3 is found throughout vulnerable brain regions in SCA3[30,49,50]. Neuronal nuclear inclusions (NNI) make up the majority of aggregates, though smaller neuronal cytoplasmic inclusions (NCIs) and distal axonal aggregates do occur[51,52]. Similarly to aggregates in other polyQ diseases, ATXN3 NNI stain positive for many other proteins, including ubiquitin, heat shock factor proteins, proteasomal subunits, transcription factors, autophagy-associated chaperones such as p62, other polyQ proteins, and non-expanded wildtype ATXN3[52-55]. The exact role that ATXN3 aggregation plays in SCA3 remains unclear, although it is generally accepted that the sequestration of critical protein quality control machinery into protein aggregates contributes to neuronal stress[56].

There remains a limited understanding of why only selective nuclei are affected in SCA3, or why there is such variability in the *CAG* repeat length threshold for disease. It is also unclear why the polyQ diseases demonstrate such significant heterogeneity in the regional distribution of aggregate neuropathology and brain atrophy, disease severity, age-of-onset, and rate of disease progression, [26]. Clearly, understanding the normal functions of each of the polyQ proteins is critical to elucidating the cause of these distinct disease features in the polyQ disorders. In the next section, I explore what we currently know regarding ATXN3 normal function and its apparent dysfunction in SCA3.

1.2 The ATXN3 protein in normal and disease states

SCA3 is caused by a pathogenic polyQ expansion in exon 10 of the gene *ATXN3* encoding the ATXN3 protein[29]. As a deubiquitinating enzyme (DUB), non-expanded

ATXN3 plays pleiotropic roles in the ubiquitin proteasome system (UPS), macroautophagy, transcriptional regulation, cytoskeletal organization, and DNA damage repair (**Fig. 1.2**)[1,57-62]. Like all polyQ disease proteins, polyQ-expanded mutant ATXN3 (mutATXN3) exhibits altered cellular localization, activity, and an increased propensity to misfold and aggregate in vulnerable brain tissue. MutATXN3 likely perturbs normal cellular processes through multiple predominantly toxic-gain-of-function mechanisms, including: (1) altered protein-protein interactions with endogenous substrates or atypical substrates; (2) altered DUB enzymatic activity; and (3) sequestration of key regulators of cellular homeostasis into NNIs[1]. However, which abnormal interactions or pathway perturbations contribute most to neuronal dysfunction and cell death in SCA3 remains unclear.

1.2.1 ATXN3 and its role in ubiquitin-dependent protein quality control

As a DUB, ATXN3 plays roles in protein surveillance and ubiquitin-dependent quality control through the editing of ubiquitin chains on poly-ubiquitinated substrates (**Fig. 1.2**)[1]. Non-pathogenic ATXN3 is approximately 42-44 kDa in size, and possesses several functional domains that contribute to its function as a DUB (**Fig. 1.3**). The structured globular amino-terminus of ATXN3 contains the highly conserved Josephin domain responsible for catalytic cleavage of ubiquitin chains. The flexible C-terminal tail of ATXN3 contains three ubiquitin interacting motifs (UIMs) that facilitate ATXN3 binding to poly-ubiquitinated chains[1]. ATXN3 is regulated itself by mono-ubiquitination on Lys117, which enhances its DUB activity[63]. Over 50 ATXN3 isoforms have been identified, but the majority of studies have focused on two full-length isoforms: one expressing all three UIMs (3UIM ATXN3) and one lacking the third UIM (2UIM ATXN3)[64]. 3UIM ATXN3 appears to be the major isoform expressed in the brain[64]. The presence or absence of the third UIM likely alters the specificity of ATXN3 towards poly-ubiquitin chains and ubiquitinated substrates[65].

Knocking out ATXN3 *in vitro* or in mice leads to increased levels of total ubiquitinated proteins, suggesting ATXN3 may be a promiscuous DUB[66]. Indeed, studies have identified over 100 substrates or binding partners of ATXN3[67]. Through the editing of ubiquitin chains, ATXN3 can alter a substrate's stability or activity in various ways depending on the substrate and the length or type of ubiquitin chain[68]. *In vitro*

studies have shown that ATXN3 preferentially edits chains of at least four ubiquitin moieties[69]. A tetraubiquitin chain is also the minimum length required for poly-ubiquitinated substrates to be recognized by the 26S proteasome[70]. By binding the minimum length poly-ubiquitin chain on substrates, ATXN3 may prevent complete removal of the ubiquitin chain by other DUBs, and thus facilitate its recognition by the 26S proteasome[56]. ATXN3 DUB activity can also prevent or diminish substrate delivery to the proteasome, such as the case for the autophagy-related substrate Beclin1 and DNA damage repair and cell cycle proteins, Chk1 and p53[71,72].

The presence of a polyQ expansion does not prevent the ability of mutant ATXN3 to bind poly-ubiquitin chains or deter its enzymatic activity *in vitro*[57]. However, the polyQ expansion may alter its substrate specificity or effect protein-protein interactions in subtle ways that are not yet fully understood. Indeed, total levels of poly-ubiquitinated proteins are increased in the SCA3 brain, which may support some loss-of-function contributions to disease[50]. Broad disruptions to UPS as a result of sequestration of UPS regulators into mutATXN3 aggregates also likely contribute to the accumulation of poly-ubiquitinated proteins in SCA3[55].

Overwhelming of the UPS by accumulation of misfolded proteins can trigger aggresome formation, a cellular pathway that serves to consolidate proteotoxic aggregates[73]. Aggresomes are dynamic perinuclear structures regulated by elements of the UPS machinery, including E3 ligases, proteasomal subunits and K63-linked poly-ubiquitin chains, and the autophagy-linked protein p62[74]. Formation of aggresomes also relies on microtubule-dependent transport of aggregated proteins. Non-pathogenic ATXN3 exhibits a preference towards K63 ubiquitin linkages, and directly interacts with many of the cytoskeletal proteins, proteasomal regulators, and autophagic proteins involved in aggresome formation, including tubulin, dynein, HDAC6, Parkin, CHIP, and p62[75-78]. ATXN3 also localizes to, and regulates formation of, aggresomes containing misfolded disease proteins implicated in neurodegenerative disease, including mutant SOD1 and CFTR[79,80]. The ability of ATXN3 to mediate aggresome formation is ablated by mutating catalytic sites or removing UIMs, suggesting that ATXN3's DUB-dependent roles are critical to aggresome formation[80].

Several studies have also identified regulatory roles for wildtype ATXN3 in macroautophagy. In particular, ATXN3 binds to and regulates levels of Beclin1, a key protein within the autophagy pathway involved in nucleation of autophagosomes[81]. The ATXN3-Beclin1 interaction leads to stabilization of Beclin1 and prevents its degradation by the proteasome[81]. PolyQ-expanded mutATXN3 similarly binds to Beclin1, but appears to facilitate its delivery and degradation by the proteasome[81]. Cellular and animal models of SCA3 exhibit altered expression of key autophagy proteins that may be caused in part by polyQ-dependent destabilization of Beclin1. SCA3 patient-derived fibroblasts exhibit reduced levels of Beclin1, decreased autophagic flux, and impaired formation of autophagosomes[82]. Beclin1 levels are significantly reduced in SCA3 patient brains, while other key-autophagy proteins, including ATG-12, LAMP-2, Rab7, Rab1A, and LC3, are significantly increased[50]. Autophagy proteins like p62 and LC3 also localize to ATXN3 aggregates in vulnerable brain regions in SCA3 patients[50]. Thus, perturbations to protein quality control in SCA3 is likely caused by the culminating effect of accumulation of mutATXN3 aggregates, sequestration of key UPS and autophagic regulators, and destabilization of Beclin1.

1.2.2 ATXN3 and the nucleus

Full-length ATXN3 possesses two nuclear export sequences (NES) and a putative nuclear localization sequence (NLS) that facilitate active transport across the nuclear membrane[83,84]. ATXN3 predominantly localizes to the cytoplasm under basal conditions[83], but cellular stressors such as oxidative stress or heat shock trigger rapid nuclear localization of ATXN3 in cells supporting nuclear functions for ATNX3[85]. Abnormal localization of mutATXN3 into neuronal nuclei is also a defining feature of SCA3 neuropathology[36]. Interestingly, preventing nuclear localization of mutATXN3 mitigates many disease features, whereas forcing mutATXN3 into the nucleus enhances disease in SCA3 mice[86]. These findings point to mutATXN3 nuclear accumulation as an important driver to pathogenesis. Therefore, understanding ATXN3's normal and abnormal functions in the nucleus is critically important if we want to understand disease pathogenesis and develop effective therapies for SCA3.

ATXN3 plays complex roles in transcriptional regulation. ATXN3 can bind DNA and directly interacts with over 20 proteins involved in transcriptional regulation[87,88].

ATXN3 has been shown to work in tandem with transcription factors to modulate expression of specific genes. For example, oxidative stress triggers ATXN3-dependent stabilization of the forkhead box O (FOXO4) transcription factor. Once bound, the ATXN3-FOXO4 complex is transported into the nucleus leading to co-activation of genes involved in the oxidative stress response, such as SOD2. PolyQ-expanded ATXN3 impairs the ability of FOXO4 to effectively activate SOD2 transcription, and thus mutATXN3 may inhibit rather than activate the oxidative stress response[60].

ATXN3 can conversely act as a transcriptional repressor. ATXN3 can directly bind to promoter DNA and repress gene expression of multiple targets through recruitment of histone deacetylase 3 (HDAC3)[87]. ATXN3 can also bind to and inhibit activity of the transcriptional activators cAMP-response-element binding (CREB)-binding protein, p300, and p300/CREB-binding protein-associated factor[59]. PolyQ-expanded mutATXN3 is less capable of transcriptional repression, which could lead to dysregulation of multiple target genes. Indeed, knocking out ATXN3 or expressing polyQ-expanded ATXN3 in cells leads to complex transcriptional changes affecting multiple cellular pathways[61,89,90]. However, more research is needed to determine whether complex transcriptional changes occur directly because of impairment to the transcriptional regulatory roles of ATXN3 or indirectly because of downstream consequences of mutATXN3-induced cellular stress.

The accumulation of DNA damage in neurons is a common feature of normal aging and various neurodegenerative diseases including SCA3[91]. Many genetic ataxias are also directly caused by mutations in genes encoding key DNA damage repair proteins. For instance, ataxia telangiectasia is caused by a mutation in the *ATM* gene, a key regulator of DNA damage repair and cellular apoptotic pathways. Mutations in other DNA repair genes such as *Aprataxin* and *TDP1* similarly cause forms of spinocerebellar ataxia, suggesting impairments in DNA repair pathways may be a shared feature of degenerative ataxias[91]. A direct role for ATXN3 in DNA damage repair was first suggested by the discovery that ATXN3 interacts with HHR23A and HHR23B in yeast, two homologs of the mammalian DNA repair protein Rad23[58]. More recent studies have identified intriguing interactions between ATXN3 and DNA end-processing enzyme polynucleotide kinase 3’-phosphatase (PNKP)[92,93]. PNKP is a key DNA repair enzyme

that contributes to neuronal genomic stability. When bound, ATXN3 enhances the phosphatase activity of PNKP, which is necessary for the non-homologous end-joining (NHEJ) DNA repair pathways. Conversely, expression of polyQ-expanded mutATXN3 inhibits PNKP activity, possibly as a result of PNKP sequestration into ATXN3 aggregates[93]. Knockdown of normal ATXN3, PNKP, or expression of mutant ATXN3 increases accumulation of DNA damage and persistent activation of the ATM/p53-dependent DNA repair pathway, suggesting ATXN3 may be a key regulator of PNKP-dependent DNA repair[92,93].

ATXN3 also regulates DNA repair through DUB-dependent stabilization of DNA repair proteins. Several DNA repair proteins, including Chk1 and p53, have been identified as substrates of ATXN3's DUB activity[71,72]. Through the cleavage of ubiquitin chains from DNA repair proteins, ATXN3 prevents their targeted degradation by the proteasome, thus stabilizing the DNA damage repair process and promoting checkpoint signaling. Reducing levels or removal of ATXN3 led to decreased levels of Chk1 and p53 *in vitro*, and increased accumulation of DNA breaks and cellular vulnerability following DNA damage[71,72]. MutATXN3 appears to have an increased affinity for p53, leading to prolonged activation of p53 target genes and p53-dependent neurotoxicity in zebrafish and mouse models of SCA3[72].

Just as with the complex role of mutATXN3 in transcriptional dysregulation in SCA3, it is impossible to identify the root for increased DNA damage in SCA3. DNA damage and DNA break repair are intrinsically linked to autophagy, protein quality control, oxidative stress, and cellular senescence[94]. Thus, accumulation of DNA damage in SCA3 may be directly or indirectly linked to the role of mutATXN3 in DNA repair pathways.

1.3 Nucleocytoplasmic transport dysfunction: A common mechanism in neurodegenerative disease?

As discussed in the previous section, nuclear accumulation of mutATXN3 appears to be a necessary precursor to neuronal dysfunction in SCA3. But many unanswered questions still remain. Why does mutATXN3 preferentially localize to the nucleus? Does sustained nuclear sequestration result from prolonged stress-induced signaling or reflect impaired nuclear export of mutATXN3? Studies thus far have

investigated how ATXN3 is transported across the nuclear membrane and what cellular stressors enhance its nuclear import[84,85]. However, whether nuclear trafficking is broadly impaired in SCA3 is yet to be determined.

Cumulative studies implicate broad impairments to nucleocytoplasmic transport (NCT) as a significant contributor to neurodegenerative proteinopathies such as ALS, AD, HD, and Frontotemporal Dementia (FTD)[95-97]. NCT of large macromolecules including RNA and proteins larger than 40 kDa requires a highly regulated, complex, multi-protein pathway that can be broken down into three key components:

1) Nuclear Pore Complexes: The transfer of all macromolecules between the nucleoplasm and cytoplasm occurs through nuclear pore complexes (NPCs) that span the nuclear membrane. NPCs are one of the largest molecular structures found in the body, each involving ~30 evolutionarily conserved proteins called nucleoporins (NUPs). The types of NUPs that make up a given NPC alter the specificity and permeability of the core to protein cargo[98].
2) Nuclear transport receptors: Nuclear import and export through NPCs is facilitated by nuclear transport receptors, also referred to as importins and exportins. Nuclear transport receptors bind to protein cargo in the nucleoplasm or cytoplasm via specific protein motifs called nuclear export sequences (NES) and nuclear localization sequences (NLS) for facilitated cargo transport through NPCs[99].
3) RAs-related Nuclear protein (Ran) GTPase and Ran binding proteins: Active transport of macromolecules is powered by GTP hydrolysis of the Ran GTPase. In the cytoplasm, GTP-bound Ran is converted to RanGDP triggering importins to bind to NLS of protein cargo for nuclear importation. Conversely, RanGDP is converted to RanGTP in the nucleus to enable exportins to bind to NES of protein cargo for nuclear exportation. Two enzymes mediate nucleotide exchange of Ran: Ran GTPase Activating Protein 1 (RanGAP1) in the nucleus and Regulator of Chromosome Condensation 1 (RCC1) in the cytoplasm. NCT depends on an imbalanced nuclear/cytoplasmic distribution of RanGDP and RanGTP, with high nuclear RanGTP and high cytoplasmic RanGDP concentrations[99].

Perturbations involving all three NCT components have been identified in neurodegenerative diseases. Examples of how each of these components is affected in

various neurodegenerative diseases are presented in the following sections and summarized in **Fig. 1.4**.

1.3.1 Evidence of NPC and nuclear receptor protein involvement in neurodegenerative disease

Key constituents of NPCs and nuclear transport receptors are sequestered into protein aggregates in multiple neurodegenerative proteinopathies. Two of the most common genetic causes of ALS are a $(GGGGCC)_n$ hexanucleotide repeat expansion in the *C9orf72* gene (C9-ALS) and mutations in the SOD1 gene (SOD1-ALS)[100,101]. Almost all ALS patients, including those with C9- and SOD1-ALS, exhibit cytoplasmic mislocalization and aggregation of the 43 kDa TAR DNA-binding protein (TDP-43)[102]. Fifteen NUPs have been found to localize to TDP-43 aggregates in C9-ALS post-mortem patient brains and patient induced pluripotent stem cell (iPSC)-derived neurons[103]. Four NUPs were also identified in TDP-43 aggregates in SOD1-ALS patient brains[104]. Components of the NPC, including NUP62 and NUP88, are similarly sequestered into nuclear polyQ-expanded HTT aggregates found in striatal neurons of HD transgenic mice[97,105]. Both TDP-43 and HD aggregates have been shown to sequester important mRNA export factors that normally localize to NPCs, such as THOC2, NFX1 and Gle1[97,103]. Expression of aggregate-prone TDP-43 fragments also induced sequestration of the nuclear transport receptors importin-α1 and importin-α3 into cytoplasmic aggregates[106].

Cytoplasmic mislocalization of NUPs independent of aggregation also occurs in several neurodegenerative diseases. AD and SOD1-ALS patient brains exhibit increased levels of diffuse cytoplasmic NUPs, and AD models have revealed enhanced interactions of cytoplasmic phospho-tau with NUP98[96,104]. Cytoplasmic stress granules in C9-ALS are also positive for NUPs, importins, and exportins[107]. Many NUPs and nuclear transport receptors contain aggregation-prone, intrinsically disordered regions. It has been suggested that sequestration of NPC components may facilitate protein misfolding in C9-ALS. NPC component genes are also significant disease modifiers of neurodegenerative disease. In a large unbiased screen, 18 NPC constituent genes were identified as disease modifiers in a transgenic fly model of C9-ALS[108], and a

genetic mutation in at least one NPC component gene, *Gle1*, is also a direct cause of ALS[109].

1.3.2 Ran GTPase and Ran binding proteins in neurodegenerative disease

As previously stated, unequal cellular distribution and nucleotide-exchange of Ran is the key driver of NCT of large macromolecules[99]. The enzyme RanGAP1 is responsible for mediating the nucleotide-bound state of Ran within the nucleus for protein export. Cumulative studies support a strong association between RanGAP1 and neurodegenerative disease. RanGAP1 was identified as a potent disease modifier in a forward genetic screen carried out in a transgenic C9orf72 *drosophila* model[110]. RanGAP1 is also sequestered into RNA foci and cytoplasmic stress granules in C9-ALS model systems and post-mortem patient brains[110]. Mutant HTT inclusions in both HD mice and HD patient brains are also strongly positive for RanGAP1[97,105]. The culmination of NPC and RanGAP1 perturbations are likely contributors to abnormal Ran distribution observed in multiple neurodegenerative diseases. A decreased Ran nuclear to cytoplasmic (N/C) ratio has been observed in patient brains or model systems of ALS, tauopathies, HD, FTD, AD, and several laminopathies[95-97,103].

1.3.3 Nuclear envelope abnormalities and loss of nuclear integrity in neurodegenerative diseases

The appearance of irregularly shaped nuclei with nuclear blebbing or deep invaginations can be features of aging or dying cells, but also appears to be a common feature in various neurodegenerative diseases. Nuclear invaginations have been observed in cells expressing mutant tau and in FTD brains[111]. Expression of TDP-43 in cells led to irregularly shaped nuclei with deep invaginations of the nuclear membrane[103]. In HD, the nuclear lamina can form large depressions around perinuclear HTT aggregates[112]. A nucleophagy-based nuclear blebbing and excretion of Laminb1-positive nuclear membrane was also observed in the polyQ disease DRPLA[113]. The nuclear envelope and nuclear membrane play an important role in chromatin stabilization and maintenance of genomic integrity, and thus destabilization of the nuclear envelope may be a major contributor to the accumulation of DNA damage in neurodegenerative diseases.

1.3.4 Perturbations to NCT in SCA3?

All the NCT-associated neurodegenerative diseases mentioned in Section 1.3 share two common features: the mislocalization of the disease-associated protein (i.e. cytoplasmic mislocalization of TDP-43 in ALS/FTD and nuclear mislocalization of mutHTT in HD); and (2) sequestration of key NCT proteins into protein aggregates, RNA foci, or stress granules. Thus, mislocalization of disease proteins may be caused by NCT impairments, and at the same time contribute to NCT impairments through an aggregation-dependent feed-forward mechanism. Though mislocalization and aggregation are also key neuropathological hallmarks of SCA3, to my knowledge no studies have investigated whether Ran-dependent NCT pathways are broadly disrupted in SCA3. This gap in our current understanding of SCA3 pathogenesis will be explored in Chapter 5 of this dissertation.

1.4 SCA3 and the case for gene silencing therapy

There are no approved drugs to slow or stop progression of neurodegeneration in patients with SCA3 or any other polyQ disease. Gaps in our current understanding of disease mechanisms have impeded the ability to identify druggable targets through traditional drug discovery routes. In the absence of a complete understanding of the critical underlying pathways in SCA3, inhibition or reduction of mutATXN3 protein may offer a direct means to mitigate disease at its source preventing downstream toxicity. Importantly, the lack of overt phenotypes following germline or conditional knockout of endogenous ATXN3 in mice suggest that ATXN3 is likely not an essential protein in mammals[114]. Thus, reducing total levels of ATXN3 protein would likely be well tolerated in SCA3 patients.

Cell-based and *in vivo* small molecule screens have identified several candidate drugs that reduce levels of mutATXN3 protein. Two such drugs, citalopram and aripiprazole, are FDA-approved for the treatment of psychiatric disorders and appear to act within the serotonergic pathway[115,116]. In published studies, chronic citalopram and aripiprazole treatment reduced levels of aggregated mutATXN3 protein in SCA3 mice. They also appeared to mitigate disease progression *in vivo*. Specifically, aripiprazole extended the lifespan of drosophila expressing mutATXN3[117], and citalopram improved motor symptoms in SCA3 mice[115,116]. The mechanism of action by which either of these

drugs suppresses mutATXN3 aggregation is not well understood, and both citalopram and aripiprazole could have potentially deleterious off-target effects in the human disease brain. Neither drug has been assessed in SCA3 clinical trials and therefore they are not approved treatments for SCA3. However, the observed improvement in disease features by mutATXN3-reducing drugs in animal models provides support for further development of disease protein-lowering strategies for SCA3.

Targeted oligonucleotide-mediated gene silencing approaches have emerged as powerful tools for selective, targeted knockdown of disease proteins. Gene silencing therapies for the treatment of several neurodegenerative diseases have progressed into ongoing or planned human clinical trials. In this section, I will discuss the two major gene silencing approaches being developed for human diseases, and the current status of these approaches within the preclinical pipeline for SCA3. The basic mechanism of gene silencing of these approaches is summarized in **Fig. 1.5**.

1.4.1 RNA interference

Since its discovery in 1998, RNA interference (RNAi) gene silencing approaches have been exploited to identify regulatory sequences within the genome, discover novel genes contributing to disease, and probe gene function by systematic knockdown of individual genes. RNAi is an evolutionary conserved process for translational suppression that requires the endogenous multi-protein RNA-induced silencing complex (RISC)[118,119,120,121]**.** The RNAi pathway begins with a several step editing process of long double stranded RNA (dsRNA) by the endonucleases Drosha and Dicer to form short duplex RNA called short-interfering RNA (siRNA)[122]. Duplex siRNA is then unwound to expose a single-stranded RNA guide strand that is loaded into assembled RISC machinery. The RNA guide strand functions as a sensor to transport RISC to target mRNA with shared sequence homology. Once bound to target mRNA, the guide strand or RISC can prevent translation of the mRNA through translational steric hindrance or through cleavage of the mRNA by the RISC catalytic protein Argonaute[121,123-125].

Introduction of siRNA, short hairpin RNA (shRNA), and artificial micro-RNA (miRNA) into cells can all trigger the RNAi pathway. However, these “naked” duplex oligonucleotides are rapidly degraded in cells limiting their therapeutic window. Long-

term gene suppression by RNAi requires the use of vector-based delivery systems such as adeno-associated virus (AAV) vectors or lentiviral vectors.

One of the major limitations to all oligonucleotide-mediated gene silencing approaches for neurological diseases is the lack of a non-invasive means to deliver vectors to vulnerable brain regions. The limited permeability of the blood-brain barrier requires the use of direct intracranial or intrathecal delivery to circumvent the nervous system's protective barrier. There are also several safety concerns associated with RNAi therapy that have slowed its clinical translation into patients with neurological diseases. A shared concern for all oligonucleotide-mediated gene silencing approaches is their potential to affect off-target genes leading to unintended toxicity. Double-stranded DNA species also have the potential to activate the cell's immune response, stimulating expression of anti-inflammatory cytokines[126]. Advancements in bioengineering and bioinformatics have decreased the risks of RNAi off-targeting and immune activation, but both are still significant concerns when translating RNAi therapies to human patients. RNAi-based therapies also run the risk of overwhelming the endogenous RNAi pathway leading to cellular toxicity[127]. Finally, the reliance of vector delivery of RNAi has the added concern that if adverse events do occur in an RNAi-treated patient, there is no rapid and efficient means to shut down or remove the RNAi delivery vectors.

1.4.2 Antisense oligonucleotides

Antisense oligonucleotide (ASO) technology began in the late 1970's following the observation that hybridized mRNA-DNA heteroduplexes are not translated into proteins in a eukaryotic cell-free system[128]. ASOs are short 12-50 bp sequences of single or double stranded oligonucleotides that bind to target mRNA through normal Watson-Crick hybridization[129]. The hybridized heteroduplex formed by target mRNA and ASOs can either prevent or modulate protein translation depending on the location of the mRNA sequence targeted and chemical modifications made to the ASO. ASOs containing at least a short sequence of unmodified nucleotides trigger cleavage of the bound mRNA molecule by the endogenous intranuclear enzyme RNaseH[129].

Native oligonucleotide sequences exhibit weak binding affinities to complementary mRNA sequences and are rapidly degraded by nucleases. Thus, ASOs

are almost always chemically modified to alter their function, stability, and specificity[130]. One of the most common ASO chemical modifications is the phosphorothioate (PS) backbone. The PS backbone modification increases ASO stability and contributes to activation of RNaseH-mediated mRNA degradation. Modifications to the 2' end of sugar moieties, such as 2'-O-methoxyethyl (MOE) and 2'-O-methyl sugar modifications, increase an ASO's target-binding affinity and specificity, reducing potential off targeting. However, sugar modifications can obstruct RNaseH activity on target mRNA, so a "gapmer" ASO design is often used to circumvent this limitation. ASO gapmers contain a combination of various backbone and sugar modifications but retain a core sequence of at least five unmodified nucleotide bases to facilitate RNaseH recruitment and cleavage[130].

Like RNAi, a major limitation of ASOs for neurological diseases is their inability to cross the blood brain barrier. Direct injection into the cerebrospinal fluid (CSF) by either intrathecal or intracerebroventricular injection (ICV) are the primary delivery routes being used in animal models and human trials. Unlike RNAi therapy, ASOs are not virally delivered and are eventually degraded by endonucleases. Sustained knockdown of disease proteins thus requires repeated invasive injections of ASOs. However, ASO modifications have enabled increasingly longer ASO half-lives *in vivo*. For example, significant ASO retention and protein suppression can be detected in the brain up to 12-14 weeks after a single ICV injection in various disease mouse models. Therefore, sustained ASO-mediated knockdown of disease proteins like mutATXN3 could be achieved in patients with a few intermittent injections per year.

1.4.3 Progress towards gene silencing therapies for SCA3

Both ASOs and RNAi have proven to be effective approaches for reducing levels of soluble and insoluble mutATXN3 and rescuing various SCA3 molecular features. Several approaches have been assessed with varying efficacy. A few studies have used ASOs aimed at modifying rather than knocking down the disease protein in an attempt to decrease toxicity while retaining normal ATXN3 function. Several studies have assessed ASOs designed to induce exon skipping of the polyQ-containing exon 10 in ATXN3, leading to sustained reduction of high molecular weight ATXN3 protein in SCA3 mice[131,132]. Another study designed an ASO aimed at inducing exon 8 and 9 of ATXN3

in an attempt to prevent formation of a mutATXN3 fragments thought to be a key driver of aggregation in SCA3[133]. This approach did decrease formation of the mutATXN3 fragment, but prevented the DUB activity of ATXN3. Whether either of these approach rescues motor impairments in mice has yet to be shown.

Most gene silencing preclinical SCA3 studies have used virally delivered RNAi or ASOs targeting non-allele specific knockdown of ATXN3 and mutATXN3. Both ASO and RNAi approaches have demonstrated similar efficacy in reducing mutATXN3 protein and preventing mutATXN3 aggregation. An important factor that has been revealed by longitudinal mouse studies of anti-*ATXN3* silencing approaches is the clinical significance of broad versus localized delivery of a gene silencing agent for SCA3. As an example, one preclinical study published in 2013 evaluated knockdown efficiency, safety, and clinical efficacy of *ATXN3*-targeting siRNA in the YACQ84.2 transgenic mouse model of SCA3[134]. Lentiviruses expressing the siRNA were bilaterally injected into cerebellar dentate nuclei leading to siRNA spread through cerebellar and some proximal brainstem nuclei. Results from this study confirmed long-term suppression of mutATXN3 protein levels in cerebellar and proximal nuclei. However, this regionally restricted silencing of mutATXN3 was not sufficient to rescue motor impairments in treated mice[134]. As will be presented at length in Chapters 2 and 3 of this dissertation, ICV delivery of an anti-*ATXN3* ASO into the same SCA3 transgenic mouse model was able to rescue motor impairments[135]. These two studies achieved comparable mutATXN3 reduction in the cerebellum. However, ICV-injected ASOs were widely delivered throughout the CNS enabling widespread mutATXN3 knockdown. As described in Section 1.1, SCA3 affects multiple brain regions spanning the brainstem, cerebellum, spinal cord, and striatum. An effective gene silencing approach for SCA3 will likely require widespread delivery to the many vulnerable brain regions in SCA3 patients.

Both ASOs and RNAi approaches can achieve widespread CNS delivery and exhibit comparable knockdown efficiencies *in vivo*. However, ASOs in general have been more successful in moving into human clinical trials for neurodegenerative diseases. The first ASO-mediated gene modifying therapy gained FDA-approval for the treatment of spinal muscular atrophy (SMA) in 2016[136]. The approved ASO, coined

nusinersen, employs a different mechanism of action than ASOs in development for SCA3 and other polyQ diseases. SMA is caused by loss-of-function mutations in the *Survival Motor Neuron 1* (*SMN1*) gene leading loss of the SMN protein (SMNP). Nusinersen alters splicing of an almost identical *SMN2* transcript to increase production of functional SMNP. Prior to FDA-approval, clinical trials demonstrated that nusinersen was well tolerated and safe, even when delivered into very young infants[137]. Intrathecal delivery also led to widespread delivery throughout the spinal cord and brain regions that are also vulnerable in SCA3. Most importantly, nusinersen treatment proved to be remarkably effective in combatting SMA pathogenesis in patients, extending lifespan, preserving muscle strength, and enabling infantile patients to reach previously unachievable motor milestones[136].

The positive safety profile of nusinersen and its extraordinary efficacy in the treatment of SMA has boosted interest in and excitement for ASO treatment of other genetic neurodegenerative diseases. Following several successful preclinical studies, a phase 1/2a clinical trial began in 2015 assessing an ASO targeting the *HTT* transcript for the treatment of HD, which will soon progress into a phase 3 clinical trial[138]. The success and continued clinical development of ASOs in the treatment of other genetic neurodegenerative diseases solidify ASOs as a feasible and potentially powerful therapy for SCA3.

1.5 Human pluripotent stem cell models of SCA3

Cell culture represents a cornerstone of biological research, enabling countless discoveries and advancements in modern medicine. Most *in vitro* research to this day has relied on immortalized cell strains such as tumor cell lines (i.e. HeLa cells) and modified tissue-derived cells (i.e. HEK 293 cells). Accommodating these cells to survive and propagate *ex vivo* has mostly been achieved through adoption of abnormal genetic and epigenetic changes that inevitably alter normal cellular pathways in unpredictable ways[139]. Beyond the acquisition of abnormal genetic and epigenetic changes, their use is also limited when considering tissue-specific differences that cannot be reflected by a single immortalized cell type/strain. Furthermore, *in vitro* studies of diseases caused by genetic mutations have traditionally relied on exogenous vector delivery of disease genes that drive expression well above endogenous levels. Thus, though they remain

important tools in the biomedical sciences, immortalized cell lines have limited utility in addressing certain biological questions, particularly with respect to tissue-specific biological phenomena.

Advancements in the derivation of human pluripotent stem cell (hPSC) lines and subsequent development of tissue-specific differentiation protocols have presented an enormous opportunity to thwart limitations set by traditional immortalized cells line. By definition, hPSCs, including human embryonic stem cells (hESCs) and human induced pluripotent stem cells (hiPSCs), possess two key characteristics that make them powerful tools for research into normal and abnormal biology: they are (1) self-renewing and can self-propagate through indefinite cell divisions; and (2) capable of undergoing directed differentiation into any somatic cell type derived from the three germinal layers.

The development of disease-specific hPSCs holds enormous potential for advancing our understanding of genetic human diseases like SCA3. This potential lies in the unique properties of hPSCs that enable scientists to probe pathogenic processes in disease-vulnerable human cell types expressing the endogenous disease-causing protein. Disease-specific hPSCs can also be powerful translational tools for assessing drugs in the preclinical pipeline for genetic diseases. The use of hPSCs to investigate SCA3 is still in its infancy, and their role in translational research will only grow as stem cell technologies improve. In this section, I will discuss the key differences in hiPSC and hESC models to understand human disease and review existing hPSC models of SCA3 and polyQ diseases.

1.5.1 Disease-specific human embryonic stem cell models of SCA3

The first hPSCs successfully grown in culture were human embryonic stem cells (hESCs)[140]. hESCs are derived from the inner cell mass formed during the blastocyst stage of early embryogenesis. All hESC lines have been established from excess human embryos created as a result of *in vitro* fertilization (IVF). Disease-specific hESC lines are derived from embryos created through IVF, but with the added step of having been subjected to pre-implantation genetic testing for aneuploidy (PGT-A) or for monogenic disease (PGT-M) to identify embryos carrying genetic mutations priors to implantation (**Fig 1.6**). IVF and PGD are offered at reproductive centers across the

United States as a means to allow at risk parents to prevent passing known disease-causing genetic mutations to offspring.

The required destruction of human embryos in order to generate hESC lines has raised ethical concerns and national debate in the United States, inevitably leading to various federal and state restrictions on hESC development and research. Federal restrictions on hESC research have fluctuated through the last two decades, but current laws restrict federal funding to research involving only those hESCs listed on the NIH registry of approved hESC lines. Currently, there are almost 400 individual lines included on the NIH Human Embryonic Stem Cell Registry. Of these approved hESC lines, over a third carry or are suspected of carrying a disease-causing genetic mutations. Currently, only two polyQ diseases are represented on the NIH registry: Huntington's disease, for which there are 16 approved lines, and SCA3, for which there is only one approved line.

Designated UM134-1 (Registration # - 0286), the SCA3 disease-specific hESC line was developed at the MStem Cell Laboratory at the University of Michigan under the direction of Dr. Gary Smith. It was added to the NIH hESC Registry on September 29, 2014, soon after I began my dissertation work with Dr. Paulson. This novel cell line has been an important tool for much of my dissertation work, and is the main focus of Chapter 4 of this dissertation. Of note, there is also one publication detailing the development of a SCA3 disease-specific hESC line derived in China that is not approved for research in the United States[141]. No data regarding the presence or absence of disease features in this SCA3 hESC line were included in the published report describing derivation of the line. Thus, it is unclear whether SCA3 hESCs other than the UM134-1 SCA3-hESC line recapitulate relevant SCA3 disease features.

1.5.2 Patient-derived human induced pluripotent stem cell models of SCA3

In 2006, Japanese researchers Takahasi and Yamanaka made the discovery that somatic cells can be "induced" or reprogrammed to resemble and behave like ESCs[142]. Their Nobel-winning discovery led many to believe that hiPSCs would supplant the role of hESCs in biomedical research. They can be generated from patient urine, blood, and skin biopsies through relatively non-invasive procedures, making it easy to generate many disease-specific hiPSC lines from multiple patients. Also,

because hiPSCs are derived from somatic tissues they do not incur the same ethical concerns or federal restrictions as hESCs.

Theoretically hiPSCs are equivalent to hESCs in terms of their pluripotency and self-renewal capabilities. However, numerous reports demonstrating physiological differences between hiPSCs and hESCs have led to concerns regarding their actual equivalency[143]. For example, several studies have reported reduced differentiation efficiency, increased propensity to senesce, and variability in transcriptional profiles of hiPSC-derived differentiated populations[144,145]. Abnormalities observed in hiPSCs can stem from incomplete somatic reprogramming and retention of “epigenetic memory” of the somatic cell of origin[146]. The frequency of distinct epigenetic patterning and subtle gene expression differences in hiPSCs generated from the same single individual has necessitated production and inclusion of several clonal hiPSC lines in published studies. The reprogramming process can also lead to chromosomal abnormalities and *de novo* mutations[147]. Thus, lines must be carefully assessed for DNA damage and chromosomal aberrations prior to use in studies. These hiPSC-specific vulnerabilities combine to increase phenotypic variability in hiPSC lines making it difficult to accurately assess disease-relevant differences between affected and control hiPSCs and differentiated cells. Despite these limitations, hiPSCs remain more widely used in biomedical research than hESCs[148].

Several SCA3 patient-derived hiPSC lines have been reported over the past decade. Most published studies perform basic validation of hiPSC properties that do not extend to phenotypic validation of disease features[149-153]. Several studies have employed neurons differentiated from SCA3 hiPSCs to investigate disease features of SCA3. One such study demonstrated that enhancing autophagy leads to decreased mutATXN3 levels in SCA3 hiPSC-derived cortical neurons[154]. Another study demonstrated that excitation induced calpain-mediated cleavage of mutATXN3 into proteotoxic fragments with a high propensity to misfold and stimulate aggregation[155]. However, this study was not successfully reproduced in another study using neurons differentiated from a different SCA3 hiPSC line[156]. A recent study demonstrated that SCA2 and SCA3 hiPSC-derived neurons exhibit altered transcription of genes involved

in glutamate signaling pathways, which is enhanced following the addition of glutamate[157].

Neither aggregation nor nuclear localization of mutATXN3 has been reported in any published SCA3 hiPSCs or derived neurons, or in fact any cell model, without application of genetic or environmental stressors. Nuclear localization and aggregation of polyQ-expanded mutATXN3 are clinical hallmarks of SCA3, and decreasing nuclear import or misfolding of mutATXN3 effectively mitigates disease features in mice. Despite the clear importance of these phenotypes within the SCA3 pathogenic cascade, we still lack answers to basic questions about their role in disease. Is sequestration of mutATXN3 into NNIs neuroprotective or instead a contributor to neuronal dysfunction? Why does mutATXN3 become sequestered in the nucleus? Identifying an SCA3 hPSC line that endogenously replicates key molecular features of SCA3 could provide a valuable tool with which to fill the remaining gaps in our understanding of disease.

1.6 Summary and aims of the dissertation

SCA3 is the most common dominantly inherited ataxia worldwide, and the second most prevalent polyQ disease. As with all other polyQ diseases, there are no approved therapies to mitigate disease progression of this debilitating and inevitably fatal disorder. As a DUB, the SCA3 disease protein ATXN3 plays diverse functions that influence multiple cellular pathways. SCA3 pathogenesis seems to be mostly mediated by toxic gain-of-function mechanisms occurring downstream of mutATXN3 nuclear localization and aggregation. Beyond aggregation, the presence of a polyQ expansion in ATXN3 also appears to interfere with many of its normal functions, which may contribute to neuronal dysfunction in indeterminate ways.

Given the incomplete picture of pathogenic cascade and lack of clear downstream drug targets for SCA3, reducing levels of the causative mutATXN3 protein may provide an opportunity to mitigate disease at one of the earliest steps in disease pathogenesis. The first aim of this dissertation is to assess the safety and efficacy of antisense oligonucleotide-mediated silencing of the *ATXN3* transcript in cellular and mouse models of SCA3. This aim is addressed in two parts. In Chapter 2, I present findings from a short-term preclinical trial assessing safety and target-engagement of several anti-*ATXN3* ASOs in two transgenic mouse models of SCA3. Chapter 3 builds

on this preliminary study to assess whether a promising ASO can rescue or prevent molecular, behavioral, and electrophysiological disease features in an SCA3 mouse model expressing the full-length human *ATXN3* disease gene.

While our results from these two preclinical studies show immense promise for the treatment of SCA3, the fact remains that there is still much to learn about this disease. Most of what we know about ATXN3's function has relied on cell or mouse model systems that drive protein expression well above endogenous levels and are inherently dissimilar from disease-relevant human neurons. Improving our understanding of SCA3 disease mechanisms will arguably require improved disease model systems that better replicate the human disease. The second aim of this dissertation is to develop and demonstrate the suitability of a unique SCA3 hESC line for disease modeling of SCA3.

Finally, the third and last aim of this dissertation addresses a key gap in our understanding of SCA3: Why does mutATXN3 become sequestered in neuronal nuclei? Chapter 5 of this dissertation takes advantage of the biological repository of non-transgenic mice, untreated SCA3 mice, and ASO-treated SCA3 mice collected during the ASO preclinical studies to determine whether impairments in nuclear trafficking may play a role in SCA3 pathogenesis.

1.7 References

1 Costa Mdo, C. & Paulson, H. L. Toward understanding Machado-Joseph disease. *Progress in neurobiology* **97**, 239-257, doi:10.1016/j.pneurobio.2011.11.006 (2012).

2 Crimmins, E. M. Lifespan and Healthspan: Past, Present, and Promise. *The Gerontologist* **55**, 901-911, doi:10.1093/geront/gnv130 (2015).

3 Niccoli, T. & Partridge, L. Ageing as a risk factor for disease. *Current biology : CB* **22**, R741-752, doi:10.1016/j.cub.2012.07.024 (2012).

4 Gooch, C. L., Pracht, E. & Borenstein, A. R. The burden of neurological disease in the United States: A summary report and call to action. *Annals of neurology* **81**, 479-484, doi:10.1002/ana.24897 (2017).

5 Global, regional, and national burden of neurological disorders during 1990-2015: a systematic analysis for the Global Burden of Disease Study 2015. *The Lancet. Neurology* **16**, 877-897, doi:10.1016/s1474-4422(17)30299-5 (2017).

6 Golde, T. E., Borchelt, D. R., Giasson, B. I. & Lewis, J. Thinking laterally about neurodegenerative proteinopathies. *The Journal of clinical investigation* **123**, 1847-1855, doi:10.1172/jci66029 (2013).

7 Kovacs, G. G. Concepts and classification of neurodegenerative diseases. *Handbook of clinical neurology* **145**, 301-307, doi:10.1016/b978-0-12-802395-2.00021-3 (2017).

8 Niccoli, T., Partridge, L. & Isaacs, A. M. Ageing as a risk factor for ALS/FTD. *Human molecular genetics* **26**, R105-R113, doi:10.1093/hmg/ddx247 (2017).

9 Chin-Chan, M., Navarro-Yepes, J. & Quintanilla-Vega, B. Environmental pollutants as risk factors for neurodegenerative disorders: Alzheimer and Parkinson diseases. *Frontiers in cellular neuroscience* **9**, 124, doi:10.3389/fncel.2015.00124 (2015).
10 Belbasis, L., Bellou, V. & Evangelou, E. Environmental Risk Factors and Amyotrophic Lateral Sclerosis: An Umbrella Review and Critical Assessment of Current Evidence from Systematic Reviews and Meta-Analyses of Observational Studies. *Neuroepidemiology* **46**, 96-105, doi:10.1159/000443146 (2016).
11 Corder, E. H. *et al.* Gene dose of apolipoprotein E type 4 allele and the risk of Alzheimer's disease in late onset families. *Science (New York, N.Y.)* **261**, 921-923 (1993).
12 Robinson, J. L. *et al.* Neurodegenerative disease concomitant proteinopathies are prevalent, age-related and APOE4-associated. *Brain : a journal of neurology* **141**, 2181-2193, doi:10.1093/brain/awy146 (2018).
13 Pihlstrom, L., Wiethoff, S. & Houlden, H. Genetics of neurodegenerative diseases: an overview. *Handbook of clinical neurology* **145**, 309-323, doi:10.1016/b978-0-12-802395-2.00022-5 (2017).
14 Brouwer, J. R., Willemsen, R. & Oostra, B. A. Microsatellite repeat instability and neurological disease. *BioEssays : news and reviews in molecular, cellular and developmental biology* **31**, 71-83, doi:10.1002/bies.080122 (2009).
15 Abecasis, G. R. *et al.* An integrated map of genetic variation from 1,092 human genomes. *Nature* **491**, 56-65, doi:10.1038/nature11632 (2012).
16 Rohilla, K. J. & Gagnon, K. T. RNA biology of disease-associated microsatellite repeat expansions. *Acta neuropathologica communications* **5**, 63, doi:10.1186/s40478-017-0468-y (2017).
17 Payseur, B. A., Jing, P. & Haasl, R. J. A genomic portrait of human microsatellite variation. *Molecular biology and evolution* **28**, 303-312, doi:10.1093/molbev/msq198 (2011).
18 Sawaya, S. *et al.* Microsatellite tandem repeats are abundant in human promoters and are associated with regulatory elements. *PloS one* **8**, e54710, doi:10.1371/journal.pone.0054710 (2013).
19 Gadgil, R., Barthelemy, J., Lewis, T. & Leffak, M. Replication stalling and DNA microsatellite instability. *Biophysical chemistry* **225**, 38-48, doi:10.1016/j.bpc.2016.11.007 (2017).
20 Brinkmann, B., Klintschar, M., Neuhuber, F., Huhne, J. & Rolf, B. Mutation rate in human microsatellites: influence of the structure and length of the tandem repeat. *American journal of human genetics* **62**, 1408-1415, doi:10.1086/301869 (1998).
21 Campbell, I. M., Shaw, C. A., Stankiewicz, P. & Lupski, J. R. Somatic mosaicism: implications for disease and transmission genetics. *Trends in genetics : TIG* **31**, 382-392, doi:10.1016/j.tig.2015.03.013 (2015).
22 Margolis, R. L. & Ross, C. A. Expansion explosion: new clues to the pathogenesis of repeat expansion neurodegenerative diseases. *Trends in molecular medicine* **7**, 479-482 (2001).
23 He, F. & Todd, P. K. Epigenetics in nucleotide repeat expansion disorders. *Seminars in neurology* **31**, 470-483, doi:10.1055/s-0031-1299786 (2011).
24 Darling, A. L. & Uversky, V. N. Intrinsic Disorder in Proteins with Pathogenic Repeat Expansions. *Molecules (Basel, Switzerland)* **22**, doi:10.3390/molecules22122027 (2017).
25 Mankodi, A. *et al.* Myotonic dystrophy in transgenic mice expressing an expanded CUG repeat. *Science (New York, N.Y.)* **289**, 1769-1773 (2000).

26 Stoyas, C. A. & La Spada, A. R. The CAG-polyglutamine repeat diseases: a clinical, molecular, genetic, and pathophysiologic nosology. *Handbook of clinical neurology* **147**, 143-170, doi:10.1016/b978-0-444-63233-3.00011-7 (2018).
27 Coutinho, P. & Andrade, C. Autosomal dominant system degeneration in Portuguese families of the Azores Islands. A new genetic disorder involving cerebellar, pyramidal, extrapyramidal and spinal cord motor functions. *Neurology* **28**, 703-709 (1978).
28 Haberhausen, G., Damian, M. S., Leweke, F. & Muller, U. Spinocerebellar ataxia, type 3 (SCA3) is genetically identical to Machado-Joseph disease (MJD). *Journal of the neurological sciences* **132**, 71-75 (1995).
29 Kawaguchi, Y. *et al.* CAG expansions in a novel gene for Machado-Joseph disease at chromosome 14q32.1. *Nature genetics* **8**, 221-228, doi:10.1038/ng1194-221 (1994).
30 Paulson, H. L. Dominantly inherited ataxias: lessons learned from Machado-Joseph disease/spinocerebellar ataxia type 3. *Seminars in neurology* **27**, 133-142, doi:10.1055/s-2007-971172 (2007).
31 Maciel, P. *et al.* Correlation between CAG repeat length and clinical features in Machado-Joseph disease. *American journal of human genetics* **57**, 54-61 (1995).
32 Maruyama, H. *et al.* Molecular features of the CAG repeats and clinical manifestation of Machado-Joseph disease. *Human molecular genetics* **4**, 807-812 (1995).
33 Durr, A. *et al.* Spinocerebellar ataxia 3 and Machado-Joseph disease: clinical, molecular, and neuropathological features. *Annals of neurology* **39**, 490-499, doi:10.1002/ana.410390411 (1996).
34 Gardiner, S. L. *et al.* Prevalence of Carriers of Intermediate and Pathological Polyglutamine Disease-Associated Alleles Among Large Population-Based Cohorts. *JAMA neurology*, doi:10.1001/jamaneurol.2019.0423 (2019).
35 Buijsen, R. A. M., Toonen, L. J. A., Gardiner, S. L. & van Roon-Mom, W. M. C. Genetics, Mechanisms, and Therapeutic Progress in Polyglutamine Spinocerebellar Ataxias. *Neurotherapeutics : the journal of the American Society for Experimental NeuroTherapeutics*, doi:10.1007/s13311-018-00696-y (2019).
36 Rub, U. *et al.* Clinical features, neurogenetics and neuropathology of the polyglutamine spinocerebellar ataxias type 1, 2, 3, 6 and 7. *Progress in neurobiology* **104**, 38-66, doi:10.1016/j.pneurobio.2013.01.001 (2013).
37 Park, H., Kim, H. J. & Jeon, B. S. Parkinsonism in spinocerebellar ataxia. *BioMed research international* **2015**, 125273, doi:10.1155/2015/125273 (2015).
38 Diallo, A. *et al.* Survival in patients with spinocerebellar ataxia types 1, 2, 3, and 6 (EUROSCA): a longitudinal cohort study. *The Lancet. Neurology* **17**, 327-334, doi:10.1016/s1474-4422(18)30042-5 (2018).
39 Rub, U. *et al.* Degeneration of the central vestibular system in spinocerebellar ataxia type 3 (SCA3) patients and its possible clinical significance. *Neuropathology and applied neurobiology* **30**, 402-414, doi:10.1111/j.1365-2990.2004.00554.x (2004).
40 Rub, U. *et al.* Thalamic involvement in a spinocerebellar ataxia type 2 (SCA2) and a spinocerebellar ataxia type 3 (SCA3) patient, and its clinical relevance. *Brain : a journal of neurology* **126**, 2257-2272, doi:10.1093/brain/awg234 (2003).
41 Fahl, C. N. *et al.* Spinal cord damage in Machado-Joseph disease. *Cerebellum (London, England)* **14**, 128-132, doi:10.1007/s12311-014-0619-7 (2015).
42 Yamada, M., Hayashi, S., Tsuji, S. & Takahashi, H. Involvement of the cerebral cortex and autonomic ganglia in Machado-Joseph disease. *Acta neuropathologica* **101**, 140-144 (2001).
43 Joers, J. M. *et al.* Neurochemical abnormalities in premanifest and early spinocerebellar ataxias. *Annals of neurology* **83**, 816-829, doi:10.1002/ana.25212 (2018).

44 Lopes, T. M. *et al.* Widespread neuronal damage and cognitive dysfunction in spinocerebellar ataxia type 3. *Journal of neurology* **260**, 2370-2379, doi:10.1007/s00415-013-6998-8 (2013).
45 Pedroso, J. L. *et al.* Sleep disorders in machado-joseph disease: frequency, discriminative thresholds, predictive values, and correlation with ataxia-related motor and non-motor features. *Cerebellum (London, England)* **10**, 291-295, doi:10.1007/s12311-011-0252-7 (2011).
46 Seshagiri, D. V. *et al.* Assessment of Sleep Spindle Density among Genetically Positive Spinocerebellar Ataxias Types 1, 2, and 3 Patients. *Annals of neurosciences* **25**, 106-111, doi:10.1159/000484516 (2018).
47 Suga, N. *et al.* Schwann cell involvement in the peripheral neuropathy of spinocerebellar ataxia type 3. *Neuropathology and applied neurobiology* **40**, 628-639, doi:10.1111/nan.12055 (2014).
48 Linnemann, C. *et al.* Peripheral Neuropathy in Spinocerebellar Ataxia Type 1, 2, 3, and 6. *Cerebellum (London, England)* **15**, 165-173, doi:10.1007/s12311-015-0684-6 (2016).
49 Schmidt, T. *et al.* An isoform of ataxin-3 accumulates in the nucleus of neuronal cells in affected brain regions of SCA3 patients. *Brain pathology (Zurich, Switzerland)* **8**, 669-679 (1998).
50 Sittler, A. *et al.* Deregulation of autophagy in postmortem brains of Machado-Joseph disease patients. *Neuropathology : official journal of the Japanese Society of Neuropathology* **38**, 113-124, doi:10.1111/neup.12433 (2018).
51 Hayashi, M., Kobayashi, K. & Furuta, H. Immunohistochemical study of neuronal intranuclear and cytoplasmic inclusions in Machado-Joseph disease. *Psychiatry and clinical neurosciences* **57**, 205-213, doi:10.1046/j.1440-1819.2003.01102.x (2003).
52 Seidel, K. *et al.* Axonal inclusions in spinocerebellar ataxia type 3. *Acta neuropathologica* **120**, 449-460, doi:10.1007/s00401-010-0717-7 (2010).
53 Chai, Y., Koppenhafer, S. L., Bonini, N. M. & Paulson, H. L. Analysis of the role of heat shock protein (Hsp) molecular chaperones in polyglutamine disease. *The Journal of neuroscience : the official journal of the Society for Neuroscience* **19**, 10338-10347 (1999).
54 Uchihara, T. *et al.* Non-expanded polyglutamine proteins in intranuclear inclusions of hereditary ataxias--triple-labeling immunofluorescence study. *Acta neuropathologica* **102**, 149-152 (2001).
55 Chai, Y., Koppenhafer, S. L., Shoesmith, S. J., Perez, M. K. & Paulson, H. L. Evidence for proteasome involvement in polyglutamine disease: localization to nuclear inclusions in SCA3/MJD and suppression of polyglutamine aggregation in vitro. *Human molecular genetics* **8**, 673-682 (1999).
56 Li, X., Liu, H., Fischhaber, P. L. & Tang, T. S. Toward therapeutic targets for SCA3: Insight into the role of Machado-Joseph disease protein ataxin-3 in misfolded proteins clearance. *Progress in neurobiology* **132**, 34-58, doi:10.1016/j.pneurobio.2015.06.004 (2015).
57 Burnett, B., Li, F. & Pittman, R. N. The polyglutamine neurodegenerative protein ataxin-3 binds polyubiquitylated proteins and has ubiquitin protease activity. *Human molecular genetics* **12**, 3195-3205, doi:10.1093/hmg/ddg344 (2003).
58 Doss-Pepe, E. W., Stenroos, E. S., Johnson, W. G. & Madura, K. Ataxin-3 interactions with rad23 and valosin-containing protein and its associations with ubiquitin chains and the proteasome are consistent with a role in ubiquitin-mediated proteolysis. *Molecular and cellular biology* **23**, 6469-6483 (2003).

59 Li, F., Macfarlan, T., Pittman, R. N. & Chakravarti, D. Ataxin-3 is a histone-binding protein with two independent transcriptional corepressor activities. *The Journal of biological chemistry* **277**, 45004-45012, doi:10.1074/jbc.M205259200 (2002).
60 Araujo, J. *et al.* FOXO4-dependent upregulation of superoxide dismutase-2 in response to oxidative stress is impaired in spinocerebellar ataxia type 3. *Human molecular genetics* **20**, 2928-2941, doi:10.1093/hmg/ddr197 (2011).
61 Evert, B. O. *et al.* Gene expression profiling in ataxin-3 expressing cell lines reveals distinct effects of normal and mutant ataxin-3. *Journal of neuropathology and experimental neurology* **62**, 1006-1018 (2003).
62 Rodrigues, A. J. *et al.* Absence of ataxin-3 leads to cytoskeletal disorganization and increased cell death. *Biochimica et biophysica acta* **1803**, 1154-1163, doi:10.1016/j.bbamcr.2010.07.004 (2010).
63 Todi, S. V. *et al.* Ubiquitination directly enhances activity of the deubiquitinating enzyme ataxin-3. *The EMBO journal* **28**, 372-382, doi:10.1038/emboj.2008.289 (2009).
64 Harris, G. M., Dodelzon, K., Gong, L., Gonzalez-Alegre, P. & Paulson, H. L. Splice isoforms of the polyglutamine disease protein ataxin-3 exhibit similar enzymatic yet different aggregation properties. *PloS one* **5**, e13695, doi:10.1371/journal.pone.0013695 (2010).
65 Weishaupl, D. *et al.* Physiological and pathophysiological characteristics of ataxin-3 isoforms. *The Journal of biological chemistry* **294**, 644-661, doi:10.1074/jbc.RA118.005801 (2019).
66 Schmitt, I. *et al.* Inactivation of the mouse Atxn3 (ataxin-3) gene increases protein ubiquitination. *Biochemical and biophysical research communications* **362**, 734-739, doi:10.1016/j.bbrc.2007.08.062 (2007).
67 Paulson, H. L., Shakkottai, V. G., Clark, H. B. & Orr, H. T. Polyglutamine spinocerebellar ataxias - from genes to potential treatments. *Nature reviews. Neuroscience* **18**, 613-626, doi:10.1038/nrn.2017.92 (2017).
68 do Carmo Costa, M. *et al.* Ataxin-3 plays a role in mouse myogenic differentiation through regulation of integrin subunit levels. *PloS one* **5**, e11728, doi:10.1371/journal.pone.0011728 (2010).
69 Winborn, B. J. *et al.* The deubiquitinating enzyme ataxin-3, a polyglutamine disease protein, edits Lys63 linkages in mixed linkage ubiquitin chains. *The Journal of biological chemistry* **283**, 26436-26443, doi:10.1074/jbc.M803692200 (2008).
70 Thrower, J. S., Hoffman, L., Rechsteiner, M. & Pickart, C. M. Recognition of the polyubiquitin proteolytic signal. *The EMBO journal* **19**, 94-102, doi:10.1093/emboj/19.1.94 (2000).
71 Tu, Y. *et al.* Ataxin-3 promotes genome integrity by stabilizing Chk1. *Nucleic acids research* **45**, 4532-4549, doi:10.1093/nar/gkx095 (2017).
72 Liu, H. *et al.* The Machado-Joseph Disease Deubiquitinase Ataxin-3 Regulates the Stability and Apoptotic Function of p53. *PLoS biology* **14**, e2000733, doi:10.1371/journal.pbio.2000733 (2016).
73 Kopito, R. R. Aggresomes, inclusion bodies and protein aggregation. *Trends in cell biology* **10**, 524-530 (2000).
74 Olzmann, J. A., Li, L. & Chin, L. S. Aggresome formation and neurodegenerative diseases: therapeutic implications. *Current medicinal chemistry* **15**, 47-60 (2008).
75 Bonanomi, M. *et al.* Interactions of ataxin-3 with its molecular partners in the protein machinery that sorts protein aggregates to the aggresome. *The international journal of biochemistry & cell biology* **51**, 58-64, doi:10.1016/j.biocel.2014.03.015 (2014).

76 Mazzucchelli, S. *et al.* Proteomic and biochemical analyses unveil tight interaction of ataxin-3 with tubulin. *The international journal of biochemistry & cell biology* **41**, 2485-2492, doi:10.1016/j.biocel.2009.08.003 (2009).
77 Scaglione, K. M. *et al.* Ube2w and ataxin-3 coordinately regulate the ubiquitin ligase CHIP. *Molecular cell* **43**, 599-612, doi:10.1016/j.molcel.2011.05.036 (2011).
78 Zhou, L. *et al.* p62/sequestosome 1 regulates aggresome formation of pathogenic ataxin-3 with expanded polyglutamine. *International journal of molecular sciences* **15**, 14997-15010, doi:10.3390/ijms150914997 (2014).
79 Wang, H., Ying, Z. & Wang, G. Ataxin-3 regulates aggresome formation of copper-zinc superoxide dismutase (SOD1) by editing K63-linked polyubiquitin chains. *The Journal of biological chemistry* **287**, 28576-28585, doi:10.1074/jbc.M111.299990 (2012).
80 Burnett, B. G. & Pittman, R. N. The polyglutamine neurodegenerative protein ataxin 3 regulates aggresome formation. *Proceedings of the National Academy of Sciences of the United States of America* **102**, 4330-4335, doi:10.1073/pnas.0407252102 (2005).
81 Ashkenazi, A. *et al.* Polyglutamine tracts regulate beclin 1-dependent autophagy. *Nature* **545**, 108-111, doi:10.1038/nature22078 (2017).
82 Onofre, I. *et al.* Fibroblasts of Machado Joseph Disease patients reveal autophagy impairment. *Scientific reports* **6**, 28220, doi:10.1038/srep28220 (2016).
83 Antony, P. M. *et al.* Identification and functional dissection of localization signals within ataxin-3. *Neurobiology of disease* **36**, 280-292, doi:10.1016/j.nbd.2009.07.020 (2009).
84 Sowa, A. S. *et al.* Karyopherin alpha-3 is a key protein in the pathogenesis of spinocerebellar ataxia type 3 controlling the nuclear localization of ataxin-3. *Proceedings of the National Academy of Sciences of the United States of America* **115**, E2624-E2633, doi:10.1073/pnas.1716071115 (2018).
85 Reina, C. P., Zhong, X. & Pittman, R. N. Proteotoxic stress increases nuclear localization of ataxin-3. *Human molecular genetics* **19**, 235-249, doi:10.1093/hmg/ddp482 (2010).
86 Bichelmeier, U. *et al.* Nuclear localization of ataxin-3 is required for the manifestation of symptoms in SCA3: in vivo evidence. *The Journal of neuroscience : the official journal of the Society for Neuroscience* **27**, 7418-7428, doi:10.1523/jneurosci.4540-06.2007 (2007).
87 Evert, B. O. *et al.* Ataxin-3 represses transcription via chromatin binding, interaction with histone deacetylase 3, and histone deacetylation. *The Journal of neuroscience : the official journal of the Society for Neuroscience* **26**, 11474-11486, doi:10.1523/jneurosci.2053-06.2006 (2006).
88 Duarte-Silva, S. & Maciel, P. Pharmacological Therapies for Machado-Joseph Disease. *Advances in experimental medicine and biology* **1049**, 369-394, doi:10.1007/978-3-319-71779-1_19 (2018).
89 Zeng, L. *et al.* Loss of the Spinocerebellar Ataxia type 3 disease protein ATXN3 alters transcription of multiple signal transduction pathways. *PloS one* **13**, e0204438, doi:10.1371/journal.pone.0204438 (2018).
90 Chou, A. H. *et al.* Polyglutamine-expanded ataxin-3 causes cerebellar dysfunction of SCA3 transgenic mice by inducing transcriptional dysregulation. *Neurobiology of disease* **31**, 89-101, doi:10.1016/j.nbd.2008.03.011 (2008).
91 Massey, T. H. & Jones, L. The central role of DNA damage and repair in CAG repeat diseases. *Disease models & mechanisms* **11**, doi:10.1242/dmm.031930 (2018).
92 Gao, R. *et al.* Inactivation of PNKP by mutant ATXN3 triggers apoptosis by activating the DNA damage-response pathway in SCA3. *PLoS genetics* **11**, e1004834, doi:10.1371/journal.pgen.1004834 (2015).

93 Chatterjee, A. *et al.* The role of the mammalian DNA end-processing enzyme polynucleotide kinase 3'-phosphatase in spinocerebellar ataxia type 3 pathogenesis. *PLoS genetics* **11**, e1004749, doi:10.1371/journal.pgen.1004749 (2015).
94 Xie, J. L. & Jarosz, D. F. Mutations, protein homeostasis, and epigenetic control of genome integrity. *DNA repair* **71**, 23-32, doi:10.1016/j.dnarep.2018.08.004 (2018).
95 Zhang, K., Grima, J. C., Rothstein, J. D. & Lloyd, T. E. Nucleocytoplasmic transport in C9orf72-mediated ALS/FTD. *Nucleus (Austin, Tex.)* **7**, 132-137, doi:10.1080/19491034.2016.1172152 (2016).
96 Eftekharzadeh, B. *et al.* Tau Protein Disrupts Nucleocytoplasmic Transport in Alzheimer's Disease. *Neuron* **99**, 925-940 e927, doi:10.1016/j.neuron.2018.07.039 (2018).
97 Grima, J. C. *et al.* Mutant Huntingtin Disrupts the Nuclear Pore Complex. *Neuron* **94**, 93-107 e106, doi:10.1016/j.neuron.2017.03.023 (2017).
98 Beck, M. & Hurt, E. The nuclear pore complex: understanding its function through structural insight. *Nature reviews. Molecular cell biology* **18**, 73-89, doi:10.1038/nrm.2016.147 (2017).
99 Izaurralde, E. & Adam, S. Transport of macromolecules between the nucleus and the cytoplasm. *RNA (New York, N.Y.)* **4**, 351-364 (1998).
100 DeJesus-Hernandez, M. *et al.* Expanded GGGGCC hexanucleotide repeat in noncoding region of C9ORF72 causes chromosome 9p-linked FTD and ALS. *Neuron* **72**, 245-256, doi:10.1016/j.neuron.2011.09.011 (2011).
101 Rosen, D. R. *et al.* A frequent ala 4 to val superoxide dismutase-1 mutation is associated with a rapidly progressive familial amyotrophic lateral sclerosis. *Human molecular genetics* **3**, 981-987 (1994).
102 Vatsavayai, S. C., Nana, A. L., Yokoyama, J. S. & Seeley, W. W. C9orf72-FTD/ALS pathogenesis: evidence from human neuropathological studies. *Acta neuropathologica* **137**, 1-26, doi:10.1007/s00401-018-1921-0 (2019).
103 Chou, C. C. *et al.* TDP-43 pathology disrupts nuclear pore complexes and nucleocytoplasmic transport in ALS/FTD. *Nature neuroscience* **21**, 228-239, doi:10.1038/s41593-017-0047-3 (2018).
104 Shang, J. *et al.* Aberrant distributions of nuclear pore complex proteins in ALS mice and ALS patients. *Neuroscience* **350**, 158-168, doi:10.1016/j.neuroscience.2017.03.024 (2017).
105 Gasset-Rosa, F. *et al.* Polyglutamine-Expanded Huntingtin Exacerbates Age-Related Disruption of Nuclear Integrity and Nucleocytoplasmic Transport. *Neuron* **94**, 48-57 e44, doi:10.1016/j.neuron.2017.03.027 (2017).
106 Woerner, A. C. *et al.* Cytoplasmic protein aggregates interfere with nucleocytoplasmic transport of protein and RNA. *Science (New York, N.Y.)* **351**, 173-176, doi:10.1126/science.aad2033 (2016).
107 Zhang, K. *et al.* Stress Granule Assembly Disrupts Nucleocytoplasmic Transport. *Cell* **173**, 958-971 e917, doi:10.1016/j.cell.2018.03.025 (2018).
108 Freibaum, B. D. *et al.* GGGGCC repeat expansion in C9orf72 compromises nucleocytoplasmic transport. *Nature* **525**, 129-133, doi:10.1038/nature14974 (2015).
109 Kaneb, H. M. *et al.* Deleterious mutations in the essential mRNA metabolism factor, hGle1, in amyotrophic lateral sclerosis. *Human molecular genetics* **24**, 1363-1373, doi:10.1093/hmg/ddu545 (2015).
110 Zhang, K. *et al.* The C9orf72 repeat expansion disrupts nucleocytoplasmic transport. *Nature* **525**, 56-61, doi:10.1038/nature14973 (2015).

111 Paonessa, F. *et al.* Microtubules Deform the Nuclear Membrane and Disrupt Nucleocytoplasmic Transport in Tau-Mediated Frontotemporal Dementia. *Cell reports* **26**, 582-593 e585, doi:10.1016/j.celrep.2018.12.085 (2019).
112 Chapple, J. P., Bros-Facer, V., Butler, R. & Gallo, J. M. Focal distortion of the nuclear envelope by huntingtin aggregates revealed by lamin immunostaining. *Neuroscience letters* **447**, 172-174, doi:10.1016/j.neulet.2008.09.075 (2008).
113 Baron, O. *et al.* Stall in Canonical Autophagy-Lysosome Pathways Prompts Nucleophagy-Based Nuclear Breakdown in Neurodegeneration. *Current biology : CB* **27**, 3626-3642 e3626, doi:10.1016/j.cub.2017.10.054 (2017).
114 Boy, J. *et al.* Reversibility of symptoms in a conditional mouse model of spinocerebellar ataxia type 3. *Hum Mol Genet* **18**, 4282-4295, doi:10.1093/hmg/ddp381 (2009).
115 Esteves, S. *et al.* Preclinical Evidence Supporting Early Initiation of Citalopram Treatment in Machado-Joseph Disease. *Molecular neurobiology*, doi:10.1007/s12035-018-1332-1 (2018).
116 Teixeira-Castro, A. *et al.* Serotonergic signalling suppresses ataxin 3 aggregation and neurotoxicity in animal models of Machado-Joseph disease. *Brain : a journal of neurology* **138**, 3221-3237, doi:10.1093/brain/awv262 (2015).
117 Costa, M. D. C. *et al.* Unbiased screen identifies aripiprazole as a modulator of abundance of the polyglutamine disease protein, ataxin-3. *Brain : a journal of neurology* **139**, 2891-2908, doi:10.1093/brain/aww228 (2016).
118 Montgomery, M. K., Xu, S. & Fire, A. RNA as a target of double-stranded RNA-mediated genetic interference in Caenorhabditis elegans. *Proceedings of the National Academy of Sciences of the United States of America* **95**, 15502-15507 (1998).
119 Fire, A. *et al.* Potent and specific genetic interference by double-stranded RNA in Caenorhabditis elegans. *Nature* **391**, 806-811, doi:10.1038/35888 (1998).
120 Hammond, S. M., Bernstein, E., Beach, D. & Hannon, G. J. An RNA-directed nuclease mediates post-transcriptional gene silencing in Drosophila cells. *Nature* **404**, 293-296, doi:10.1038/35005107 (2000).
121 Hammond, S. M., Boettcher, S., Caudy, A. A., Kobayashi, R. & Hannon, G. J. Argonaute2, a link between genetic and biochemical analyses of RNAi. *Science (New York, N.Y.)* **293**, 1146-1150, doi:10.1126/science.1064023 (2001).
122 Bernstein, E., Caudy, A. A., Hammond, S. M. & Hannon, G. J. Role for a bidentate ribonuclease in the initiation step of RNA interference. *Nature* **409**, 363-366, doi:10.1038/35053110 (2001).
123 Elbashir, S. M. *et al.* Duplexes of 21-nucleotide RNAs mediate RNA interference in cultured mammalian cells. *Nature* **411**, 494-498, doi:10.1038/35078107 (2001).
124 Yang, D., Lu, H. & Erickson, J. W. Evidence that processed small dsRNAs may mediate sequence-specific mRNA degradation during RNAi in Drosophila embryos. *Current biology : CB* **10**, 1191-1200 (2000).
125 Martinez, J., Patkaniowska, A., Urlaub, H., Luhrmann, R. & Tuschl, T. Single-stranded antisense siRNAs guide target RNA cleavage in RNAi. *Cell* **110**, 563-574 (2002).
126 Sioud, M. Induction of inflammatory cytokines and interferon responses by double-stranded and single-stranded siRNAs is sequence-dependent and requires endosomal localization. *Journal of molecular biology* **348**, 1079-1090, doi:10.1016/j.jmb.2005.03.013 (2005).
127 Barik, S. RNAi in moderation. *Nature biotechnology* **24**, 796-797, doi:10.1038/nbt0706-796 (2006).
128 Paterson, B. M., Roberts, B. E. & Kuff, E. L. Structural gene identification and mapping by DNA-mRNA hybrid-arrested cell-free translation. *Proceedings of the National Academy of Sciences of the United States of America* **74**, 4370-4374 (1977).

129 Crooke, S. T. Molecular Mechanisms of Antisense Oligonucleotides. *Nucleic acid therapeutics* **27**, 70-77, doi:10.1089/nat.2016.0656 (2017).
130 Khvorova, A. & Watts, J. K. The chemical evolution of oligonucleotide therapies of clinical utility. *Nature biotechnology* **35**, 238-248, doi:10.1038/nbt.3765 (2017).
131 Evers, M. M. *et al.* Ataxin-3 protein modification as a treatment strategy for spinocerebellar ataxia type 3: removal of the CAG containing exon. *Neurobiology of disease* **58**, 49-56, doi:10.1016/j.nbd.2013.04.019 (2013).
132 Toonen, L. J. A., Rigo, F., van Attikum, H. & van Roon-Mom, W. M. C. Antisense Oligonucleotide-Mediated Removal of the Polyglutamine Repeat in Spinocerebellar Ataxia Type 3 Mice. *Molecular therapy. Nucleic acids* **8**, 232-242, doi:10.1016/j.omtn.2017.06.019 (2017).
133 Toonen, L. J., Schmidt, I., Luijsterburg, M. S., van Attikum, H. & van Roon-Mom, W. M. Antisense oligonucleotide-mediated exon skipping as a strategy to reduce proteolytic cleavage of ataxin-3. *Scientific reports* **6**, 35200, doi:10.1038/srep35200 (2016).
134 Costa Mdo, C. *et al.* Toward RNAi therapy for the polyglutamine disease Machado-Joseph disease. *Molecular therapy : the journal of the American Society of Gene Therapy* **21**, 1898-1908, doi:10.1038/mt.2013.144 (2013).
135 McLoughlin, H. S. *et al.* Oligonucleotide therapy mitigates disease in spinocerebellar ataxia type 3 mice. *Annals of neurology* **84**, 64-77, doi:10.1002/ana.25264 (2018).
136 Paton, D. M. Nusinersen: antisense oligonucleotide to increase SMN protein production in spinal muscular atrophy. *Drugs of today (Barcelona, Spain : 1998)* **53**, 327-337, doi:10.1358/dot.2017.53.6.2652413 (2017).
137 Finkel, R. S. *et al.* Treatment of infantile-onset spinal muscular atrophy with nusinersen: a phase 2, open-label, dose-escalation study. *Lancet (London, England)* **388**, 3017-3026, doi:10.1016/s0140-6736(16)31408-8 (2016).
138 Lane, R. M. *et al.* Translating Antisense Technology into a Treatment for Huntington's Disease. *Methods in molecular biology (Clifton, N.J.)* **1780**, 497-523, doi:10.1007/978-1-4939-7825-0_23 (2018).
139 Gisselsson, D. *et al.* Clonal evolution through genetic bottlenecks and telomere attrition: Potential threats to in vitro data reproducibility. *Genes, chromosomes & cancer*, doi:10.1002/gcc.22685 (2018).
140 Thomson, J. A. *et al.* Embryonic stem cell lines derived from human blastocysts. *Science (New York, N.Y.)* **282**, 1145-1147 (1998).
141 Liu, L. *et al.* Generation of human embryonic stem cell line chHES-472 from abnormal embryos diagnosed with Spinocerebellar ataxia type 3. *Stem cell research* **17**, 584-586, doi:10.1016/j.scr.2016.10.001 (2016).
142 Takahashi, K. & Yamanaka, S. Induction of pluripotent stem cells from mouse embryonic and adult fibroblast cultures by defined factors. *Cell* **126**, 663-676, doi:10.1016/j.cell.2006.07.024 (2006).
143 Narsinh, K. H., Plews, J. & Wu, J. C. Comparison of human induced pluripotent and embryonic stem cells: fraternal or identical twins? *Molecular therapy : the journal of the American Society of Gene Therapy* **19**, 635-638, doi:10.1038/mt.2011.41 (2011).
144 Hu, B. Y. *et al.* Neural differentiation of human induced pluripotent stem cells follows developmental principles but with variable potency. *Proceedings of the National Academy of Sciences of the United States of America* **107**, 4335-4340, doi:10.1073/pnas.0910012107 (2010).
145 Narsinh, K. H. *et al.* Single cell transcriptional profiling reveals heterogeneity of human induced pluripotent stem cells. *The Journal of clinical investigation* **121**, 1217-1221, doi:10.1172/jci44635 (2011).

146 Bock, C. *et al.* Reference Maps of human ES and iPS cell variation enable high-throughput characterization of pluripotent cell lines. *Cell* **144**, 439-452, doi:10.1016/j.cell.2010.12.032 (2011).
147 Gore, A. *et al.* Somatic coding mutations in human induced pluripotent stem cells. *Nature* **471**, 63-67, doi:10.1038/nature09805 (2011).
148 Guhr, A. *et al.* Recent Trends in Research with Human Pluripotent Stem Cells: Impact of Research and Use of Cell Lines in Experimental Research and Clinical Trials. *Stem cell reports* **11**, 485-496, doi:10.1016/j.stemcr.2018.06.012 (2018).
149 Hansen, S. K. *et al.* Generation of spinocerebellar ataxia type 3 patient-derived induced pluripotent stem cell line SCA3.A11. *Stem cell research* **16**, 553-556, doi:10.1016/j.scr.2016.02.040 (2016).
150 Hansen, S. K. *et al.* Generation of spinocerebellar ataxia type 3 patient-derived induced pluripotent stem cell line SCA3.B11. *Stem cell research* **16**, 589-592, doi:10.1016/j.scr.2016.02.042 (2016).
151 Soong, B. W. *et al.* Generation of induced pluripotent stem cells from a patient with spinocerebellar ataxia type 3. *Stem cell research* **18**, 29-32, doi:10.1016/j.scr.2016.12.017 (2017).
152 Hayer, S. N. *et al.* Generation of an induced pluripotent stem cell line from a patient with spinocerebellar ataxia type 3 (SCA3): HIHCNi002-A. *Stem cell research* **30**, 171-174, doi:10.1016/j.scr.2018.06.006 (2018).
153 Wang, Y. *et al.* Generation of induced pluripotent stem cell line (ZZUi004-A) from urine sample of a patient with spinocerebellar ataxia type 3. *Stem cell research* **28**, 71-74, doi:10.1016/j.scr.2018.01.027 (2018).
154 Ou, Z. *et al.* Autophagy Promoted the Degradation of Mutant ATXN3 in Neurally Differentiated Spinocerebellar Ataxia-3 Human Induced Pluripotent Stem Cells. *BioMed research international* **2016**, 6701793, doi:10.1155/2016/6701793 (2016).
155 Koch, P. *et al.* Excitation-induced ataxin-3 aggregation in neurons from patients with Machado-Joseph disease. *Nature* **480**, 543-546, doi:10.1038/nature10671 (2011).
156 Hansen, S. K. *et al.* Induced pluripotent stem cell - derived neurons for the study of spinocerebellar ataxia type 3. *Stem cell research* **17**, 306-317, doi:10.1016/j.scr.2016.07.004 (2016).
157 Chuang, C. Y. *et al.* Modeling spinocerebellar ataxias 2 and 3 with iPSCs reveals a role for glutamate in disease pathology. *Scientific reports* **9**, 1166, doi:10.1038/s41598-018-37774-2 (2019).

1.8 Figures

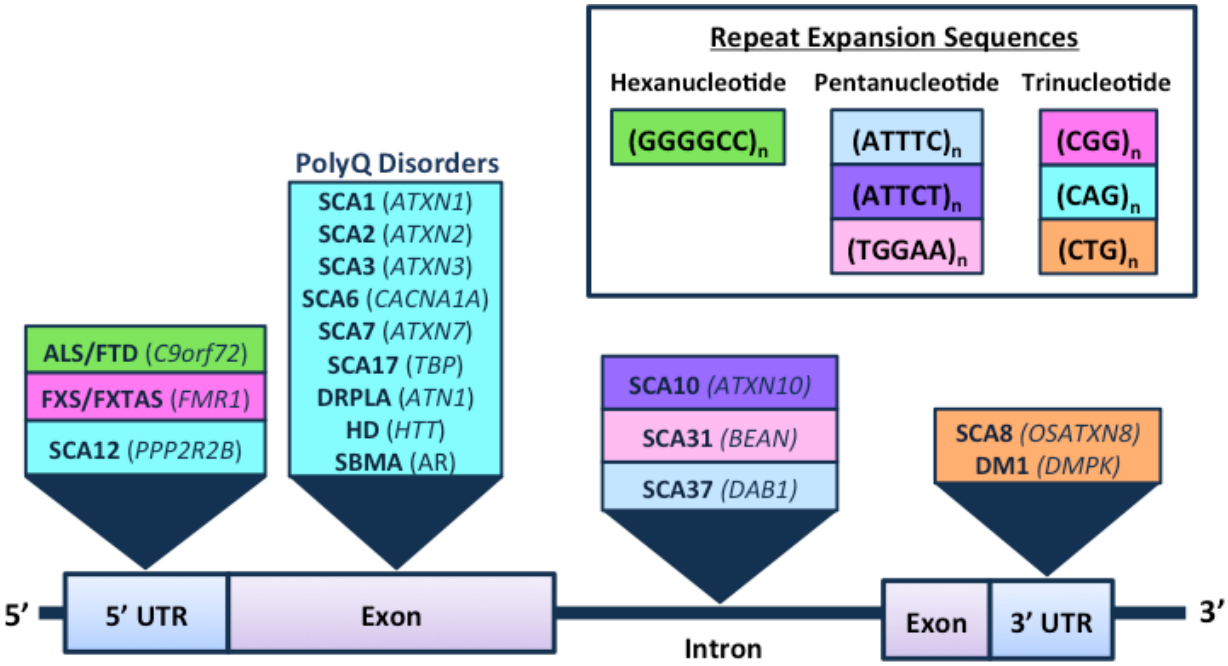

Figure 1.1. Microsatellite repeat expansion disorders and their causative mutations. Diagram summarizing several microsatellite disorders caused by repeat expansions within the 5'UTR, coding exons, intronic regions, or the 3'UTR. Affected genes are listed in parenthesis next to the diseases they cause. Microsatellites are also color coded according to the sequence of nucleotide repeats.

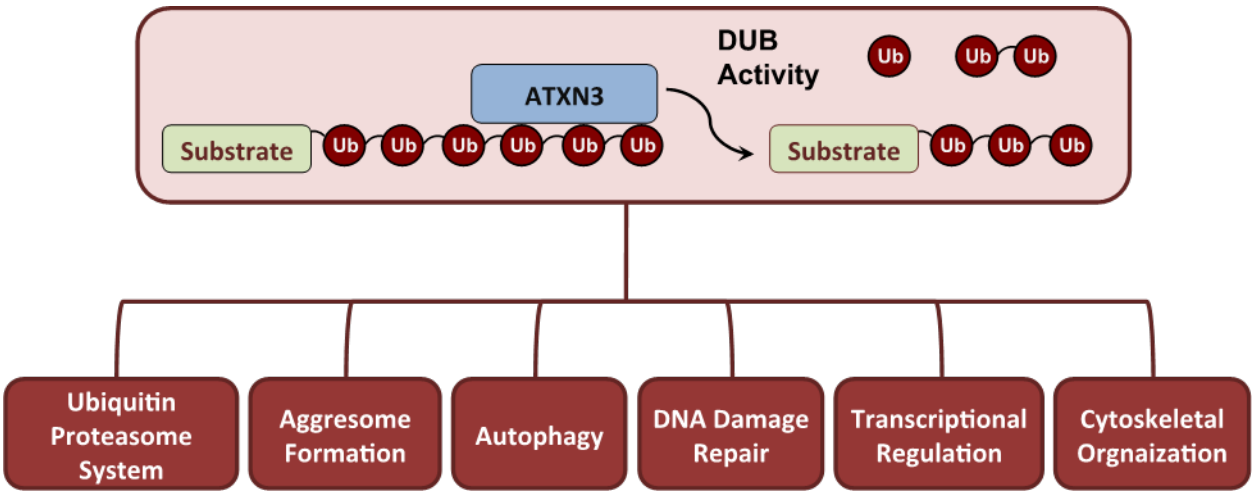

Figure 1.2. ATXN3 deubiquitinase activity plays a regulatory role in multiple cellular homeostatic processes. ATXN3 is a deubiquitinating (DUB) enzyme that edits ubiquitin chains on poly-ubiquitinated substrates. Identified ATXN3 substrates span key cellular pathways, including the ubiquitin proteasome system, aggresome formation, macroautophagy, DNA damage repair, transcriptional regulation, and cytoskeletal organization. (Ub = ubiquitin).

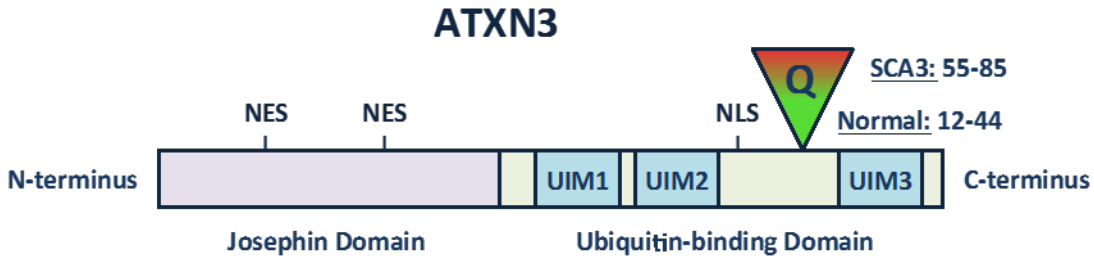

Figure 1.3. Functional domains of the ATXN3 protein. The ATXN3 protein contains a catalytic N-terminal Josephin domain involved in editing of ubiquitin chains, and a flexible C-terminal ubiquitin-binding domain that possesses three ubiquitin interacting motifs (UIMs). The SCA3 causative polyglutamine (polyQ) is located between UIMs 2 and 3. ATXN3 also possess two nuclear export sequences (NES) and a weak nuclear localization sequence (NLS).

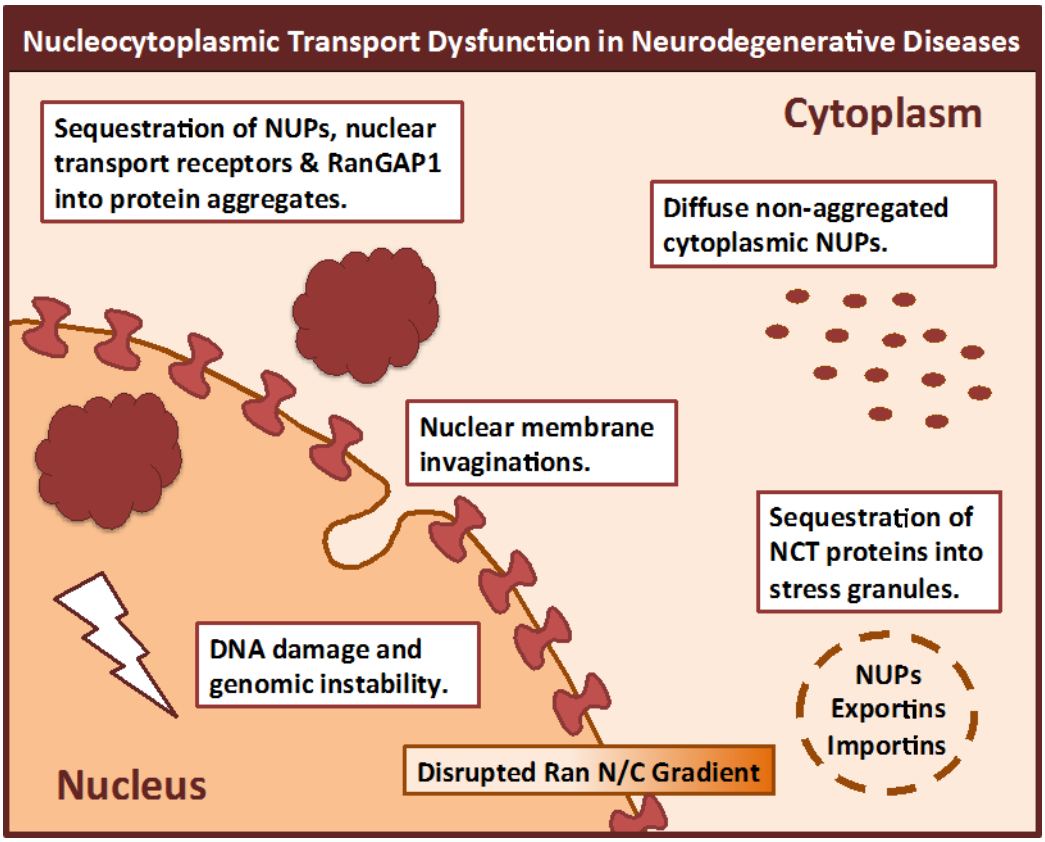

Figure 1.4. Perturbations to nucleocytoplasmic transport (NCT) in neurodegenerative diseases. Summary of identified NCT abnormalities identified in neurodegenerative proteinopathies. (NUPs = nucleoporins; N/C = nuclear to cytoplasmic ratio).

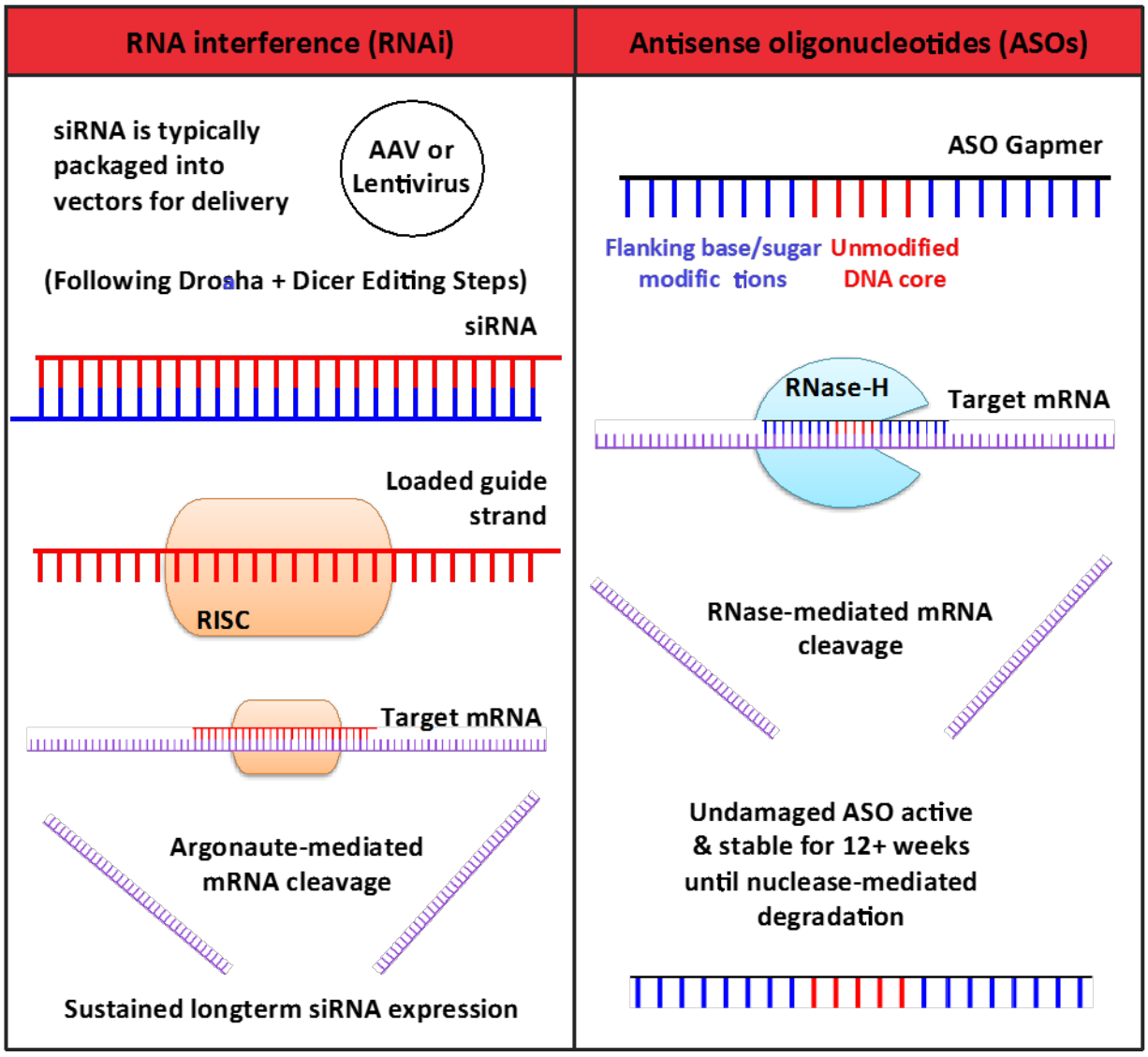

Figure 1.5. RNA interference (RNAi) and antisense oligonucleotide (ASO) gene silencing mechanisms. Mechanisms of action of RNAi and ASO-mediated gene silencing technologies. (AAV = adeno-associated virus; siRNA = short interfering RNA; RISC = RNA-induced silencing complex; RNase-H = ribonuclease H).

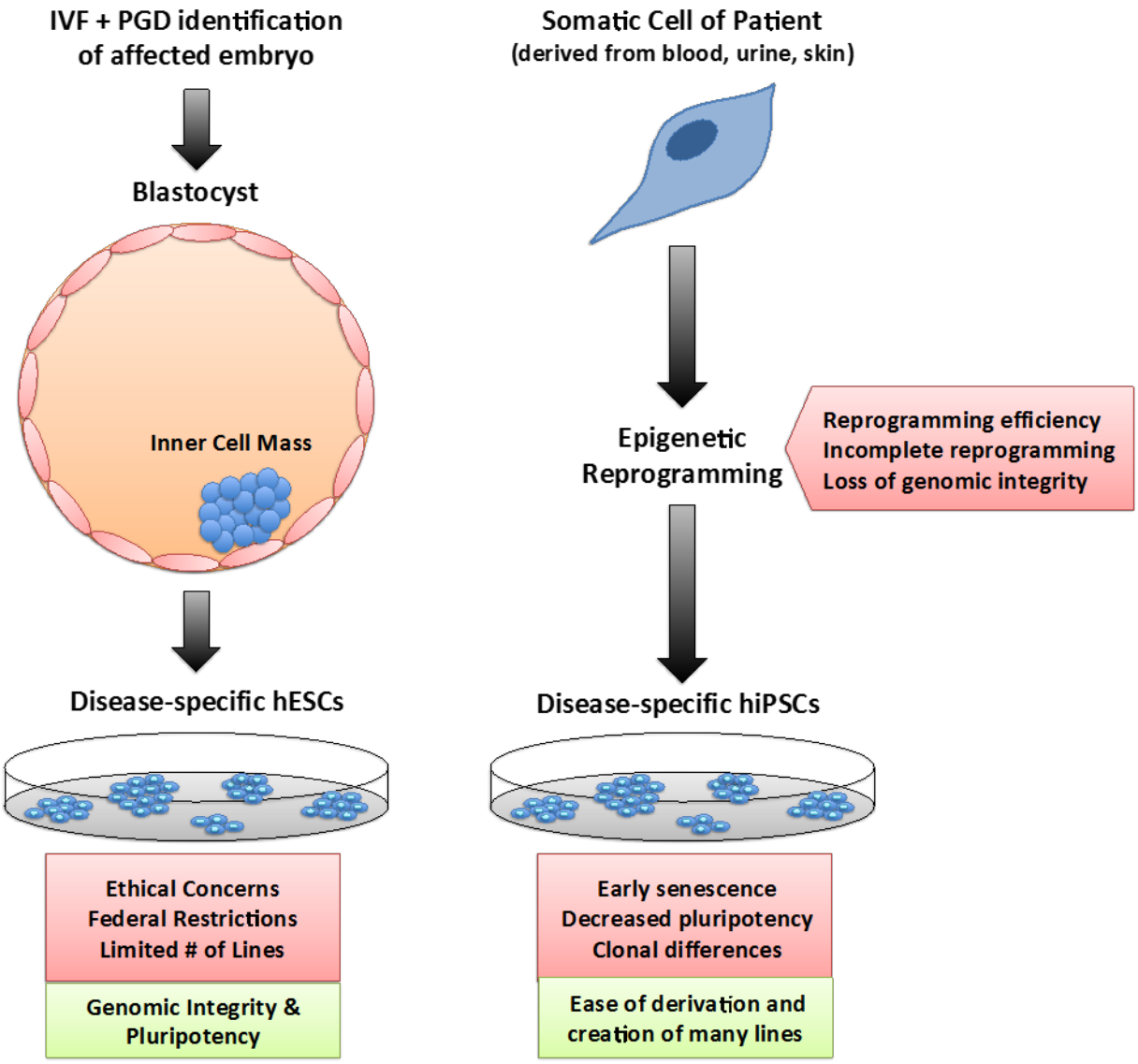

Figure 1.6. Sources and limitations of disease-specific human pluripotent stem cells (hPSCs). Disease-specific human embryonic stem cells (hESCs) are derived from the inner cell mass of affected embryos during the blastocyst stage of embryogenesis. Affected embryos are generated through *in vitro* fertilization (IVF) and identified through pre-implantation genetic diagnosis (PGD). Human induced pluripotent stem cells (hiPSCs) are derived from patient somatic cells and undergo epigenetic reprograming to achieve a hESC-like state. Several pros (green) and potential limitations (red) of each hPSC are listed.

1.9 Tables

Table 1.1. Genetic and clinical features of the polyglutamine diseases.

Disease	Gene; Protein	Protein Function	Clinical features	Neuropathology
SCA1	*ATXN1;* ATXN1	Transcription, RNA metabolism, extracellular matrix organization	Rapid progressing cerebellar ataxia, balance and gait disturbances, oculomotor abnormalities	Cerebellar and brainstem atrophy
SCA2	*ATXN2*; ATXN2	RNA metabolism, translation, stress granule and P-body formation	Progressive cerebellar ataxia, oculomotor abnormalities, tremors, myoclonus, Parkinsonism, sleep disturbances, autonomic dysfunction	Cerebellar atrophy with severe Purkinje cell loss, spinal cord, pontine, medulla nuclei
SCA3	*ATXN3*; ATXN3	Ubiquitin proteasome system, transcription, DNA repair, autophagy cytoskeletal organization, aggresome assembly,	Cerebellar ataxia, oculomotor abnormalities, sleep disturbances, dysarthria, dysphagia, dystonia, peripheral neuropathy	Cerebellar dentate nuclei, pontine and brainstem nuclei, substantia nigra, spinal cord
SCA6	*CACNA1A*; CACNA1A	Subunit of P/Q-type voltage-gated calcium channel, transcription	Slowly progressing cerebellar ataxia, dysarthria, nystagmus, dystonia	Cerebellar atrophy affecting Purkinje cells, basal ganglia
SCA7	*ATXN7*; ATXN7	Cytoskeletal organization, transcription	Retinal degeneration, progressive cerebellar ataxia, dysphagia, dysarthria, hyperreflexia, spasticity	Extensive retinal degeneration, cerebellar and pontine atrophy
SCA17	*TBP*; TBP	Transcription initiation	Cerebellar ataxia, pyramidal signs, chorea, dystonia, psychiatric symptoms	Striatum, Purkinje cells, ventral thalamic nuclei, dentate nucleus, , inferior olive, substantia nigra, hippocampus
HD	*HTT*; HTT	Transcription factor	Chorea, psychiatric symptoms,	Striatum, cerebral cortex, thalamus, pallidum, brainstem
DRPLA	*ATN1*; ATN1	Transcription, vesicular trafficking, DNA repair	Cerebellar ataxia, myoclonus, epilepsy, dementia	Basal ganglia atrophy, brainstem, dentate nuclei
SBMA	*AR*; AR	Steroid hormone nuclear receptor, transcription factor	Muscle atrophy and weakness, fasciculation, androgen insensitivity	Degeneration of lower motor neurons of the anterior horn

CHAPTER 2

Evaluation of Antisense Oligonucleotides Targeting ATXN3 in SCA3 Mouse Models

2.1 Abstract

The most common dominantly inherited ataxia, spinocerebellar ataxia type 3 (SCA3) is an incurable neurodegenerative disorder caused by a CAG repeat expansion in the *ATXN3* gene that encodes an abnormally long polyglutamine tract in the disease protein, ATXN3. Mice lacking ATXN3 are phenotypically normal, hence disease gene suppression offers a compelling approach to slow the neurodegenerative cascade in SCA3. Here we tested antisense oligonucleotides (ASOs) that target human *ATXN3* in two complementary mouse models of SCA3: YAC MJD-Q84.2 (Q84) mice expressing the full-length human *ATXN3* gene and CMV MJD-Q135 (Q135) mice expressing a human *ATXN3* cDNA. Intracerebroventricular injection of ASOs resulted in widespread delivery to the most vulnerable brain regions in SCA3. In treated Q84 mice, three of five tested ASOs reduced disease protein levels by >50% in the brainstem, cerebellum, and cervical spinal cord. Two ASOs also significantly reduced mutant ATXN3 in the mouse forebrain and resulted in no signs of astrogliosis or microgliosis. In Q135 mice expressing a single ATXN3 isoform via a cDNA transgene, ASOs did not result in similar robust ATXN3 silencing. Our results indicate that ASOs targeting full-length human *ATXN3* would likely be well tolerated and could lead to a preventative therapy for SCA3. All of the work of this chapter has been published in:

Moore LR *et al.* Evaluation of Antisense Oligonucleotides Targeting ATXN3 in SCA3 Mouse Models. *Mol Ther Nucleic Acids.* 2017 Jun 16;7:200-210.

2.2 Introduction

Spinocerebellar ataxia type 3 (SCA3) is one of nine polyglutamine expansion diseases and the most common dominantly inherited ataxia in the world[1]. While certain symptoms in SCA3 may respond to symptomatic therapy there is still no effective treatment for this relentlessly progressive and fatal neurodegenerative disease. SCA3 is caused by a CAG repeat expansion in the *ATXN3* gene, resulting in an abnormally long polyglutamine stretch in the encoded ATXN3 protein. Because expression of mutant ATXN3 is an early and necessary step in disease pathogenesis, strategies to reduce expression of the disease gene itself are high on the list of potential therapies[2-6]. Mice lacking the homologous *Atxn3* gene appear normal, suggesting that human ATXN3 may not be an essential protein[7]. Thus lowering expression of the disease gene in SCA3 may be well tolerated. Additionally, in a doxycycline-regulatable transgenic mouse model of SCA3, reducing production of mutant *ATXN3* transcripts via doxycycline treatment beginning at nine weeks eliminated disease features[8]. This result implies that treatment at an early symptomatic stage, prior to extensive irreversible tissue damage, holds promise for SCA3 therapy.

Among gene suppression approaches, viral-mediated gene therapy has been explored by us and others in mouse models of SCA3. In transgenic mice expressing the full human *ATXN3* disease gene, bilateral delivery of small interfering RNA targeting *ATXN3* to the deep cerebellar nuclei (DCN) was well tolerated and led to sustained suppression of mutant ATXN3 in the cerebellum[9], but did not rescue motor deficits and lifespan in these mice[3]. Because degeneration in SCA3 patients extends beyond the cerebellum to include selective brainstem nuclei, striatum and thalamus, effective gene therapy for SCA3 may require broader central nervous system (CNS) delivery[10]. Additional RNA interference studies targeting *ATXN3* succeeded in preventing motor deficits in a lentiviral mouse model of SCA3 in which expanded *ATXN3* was virally delivered to the cerebellum[2,5], but these studies have not yet been replicated in mouse models expressing mutant ATXN3 throughout the CNS.

Antisense oligonucleotides (ASOs) represent a therapeutic non-viral gene suppression approach that is increasingly being tested in neurodegenerative and metabolic disorders. ASOs are short single strands of chemically modified

oligonucleotides that selectively bind complementary mRNA via Watson-Crick hybridization to drive RNase H-mediated cleavage of the targeted mRNA[11]. ASOs targeting disease-causing genes have been tested in rodent models of various neurodegenerative disorders and have advanced into human clinical trials, including ASOs for spinal muscular atrophy (SMA), familial amyotrophic lateral sclerosis (ALS), and Huntington's disease (HD)[12-17]. ASOs targeting *ATXN3* have been developed and tested in cellular and *in vivo* models of SCA3, with some limitations[6,18-22]. Allele-specific ASOs that selectively target the CAG repeat expansion in an effort to preserve wild type ATXN3 function have been tested in SCA3 cellular models, but the ubiquity of CAG repeats in the human transcriptome may pose challenging off-target effects[18-21]. Splice-switching ASOs have also been developed but failed to achieve greater than 50% knockdown of full-length mutant ATXN3 in ASO-treated mouse cerebellum and did not preserve the deubiquitinating function of ATXN3[6,22].

Here we evaluate the efficiency of non-allele specific ASOs targeting human *ATXN3* in two complementary transgenic mouse models of SCA3: the YAC MJD-Q84.2 (Q84) model expressing the full-length human *ATXN3* disease gene with 84 CAG repeats, and the CMV MJD-Q135 (Q135) model expressing a single human ATXN3 isoform from an *ATXN3* cDNA with 135 CAG repeats[23,24]. Overall, two candidate ASOs led to widespread delivery and efficient silencing of mutant human ATXN3 with no immune response in the Q84 mouse model of SCA3. Our results support the continued development of anti-ATXN3 ASOs as therapy for SCA3.

2.3 Results

2.3.1 Identification of human ATXN3 antisense oligonucleotides

To identify active *ATXN3* ASOs, ASOs complementary to human *ATXN3* coding and non-coding regions were screened at a single dose in HEPG2 cells, a human cell line that expresses *ATXN3* transcripts. Following ASO treatment the ability of the ASOs to suppress normal *ATXN3* transcripts was quantified (**Fig 2.1a**). The most active ASOs were subjected to dose response to determine their *in vitro* IC50, and from these five anti-ATXN3 ASOs with similar IC50s (1.2-2 μM) (**Fig 2.1b**) targeting coding or non-coding regions of the human *ATXN3* transcript were selected for further characterization (**Fig 2.1c**). All five anti-ATXN3 ASOs, denoted ASO-1 through ASO-5, as well as a

scrambled control ASO (ASO-Ctrl), shared a 5-8-5 MOE gapmer design with phosphorothioate backbone modifications, as well as 5-mer blocks of 2'-O-methoxyethyl (MOE) modified ribonucleotides flanking an 8-mer block of deoxynucleotides without sugar modifications (**Fig 2.1d**). This MOE gapmer design has previously been shown to increase stability and potency of ASOs and is the design taken into clinical trials for SMA, ALS and HD[15,25,26].

2.3.2 Anti-ATXN3 ASOs Suppress Mutant and Wild-type ATXN3 in SCA3 Patient Fibroblasts

To assess target efficiency of ASOs in patient cells, SCA3 patient-derived fibroblasts (GM06153) were transfected with ASO candidates, ASO-Ctrl, or phosphate-buffered saline (PBS) vehicle alone. GM06153 fibroblasts are heterozygous for the mutant *ATXN3* allele harboring a CAG expansion with 71 repeats and a non-pathological repeat of 23. Cells were transfected with ASOs (4 μM) and harvested 48 or 72 hours later for RNA or protein assessment, respectively. The experimenter was blinded to treatments prior to testing. All five ASOs targeting ATXN3 robustly suppressed ATXN3 transcript and protein levels ($p<0.0001$) (**Figs 2.1e,f**). ASOs suppressed expanded and wild type ATXN3 similarly, indicating no allele selectivity. Only one of the five ASOs, ASO-4, exhibited any toxicity following transfection, with visible detachment of a fraction of treated cells (data not shown).

2.3.3 In Vivo Assessment of ASOs in Hemizygous Q84 Transgenic Mice

All five ASO candidates were subjected to *in vivo* tolerability screening in non-transgenic mice. Animals received a single 700 μg intracerebroventricular (ICV) bolus injection into the right lateral ventricle, and animals were monitored for seven weeks after injection. Animals were weighed and examined weekly. ASO treated animals did not exhibit any overt behavioral deficits or differences in body weight compared to PBS treated controls (data not shown). One ASO-2 treated animal died during surgery, but this was deemed non-drug related. At the conclusion of the study, *Iba1* mRNA in the cortex immediately adjacent to the injection site was quantified as a surrogate for microglial activation, and no significant changes were observed between ASO groups and PBS (data not shown). Thus, all five ASO candidates were selected for further *in vivo* assessment in the Q84 transgenic mouse model of SCA3.

Hemizygous Q84 mice express the full-length human *ATXN3* gene with a pathogenic expansion of 84 CAG repeats at near endogenous ATXN3 expression levels, and thus represent a biologically relevant model of the human disease[24]. This mouse line has been validated in previous SCA3 gene therapy studies[3,24]. Neuropathological features of SCA3, such as enhanced mutant ATXN3 nuclear burden and the formation of cytoplasmic and intranuclear inclusions in neurons, are apparent as early as six weeks of age in hemizygous Q84 mice[3,24].

To assess whether anti-*ATXN3* ASO intervention early in the disease process can suppress accumulation of mutant ATXN3 protein *in vivo*, we injected eight-week-old sex-matched hemizygous Q84 mice with a single stereotaxic ICV bolus injection into the right lateral ventricle. Each mouse received 500 µg ASOs diluted in 10 µL PBS at an injection rate of 0.5 µL per second to enhance ASO spread[12]. Wild type littermates were also injected with PBS vehicle for comparison. Mice were subsequently monitored according to University of Michigan Committee on Use and Care of Animals (UCUCA) guidelines, with no post-surgical adverse events or deaths occurring. Treated brains were harvested four weeks after injection and bisected along the midline. The left hemisphere contralateral to injection was further dissected into forebrain, cerebellum, brainstem and cervical spinal cord for protein and RNA analysis, while the right hemisphere ipsilateral to the injection site was processed for immunohistochemical (IHC) analysis (**Fig 2.2a**). All treatment groups were blinded to the experimenter prior to analysis.

In SCA3, many neuronal populations in the brainstem appear selectively vulnerable and exhibit ATXN3-positive aggregate pathology[27,28]. Four of the five ASO candidates significantly reduced mutant *ATXN3* transcripts in the brainstem relative to vehicle-treated mice, assessed by quantitative RT-PCR (**Fig 2.2b**). Two ASOs targeting the 3'UTR of *ATXN3*, ASO-4 and ASO-5, achieved the greatest transcript reduction in the brainstem, reducing mutant *ATXN3* transcript levels by 63.8 ± 6.8 % ($p<0.001$) and 83.9 ± 4.6 % ($p<0.0001$), respectively, relative to vehicle-treated mice. ASO-1 and ASO-2 treated mice also showed significant transcript reduction in the brainstem (58.2 ± 24.5%, 56.4 ± 23.7%, respectively, $p<0.01$).

Suppression of mutant ATXN3 protein expression was assessed by western blot of left forebrain, cerebellum, brainstem and cervical spinal cord protein lysates from treated mice (**Figs 2.2c,d**). Mirroring the reduction in brainstem transcript levels, mutant ATXN3 protein levels were significantly reduced in the brainstem, cerebellum and cervical spinal cord of mice treated with ASO-2 ($p<0.05$), ASO-4 ($p<0.05$) or ASO-5 ($p<0.01$). Additionally, significant mutant ATXN3 reduction was found in forebrain lysates of ASO-2 ($p<0.05$) and ASO-5 ($p<0.01$) treated mice. In ASO-1 treated mice, high variability in mutant ATXN3 protein levels was observed in all analyzed brain regions, with four of six mice exhibiting mutant ATXN3 suppression of more than 50% relative to vehicle treated mice, while the remaining two mice exhibited no decrease in mutant ATXN3 levels.

Levels of high-molecular-weight (HMW) ATXN3 aggregate species resolvable by SDS-PAGE were also quantified in brainstem protein lysates from treated mice. HMW ATXN3 levels were significantly reduced by 63.7 ± 7.7% and 68.5 ± 7.3% in the brainstem of mice treated with ASO-2 ($p<0.05$) and ASO-5 ($p<0.05$), respectively, relative to vehicle-treated Q84 mice (**Fig 2.2e,f)**. HMW ATXN3 trended towards a decrease in ASO-4 treated mice, but failed to reach significance due to variability across mice ($p=0.09$).

Analysis of brainstem protein lysates also revealed a significant decrease in endogenous murine ATXN3 protein in ASO-1 (42.9 ± 8.3%; $p<0.05$), ASO-2 (40.2 ± 14.4%; $p<0.05$), ASO-4 (42.0 ± 12.0%; $p<0.05$), and ASO-5 (82.6 ± 9.3%; $p<0.0001$) treated Q84 mice relative to vehicle-treated Q84 mice (**Fig 2.2g**). Of the five ASOs tested, only ASO-5 was expected to directly target the murine mRNA transcript due to species conservation of its target sequence in the human and murine *ATXN3* gene (**Fig 2.2b)**. Previous studies have shown that mutant expanded ATXN3 can oligomerize with non-expanded ATXN3, leading to increased retention of both pathogenic and non-pathogenic ATXN3 proteins[29]. Thus, reduction of murine ATXN3 protein may be attributed to decreased interactions with the mutant protein leading to normalization of protein clearance rate. Furthermore, vehicle-treated Q84 mice exhibited paradoxical decreases in *Atxn3* transcript levels ($p<0.05$) (**Fig 2.2b**) and increased endogenous protein levels of murine ATXN3 relative to vehicle-treated wild type animals ($p<0.001$)

(**Fig 2.2g).** This may reflect a negative regulatory feedback effect on *Atxn3* transcription in disease.

ASO delivery and potency in disease-relevant neuronal populations were further investigated with anti-ATXN3 and anti-ASO immunofluorescence on brain sections from the injected hemisphere. Four weeks following injection, all ASOs were widely distributed throughout the brain, including in the striatum, cerebellar lobules, DCN, pons, hippocampus and cerebral cortex (**Fig 2.3a**). Areas of high vulnerability in SCA3, including DCN and pontine nuclei, exhibited high levels of delivered ASO corresponding to clearly apparent decreased levels of ATXN3 expression in these regions (Fig. 3b-3c). Furthermore, in SCA3 ATXN3 abnormally accumulates in neuronal nuclei. Q84 mice treated with ASO-2, ASO-4, and ASO-5 exhibited markedly decreased neuronal nuclear ATXN3 staining in the DCN and pons ($p<0.0001$), two neuronal populations that are highly affected in SCA3, relative to vehicle-treated Q84 mice (**Figs 2.4a-c**). ASO-5 led to the greatest reduction in ATXN3 immunostaining in the DCN and pons, likely due to the fact that it is the only tested ASO that targets both human and murine *ATXN3* transcripts.

To investigate tolerability and safety of ASOs *in vivo*, we assessed transcript levels of markers of immune-reactive cell types, namely astrocytes (*GFAP*) and microglia (*Iba1*), in the brainstem of treated mice. *GFAP* levels were not altered in mice treated with ASO-2 or ASO-5, but were significantly increased in mice treated with ASO-4 ($p<0.05$) (**Fig 2.5a**), the only ASO that also exhibited cellular toxicity in patient fibroblasts. *Iba1* transcript levels were not increased in the brainstem of ASO-2 or ASO-4 treated mice, though *Iba1* levels trended toward an increase in ASO-4 treated mice, mirroring the increased *GFAP* transcript levels in ASO-4 treated mice and further supporting possible toxicity of this ASO. Intriguingly, ASO-5 treatment of Q84 mice actually led to a significant decrease ($p<0.05$) in *Iba1* transcript levels in the brainstem relative to vehicle or ASO-Ctrl treated mice (**Fig 2.5b**). This result suggests a possible rescue of disease-related neuroinflammatory changes in SCA3 mice by ASO-5 treatment.

Immunofluorescence assessment of reactive astrocytes and microglia was performed throughout the brain of the injected hemisphere. Unexpectedly, we noted a

discrepancy in astrocyte-microglia patterning in the DCN of mice treated with ASO-4, specifically. The DCN typically exhibits a pattern of GFAP-positive astrocytes forming a rim around the nucleus, which in turn is dominated by Iba1-positive microglia, with little overlap between the two cell types. However, ASO-4 treated mice consistently demonstrated infiltration of astrocytes from the surrounding region into the DCN, indicative of possible ASO-4 toxicity leading to inflammatory changes in this brain region (**Fig 2.5c**). All mice, including vehicle, ASO-Ctrl, and anti-ATXN3 ASO-treated mice, exhibited similar local gliosis immediately surrounding the injection site (data not shown) but, consistent with our earlier screens in wild type mice, there were no differences in Iba1 or GFAP expression levels in the cerebral cortex neighboring the injection site, where local ASO concentrations were high (**Fig 2.5d**). No apparent difference in the density of GFAP- and Iba1-positive cells was identified in pontine nuclei or any other assessed brain region of ASO-2 and ASO-5 treated mice. Qualitatively, however, more GFAP-positive cells were apparent in the pons of ASO-4 treated mice (**Fig 2.5e**).

2.3.4 In Vivo Assessment of ASOs in Q135 SCA3 Transgenic Mice

The top ASO candidates identified in Q84 mice were similarly evaluated in hemizygous Q135 mice, a transgenic model of SCA3 that expresses an *ATXN3* cDNA splice isoform with a 135 CAG repeat expansion[23]. Of the three ASOs demonstrating significant ATXN3 knockdown in brain regions of Q84 mice, only ASO-4 and ASO-5 target sequences are present in the *ATXN3* cDNA transcript expressed in Q135 mice. Thus, only these two ASOs could be evaluated in Q135 mice (**Fig 2.6a**).

Sex-matched eight-week-old Q135 mice received a single ICV bolus injection of 500 µg ASO-4, 700 µg ASO-5, 700 µg ASO-Ctrl, or PBS into the right lateral ventricle, and brains were harvested four weeks later. The ASO-5 dose was increased to 700 µg to increase potential efficacy, while ASO-4 dose was maintained at 500 µg due to toxicity concerns from previous Q84 mouse studies. As in the Q84 mouse experiment, Q135 brains were bisected along the midline with the left hemisphere used for protein and RNA analysis and the right hemisphere for immunofluorescence with anti-ASO and anti-ATXN3 antibodies.

Mutant *ATXN3* transcript levels were not significantly reduced in the brainstem of either ASO-4 or ASO-5 treated mice relative to vehicle or ASO-Ctrl treated mice,

assessed by quantitative RT-PCR (**Fig 2.6b**). In contrast, wild type *ATXN3* transcript levels were significantly reduced ($p<0.0001$) in ASO-5 treated mice, but not in ASO-4 treated mice, consistent with the conservation of target sequence for ASO-5 but not ASO-4. This reduction in wild type ATXN3 transcript levels confirms effective ASO-5 delivery to the brainstem for targeting, but also supports a greatly reduced targeting capacity of the ASOs for the cDNA transgene relative to the wild type gene. Immunoblotting for ATXN3 also revealed no significant difference in mutant ATXN3 levels in the cerebellum of treated mice (**Fig 2.6c**).

Anti-ASO immunofluorescence confirmed that ASOs were delivered successfully to the cerebellum and pons of Q135 mice, as in Q84 mice (**Figs 2.6d,e**). Anti-ATXN3 fluorescence revealed no visible difference in diffuse ATXN3 protein staining or in ATXN3-positive punctate pathology in ASO-4 treated mice relative to ASO-Ctrl and vehicle-treated mice in the DCN (**Fig 2.6d**) or pons (**Fig 2.6e**). ASO-5 treated mice exhibited almost total silencing of diffuse ATXN3 staining, which we attribute to efficient knockdown of endogenous murine ATXN3. However, ATXN3-positive punctate neuropathology did not appear markedly reduced in the Q135 pontine nuclei of twelve-week-old mice (**Fig 2.6e**).

2.4 Discussion

Our studies here strongly support the promise of ASO-mediated targeting of *ATXN3* as a potentially effective therapeutic approach for SCA3. Several tested ASOs were effective in reducing levels of the pathogenic ATXN3 protein both in human disease fibroblasts and in a mouse model expressing the full-length human mutant *ATXN3* gene.

SCA3 brains exhibit widespread degenerative and neuropathological changes including neuronal loss and gliosis in the DCN, vestibular and other brainstem nuclei, spinocerebellar tracts, substantia nigra, thalamus, and the globus pallidus[27,30]. This broad distribution highlights the need for broad targeting of a therapeutic agent to affected brain regions. Here we identified several ASOs that effectively target the full-length *ATXN3* human transcript in SCA3 patient fibroblasts, including exonic, intronic, and 3'UTR targets. All five ASOs were carried forward in a short-term assessment in the Q84 mouse model of SCA3. Similar to previous ASO studies[17,31-33], we directly injected

ASOs into the lateral ventricle to allow the natural flow of the cerebrospinal fluid to deliver the ASO therapy to affected brain regions of interest. Similar broad ASO delivery throughout the CNS was shown in other rodent models following ICV injection and non-human primates following intrathecal injection in HD ASO studies[12]. Importantly, for three of the five tested ASOs a single ASO injection into symptomatic Q84 transgenic mice was sufficient to significantly reduce (>50%) ATXN3 protein levels in the cerebellum, brainstem and cervical spinal cord. The top ASO candidates also caused a marked reduction in HMW aggregated ATXN3 in the brainstem, detectable on denaturing gels.

In contrast to the robust suppression in Q84 mice, we failed to observe robust ASO-mediated reduction of mutant ATXN3 in a second transgenic model, the Q135 mouse. This lack of efficacy was not due to insufficient delivery since ASO-5 reduced endogenous *Atxn3* levels in Q135 mice much as it did in Q84 mice. Decreased potency of ASO targeting in Q135 mice may be the result of key differences between cDNA-derived and full-length transgenic models of disease. First, the exclusion of intronic sequences in the *ATXN3* transcript of Q135 may significantly alter RNA processing dynamics of the mutant transcript which could have direct effects on ASO targeting capacity. In addition, Q135 mice express a single isoform of human *ATXN3*, the mRNA structure of which may be less accessible to ASO binding than other isoforms. In support of this argument, two previous studies investigating ASO therapy for the polyglutamine disease spinal bulbar muscular atrophy (SBMA) noted much less suppression of the targeted transcript in a cDNA transgenic mouse model than in a mouse model of SBMA expressing the full-length gene[34,35]. Future studies could include other biologically relevant models of SCA3 such as recently available knock-in models to further validate ASO potency[36].

We further assessed the tolerability of the three most effective ASOs *in vivo*. ASO-2 and ASO-5 proved to be safe and well tolerated, as evidenced by the absence of astrocytic or microglial activation after treatment. ASO-5 even decreased transcript levels of the microglia marker *Iba1* in Q84 mice, suggesting a partial rescue of neuroinflammatory changes that occur in SCA3 patient brains as well as in transgenic SCA3 mouse models[23,37]. In contrast to ASO-2 and ASO-5, ASO-4 caused significant

elevation of *GFAP* transcript levels in the brainstem and increased astrocytic invasion into the DCN. Although ASO-4 was designed to have low off-targeting potential, the apparent toxicity in fibroblast and animal models of disease do not support further development of ASO-4 as a potential therapeutic in SCA3. Importantly, the lack of an overt immune response following endogenous ATXN3 suppression, either in the presence or absence of the human disease protein, support previous findings that ATXN3 is likely not an essential protein and non-allele specific silencing of ATXN3 may be well tolerated as a therapeutic approach[7,8]. Future studies may employ additional *in vivo* safety and toxicity evaluations, such as transcriptome analysis or stereology in treated SCA3 mice.

The immediate next step is to move the safe and efficacious ASOs, ASO-2 and ASO-5, into a long-term trial to assess their impact on behavioral phenotypes and animal survival. While hemizygous Q84 mice used in these studies express the full-length human *ATXN3* gene, they display relatively subtle behavioral phenotypes[24]. For a long-term trial, we will need to employ homozygous Q84 mice, which recapitulate numerous aspects of the human disease including quantifiable motor deficits, robust aggregate pathology, and early lethality[3,24]. In summary, we have established the first proof of concept for ASO efficacy and tolerability in a SCA3 mouse model of disease.

2.5 Materials and methods

2.5.1 Animals

All animal procedures were approved by the University of Michigan Committee on the Use and Care of Animals (UCUCA). YACMJD84.2Q-C57BL/6 and CMVMJDQ135-C57BL/6 transgenic mice were housed in cages with a maximum number of five animals and maintained in a standard 12-hour light/dark cycle with food and water *ad libitum*. Genotyping was performed using DNA isolated from tail biopsy at the time of weaning, as previously described[24]. YACMJD84.2Q transgenic mice hemizygosity was determined by standard PCR using GoTaq Green Master Mix (Promega, Madison, WI) to amplify a fragment of the *ATXN3* transgene with primer sequences 5′TGGCCTTCACATGGATGTGAA and 5′CCAGTGACTACTTTGATTCG, and normalizing to a genomic fragment of mouse *Atxn3* chromosome 7 with primer sequences 5′CTCTGTACAGACAGGGAGATGTGAG and

5′GAGGATGCAAAGGAGCCAAGTGACC. CMVMJDQ135 mouse hemizygosity was similarly determined using the CMV primer sequences 5′GAAGACACCGGGACCGATCCAG and 5′CCAGAAGGCTGCTGTAAAAACGTGC. The reactions were performed using a T100 thermocycler (Bio-RAD, Hercules, CA). Genotypes of all studied mice were confirmed using DNA extracted from tails collected postmortem. Animals were euthanized four weeks after ASO ICV bolus, anesthetized with 100 mg/kg ketamine per 10 mg/kg xylazine intraperitoneally, and perfused transcardially with phosphate-buffered saline (PBS).

2.5.2 Antisense Oligonucleotides

The five candidate anti-ATXN3 ASOs and scrambled control ASO used in this study are 18 nucleotides in length with 8 unmodified deoxynucleotides with native sugar-phosphate backbone flanked by five 2'-O-methoxyethylribose modified ribonucleotides on the 5'- and 3'- termini with a phosphorothioate backbone. These ASOs were designed to target the intron, exon or 3'UTR of human *ATXN3*. Oligonucleotides were synthesized as described previously[38,39]. ASOs were solubilized in PBS (without Ca2+ or Mg2+).

2.5.3 Cell lines, electroporation and transfection

SCA3 patient-derived fibroblasts (GM06153) containing an expanded ATXN3 allele (23Q/71Q) were obtained from Coriell Cell Repositories (Camden, NJ). Fibroblasts were maintained at 37°C and 5% CO_2 in DMEM media (HyClone, Pittsburgh, PA) supplemented with 15% fetal bovine serum. HEPG2 cells were obtained from ATCC (Manassas, VA), and maintained in EMEM media (ATCC, Manassas, VA) supplemented with 10% FBS, 1% NEAA and 1% Sodium pyruvate.

HEPG2 cells were electroporated at 165V, in 100 µL media with 20,000 cells per well on the High Throughput Electroporation system, BTX from Harvard Apparatus (Holliston, MA). Following electroporation cells were transferred to a collagen coated plate and placed in an incubator overnight. Twenty-four hours post-treatment, cells were washed with PBS, then lysed with GTC for RNA purification.

SCA3 patient-derived fibroblasts were plated into 12-well plates at 80,000 cells/well density in supplemented DMEM media two days prior to transfection. ASO transfections were performed using Lipofectamine LTX with PLUS Reagent (Life

Technologies, Carlsbad, CA) at a final ASO concentration of 4 μM/well according to the manufacturer's instructions. Cells were harvested 48 hours after transfection in Trizol (Invitrogen, Carlsbad, CA) for RNA analysis or 72 hours after transfection using radioimmunoprecipitation assay (RIPA) buffer containing protease inhibitors (Complete mini; Roche Diagnostics, Indianapolis, IN).

2.5.4 RNA isolation and Quantitative PCR

Total RNA was isolated from transfected fibroblasts and dissected brain tissue using Trizol reagent according to manufacturer's protocol (Invitrogen, Carlsbad, CA). Reverse transcription was performed on 1 μg of total RNA using the iScript cDNA synthesis kit according to manufacturer's instructions (Biorad, Carlsbad, CA). The cDNA was diluted 1:10 in nuclease-free water. iQ SYBR green quantitative PCR was performed on the diluted cDNA following the manufacturer's protocol (Biorad, Carlsbad, CA). Analysis was performed using average adjusted relative quantification using the following primers: human *ATXN3* (5' GAAGCTGACCAACTCCTGC 3' and 5' CTTCTAACACTCGTTCCAGG 3'), mouse *Beta Actin* (5' GAACGGACAGCCATGGGCGGG 3' and 5' GTGTGTCCCCAAGCCCCACG 3'), mouse *Gfap* (5' GAAAACCGCATCACCATTCC 3' and 5' CTTATTGACCTCACCATCCCG 3'), mouse *Iba1* (5' CCACCGTGTCAGAATCCAC 3' and 5' ATGCTGGGCAAGAGATCT 3'), human *GAPDH* (5' CTCCGGGTGATGCTTTTCCT and 5' ACATGTAAACCATGTAGTTGAGGT), and mouse *Atxn3* (5' TGTCTTGTTACAGAAAGATCAG and 5' GTTACAAGAACAGAGCTGACT).

2.5.5 Immunoblotting

Protein lysates from SCA3 fibroblasts were produced by lysis in RIPA buffer containing protease inhibitors (Complete mini; Roche Diagnostics, Indianapolis, IN), followed by centrifugation. Protein lysates from perfused and dissected mouse forebrain, brainstem, cerebellum and cervical spinal cord were produced by lysis and homogenization in RIPA buffer containing protease inhibitors (Complete mini; Roche Diagnostics, Indianapolis, IN) via dounce homogenizers, followed by sonication and centrifugation. Total protein concentrations of extracted supernatants were determined using the BCA method (Pierce, Rockford, IL) and stored at -80°C. A total of 50 μg total mouse brain protein lysate or 5 μg total fibroblast protein lysate were resolved in 10%

sodium dodecyl sulfate-polyacrylamide (SDS) electrophoresis gels and transferred to polyvinylidene difluoride (PVDF) membranes. Membranes were incubated overnight at 4°C with various antibodies: mouse anti-ATXN3 (1H9) (1:1000, MAB5360; Millipore, Billerica MA), rabbit anti-MJD antibody (1:10000, Paulson et al Annals Neurology 1997), mouse anti-GAPDH (1:5000, MAB374; Millipore, Billerica, MA), rabbit anti-α-Tubulin (1:5000, #S2144; Cell Signaling Technologies, Danvers, MA). Bound primary antibodies were visualized by incubation with a peroxidase-conjugated anti-mouse or anti-rabbit secondary antibody (1:10000; Jackson Immuno Research Laboratories, West Grove, PA) followed by treatment with the ECL-plus reagent (Western Lighting; PerkinElmer, Waltham, MA) and exposure to autoradiography films. Band intensities were quantified using ImageJ analysis software (NIH, Bethesda, MD).

2.5.6 Stereotaxic mouse ICV ASO bolus delivery

Stereotaxic administration of ASOs into the right lateral ventricle via ICV injections was performed on mice under vaporized isoflurane anesthesia. Eight-week-old mice received a single ICV bolus injection using established protocols[31]. Six sex-matched Q84, Q135, or wild type littermates were included per experimental treatment group. All treatment groups were blinded to the experimenter prior to analysis. For each injection, a small incision was made, the skull exposed, and a small burr hole drilled at the proper coordinates: anterior-posterior +0.3mm, medio-lateral -1.0mm, dorso-ventral -3.0mm relative to bregma. Three minutes after the needle (7758-04, Hamilton, Reno, NV) connected to a 10 uL syringe (7653-01, Hamilton, Reno, NV) was placed into the proper coordinates, a total of 500-700 µg of ASO diluted in 10 µL PBS (without Ca2+ or Mg2+) was delivered at an infusion rate of 0.5 µL/sec using an injection pump (UMC4, World Precision Instruments, Inc., Sarasota, FL). For all ASO studies in Q84 mice, mice received 500 ug of the five active ASOs or control ASO. In the Q135 ASO studies, mice received 500 ug ASO-4, 700 ug ASO-5, or 700 ug ASO-Ctrl. Five minutes after the infusion was completed the needle was retracted at a rate of 1 mm/sec. The incision site was sutured with synthetic absorbable sutures (V1D397, Vet One, Boise, ID) and the mouse allowed to recover in a temperature controlled environment. Following surgery, weight, grooming activity, and home cage activity were recorded for up to 10 days according to UCUCA guidelines.

2.5.7 Immunohistochemistry.

Whole brains perfused with PBS were post-fixed for 48 hours at 4°C in 4% paraformaldehyde solution, immersed in 30% sucrose until saturated, and 40 µm sagittally sectioned on a sledge microtome (SM200R, Leica Biosystems, Wetzler, Germany). Sections were stored in cryoprotectant solution at -20°C until processed for immunofluorescence. Brain sections were subjected to a basic antigen retrieval, washed, blocked and incubated overnight at 4°C in primary antibody supplemented with 0.025% Triton X-100, 0.5% BSA, and 5% serum from host line for secondary antibodies (Donkey or Goat). Primary antibodies used in these studies include: mouse anti-ATXN3 (1H9) (1:1000; MAB5360 Millipore, Billerica, MA), rabbit anti-ASO (1:5000; Ionis Pharmaceuticals, Carlsbad, CA), rabbit anti-NeuN-488 conjugated (1:1000; ABN78A4 Millipore, Billerica, MA), mouse anti-GFAP (1:1000, #3670 Cell Signaling, Danvers, MA), and rabbit anti-Iba1 (1:1000, 019-19741 Wako Chemicals USA, Richmond, VA). Primary incubated sections were then washed and incubated with the corresponding secondary Alexa Fluor 488 or 568 antibodies (1:1000; Invitrogen, Carlsbad, CA). All sections were stained with DAPI (Sigma, St. Louis, MO) for 15 minutes at room temp, mounted with Prolong Gold Antifade Reagent (Invitrogen, Carlsbad, CA), and imaged using an IX71 Olympus inverted microscope (Melville, NY) or Nikon-A1 (Melville, NY) confocal microscope. NeuN-positive ATXN3 nuclear accumulation was calculated using ImageJ software (NIH, Bethesda, MD). Corrected total neuronal nuclear ATXN3 fluorescence = (nuclear area x mean ATXN3 fluorescence) – (nuclear area x mean fluorescence of background readings).

2.6 Acknowledgements and author contributions

We thank Patricia Maciel for providing the CMVMJD-Q135 mouse model. Ionis Pharmaceutics identified and generated the anti-ATXN3 ASOs. This work was supported in part by a research contract from Ionis Pharmaceuticals to H. Paulson, the National Ataxia Foundation Postdoctoral Fellowship Award (Rajpal), NIH/National Center for Advancing Translational Sciences UL1 TR000433 (Rajpal), the Michigan Brain Initiative Predoctoral Fellowship for Neuroscience (Moore), G015616 Becky Babcox Fund Pilot Research Award (McLoughlin, PI), NIH T32 NS007222-33 (McLoughlin), and NIH R01 NS038712 (Paulson, PI).

Conceptualization, L.R.M, G.R., G.H., H.B.K., H.L.P., H.S.M; Methodology, L.R.M, G.R., H.B.K., H.S.M ; Investigation, L.R.M, G.R., I.T.D., M.Q., K.G.B., D.G., H.S.M.; Writing, L.R.M, G.R., H.B.K., H.L.P.,H.S.M; Funding Acquisition, L.R.M, G.R., H.L.P., H.S.M; Supervision, G.H., H.B.K.; H.L.P., H.S.M. D.G., G.H., and H.B.K. are employees of Ionis Pharmaceuticals. This work was supported in part by Ionis Pharmaceuticals.

2.7 References

1 Costa Mdo, C. & Paulson, H. L. Toward understanding Machado-Joseph disease. *Prog Neurobiol* **97**, 239-257, doi:10.1016/j.pneurobio.2011.11.006 (2012).

2 Alves, S. *et al.* Allele-specific RNA silencing of mutant ataxin-3 mediates neuroprotection in a rat model of Machado-Joseph disease. *PLoS One* **3**, e3341, doi:10.1371/journal.pone.0003341 (2008).

3 Costa Mdo, C. *et al.* Toward RNAi therapy for the polyglutamine disease Machado-Joseph disease. *Mol Ther* **21**, 1898-1908, doi:10.1038/mt.2013.144 (2013).

4 Rodriguez-Lebron, E. *et al.* Silencing mutant ATXN3 expression resolves molecular phenotypes in SCA3 transgenic mice. *Mol Ther* **21**, 1909-1918, doi:10.1038/mt.2013.152 (2013).

5 Nobrega, C. *et al.* Silencing mutant ataxin-3 rescues motor deficits and neuropathology in Machado-Joseph disease transgenic mice. *PLoS One* **8**, e52396, doi:10.1371/journal.pone.0052396 (2013).

6 Evers, M. M. *et al.* Ataxin-3 protein modification as a treatment strategy for spinocerebellar ataxia type 3: removal of the CAG containing exon. *Neurobiol Dis* **58**, 49-56, doi:10.1016/j.nbd.2013.04.019 (2013).

7 Schmitt, I. *et al.* Inactivation of the mouse Atxn3 (ataxin-3) gene increases protein ubiquitination. *Biochem Biophys Res Commun* **362**, 734-739, doi:10.1016/j.bbrc.2007.08.062 (2007).

8 Boy, J. *et al.* Reversibility of symptoms in a conditional mouse model of spinocerebellar ataxia type 3. *Human molecular genetics* **18**, 4282-4295, doi:10.1093/hmg/ddp381 (2009).

9 Rodriguez-Lebron, E. *et al.* Silencing mutant ATXN3 expression resolves molecular phenotypes in SCA3 transgenic mice. *Mol Ther* **21**, 1909-1918, doi:10.1038/mt.2013.152 (2013).

10 Seidel, K. *et al.* Brain pathology of spinocerebellar ataxias. *Acta Neuropathol* **124**, 1-21, doi:10.1007/s00401-012-1000-x (2012).

11 Cerritelli, S. M. & Crouch, R. J. Ribonuclease H: the enzymes in eukaryotes. *FEBS J* **276**, 1494-1505, doi:10.1111/j.1742-4658.2009.06908.x (2009).

12 Kordasiewicz, H. B. *et al.* Sustained therapeutic reversal of Huntington's disease by transient repression of huntingtin synthesis. *Neuron* **74**, 1031-1044, doi:10.1016/j.neuron.2012.05.009 (2012).

13 Passini, M. A. *et al.* Antisense oligonucleotides delivered to the mouse CNS ameliorate symptoms of severe spinal muscular atrophy. *Sci Transl Med* **3**, 72ra18, doi:10.1126/scitranslmed.3001777 (2011).

14 Hua, Y. *et al.* Peripheral SMN restoration is essential for long-term rescue of a severe spinal muscular atrophy mouse model. *Nature* **478**, 123-126, doi:10.1038/nature10485 (2011).

15 Chiriboga, C. A. *et al.* Results from a phase 1 study of nusinersen (ISIS-SMN(Rx)) in children with spinal muscular atrophy. *Neurology* **86**, 890-897, doi:10.1212/WNL.0000000000002445 (2016).

16 Miller, T. M. *et al.* An antisense oligonucleotide against SOD1 delivered intrathecally for patients with SOD1 familial amyotrophic lateral sclerosis: a phase 1, randomised, first-in-man study. *The Lancet. Neurology* **12**, 435-442, doi:10.1016/s1474-4422(13)70061-9 (2013).
17 Lagier-Tourenne, C. *et al.* Targeted degradation of sense and antisense C9orf72 RNA foci as therapy for ALS and frontotemporal degeneration. *Proc Natl Acad Sci U S A* **110**, E4530-4539, doi:10.1073/pnas.1318835110 (2013).
18 Hu, J. *et al.* Allele-specific silencing of mutant huntingtin and ataxin-3 genes by targeting expanded CAG repeats in mRNAs. *Nature biotechnology* **27**, 478-484, doi:10.1038/nbt.1539 (2009).
19 Hu, J. *et al.* Allele-selective inhibition of ataxin-3 (ATX3) expression by antisense oligomers and duplex RNAs. *Biological chemistry* **392**, 315-325, doi:10.1515/bc.2011.045 (2011).
20 Aiba, Y. *et al.* Allele-selective inhibition of expression of huntingtin and ataxin-3 by RNA duplexes containing unlocked nucleic acid substitutions. *Biochemistry* **52**, 9329-9338, doi:10.1021/bi4014209 (2013).
21 Evers, M. M. *et al.* Targeting several CAG expansion diseases by a single antisense oligonucleotide. *PLoS One* **6**, e24308, doi:10.1371/journal.pone.0024308 (2011).
22 Toonen, L. J., Schmidt, I., Luijsterburg, M. S., van Attikum, H. & van Roon-Mom, W. M. Antisense oligonucleotide-mediated exon skipping as a strategy to reduce proteolytic cleavage of ataxin-3. *Scientific reports* **6**, 35200, doi:10.1038/srep35200 (2016).
23 Silva-Fernandes, A. *et al.* Motor uncoordination and neuropathology in a transgenic mouse model of Machado-Joseph disease lacking intranuclear inclusions and ataxin-3 cleavage products. *Neurobiol Dis* **40**, 163-176, doi:10.1016/j.nbd.2010.05.021 (2010).
24 Cemal, C. K. *et al.* YAC transgenic mice carrying pathological alleles of the MJD1 locus exhibit a mild and slowly progressive cerebellar deficit. *Human molecular genetics* **11**, 1075-1094 (2002).
25 Bennett, C. F. & Swayze, E. E. RNA targeting therapeutics: molecular mechanisms of antisense oligonucleotides as a therapeutic platform. *Annual review of pharmacology and toxicology* **50**, 259-293, doi:10.1146/annurev.pharmtox.010909.105654 (2010).
26 Yu, R. Z. *et al.* Tissue disposition of 2'-O-(2-methoxy) ethyl modified antisense oligonucleotides in monkeys. *Journal of pharmaceutical sciences* **93**, 48-59, doi:10.1002/jps.10473 (2004).
27 Rub, U. *et al.* Clinical features, neurogenetics and neuropathology of the polyglutamine spinocerebellar ataxias type 1, 2, 3, 6 and 7. *Prog Neurobiol* **104**, 38-66, doi:10.1016/j.pneurobio.2013.01.001 (2013).
28 Riess, O., Rub, U., Pastore, A., Bauer, P. & Schols, L. SCA3: neurological features, pathogenesis and animal models. *Cerebellum* **7**, 125-137, doi:10.1007/s12311-008-0013-4 (2008).
29 Haacke, A. *et al.* Proteolytic cleavage of polyglutamine-expanded ataxin-3 is critical for aggregation and sequestration of non-expanded ataxin-3. *Human molecular genetics* **15**, 555-568, doi:10.1093/hmg/ddi472 (2006).
30 Rosenberg, R. N. Machado-Joseph disease: an autosomal dominant motor system degeneration. *Mov Disord* **7**, 193-203, doi:10.1002/mds.870070302 (1992).
31 DeVos, S. L. & Miller, T. M. Direct intraventricular delivery of drugs to the rodent central nervous system. *Journal of visualized experiments : JoVE*, e50326, doi:10.3791/50326 (2013).
32 Ostergaard, M. E. *et al.* Rational design of antisense oligonucleotides targeting single nucleotide polymorphisms for potent and allele selective suppression of mutant Huntingtin in the CNS. *Nucleic Acids Res* **41**, 9634-9650, doi:10.1093/nar/gkt725 (2013).

33 Southwell, A. L. *et al.* In vivo evaluation of candidate allele-specific mutant huntingtin gene silencing antisense oligonucleotides. *Molecular therapy : the journal of the American Society of Gene Therapy* **22**, 2093-2106, doi:10.1038/mt.2014.153 (2014).
34 Lieberman, A. P. *et al.* Peripheral androgen receptor gene suppression rescues disease in mouse models of spinal and bulbar muscular atrophy. *Cell reports* **7**, 774-784, doi:10.1016/j.celrep.2014.02.008 (2014).
35 Sahashi, K. *et al.* Silencing neuronal mutant androgen receptor in a mouse model of spinal and bulbar muscular atrophy. *Human molecular genetics* **24**, 5985-5994, doi:10.1093/hmg/ddv300 (2015).
36 Ramani, B. *et al.* A knockin mouse model of spinocerebellar ataxia type 3 exhibits prominent aggregate pathology and aberrant splicing of the disease gene transcript. *Hum Mol Genet* **24**, 1211-1224, doi:10.1093/hmg/ddu532 (2015).
37 Evert, B. O. *et al.* Inflammatory genes are upregulated in expanded ataxin-3-expressing cell lines and spinocerebellar ataxia type 3 brains. *The Journal of neuroscience : the official journal of the Society for Neuroscience* **21**, 5389-5396 (2001).
38 Cheruvallath, Z. S., Kumar, R. K., Rentel, C., Cole, D. L. & Ravikumar, V. T. Solid phase synthesis of phosphorothioate oligonucleotides utilizing diethyldithiocarbonate disulfide (DDD) as an efficient sulfur transfer reagent. *Nucleosides Nucleotides Nucleic Acids* **22**, 461-468, doi:10.1081/NCN-120022050 (2003).
39 McKay, R. A. *et al.* Characterization of a potent and specific class of antisense oligonucleotide inhibitor of human protein kinase C-alpha expression. *J Biol Chem* **274**, 1715-1722 (1999).

2.8 Figures

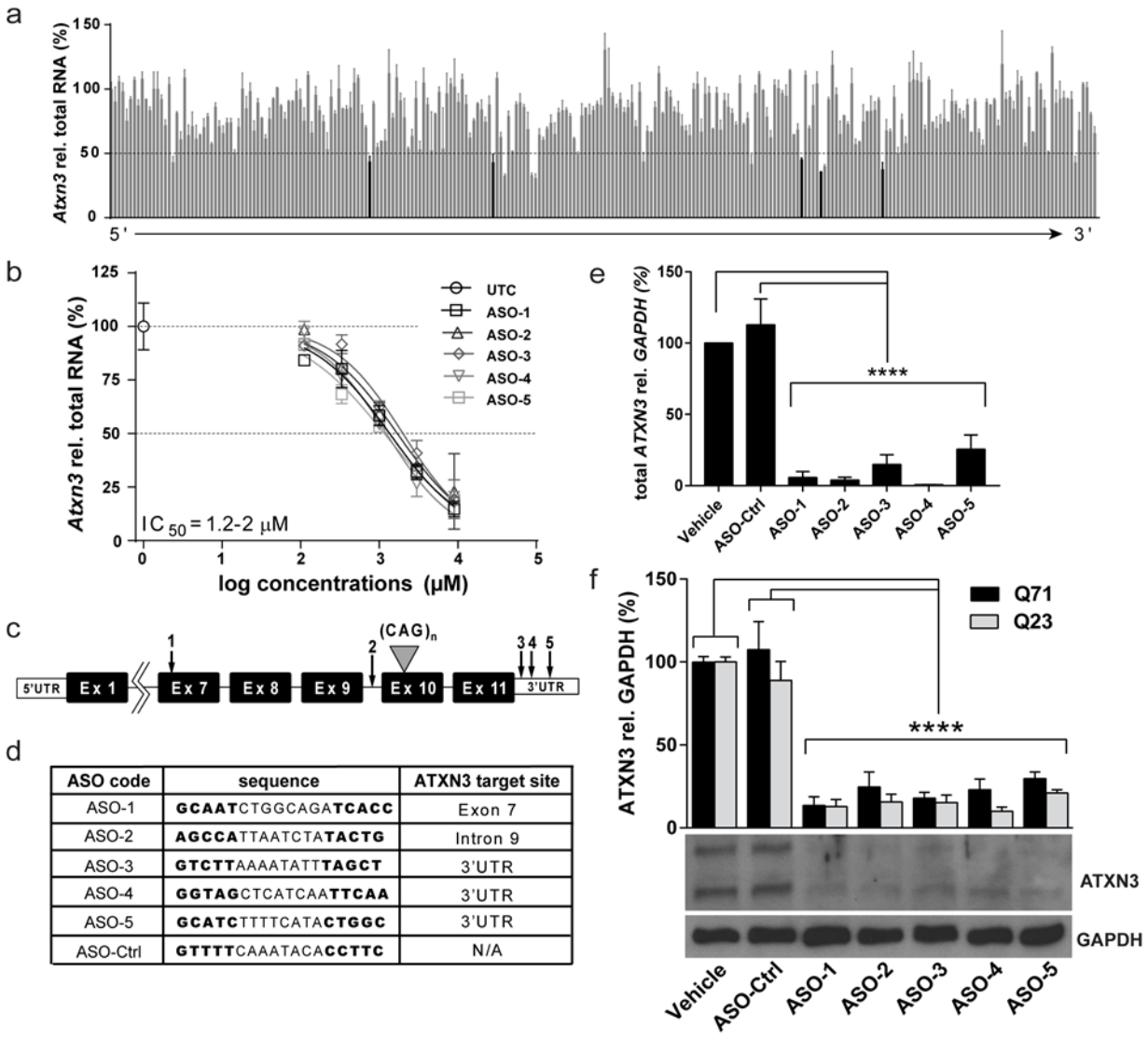

Figure 2.1. Identification of human ATXN3 antisense oligonucleotides. (a) Screen of ASOs complementary to human *ATXN3* in HEPG2 Cells. 2 µM of ASO was electroporated into HEPG2 cells, 24 hours post-treatment *ATXN3* mRNA levels were quantified by qPCR and normalized to total RNA levels. Data expressed as percent of untransfected control cells. ASOs listed in order of relative binding site on *ATXN3* transcript (5' to 3'). Five ASOs characterized further are noted in black. **(b)** Dose response of top five ASOs in HEPG2 cells. IC50s calculated from 4 point non-linear fit dose response curve. **(c)** Schematic of anti-ATXN3 ASO target sites on the human *ATXN3* transcript. **(d)** Anti-ATXN3 ASOs and non-specific ASO-Ctrl nucleotide sequence possess a 5-8-5 MOE gapmer design in which an 8-mer block of unmodified deoxynucleotides is flanked by 5-mer blocks of 2'-O-methoxy-ethyl (MOE) modified ribonucleotides indicated in bold. **(e)** Total *ATXN3* transcript levels in SCA3 patient fibroblasts 48 hours after transfection with anti-ATXN3 ASOs (4 µM), ASO-Ctrl, or

vehicle. Data (mean ± SEM) are reported relative to fibroblasts treated with vehicle alone (n=6 per group). One-way ANOVA statistical analysis performed with post-hoc Tukey's test (****p<0.0001). **(f)** Immunoblotting and quantification of expanded (Q71) and wild type (Q23) ATXN3 protein in SCA3 patient fibroblasts 72 hours after transfection with anti-ATXN3 ASOs, ASO-Ctrl, or vehicle. Data (mean ± SEM) are reported relative to fibroblasts treated with vehicle (n=6 per group). One-way ANOVA performed with post-hoc Tukey's test (****p<0.0001).

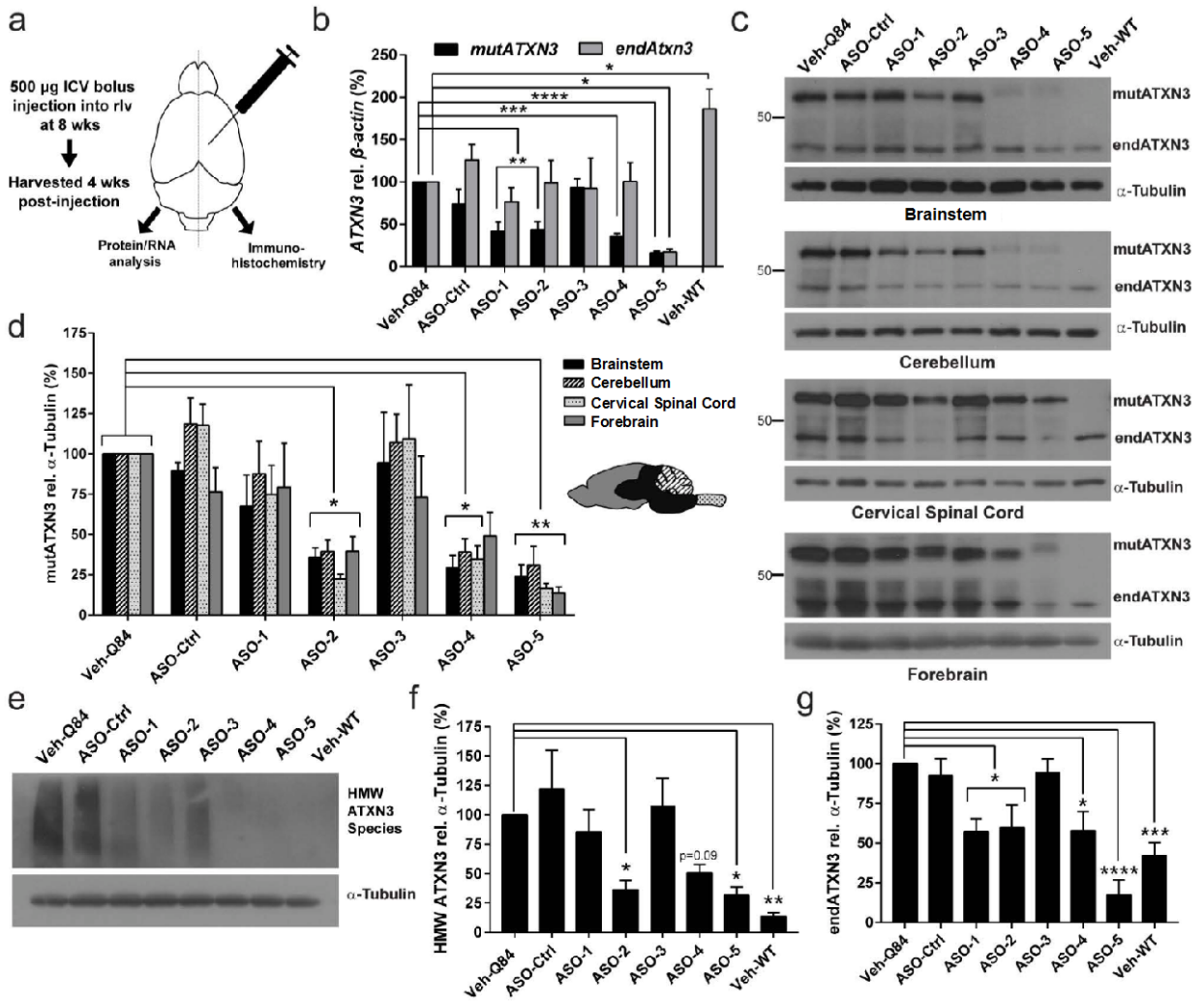

Figure 2.2. *In vivo* suppression of mutant ATXN3 by anti-ATXN3 ASOs in Q84 mice, a YAC transgenic mouse model of SCA3. (a) Schematic of anti-ATXN3 ASO trial design. Sex-matched hemizygous Q84 mice received a single ICV bolus injection of 500 µg ASO or vehicle into the right lateral ventricle (rlv) at 8 weeks of age. Brains were harvested and dissected 4 weeks later for RNA, protein and immunohistochemical analysis. **(b)** Quantification of endogenous *Atxn3 (endAtxn3)* and mutant *ATXN3 (mutATXN3)* transcripts in the of vehicle (Veh-Q84 and Veh-WT), ASO-Ctrl, and anti-ATXN3 ASO-treated mice. **(c)** Representative western blots of mutant ATXN3 (mutATXN3) and endogenous ATXN3 (endATXN3) protein expression in major brain regions of treated mice. **(d)** Quantification of mutATXN3 protein expression in major brain regions of treated mice. **(e)** Representative western blot and **(f)** quantification of high molecular weight (HMW) ATXN3 species in the brainstem of treated mice. **(g)** Quantification of endATXN3 protein expression in the brainstem of treated mice. Data (mean ± SEM) are reported relative to mice treated with vehicle (n=6 per group). One-way ANOVA performed with post-hoc Dunnett's test (*p<0.05, **p<0.01, ***p<0.001, ****p<0.0001).

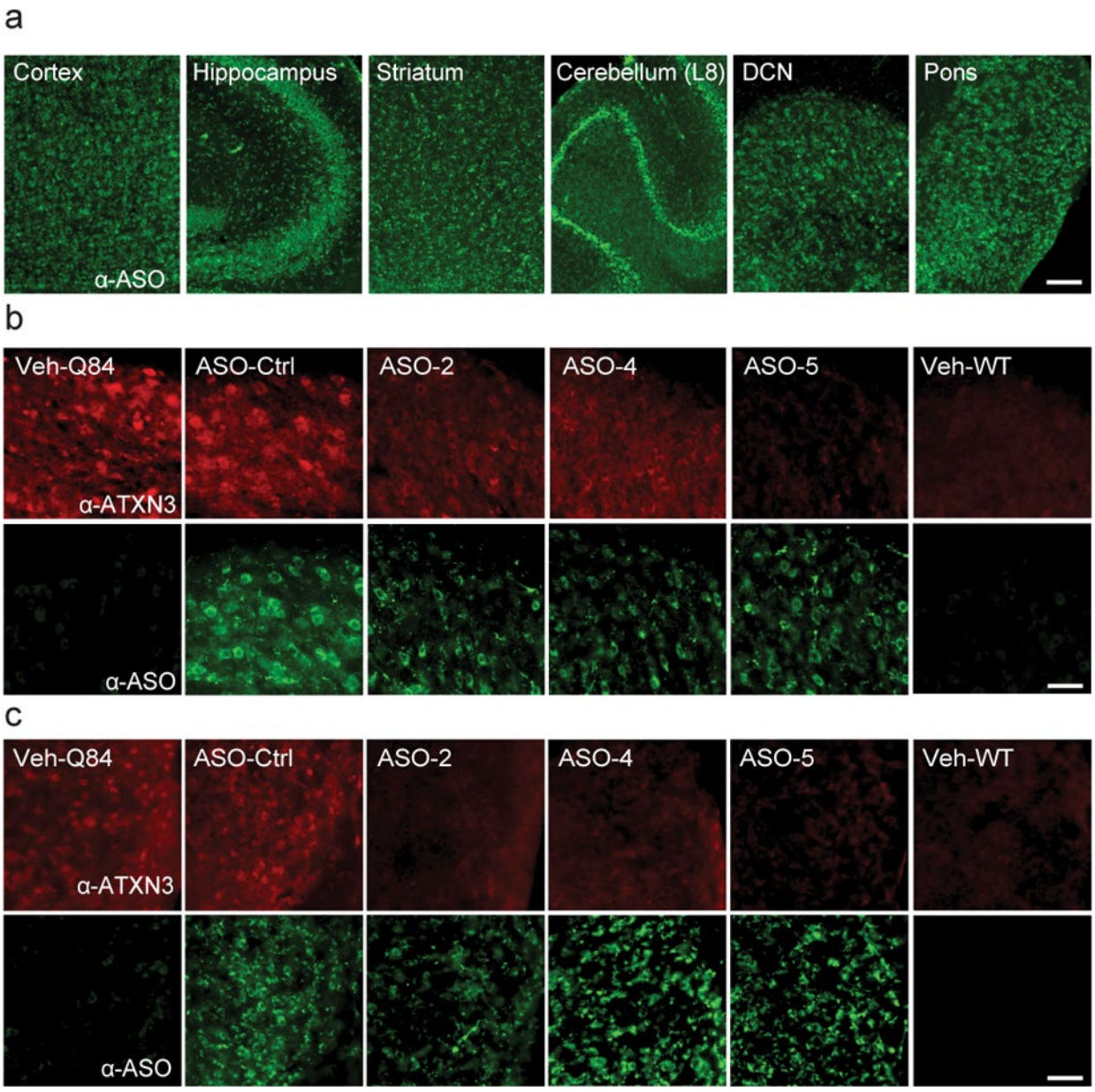

Figure 2.3. Anti-ATXN3 ASOs distribute widely throughout the CNS and suppress ATXN3 protein expression in Q84 mice. (a) Representative immunofluorescence images of ASO (green) distributed throughout key SCA3-affected brain regions in Q84 hemizygous mice 4 weeks after injection. Scale bar, 200 μm. Representative immunofluorescence images of ASO (green) mediated suppression of ATXN3 (red) in **(b)** deep cerebellar nuclei (DCN) and **(c)** pontine nuclei of Q84 hemizygous mice 4 weeks post-treatment. Scale bars in b and c, 50 μm.

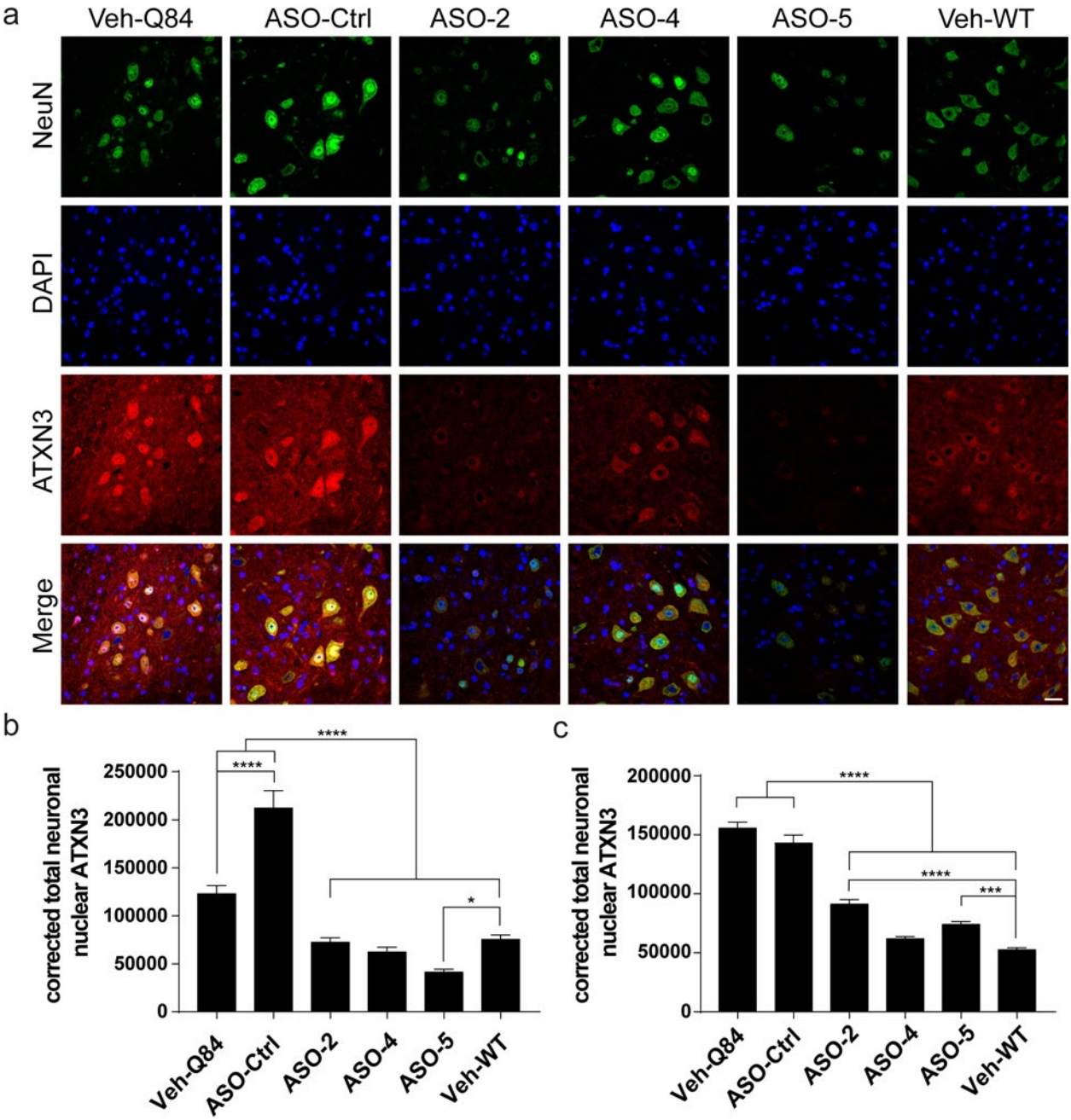

Figure 2.4. ASOs significantly suppress ATXN3 accumulation within neuronal nuclei. (a) Representative immunofluorescence images of ATXN3 (red) reduction within neuronal nuclei (NeuN, green; DAPI, blue) in the deep cerebellar nuclei (DCN) of Q84 hemizygous mice 4 weeks post-treatment. Quantification of total corrected neuronal nuclear ATXN3 fluorescence in **(b)** DCN and **(c)** pontine nuclei. Data (mean ± SEM) are reported relative to Q84 vehicle-treated mice (n=3 per group). One-way ANOVA performed with post-hoc Tukey's test (*p<0.05, ***p<0.001, ****p<0.0001).

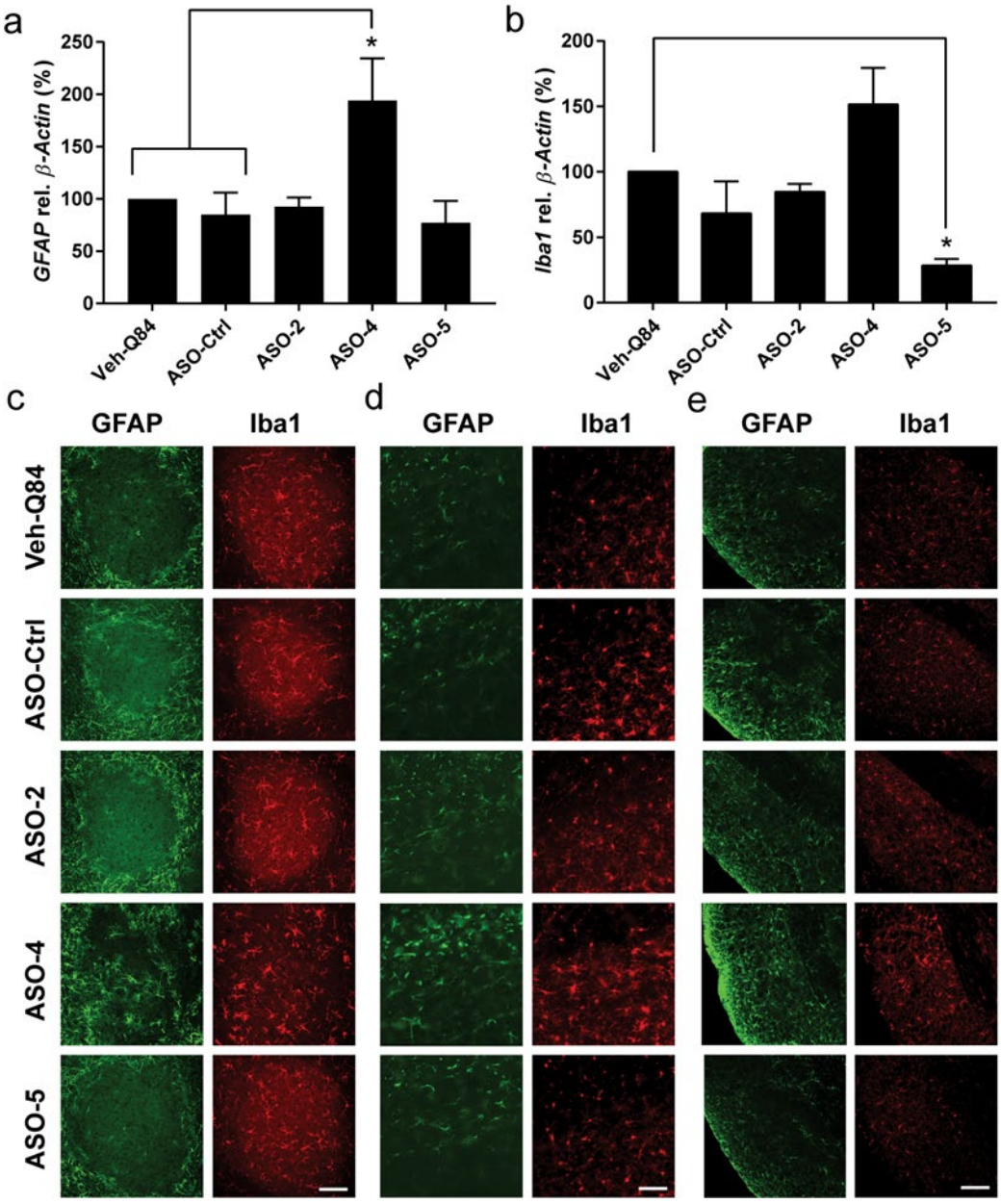

Figure 2.5. ASOs result in limited immunoreactive changes in Q84 mice. Transcript levels of the astrocytic marker *Gfap* **(a)** and microglial marker *Iba1* **(b)** in the left brainstem of vehicle and ASO-treated mice four weeks after injection. Mean ± SEM are reported relative to Q84 vehicle-treated mice (n=6 per group). One-way ANOVA statistical analysis performed with post-hoc Tukey's test (*$p<0.05$). Representative GFAP (green) and Iba1 (red) immunofluorescence images of the **(c)** deep cerebellar nuclei (DCN) (scale bar, 100 μm), **(d)** cerebral cortex (scale bar, 100 μm), and **(e)** body of the pons (scale bar, 50 μm).

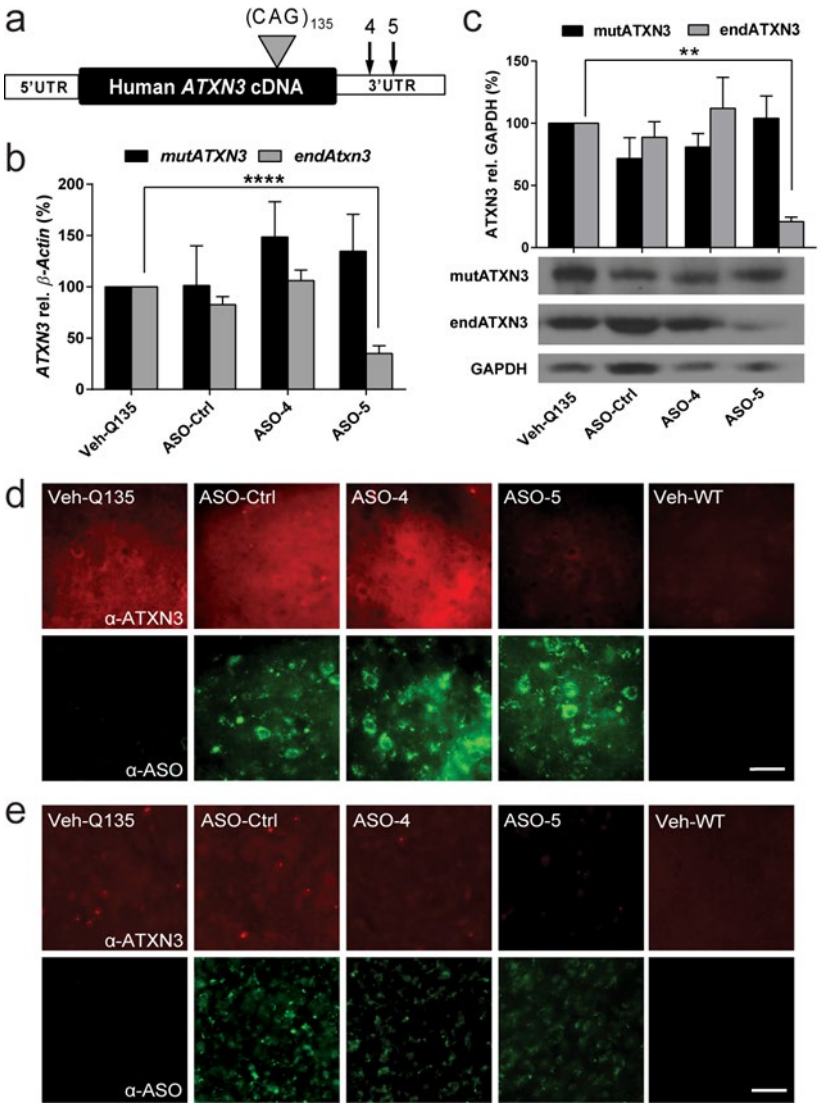

Figure 2.6. ASOs do not reduce mutant ATXN3 expression in a second model, the Q135 cDNA transgenic mouse, despite effective delivery. (a) Schematic of anti-ATXN3 ASO target sites on the CMV MJD-Q135 *ATXN3* cDNA transcript. **(b)** Mutant *ATXN3* (*mutATXN3*) and endogenous *Atxn3* (*endAtxn3*) transcript levels in the brainstem of Q135 mice 4 weeks after injection (n=6 per group). Data shown are mean ± SEM relative to Q135 vehicle-treated mice (n=6 per group). One-way ANOVA statistical analysis performed with post-hoc Dunnett's test (****p<0.01, p<0.0001). **(c)** Western blotting and quantification of mutant human ATXN3 and endogenous murine ATXN3 expression in Q135 brainstem 4 weeks after injection. **(d)** Representative ATXN3 (red) and ASO (green) immunofluorescence images of the deep cerebellar nuclei (DCN) (scale bar, 50 μm) and **(e)** pontine nuclei (scale bar, 50 μm).

CHAPTER 3

Oligonucleotide Therapy Mitigates Disease in Spinocerebellar Ataxia Type 3 Mice

3.1 Abstract

Spinocerebellar ataxia type 3 (SCA3), also known as Machado-Joseph disease, is the most common dominantly inherited ataxia. Despite advances in understanding this CAG repeat/polyglutamine expansion disease, there are still no therapies to alter its progressive fatal course. Here we investigate whether an antisense oligonucleotide (ASO) targeting the SCA3 disease gene, *ATXN3*, can prevent molecular, neuropathological, electrophysiological and behavioral features of the disease in a mouse model of SCA3. The top *ATXN3*-targeting ASO from an *in vivo* screen was injected intracerebroventricularly into early symptomatic transgenic SCA3 mice that express the full human disease gene and recapitulate key disease features. Following a single ASO treatment at 8 weeks of age, mice were evaluated longitudinally for ATXN3 suppression and rescue of disease-associated pathological changes. Mice receiving an additional repeat injection at 21 weeks were evaluated longitudinally up to 29 weeks for motor performance. The *ATXN3*-targeting ASO achieved sustained reduction of polyglutamine-expanded ATXN3 up to 8 weeks after treatment and prevented oligomeric and nuclear accumulation of ATXN3 up to at least 14 weeks after treatment. ASO therapy rescued motor impairment in SCA3 mice, and this rescue was associated with a recovery of defects in Purkinje neuron firing frequency and afterhyperpolarization. This preclinical study established efficacy of *ATXN3*-targeted ASOs as a disease-modifying therapeutic strategy for SCA3. These results support further efforts to develop ASOs for human clinical trials in this polyglutamine disease as well as in other

dominantly inherited disorders caused by toxic gain of function. The work of this chapter has been published in:

McLoughlin HS and Moore LR, *et al.* Oligonucleotide therapy mitigates disease in spinocerebellar ataxia type 3 mice. *Ann Neurol.* 2018 Jul;84(1):64-77.

3.2 Introduction

Spinocerebellar ataxia type 3 (SCA3), also known as Machado-Joseph disease, is the most common dominantly inherited ataxia in the world, affecting an estimated 1 in 20,000 people[1]. Affected persons progressively lose motor control, leading to death within 10 to 20 years[2]. The progressive changes in SCA3 reflect widespread degenerative and neuropathological changes, including neuronal loss and gliosis in the deep cerebellar nuclei (DCN), pons, vestibular nuclei and other brainstem nuclei, spinocerebellar tracts, substantia nigra, thalamus, and globus pallidus[3,4]. SCA3 is one of nine neurodegenerative diseases caused by an expanded, polyglutamine-coding repeat in the disease gene[5]. The mutant SCA3 disease protein, ATXN3, acts through a dominant toxic mechanism that is still poorly understood[1,6], and mice lacking ATXN3 are phenotypically normal[7]. Thus, suppression of the disease gene, *ATXN3*, represents a promising approach to slow or block the neurodegenerative cascade in SCA3.

Currently there is no effective treatment for this relentlessly progressive and fatal disease. In this report, we test antisense oligonucleotides (ASOs) as a potential therapy for SCA3. ASOs represent a non-viral gene suppression approach that has emerged as a compelling therapeutic strategy for neurologic, oncologic, cardiac and metabolic disorders. Chemically modified ASOs can be designed to selectively bind complementary target RNA, resulting in RNase H-mediated cleavage of the targeted RNA or induced exon skipping[8]. ASOs targeting many neurodegenerative disease genes have undergone preclinical assessment in rodent models and, in some diseases, have advanced into human clinical trials including familial amyotrophic lateral sclerosis (ALS) and Huntington's disease (HD)[9-11]. The first disease-modifying therapy in spinal muscular atrophy (SMA) employing exon-skipping ASOs was recently FDA- and EMA-approved following successful human clinical trials[12,13]. Our group and others previously tested nucleotide-based gene silencing strategies as potential disease-

modifying therapy in SCA3, including viral-mediated RNA interference[14-16] and exon-skipping approaches[17,18]. While promising, these prior studies have been limited by various factors including – depending on the study – short-term treatment, spatially restricted silencing in the central nervous system (CNS), limited reduction of mutant ATXN3, or concerns about the extent to which the animal model replicates aspects of the human disease. Here we set out to perform an efficacy study not limited by these factors, building on our recent proof-of-principle study that established widespread ASO delivery and silencing of human mutant *ATXN3* in a mouse model of SCA3[19]. In this earlier study, we evaluated a collection of chemically modified ASOs targeting *ATXN3* in cellular and mouse models of SCA3[19]. We achieved widespread ASO delivery and efficient silencing of human mutant *ATXN3* throughout affected brain regions, without signs of an adverse immune response to treatment. ASOs were delivered directly into the CNS by intracerebroventricular (ICV) injection, allowing the natural flow of cerebrospinal fluid (CSF) to distribute ASOs throughout the CNS, as supported by histological assessment in ASO-treated rodent and non-human primate studies[19-22]. From this short-term safety and efficacy study, we selected the best ASO candidate, ASO-5, for further evaluation here in a longitudinal preclinical study. Using a well characterized mouse model of SCA3 that expresses the full human disease gene, we sought to determine whether sustained suppression of the ATXN3 disease protein rescues key molecular, pathological, electrophysiological, and behavioral hallmarks of disease.

3.3 Results

3.3.1 Dose-dependent ASO suppression of mutant ATXN3 in SCA3 transgenic mice.

Our initial limited, proof-of-principle study identified ASO-5 as a promising anti-*ATXN3* ASO[19]. In preparation for a longitudinal efficacy study, we first sought to determine an optimal ASO-5 dose for safe and effective suppression of mutant ATXN3 (mutATXN3) in homozygous YAC-Q84 (Q84/Q84) transgenic mice. The Q84/Q84 SCA3 mouse model expresses the full-length human *ATXN3* disease gene harboring a pathogenic CAG expansion at near endogenous levels and exhibits disease-relevant neuropathological changes and motor deficits as early as 6 weeks of age that progress

in severity with age[16,27]. Its expression of the full human disease gene and recapitulation of human disease hallmarks make Q84/Q84 mice well-suited for longitudinal preclinical assessment of potential SCA3 therapies.

Sex-matched 8-week-old Q84/Q84 mice were administered an ASO-5 dose ranging from 300 to 1000 μg (n=4 mice per dose) by stereotaxic ICV injection into the right lateral ventricle (**Fig 3.1A**). For comparison, Q84/Q84 or wild type (WT) littermate controls (n=4 mice per genotype) received PBS vehicle-only ICV injections. Mice were subsequently monitored according to University of Michigan Animal Care and Use Committee guidelines, with no post-surgical adverse events occurring at any tested dose. Treated mice were sacrificed four weeks after injection and brains bisected along the midline. The left and right hemispheres were processed for biochemical and immunohistochemical analysis, respectively. All treatment groups were blinded to the experimenter prior to analysis.

Because of the high concentration of affected brainstem nuclei in post-mortem SCA3 patient brains (e.g. pons, olivary nuclei, vestibular nuclei, cranial nerve nuclei), we focused our biochemical analysis on brainstem tissue[3,28,29]. By immunoblot analysis, ASO-5 significantly reduced brainstem mutATXN3 expression in a dose-dependent manner, though all doses showed efficacy ($p<0.05$) (**Fig 3.1B, C**). Mice that received 750 μg of ASO-5 exhibited the greatest mutATXN3 suppression, reducing levels to 29% ± 9% relative to vehicle-treated Q84/Q84 mice. Immunoblot analysis also revealed a striking rescue in the accumulation of high molecular weight (HMW) ATXN3 oligomers at all doses, reducing ATXN3 accumulation by more than 75% at the smallest dose (300 μg) and by about 90% for all doses greater than 500 μg relative to vehicle-treated Q84/Q84 mice ($p<0.01$) (**Fig 3.1B and 3.1D**).

3.3.2 No evidence of apoptosis or gliosis upon ASO-5 treatment in SCA3 mouse brain.

To evaluate possible ASO-induced cellular toxicity with increasing doses, immunoblot analysis was performed for the pro- and anti-apoptotic proteins BAX and BCL-2, respectively. Quantitation of BAX and BCL-2 revealed no increase in the BAX/BCL-2 ratio with increasing ASO doses in the mouse brainstem relative to vehicle-treated WT or Q84/Q84 littermates four weeks after injection, indicating no evident

toxicity at tested doses (**Fig 3.1E**). Gliosis is present in post-mortem SCA3 patient brains[3,30] and can also be a potential adverse effect of ASO treatment[31]. To determine the tolerability of ASOs at increasing doses, treated mice were assessed for astrogliosis and microgliosis four weeks after treatment. Immunoblot analysis revealed no ASO-mediated increases in the astrocyte marker GFAP (**Fig 3.1F**) or microglia marker IBA1 (**Fig 3.1G**) in the brainstem at any tested dose relative to vehicle-treated WT or Q84/Q84 littermates, although a significant decrease in GFAP protein was observed in mice receiving 300 µg and 500 µg ($p<0.05$) (**Fig 3.1F**). Immunohistochemical analysis revealed no observable differences in astrocyte or microglia density, cellular structure, or localization four weeks following any ASO-5 dose (**Fig 3.1H**). Thus, no overt gliosis occurred at effective ASO-5 doses.

3.3.3 Sustained ASO-mediated suppression of mutant and oligomeric ATXN3 protein at least eight weeks after injection into SCA3 mice.

Guided by the above results, we selected 700 µg of ASO-5 as an effective and safe dose to advance into preclinical studies. To determine the duration of ASO-5-mediated suppression of mutATXN3, we performed longitudinal biochemical assessments of Q84/Q84 or WT mice following treatment. Sex- and littermate-matched Q84/Q84 mice (n=6 per experimental group) received an ICV bolus injection of PBS vehicle, ASO-5, or non-specific control ASO (ASO-Ctrl) at 8 weeks of age. For comparison, WT sex-matched littermates similarly received an ICV injection of vehicle. Treated brains were harvested 4, 8, or 14 weeks after injection (i.e. at 12, 16, or 22 weeks of age) and bisected for biochemical and immunohistochemical analysis (**Fig 3.2A**). The following biochemical results are reported for the brainstem dissected from the left hemisphere.

By quantitative PCR, ASO-5 suppressed *mutATXN3* transcript levels by ~50% over time (**Fig 3.2B**), and this transcriptional repression was maintained up to at least 22 weeks of age ($p<0.05$). A significant reduction in endogenous murine *Atxn3* transcript levels was also observed in treated mice up to at least 22 weeks of age ($p<0.01$), consistent with the fact that ASO-5 targets both human and murine *ATXN3* transcripts (**Fig 3.2C**).

Anti-ATXN3 immunoblot analysis confirmed highly stable and efficient suppression of the human disease protein (**Fig 3.2D**). MutATXN3 protein expression levels were significantly reduced in ASO-treated mice at both 12 weeks ($p<0.05$) and 16 weeks ($p<0.01$), with the greatest reduction occurring at 16 weeks of age (10.77% ± 2.08%) relative to vehicle-treated Q84/Q84 mice. Whereas soluble mutATXN3 levels returned to vehicle-treated Q84/Q84 mouse levels by 22 weeks (**Fig 3.2E**), complete reduction of oligomeric HMW ATXN3 to vehicle-treated WT mouse levels persisted at all time points ($p<0.01$) (**Fig 3.2F**). ASO-5 treated mice also exhibited significant reductions in endogenous ATXN3 protein levels at all time points, with the greatest reduction also occurring at 16 weeks (11.49% ± 4.99%, $p<0.001$) (**Fig 3.2G**).

The above protein and RNA analysis of brainstem lysates confirmed ASO delivery and ATXN3 suppression broadly in the brainstem but does not shed light on whether selectively vulnerable neuronal populations in the SCA3 brain were successfully targeted. Employing immunofluorescence with an anti-ASO antibody, we assessed ASO-5 delivery and retention in the pons and DCN (**Fig 3.2H)**, two subcortical regions known to undergo significant neuronal loss in post-mortem SCA3 patient brains[3,28,29]. Four weeks after injection, ASO levels in the pons and DCN were equal to or greater than that of surrounding brain structures, confirming that these key disease-affected regions are readily targetable. ASO signal intensity remained high at the 16-week time point but was diminished by 22 weeks in both the pons and DCN. This loss of ASO signal at 22 weeks was accompanied by a concomitant increase in some immunoblotted ATXN3 protein species.

3.3.4 ASO-5 prevents nuclear sequestration of ATXN3 in vulnerable brain regions at least 14 weeks after injection.

Redistribution of polyglutamine-expanded ATXN3 from the cytoplasm into neuronal nuclei appears to be an early and critical step in the SCA3 disease process[1]. For example, expressing polyglutamine-expanded ATXN3 attached to a nuclear export signal ameliorated disease in a mouse model of SCA3[32]. The Q84/Q84 mouse is known to show increased nuclear concentration of ATXN3 as early as 6 weeks of age[16], two weeks before ASO injection in our study. Thus, we next sought to investigate whether ASO-5 ICV injection into already symptomatic 8-week-old Q84/Q84 mice could rescue

and prevent further nuclear accumulation of ATXN3 in affected neuronal nuclei over time.

Brain sections harvested from treated mice at 12, 16, and 22 weeks were immunofluorescently labeled with anti-NeuN (data not shown) and anti-ATXN3 antibodies, then co-stained with DAPI to label nuclei. Average integrated density of ATXN3 signal contained within NeuN-positive neuronal nuclei was calculated from confocal images taken of pons (**Fig 3.3A, B**) and DCN (**Fig 3.3D, E**) using ImageJ analysis software (n=6 mice per treatment group, 3 images per mouse). A single ASO-5 treatment reduced neuronal nuclear ATXN3 to vehicle-treated WT levels in pontine and DCN neurons up to at least 22 weeks of age ($p<0.0001$). These results also imply that the nuclear accumulation of ATXN3 that occurred prior to injection at 8 weeks of age was reversed by ASO-5 treatment.

It is important to note that at 16 weeks ASO-Ctrl also lead to a very extensive reduction in both neuronal and non-neuronal nuclear accumulation of ATXN3 compared to vehicle (**Fig 3.3A-E**). This result was very intriguing to us, as the 16-week time point is where we see the strongest effects of ASO-5 ATXN3 reduction and may point to a non-specific effect of ASO therapy. However, we did not investigate this result further as ASO-Ctrl showed no effect on mutant ATXN3 soluble or high molecular weight species (**Fig 3.2D-F**).

3.3.5 ASO-5 rescues differentially expressed pontine SCA3 mouse transcripts.

A recent study by our group revealed pontine transcriptional changes in several SCA3 mouse models particularly in non-neuronal cells, suggesting astrocytes and oligodendrocytes play an underappreciated role in disease[6]. To investigate whether glial cells are susceptible to ASO treatment, we quantified ATXN3 nuclear density in NeuN-negative, non-neuronal cells in the pons (**Fig 3.3A, C**) and DCN (**Fig 3.3D, F**). Analysis confirmed that nuclear accumulation of ATXN3 is indeed enriched in glial cells in Q84/Q84 mice and is reduced to and maintained at vehicle-treated WT levels for at least 14 weeks after ASO-5 treatment ($p<0.0001$). To determine whether reduction of nuclear ATXN3 in non-neuronal cell types was the direct result of ASO uptake, ASO-treated brain sections were immunofluorescently labeled with antibodies against ASO-5 and the astrocyte marker GFAP or the oligodendrocyte marker OLIG2. Confocal

imaging of the pons confirmed ASO uptake into both astrocytes and oligodendrocytes (**Fig 3.4A**), confirming non-neuronal cells are directly susceptible to ASO delivery and that ASO-mediated reductions in non-neuronal nuclear ATXN3 is likely not the result of an indirect non-cell autonomous mechanism.

Prevention of ATXN3 nuclear accumulation by ASO-5 coincided with transcriptional rescue of several key oligodendrocyte-enriched genes dysregulated in the pons of SCA3 mice. Disease-specific oligodendrocyte-enriched genes[6] were selected for transcriptional analysis in the brainstem of vehicle-treated versus ASO-5 treated mice at 22 weeks of age (**Fig 3.4B**). Of the eight transcripts analyzed, six were confirmed to exhibit significant gene expression changes in vehicle-treated Q84/Q84 mice compared to WT mice. Disease-specific differential expression of three of the six significantly altered genes (*Acy3*, *Slc45a3*, *Tnfrsf13c*) was fully rescued in ASO-5 treated Q84/Q84 mice, and expression of the remaining three genes trended towards WT expression levels but did not reach statistical significance. Thus, ASO-5 treatment partially rescues SCA3-specific transcriptional changes in Q84/Q84 mice.

3.3.6 ASO-5 rescues motor phenotypes in Q84/Q84 mice.

We next sought to determine whether sustained ASO-mediated mutATXN3 suppression could rescue motor deficits in symptomatic Q84/Q84 mice. A previous study of Q84/Q84 mice identified motor deficits by 6 weeks of age that worsened over time[16]. For the current study, longitudinal behavioral assessments included open field activity and balance beam performance, which were assessed at 7 weeks, one week before the first ASO-5 or vehicle injection, and then again at 4 or 5-week intervals after injection up to 29 weeks of age. Because the ASO concentration in Q84/Q84 mouse brain was substantially diminished by 22 weeks of age, we added a second ASO-5 or vehicle injection at 21 weeks (**Fig 3.5A**). Experimental groups included sex- and littermate-matched, vehicle-treated WT and Q84/Q84 mice, and ASO-5 treated Q84/Q84 mice (n=12-19 mice per group).

Open field activity assessment confirmed decreased locomotor activity in Q84/Q84 mice at 7 weeks of age, just prior to ASO treatment (**Fig 3.5B**). At 12 weeks, the time of first assessment after injection, ASO-5 treated mice exhibited a complete rescue in open field locomotor activity which persisted at the 29-week endpoint (**Fig**

3.5B). Abnormalities in the balance beam test (increased traversal time and beam slips), which first became evident in vehicle-treated Q84/Q84 mice at 12- and 16-weeks, respectively, were also rescued by ASO-5 treatment at the endpoint assessment ($p<0.05$) (**Fig 3.5C, D**). Decreased weight, which is characteristic of Q84/Q84 mice, was not altered by ASO-5 treatment at any time point (data not shown), suggesting no overt effect of ASO-5 on peripheral tissues.

3.3.7 ASO-5 reverses slowed firing frequency in SCA3 Purkinje neurons.

Abnormalities in Purkinje neuron physiology have previously been observed in Q84 mice[25]. To determine whether ASO-5 treatment rescues SCA3 Purkinje neuron function, extracellular recordings were performed in cerebellar slices from Purkinje neurons of WT and hemizygous Q84/WT mice at 16 weeks of age, 8 weeks after ASO-5 or vehicle injection (n=8-10 mice, **Fig 3.6A**). Purkinje neurons normally exhibit spontaneous repetitive spiking[33]. In vehicle-treated Q84/WT Purkinje neurons, recordings revealed an increased proportion of cells firing at an abnormally low frequency (**Fig 3.6B, C**). Median firing frequency was significantly reduced in vehicle-treated Q84/WT mice relative to vehicle-treated WT mice, and this slowed firing phenotype was rescued in ASO-5 treated Q84/WT mice (**Fig 3.6D**). This finding is reminiscent of a recent study in mouse models of another polyglutamine ataxia, spinocerebellar ataxia type 2 (SCA2), showing that an ASO targeting ATXN2 could rescue slowed firing of Purkinje neurons[22]. Together, these findings point to Purkinje neuron function as a target for ASO therapy across multiple ataxia models.

Slow Purkinje neuron firing, which is observed in many models of ataxia[34-36], has been linked in SCA1 and SCA2 to deepening of the afterhyperpolarization (AHP) following each spike[34,35]. Consistent with findings in other models of ataxia, whole-cell patch clamp recordings of Purkinje neurons from treated mice (**Fig 3.6E**) revealed a deeper AHP in vehicle-treated Q84/WT mice that is rescued by ASO-5 treatment ($p<0.05$) (**Fig 3.6F**). Together, these data suggest that the deeper AHP observed in Q84/WT mice underlies the slowed Purkinje cell firing and that reducing mutATXN3 levels with ASO-5 treatment can improve aberrant electrophysiology in this critically important neuronal population in SCA3.

3.3.8 No evidence of macroautophagy exacerbation in ASO-5 Q84/Q84 treated mouse brains.

Impairments in autophagy have been associated with age- and disease-related neuronal dysfunction[37,38]. A recent report suggests that, in addition to autophagy's role in regulating clearance of misfolded proteins like polyglutamine-expanded ATXN3, autophagy may itself be regulated by ATXN3 in normal and disease states[39,40]. Specifically, WT ATXN3 has been reported to stabilize the essential autophagy adapter protein Beclin1, whereas reducing ATXN3 levels or introducing a polyglutamine-expansion into ATXN3 destabilizes and therefore reduces Beclin1 levels, in the process impairing autophagy[39]. Consistent with these observations, a recent study reported reduced Beclin1 protein levels in post-mortem SCA3 human disease brains[39,41]. Thus, it is conceivable that ASO-mediated reduction of ATXN3 could have the unintended, and potentially deleterious, effect of altering autophagy pathways.

Accordingly, we assessed the effect of mutATXN3 expression, as well as of ASO-mediated reduction in ATXN3 levels, on autophagy-related proteins in Q84/Q84 mice. Anti-Beclin1 immunofluorescence in the pons at 16 weeks revealed reduced Beclin1 expression in vehicle and ASO-5 treated Q84/Q84 mice relative to WT mice **(Fig 3.7A)**. Protein analysis of brainstem lysates at 16 weeks (**Fig 3.7C, D**) confirmed that vehicle-treated WT mice had approximately 50% greater Beclin1 protein level than either vehicle or ASO-5 treated Q84/Q84 mice ($p<0.001$, n=5-6 mice per treatment group). Importantly, ASO-5 mediated suppression of ATXN3 did not further magnify the reduction in Beclin1 expression in Q84/Q84 mice, evidenced both by immunoblot analysis and immunofluorescence of the pons in treated mice. In contrast to the pons, the cerebellum of vehicle or ASO-5 treated Q84/Q84 mice showed no change in Beclin1 levels relative to WT vehicle-treated mice (**Fig 3.7F, G),** suggesting potential region-specific autophagic dysfunction in SCA3.

Finally, we assessed the expression and localization of the ubiquitin-binding adapter protein p62, which is involved in selective autophagy. Previous studies have shown that p62 localizes to protein aggregates in many neurodegenerative diseases including SCA3 and may play a protective role in autophagic clearance of polyglutamine disease proteins[28,29,41,42]. By immunoblot analysis, brainstem (**Fig 3.7C, E**) and

cerebellar (**Fig 3.7F, H**) p62 expression levels did not differ across vehicle-treated WT, vehicle-treated Q84/Q84, or ASO-5 treated mice. We did, however, observe small, nuclear p62-positive puncta in the pons of Q84/Q84 vehicle-treated mice at 16 weeks of age, which were nearly absent in vehicle-treated WT or ASO-5 treated Q84/Q84 mice **(Fig 3.7B).** Rather than forming single large intranuclear aggregates of ATXN3, Q84/Q84 mice typically exhibit small, intranuclear ATXN3-positive inclusions in pontine neurons. Thus, the presence of p62-positive nuclear structures in neurons of Q84/Q84 mice may reflect p62 localization to ATXN3 oligomers or aggregates, which are ameliorated following ASO-5 mediated reduction of mutATXN3 treatment.

3.4 Discussion

Currently there are no disease-modifying therapies available for dominantly inherited neurodegenerative diseases. The present study establishes robust and prolonged suppression of mutant expanded ATXN3 by an RNA-targeting therapy in Q84/Q84 mice, a progressive model of SCA3 expressing the precise human disease gene target. Sustained suppression of the disease protein resulted in the correction of a wide range of disease-associated features including molecular, physiological, neuropathological and behavioral phenotypes. This represents one of the first studies to establish the ability of nucleotide-based gene silencing to mitigate the broad range of disease phenotypes associated with expression of the mutant human *ATXN3* gene. The results add to the growing promise of ASO therapy for dominantly inherited diseases, including other polyglutamine diseases such as HD, spinobulbar muscular atrophy and SCA2.

While previous gene silencing approaches for SCA3 have shown promise, they have not always achieved sufficient efficacy and safety *in vivo* to support continuation into human clinical trials. For example, our previous RNA interference preclinical study achieved safe and life-long suppression of mutATXN3 in Q84/Q84 mouse cerebellum, but failed to rescue any motor deficits, presumably due to the localized nature of delivery[16]. In contrast, ASO-5 treatment of post-symptomatic Q84/Q84 mice in the current study fully rescued locomotor activity, suggesting that CSF-dependent ASO delivery reaches the various nuclei and circuitry underlying the progressive motor, balance, and coordination deficits in SCA3. Importantly, sustained ASO-5 exposure

was not accompanied by evidence of induced gliosis or apoptosis in vulnerable brain regions, and no adverse events were observed even at the highest ASO doses. These results further support the growing evidence from preclinical animal and human clinical ASO trials demonstrating sustained, widespread, and well-tolerated ASO delivery to the CNS following longitudinal ICV or intrathecal delivery[20,22]. In support of the tolerability of ASOs for SCA3, recent elegant work from Toonen *et al.,* assessed exon-skipping of the CAG repeat containing exon 10 in ATXN3[18]. While this exon-specific approach has the advantage that it would likely prevent deleterious effects of loss of ATXN3 function, whether it is sufficiently robust to effectively silence the disease gene requires further study.

To date, published SCA3 studies reveal a neuron-centric view of disease. Though neuronal loss must be a major contributor to the progressive symptoms of SCA3, studies have also begun to implicate non-neuronal cell dysfunction in SCA3[6,43]. For example, in our recent study exploring differentially expressed genes in mouse models of SCA3, the most abundantly altered transcripts reside in oligodendrocytes[6]. The reasons for this preferential effect on oligodendrocytic transcription are unclear, but our demonstration here that ATXN3 accumulates in the nuclei of non-neuronal cells in the brainstem of Q84/Q84 mice is consistent with a cell-autonomous effect. ASO-5 treatment and confirmed ASO uptake in astroglia and oligodendrocytes eliminated this nuclear accumulation of mutATXN3 in non-neuronal cells with a corresponding transcriptional rescue of several oligodendrocyte-enriched genes, consistent with a direct effect of ATXN3 on non-neuronal cells in disease. The ability of ASOs to target both neuronal and non-neuronal cells may prove advantageous for SCA3 therapy. It is worth stating that ASO-Ctrl at 16 weeks lead to a very extensive reduction in both neuronal and non-neuronal nuclear accumulation of ATXN3 compared to vehicle and may point to a non-specific effect of ASO therapy, however further studies are needed to adequately assess this hypothesis.

Our finding of reduced Purkinje neuron firing frequency in Q84/WT mice adds to the literature identifying altered Purkinje neuron firing frequency in other polyglutamine ataxia models, including transgenic mouse models of SCA1[35] and SCA2[44] as well as a viral rodent model of SCA6[36]. The reduction in firing frequency we observed is

associated with a deeper AHP, and ASO treatment in Q84/WT mice normalizes the AHP and rescues slowed firing. Although the molecular mechanism causing slowed firing in Q84/WT mice was not explored here, previous experiments have suggested that impairment of K_v3 family potassium channels in this mouse model[25] contribute to spiking abnormalities, and Purkinje neurons from $K_v3.3$ knockout mice show slower firing and a deeper AHP[45]. Moreover, the rescue of motor impairment through pharmacologic targeting of ion channels in SCA1 mice[46] and ASO treatment in SCA2 mice[22] is associated with normalizing of Purkinje neuron firing frequency, suggesting that ASO treatment in SCA3 mice improves Purkinje neuron physiology in a behaviorally relevant manner. That said, the neural circuitry underlying motor activity is far more complex than simply the regulation of Purkinje neuron firing. Indeed, the more widespread CNS distribution of ASO-5 in the current study compared to our earlier miRNA-based study[16], in which ATXN3 reduction was confined to the cerebellum, may explain why correction of motor deficits was observed in the current but not in the prior study.

Recent studies suggest a role for ATXN3 in autophagy, both normally and in the disease state[37-41,47,48]. This putative function of ATXN3 poses a potential concern for unintended impairments in autophagy following ATXN3 silencing. We found that a key autophagic marker, Beclin1, is indeed decreased in Q84/Q84 mice, consistent with reports in other SCA3 disease models and human disease brain. We did not, however, observe further reductions in Beclin1 with ASO-5 treatment, suggesting that inadvertent disruption of autophagy is not likely to occur with ASO-mediated reduction of ATXN3. In fact, reducing mutATXN3 prevented the accumulation of p62-positive intranuclear puncta in pontine neurons of Q84/Q84 mice, implying that ASO-5 rescues localization of at least one selective autophagy protein following sustained mutATXN3 suppression *in vivo*. We investigated only these two markers of autophagy, which have been shown to be altered in SCA3[39,41,42], to assess for potential rescue or exacerbation of autophagy following ASO treatment. Future studies are needed to clarify the role of ATXN3 in autophagy both in healthy and diseased brain.

A limitation of this study is that we did not extend the treatment and evaluation beyond 29 weeks, and thus have not established whether ASO-5 treatment can prolong

life in Q84/Q84 mice, which are reported to have early lethality[16]. The basis for early lethality in this mouse model as well as the human disease is uncertain. Selective vulnerability to vital brainstem nuclei and DCN likely contributes to early lethality in SCA3[3]. In this light, the evidence presented here for robust silencing of mutant ATXN3 in the brainstem and DCN is encouraging.

As demonstrated by FDA approval in 2016 of the first CNS-targeted ASO therapy for treatment of infantile onset spinal muscular atrophy, ASO-mediated transcriptional repression holds promise as a potential therapy for many fatal, as yet untreatable, neurodegenerative diseases. In addition to the current preclinical longitudinal study, ASO preclinical development has been completed for several other polyglutamine diseases, with sustained ASO-mediated phenotypic rescue similarly reported[20,22,49,50]. Notably, the very ASO assessed here, ASO-5, possesses the same ASO chemistry as a therapeutic approach that has already progressed into early stage clinical trials for the treatment of HD. Although we tested the efficacy of only this single ASO targeting human *ATXN3*, our preclinical assessment in a progressive disease model expressing the actual human target gene provides proof-of-principle efficacy and safety to justify further efforts to identify ASO candidates for human SCA3 therapy.

3.5 Materials and Methods

3.5.1 Animals

All animal procedures were approved by the University of Michigan Institutional Animal Care and Use Committee and conducted in accordance with the United States Public Health Service's Policy on Humane Care and Use of Laboratory Animals. Genotyping was performed using tail biopsy DNA isolated prior to weaning and confirmed post mortem, as previously described[19]. Fragment analysis was used to assess the human *ATXN3* repeat expansions (Laragen, San Diego, CA), with animals expressing repeat expansion of Q75 or greater included in behavioral studies. Animals were sex-, littermate- and age-matched for each study. For biochemical and histological analysis, animals were euthanized either at 12, 16, or 22 weeks of age after ASO treatment at 8 weeks, and tissue macro-dissected for histology and biochemical assessments, as previously described[19]. All treatment groups were blinded to the experimenter prior to analysis.

3.5.2 Antisense oligonucleotides.

The anti-*ATXN3* candidate ASO (ASO-5; GCATCTTTTCATTACTGGC) and a scrambled ASO control (ASO-Ctrl; GTTTTCAAATACACCTTC) used in this study were previously described[19]. Specifically, the ASOs have a gapmer design[10] with eight unmodified deoxynucleotides with native sugar-phosphate backbone flanked on both sides by five 2'-O-methoxyethylribose modified ribonucleotides with phosphorothioate backbones. ASO-5 targets the 3'UTR of both human and mouse *ATXN3*. Oligonucleotides were synthesized as previously described[23,24] and solubilized in PBS (without Ca2+ or Mg2+).

3.5.3 Stereotaxic mouse ICV ASO delivery.

Stereotaxic administration of ASOs into the right lateral ventricle via ICV injections was performed as previously described[19]. Following surgery, weight, grooming activity and home cage activity were recorded for up to ten days.

3.5.4 RNA isolation and quantitative PCR.

Total RNA was isolated from dissected brain tissue using Trizol reagent according to the manufacturer's protocol (Invitrogen, Carlsbad, CA). Reverse transcription was performed on 0.5-1 µg of total RNA using the iScript cDNA synthesis kit according to the manufacturer's instructions (Bio-Rad, Hercules, CA). The cDNA was diluted 1:20 in nuclease-free water. iQ SYBR green quantitative PCR was performed on the diluted cDNA following the manufacturer's protocol (Bio-Rad, Hercules, CA). Average adjusted relative quantification analysis was performed using previously described primers[6,19].

3.5.5 Immunoblotting.

Protein lysates from macro-dissected brainstem and cerebellar tissue were processed as previously described[19] and stored at -80°C. 40 µg total mouse brain protein lysate were resolved in 4-20% gradient sodium dodecyl sulfate-polyacrylamide (SDS) electrophoresis gels and transferred to 0.45 µm nitrocellulose membranes. Membranes were incubated overnight at 4°C with various antibodies: mouse anti-ATXN3 (1H9) (1:1000, MAB5360; Millipore, Billerica, MA), mouse anti-GFAP (1:20000, 3670S; Cell Signaling Technology, Danvers, MA), rabbit anti-IBA1 (1:500, 016-20001; Wako, Osaka, Japan), rabbit anti-BAX (1:500, 2772S; Cell Signaling Technology,

Danver, MA), mouse anti-BCL-2 (1:500, 610538; BD Biosciences, San Jose, CA), mouse anti-p62 (1:1000, ADI-SPA-902-D; Enzo Life Sciences, New York, NY), rabbit anti-BECLIN1 (1:1000, ab207612; Abcam, Cambridge, UK), mouse anti-GAPDH (1:5000, MAB374; Millipore, Billerica, MA), and rabbit anti-α-Tubulin (1:5000, #S2144; Cell Signaling Technology, Danvers, MA). Bound primary antibodies were visualized by incubation with peroxidase-conjugated anti-mouse or anti-rabbit secondary antibody (1:10000; Jackson Immuno Research Laboratories, West Grove, PA) followed by treatment with the ECL-plus reagent (Western Lighting; PerkinElmer, Waltham, MA) and exposure to autoradiography films. Band intensities were quantified using ImageJ analysis software (NIH, Bethesda, MD).

3.5.6 Immunohistochemistry.

Whole brains perfused with PBS were processed as previously described[19]. Primary antibodies assessed include: mouse anti-ATXN3 (1H9) (1:1000, MAB5360; Millipore, Billerica, MA), rabbit anti-ASO (1:5000; Ionis Pharmaceuticals, Carlsbad, CA), rabbit anti-NeuN-488 conjugated (1:1000, ABN78A4; Millipore, Billerica, MA), mouse anti-GFAP (1:1000, #3670; Cell Signaling Technology, Danvers, MA), rabbit anti-IBA1 (1:1000, 019-19741, WAKO, Richmond, VA), goat anti-OLIG2 (1:500, sc-19969, Santa Cruz Biotechnology, Dallas, TX), mouse anti-p62 (1:1000, ADI-SPA-902-D; Enzo Life Sciences, New York, NY), and rabbit anti-BECLIN1 (1:1000, ab207612; Abcam, Cambridge, UK). Imaging was performed using an IX71 Olympus inverted microscope (Melville, NY) or Nikon-A1 confocal microscope (Melville, NY) in the basilar pontine nuclei (denoted as pons) and deep cerebellar nuclei (DCN). Nuclear ATXN3 accumulation was quantified as previously described[19].

3.5.7 Motor evaluation.

Balance and coordination were tested by measuring the time needed to traverse a 5-mm square beam, as previously described[16]. Traversal time was recorded for each trial with a maximum of 20 seconds; falls from the beam were scored as 20 seconds. Paw slips below the beam and hind limb dragging were also recorded for each trial. Locomotor activities were measured by placing the mice in a photobeam activity system open field apparatus (San Diego Instruments, San Diego, CA) for 30-minute trials on days when no other testing occurred. Total activity was calculated by measuring the

total number of x/y-axis beam breaks. Body weights were recorded on the first day of behavior testing at each time point.

3.5.8 Brain slice preparation and electrophysiology.

Parasagittal cerebellar slices were prepared as described previously[25]. Purkinje neurons from cerebellar lobules II-V were recorded using borosilicate glass patch pipettes with a 3–5 MΩ and filled with internal pipette recording solution containing the following (in mM): 119 K gluconate, 2 Na gluconate, 6 NaCl, 2 $MgCl_2$, 0.9 EGTA, 10 HEPES, 14 Tris-phosphocreatine, 4 MgATP, 0.3 tris-GTP, pH 7.3, osmolarity 290 mOsm. Recordings were made 1-5 hours after slice preparation in a recording chamber continuously perfused with carbogen-bubbled ACSF at 33°C at a flow rate of 2–3 mL/min. Data were acquired using an Axon CV-7B headstage amplifier, Axon Multiclamp 700B amplifier, Digidata 1440A interface, and pClamp-10 software (MDS Analytical Technologies, Sunnyvale, CA). In all cases, acquired data were digitized at 100 kHz. Voltage data were acquired in current-clamp mode with bridge balance compensation and filtered at 2 kHz. Cells were rejected if the series resistance changed by >20% during recording. Whole-cell somatic recordings were rejected if the series resistance rose above 15 MΩ, with most recordings having a series resistance of <10 MΩ. All voltages were corrected for a liquid junction potential of +10 mV[26]. Firing frequency was determined in Clampfit 1.2 (MDS Analytical Technologies) using a single 10 second cell-attached recording. Firing frequency histogram reflects compiled firing frequencies for all cells of each genotype divided into 25 Hz bins. Analysis of the afterhyperpolarization (AHP) was performed on recordings where the cell was held at -80 mV and injected with a series of escalating 1 second current pulses. The AHP was analyzed using the first spike from the first trace where there was no greater than a 50-millisecond delay to the spike from current injection onset. Reported AHP values were calculated by taking V_m at each time point (indicated times are the time after spike peak) and subtracting it from threshold. Threshold for each spike was defined as the V_m where dV/dt crosses 5% of the peak dV/dt during the rising phase of the spike.

3.5.9 Statistics.

All statistical analyses were performed using Prism (7.0; GraphPad Software, La Jolla, CA). All statistical significance, except firing frequency, was tested using analysis

of variance with a post hoc Tukey's multiple comparisons test. Variability about the mean is expressed as mean ± standard error of the mean. Firing frequency, which didn't exhibit Gaussian distribution, was reported using box (25-75 percentile) and whiskers (1-99 percentile) plot and assessed with Kruskal-Wallis test with a post hoc Dunn's multiple comparisons test. All tests set the level of significance at $p<0.05$.

3.6 Acknowledgements and Author Contributions

Ionis Pharmaceuticals identified and generated the anti-ATXN3 ASOs. This work was supported in part by a research contract from Ionis Pharmaceuticals (to H.L.P.), a Michigan Brain Initiative Predoctoral Fellowship for Neuroscience (to L.R.M.), a Becky Babcox Fund Pilot Research Award (G015616 to H.S.M.), and grants from the NIH (T32-NS007222-33 to H.S.M. and R01- NS038712 to PI H.L.P.). H.S.M., L.R.M., R.C., H.Z., H.B.Z., V.G.S., and H.L.P conceptualized and designed the study. H.S.M., L.R.M., R.C., R.K., M.M., and K.G.B. acquired and analyzed the data. H.S.M., L.R.M., R.C., and H.L.P. drafted the text and prepared the figures. Ionis Pharmaceuticals solely owns Intellectual Property directed to SCA3 ASOs. H.Z. and H.B.K. are employees of Ionis Pharmaceuticals. This work was supported in part by Ionis Pharmaceuticals.

3.7 References

1 Costa Mdo, C. & Paulson, H. L. Toward understanding Machado-Joseph disease. *Progress in neurobiology* **97**, 239-257, doi:10.1016/j.pneurobio.2011.11.006 (2012).

2 Monin, M. L. *et al.* Survival and severity in dominant cerebellar ataxias. *Ann Clin Transl Neurol* **2**, 202-207, doi:10.1002/acn3.156 (2015).

3 Rub, U. *et al.* Clinical features, neurogenetics and neuropathology of the polyglutamine spinocerebellar ataxias type 1, 2, 3, 6 and 7. *Progress in neurobiology* **104**, 38-66, doi:10.1016/j.pneurobio.2013.01.001 (2013).

4 Rosenberg, R. N. Machado-Joseph disease: an autosomal dominant motor system degeneration. *Mov Disord* **7**, 193-203, doi:10.1002/mds.870070302 (1992).

5 Paulson, H. L., Shakkottai, V. G., Clark, H. B. & Orr, H. T. Polyglutamine spinocerebellar ataxias - from genes to potential treatments. *Nat Rev Neurosci* **18**, 613-626, doi:10.1038/nrn.2017.92 (2017).

6 Ramani, B. P., B.; Moore, L.R.; Wang, B.; Huang, R.; Guan, Y.; Paulson, HL. Comparison of spinocerebellar ataxia type 3 mouse models identifies early gain-of-function, cell-autonomous transcriptional changes in oligodendrocytes. *Human Molecular Genetics* doi:doi.org/10.1093/hmg/ddx224 (2017).

7 Schmitt, I. *et al.* Inactivation of the mouse Atxn3 (ataxin-3) gene increases protein ubiquitination. *Biochemical and biophysical research communications* **362**, 734-739, doi:10.1016/j.bbrc.2007.08.062 (2007).

8 Cerritelli, S. M. & Crouch, R. J. Ribonuclease H: the enzymes in eukaryotes. *FEBS J* **276**, 1494-1505, doi:10.1111/j.1742-4658.2009.06908.x (2009).

9 Chiriboga, C. A. *et al.* Results from a phase 1 study of nusinersen (ISIS-SMN(Rx)) in children with spinal muscular atrophy. *Neurology* **86**, 890-897, doi:10.1212/WNL.0000000000002445 (2016).
10 Bennett, C. F. & Swayze, E. E. RNA targeting therapeutics: molecular mechanisms of antisense oligonucleotides as a therapeutic platform. *Annu Rev Pharmacol Toxicol* **50**, 259-293, doi:10.1146/annurev.pharmtox.010909.105654 (2010).
11 Yu, R. Z. *et al.* Tissue disposition of 2'-O-(2-methoxy) ethyl modified antisense oligonucleotides in monkeys. *J Pharm Sci* **93**, 48-59, doi:10.1002/jps.10473 (2004).
12 Finkel, R. S. *et al.* Treatment of infantile-onset spinal muscular atrophy with nusinersen: a phase 2, open-label, dose-escalation study. *Lancet* **388**, 3017-3026, doi:10.1016/S0140-6736(16)31408-8 (2016).
13 Finkel, R. S. *et al.* Nusinersen versus Sham Control in Infantile-Onset Spinal Muscular Atrophy. *N Engl J Med* **377**, 1723-1732, doi:10.1056/NEJMoa1702752 (2017).
14 Alves, S. *et al.* Allele-specific RNA silencing of mutant ataxin-3 mediates neuroprotection in a rat model of Machado-Joseph disease. *PloS one* **3**, e3341, doi:10.1371/journal.pone.0003341 (2008).
15 Nobrega, C. *et al.* Silencing mutant ataxin-3 rescues motor deficits and neuropathology in Machado-Joseph disease transgenic mice. *PloS one* **8**, e52396, doi:10.1371/journal.pone.0052396 (2013).
16 Costa Mdo, C. *et al.* Toward RNAi therapy for the polyglutamine disease Machado-Joseph disease. *Molecular therapy : the journal of the American Society of Gene Therapy* **21**, 1898-1908, doi:10.1038/mt.2013.144 (2013).
17 Evers, M. M. *et al.* Ataxin-3 protein modification as a treatment strategy for spinocerebellar ataxia type 3: removal of the CAG containing exon. *Neurobiol Dis* **58**, 49-56, doi:10.1016/j.nbd.2013.04.019 (2013).
18 Toonen, L. J. A., Rigo, F., van Attikum, H. & van Roon-Mom, W. M. C. Antisense Oligonucleotide-Mediated Removal of the Polyglutamine Repeat in Spinocerebellar Ataxia Type 3 Mice. *Mol Ther Nucleic Acids* **8**, 232-242, doi:10.1016/j.omtn.2017.06.019 (2017).
19 Moore, L. R. *et al.* Evaluation of Antisense Oligonucleotides Targeting ATXN3 in SCA3 Mouse Models. *Mol Ther Nucleic Acids* **7**, 200-210, doi:10.1016/j.omtn.2017.04.005 (2017).
20 Kordasiewicz, H. B. *et al.* Sustained therapeutic reversal of Huntington's disease by transient repression of huntingtin synthesis. *Neuron* **74**, 1031-1044, doi:10.1016/j.neuron.2012.05.009 (2012).
21 Passini, M. A. *et al.* Antisense oligonucleotides delivered to the mouse CNS ameliorate symptoms of severe spinal muscular atrophy. *Science translational medicine* **3**, 72ra18, doi:10.1126/scitranslmed.3001777 (2011).
22 Scoles, D. R. *et al.* Antisense oligonucleotide therapy for spinocerebellar ataxia type 2. *Nature* **544**, 362-366, doi:10.1038/nature22044 (2017).
23 Cheruvallath, Z. S., Kumar, R. K., Rentel, C., Cole, D. L. & Ravikumar, V. T. Solid phase synthesis of phosphorothioate oligonucleotides utilizing diethyldithiocarbonate disulfide (DDD) as an efficient sulfur transfer reagent. *Nucleosides, nucleotides & nucleic acids* **22**, 461-468, doi:10.1081/NCN-120022050 (2003).
24 McKay, R. A. *et al.* Characterization of a potent and specific class of antisense oligonucleotide inhibitor of human protein kinase C-alpha expression. *The Journal of biological chemistry* **274**, 1715-1722 (1999).
25 Shakkottai, V. G. *et al.* Early changes in cerebellar physiology accompany motor dysfunction in the polyglutamine disease spinocerebellar ataxia type 3. *J Neurosci* **31**, 13002-13014, doi:10.1523/JNEUROSCI.2789-11.2011 (2011).

26 Telgkamp, P. & Raman, I. M. Depression of inhibitory synaptic transmission between Purkinje cells and neurons of the cerebellar nuclei. *J Neurosci* **22**, 8447-8457 (2002).
27 Cemal, C. K. *et al.* YAC transgenic mice carrying pathological alleles of the MJD1 locus exhibit a mild and slowly progressive cerebellar deficit. *Hum Mol Genet* **11**, 1075-1094 (2002).
28 Seidel, K. *et al.* On the distribution of intranuclear and cytoplasmic aggregates in the brainstem of patients with spinocerebellar ataxia type 2 and 3. *Brain Pathol* **27**, 345-355, doi:10.1111/bpa.12412 (2017).
29 Seidel, K. *et al.* Brain pathology of spinocerebellar ataxias. *Acta Neuropathol* **124**, 1-21, doi:10.1007/s00401-012-1000-x (2012).
30 Evert, B. O. *et al.* Inflammatory genes are upregulated in expanded ataxin-3-expressing cell lines and spinocerebellar ataxia type 3 brains. *J Neurosci* **21**, 5389-5396 (2001).
31 Schoch, K. M. & Miller, T. M. Antisense Oligonucleotides: Translation from Mouse Models to Human Neurodegenerative Diseases. *Neuron* **94**, 1056-1070, doi:10.1016/j.neuron.2017.04.010 (2017).
32 Bichelmeier, U. *et al.* Nuclear localization of ataxin-3 is required for the manifestation of symptoms in SCA3: in vivo evidence. *J Neurosci* **27**, 7418-7428, doi:10.1523/JNEUROSCI.4540-06.2007 (2007).
33 Raman, I. M. & Bean, B. P. Ionic currents underlying spontaneous action potentials in isolated cerebellar Purkinje neurons. *J Neurosci* **19**, 1663-1674 (1999).
34 Dell'Orco, J. M., Pulst, S. M. & Shakkottai, V. G. Potassium channel dysfunction underlies Purkinje neuron spiking abnormalities in spinocerebellar ataxia type 2. *Hum Mol Genet* **26**, 3935-3945, doi:10.1093/hmg/ddx281 (2017).
35 Dell'Orco, J. M. *et al.* Neuronal Atrophy Early in Degenerative Ataxia Is a Compensatory Mechanism to Regulate Membrane Excitability. *J Neurosci* **35**, 11292-11307, doi:10.1523/JNEUROSCI.1357-15.2015 (2015).
36 Mark, M. D. *et al.* Spinocerebellar ataxia type 6 protein aggregates cause deficits in motor learning and cerebellar plasticity. *J Neurosci* **35**, 8882-8895, doi:10.1523/JNEUROSCI.0891-15.2015 (2015).
37 Jimenez-Sanchez, M., Thomson, F., Zavodszky, E. & Rubinsztein, D. C. Autophagy and polyglutamine diseases. *Progress in neurobiology* **97**, 67-82, doi:10.1016/j.pneurobio.2011.08.013 (2012).
38 Wong, E. & Cuervo, A. M. Autophagy gone awry in neurodegenerative diseases. *Nat Neurosci* **13**, 805-811, doi:10.1038/nn.2575 (2010).
39 Ashkenazi, A. *et al.* Polyglutamine tracts regulate beclin 1-dependent autophagy. *Nature* **545**, 108-111, doi:10.1038/nature22078 (2017).
40 Nascimento-Ferreira, I. *et al.* Beclin 1 mitigates motor and neuropathological deficits in genetic mouse models of Machado-Joseph disease. *Brain* **136**, 2173-2188, doi:10.1093/brain/awt144 (2013).
41 Sittler, A. *et al.* Deregulation of autophagy in postmortem brains of Machado-Joseph disease patients. *Neuropathology*, doi:10.1111/neup.12433 (2017).
42 Saitoh, Y. *et al.* p62 plays a protective role in the autophagic degradation of polyglutamine protein oligomers in polyglutamine disease model flies. *The Journal of biological chemistry* **290**, 1442-1453, doi:10.1074/jbc.M114.590281 (2015).
43 Switonski, P. M., Szlachcic, W. J., Krzyzosiak, W. J. & Figiel, M. A new humanized ataxin-3 knock-in mouse model combines the genetic features, pathogenesis of neurons and glia and late disease onset of SCA3/MJD. *Neurobiol Dis* **73**, 174-188, doi:10.1016/j.nbd.2014.09.020 (2015).

44 Hansen, S. T., Meera, P., Otis, T. S. & Pulst, S. M. Changes in Purkinje cell firing and gene expression precede behavioral pathology in a mouse model of SCA2. *Hum Mol Genet* **22**, 271-283, doi:10.1093/hmg/dds427 (2013).
45 Akemann, W. & Knopfel, T. Interaction of Kv3 potassium channels and resurgent sodium current influences the rate of spontaneous firing of Purkinje neurons. *J Neurosci* **26**, 4602-4612, doi:10.1523/JNEUROSCI.5204-05.2006 (2006).
46 Hourez, R. *et al.* Aminopyridines correct early dysfunction and delay neurodegeneration in a mouse model of spinocerebellar ataxia type 1. *J Neurosci* **31**, 11795-11807, doi:10.1523/JNEUROSCI.0905-11.2011 (2011).
47 Rubinsztein, D. C. The roles of intracellular protein-degradation pathways in neurodegeneration. *Nature* **443**, 780-786, doi:10.1038/nature05291 (2006).
48 Puorro, G. *et al.* Peripheral markers of autophagy in polyglutamine diseases. *Neurol Sci*, doi:10.1007/s10072-017-3156-6 (2017).
49 Lieberman, A. P. *et al.* Peripheral androgen receptor gene suppression rescues disease in mouse models of spinal and bulbar muscular atrophy. *Cell Rep* **7**, 774-784, doi:10.1016/j.celrep.2014.02.008 (2014).
50 Sahashi, K. *et al.* Silencing neuronal mutant androgen receptor in a mouse model of spinal and bulbar muscular atrophy. *Hum Mol Genet* **24**, 5985-5994, doi:10.1093/hmg/ddv300 (2015).

3.8 Figures

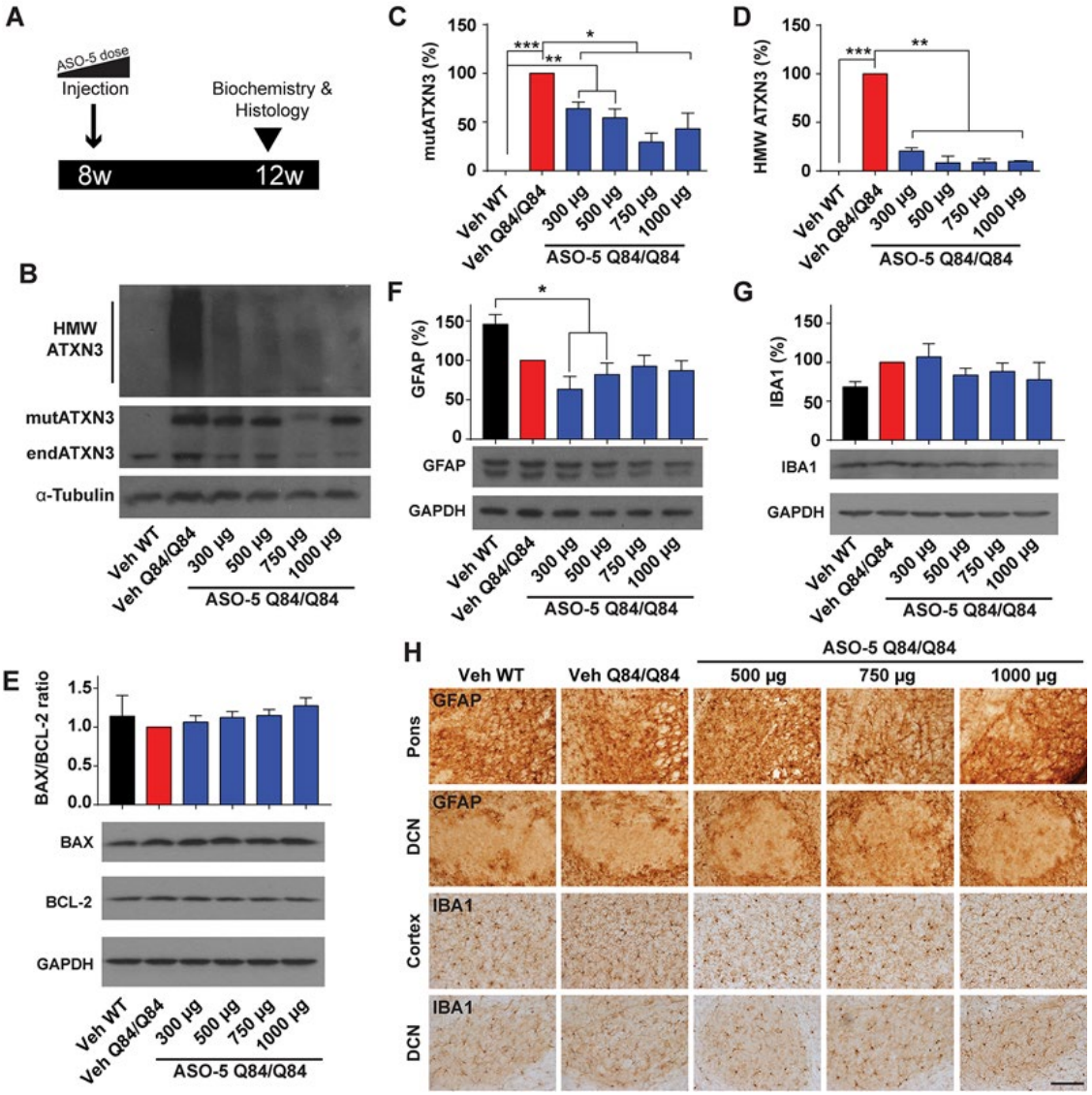

Figure 3.1. Dose-dependent ASO suppression of mutant ATXN3 and tolerability in homozygous SCA3 transgenic mice. (A) ASO-5 dose response study design. Sex- and littermate-matched Q84/Q84 mice received an intracerebroventricular injection of ASO-5 (300-1000 µg) or vehicle (Veh) at 8 weeks of age. Brains were harvested four weeks after injection for analysis. **(B)** Representative western blot and quantification of **(C)** soluble mutant human ATXN3 (mutATXN3) and **(D)** high molecular weight (HMW) ATXN3 protein levels from brainstem protein lysates four weeks after ASO injection. **(E)** Western blot and quantification of BAX/BCL-2 protein expression ratio in the mouse brainstem four weeks after treatment. **(F)** Western blot and quantification of GFAP and **(G)** IBA1 protein levels in the mouse brainstem four weeks following treatment. **(H)** Anti-GFAP immunohistochemical staining of pons and DCN and anti-IBA1 staining of cortex and DCN four weeks following ASO injection. Data (mean ± SEM) are reported relative to Veh Q84/Q84 treated mice (n=4 per dose). One-way ANOVA with a post hoc Tukey test (*p<0.05; **p<0.01; ***p<0.001). Scale bar, 200 µm.

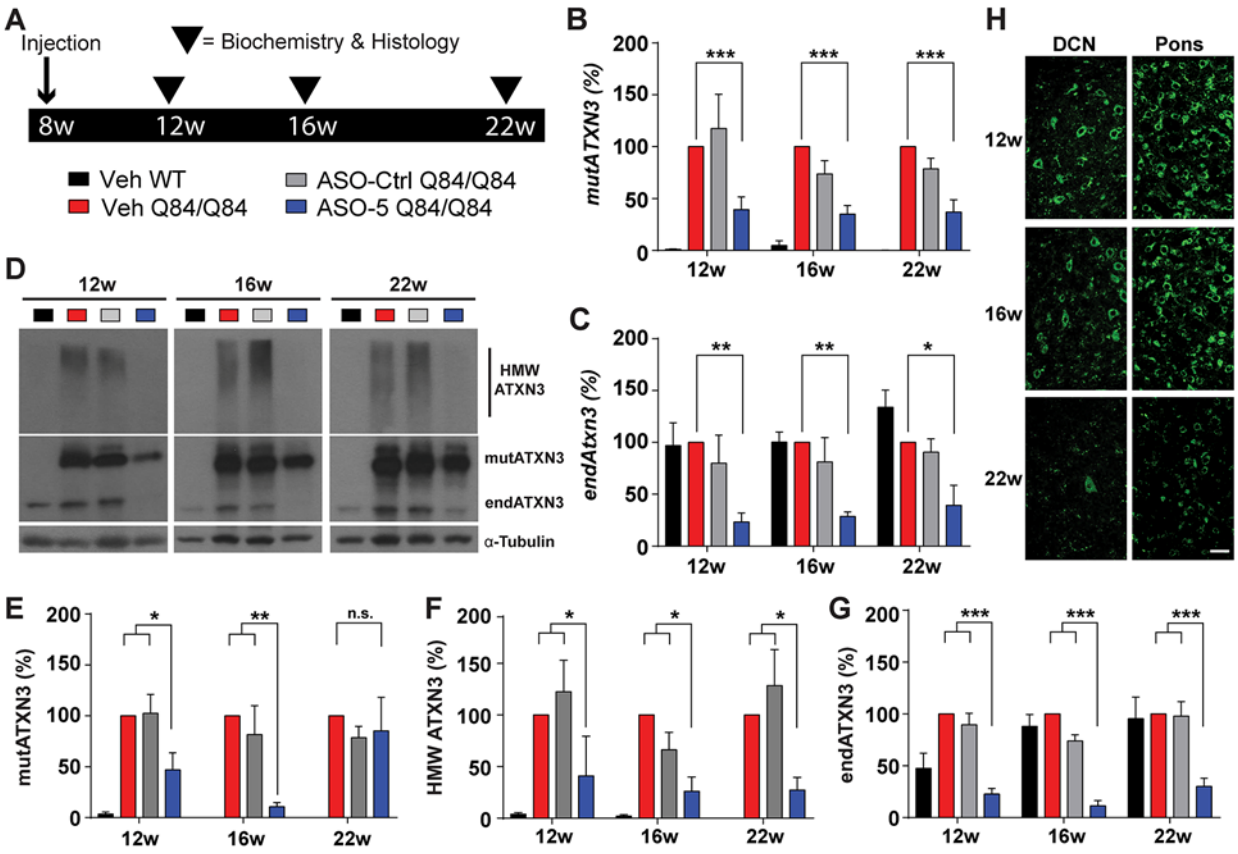

Figure 3.2. ASO-mediated suppression of mutant and oligomeric ATXN3 protein is sustained at least eight weeks after injection in SCA3 mice. (A) Longitudinal trial design to assess sustained ATXN3 reduction in Q84/Q84 mice. Sex- and littermate-matched homozygous mice received an intracerebroventricular (ICV) injection of ASO-5 (700 µg) or vehicle (Veh) at 8 weeks of age. Brains were harvested at 12, 16 or 22 weeks of age for biochemical and histological analyses. Quantification of **(B)** human mutant *ATXN3* (*mutATXN3*) and **(C)** mouse endogenous (*endATXN3*) *Atxn3* transcript levels from treated mouse brainstem. **(D)** Representative immunoblots and quantification of **(E)** soluble mutant ATXN3 (mutATXN3), **(F)** high molecular weight (HMW) ATXN3, and **(G)** endogenous ATXN3 (endATXN3) protein in the brainstem at 12 weeks, 16 weeks, and 22 weeks of age. Data (mean ± SEM) are reported relative to vehicle-treated Q84/Q84 samples (n=4-6 per condition). Two-way ANOVA with a post hoc Tukey test (*p<0.05; **p<0.01; ***p<0.001). **(H)** Representative anti-ASO immunofluorescent images of pons and DCN of ASO-treated mice at 12, 16, and 22 weeks. Scale bar, 25 µm.

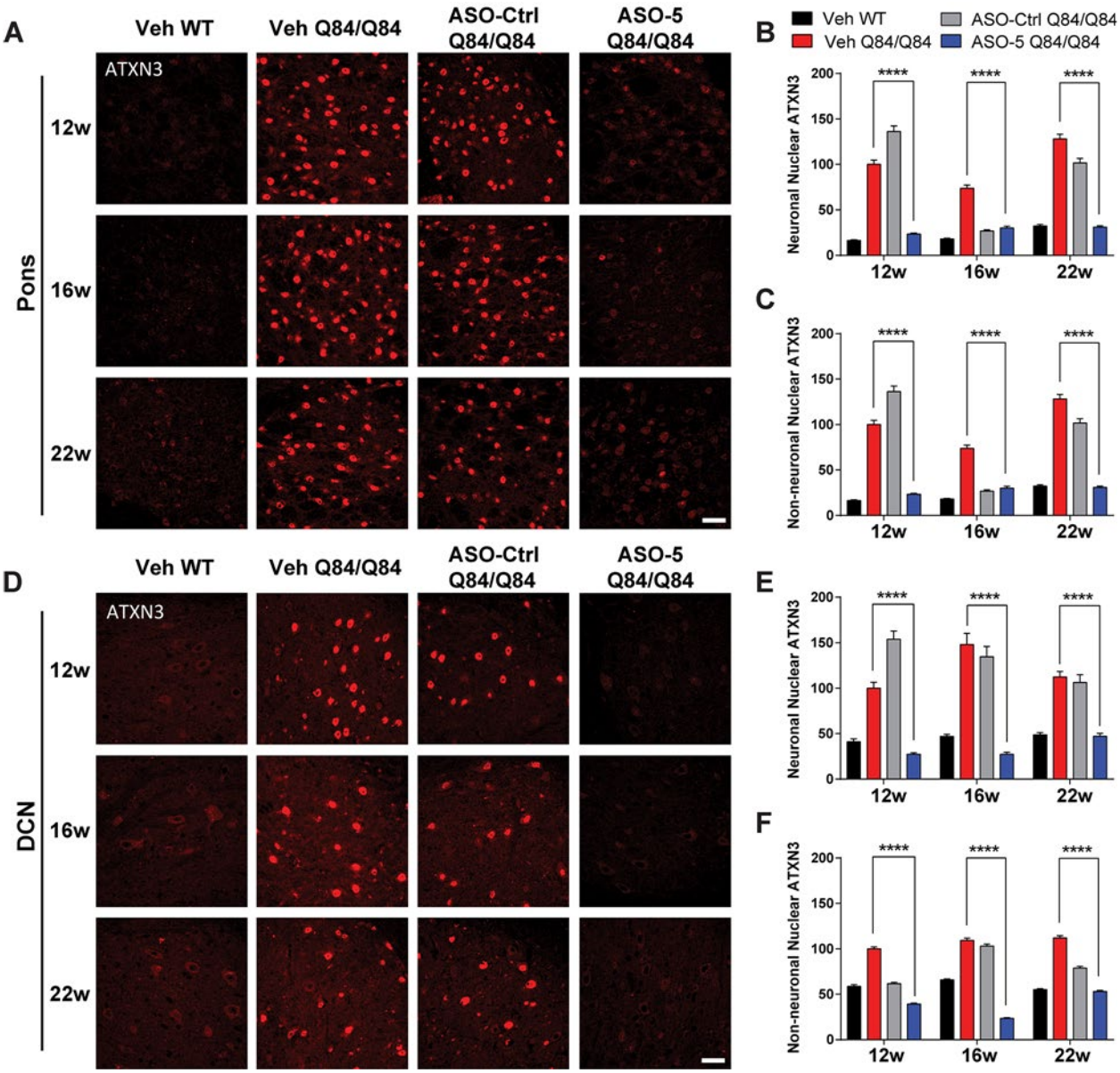

Figure 3.3. A single ASO-5 injection prevents nuclear accumulation of ATXN3 in vulnerable brain regions of SCA3 mice. (A) Anti-ATXN3 immunofluorescence in pons at 12, 16, and 22 weeks of age in ASO- or vehicle-treated mice. Quantified integrated density of ATXN3 immunofluorescence in (**B)** NeuN-positive neuronal nuclei and **(C)** NeuN-negative non-neuronal nuclei in the pons. **(D)** Anti-ATXN3 immunofluorescence in DCN at 12, 16, and 22 weeks of age in ASO or vehicle-treated mice. Quantified integrated density of ATXN3 immunofluorescence in (**E)** NeuN-positive neuronal nuclei and **(F)** NeuN-negative non-neuronal nuclei in the DCN. n=6 mice per condition, 3 images from pons or DCN quantified per mouse. Data (mean ± SEM) are reported relative to vehicle-treated Q84/Q84 mice. Two-way ANOVA with a post hoc Tukey test (****p<0.0001). Scale bar, 25 μm.

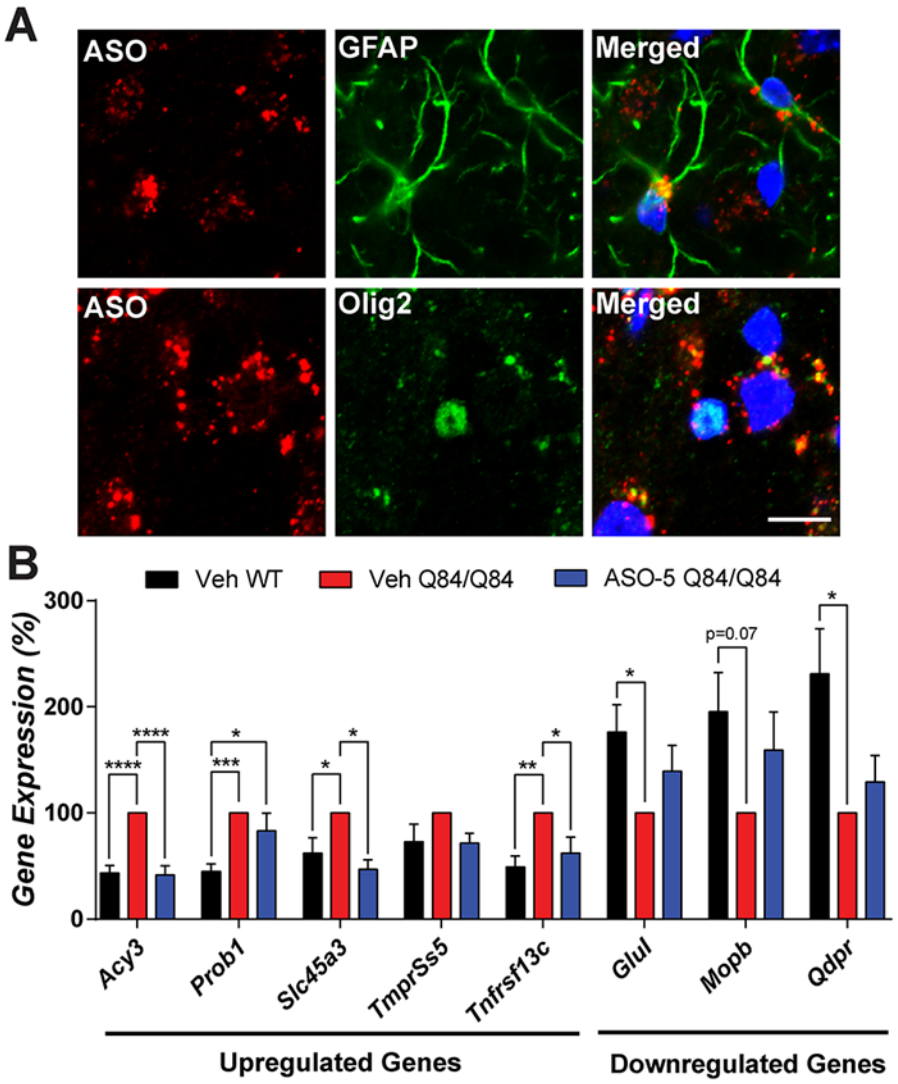

Figure 3.4. ASO-5 treatment rescues key differentially expressed brainstem transcripts in SCA3 mice. (A) Anti-ASO and anti-GFAP or anti-OLIG2 immunofluorescence in pons at 16 weeks of age in ASO-treated mice. **(B)** The differentially expressed transcripts in SCA3 mice shown were originally identified by Ramani *et. al.*, 2017 *HMG*. Vehicle-treated WT (Veh WT, black), vehicle-treated Q84/Q84 (Veh Q84/Q84, red) and ASO-5 treated Q84/Q84 (ASO-5 Q84/Q84, blue) mice were injected at 8 weeks, and brainstem transcripts were then assessed at 22 weeks of age. Data (mean ± SEM) are reported relative to vehicle treated Q84/Q84 mice (n=4-6). One-way ANOVA with a post hoc Tukey test (*p<0.05; **p<0.01; ***p<0.001; ****p<0.0001). Scale bar, 10 μm.

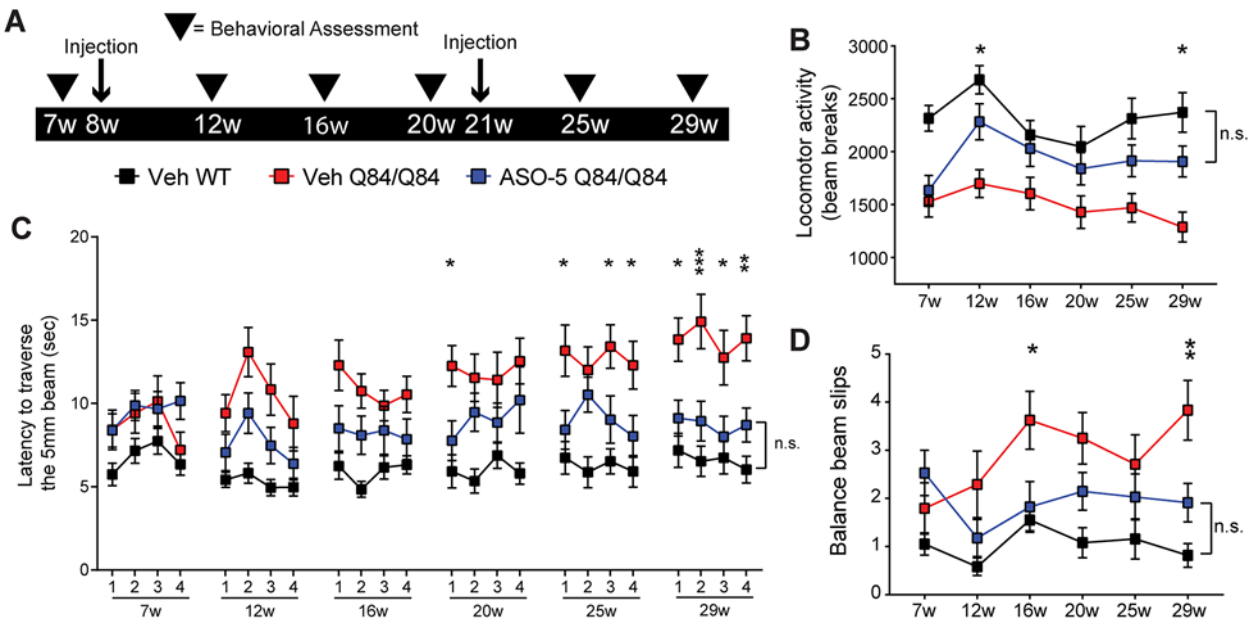

Figure 3.5. ASO-5 fully rescues motor phenotypes in SCA3 mice. (A) Longitudinal trial design to assess effect of sustained ATXN3 reduction on motor phenotypes in Q84/Q84 mice. Sex- and littermate-matched homozygous mice received two intracerebroventricular (ICV) injections of ASO-5 (700 µg) or vehicle (Veh), at 8 and 21 weeks of age. Behavioral assessments (arrowheads) were completed pre- and post-treatment at 7, 12, 16, 20, 25, and 29 weeks of age. **(B)** Quantification of average locomotor activity over time in vehicle-treated Q84/Q84 (Veh Q84/Q84, red), ASO-5 treated Q84/Q84 mice (ASO-5 Q84/Q84, blue), and vehicle-treated WT mice (Veh WT, black), determined by mean number of beam breaks in a 30-minute open-field test (mean ± SEM). Quantification of (**C**) time to traverse the beam (points represent the mean of two consecutive trials on each of the four days of testing ± SEM) on 5-mm-squared beam and (**D**) number of limb slips (points represent average number of slips on day 4 ± SEM). Test group size used in motor tests ranged from 12-19 animals. Two-way repeated measures ANOVA with a post hoc Tukey test, graphs present statistical data comparisons of Veh Q84/Q84 relative to ASO-5 Q84/Q84 (*p<0.05; **p<0.01; ***p<0.001; n.s.= not significant).

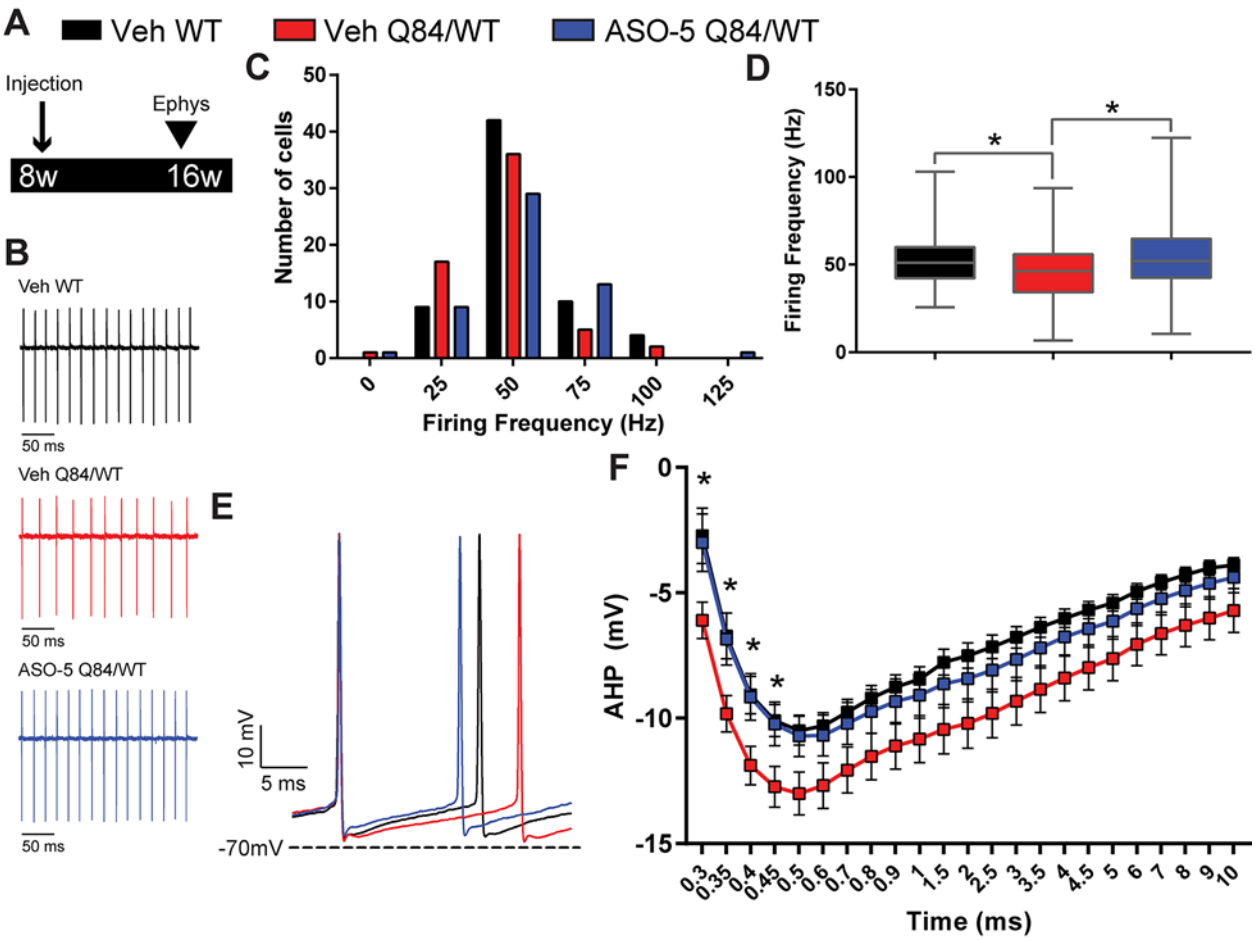

Figure 3.6. ASO-5 treatment reverses slowed firing frequency in SCA3 Purkinje neurons. (**A**) Schematic of electrophysiologic study design. Hemizygous Q84/WT mice were injected with either vehicle or ASO-5 (700 µg) at 8 weeks of age and Purkinje cells were recorded at 16 weeks of age. **(B)** Representative patch clamp recordings of spontaneous firing in Purkinje neurons from vehicle-treated WT (Veh WT, black, n=65), vehicle-treated Q84/WT (Veh Q84/WT, red, n=61), and ASO-5 treated Q84/WT (ASO-5 Q84/WT, blue, n=53) mice. **(C)** Histogram of Purkinje neuron firing frequencies with 25 Hz bins. **(D)** Median firing frequency plotted using box (25-75 percentile) and whiskers (1-99 percentile) plot. Kruskal-Wallis test with a post hoc Dunn's multiple comparisons test (*p<0.05). **(E)** Representative traces and **(F)** quantification (mean ± SEM) of afterhyperpolarization (AHP) in Veh Q84/WT, Veh WT and ASO-5 Q84/WT Purkinje cells. Two-way repeated measures ANOVA with a post hoc Tukey test (*p<0.05).

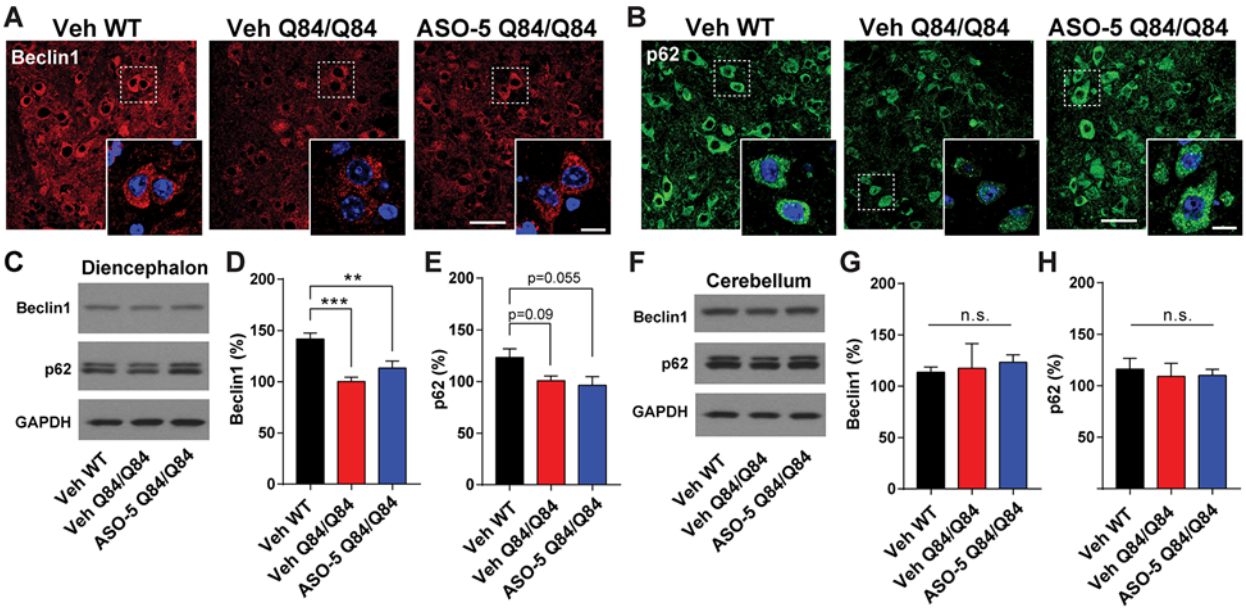

Figure 3.7. ASO-5 reduction of ATXN3 does not exacerbate changes in autophagy pathway proteins. Vehicle-treated WT (Veh WT), Vehicle-treated Q84/Q84 (Veh Q84/Q84) and ASO-5 treated Q84/Q84 (ASO-5 Q84/Q84) mice were injected at 8 weeks and tissue harvested at 16 weeks for histological and biochemical assessment (n=6 per condition). Representative immunofluorescence images of **(A)** Beclin1 and **(B)** p62 in the pons with magnification insets. Scale bar, 50 μm; inset scale bar, 10 μm. Representative western blots and quantification of Beclin1 and p62 protein expression in the **(C-E)** brainstem and **(F-H)** cerebellum of treated mice. Data (mean ± SEM) are reported relative to Veh Q84/Q84-treated mice (n=6). One-way ANOVA with a post hoc Tukey test (*p<0.05; ***p<0.001; n.s.= not significant).

CHAPTER 4
Distinct Pathogenic Features in a Human Embryonic Stem Cell Model of SCA3

4.1 Abstract

Spinocerebellar ataxia type 3 (SCA3) is a fatal, late-onset neurodegenerative disorder characterized by selective neuropathology in the brainstem, cerebellum, spinal cord, and substantia nigra. Here, we characterize the first NIH-approved human embryonic stem cell (hESC) line derived from an embryo harboring the SCA3 mutation. Referred here as SCA3-hESC, this line is heterozygous for the mutant polyglutamine-encoding *CAG* repeat expansion in the *ATXN3* gene within the pathogenic repeat range for SCA3. We observed relevant molecular hallmarks of the human disease at all differentiation stages from stem cells to cortical neurons, including robust ATXN3 aggregation and altered expression of key components of the protein quality control machinery. Finally, antisense oligonucleotide-mediated reduction of ATXN3 prevented the formation of p62-positive aggresomes in SCA3-hESCs. The SCA3-hESC line offers a unique and highly relevant human disease model that holds strong potential to advance understanding of SCA3 disease mechanisms and facilitate the evaluation of possible SCA3 therapies.

4.2 Introduction

Spinocerebellar ataxia type 3 (SCA3) is a late-onset neurological disorder and the most common autosomal dominant ataxia worldwide[1]. One of nine polyglutamine (polyQ) diseases, SCA3 is caused by a heterozygous *CAG* trinucleotide repeat expansion that produces an abnormally long, aggregate-prone polyQ sequence in the encoded disease protein[2]. In SCA3, this polyQ expansion occurs in ATXN3, a deubiquitinase with wide-ranging functions in the ubiquitin proteasome system, macroautophagy, DNA damage repair, and transcriptional regulation[1,3]. Despite

ubiquitous expression, polyQ-expanded ATXN3 inflicts neuronal dysfunction and loss in discrete brain nuclei spanning the brainstem, cerebellum, spinal cord, substantia nigra, brainstem, and striatum through a presumed dominant toxic gain-of-function mechanism[4,5]. There remains limited understanding of the pathogenic cascade leading to neurodegeneration, particularly in prodromal SCA3 stages, as well as a lack of well-supported hypotheses for tissue-specific vulnerabilities, and no approved treatments to slow or stop progression of this fatal disease[1,2].

Disease-specific human pluripotent stem cell (hPSC) lines, including patient-derived induced pluripotent stem cell (iPSC) lines and human embryonic stem cell (hESC) lines derived from donated disease embryos, are proving to be increasingly important model systems for the study of neurodegenerative diseases[6,7]. Disease-specific hPSC lines enable the study of disease processes in human disease-vulnerable differentiated cellular populations that express endogenous levels of pathogenic genes. In the past decade, several hPSC lines carrying the SCA3 mutation have been developed, including several SCA3 patient-derived iPSC lines[8-18] and one hESC line harboring the SCA3 mutation[19]. This SCA3 hESC line, however, is not approved for research use in the United States. While the production of these lines represents progress towards improved human disease model systems, few or in some cases conflicting studies have been performed to verify that these developed SCA3 hPSC lines replicate well-established SCA3 molecular phenotypes. Identification of quantifiable, disease-dependent molecular phenotypes is arguably needed in order to use such SCA3 hPSC lines to investigate disease mechanisms or in preclinical testing of potential therapeutic agents for SCA3.

Here we report the validation and characterization of the first SCA3 disease-specific hESC line added to the NIH registry of approved hESC lines, designated UM134-1 on the NIH registry but referenced here as SCA3-hESC. In addition to confirming stem cell-like properties of undifferentiated SCA3-hESC, we evaluate well-established molecular phenotypes of SCA3 in undifferentiated stem cells and in differentiated neural progenitor cells and forebrain cortical neurons. We also demonstrate the potential for SCA3-hESC to serve as a disease model to facilitate preclinical drug development by assessing whether molecular phenotypes are rescued

following treatment with an anti-*ATXN3* antisense oligonucleotide (ASO) recently validated in preclinical SCA3 transgenic mouse studies[20,21]. Together the findings support the SCA3-hESC line as an important new biological reagent for the SCA3 field, and establish its potential to improve human SCA3 disease modeling and preclinical drug assessment.

4.3 Results

4.3.1 Derivation and characterization of SCA3-hESC line UM134-1

The SCA3-affected embryo was originally created by assistive reproductive technologies for the purpose of procreation. The embryo was donated to the University of Michigan following single gene preimplantation genetic testing, which identified the embryo as heterozygous for a pathogenic *CAG* repeat expansion in *ATXN3.* The derived UM134-1 hESC line (referred to here as SCA3-hESC) was accepted to the NIH registry of approved hESC lines in 2014 (#0286). The unrelated hESC line UM4-6 (#0147, referred to here as WT-hESC), developed previously under the same protocol at the University of Michigan and also accepted to the NIH registry, was used throughout these studies as a comparative control[22].

Undifferentiated SCA3-hESC exhibited a cellular morphology characteristic of pluripotent stem cells and expressed pluripotency markers OCT3/4, SOX2 and NANOG (**Fig. 4.1A**). Quantitative real-time PCR (qRT-PCR) confirmed that SCA3-hESC express pluripotency markers *LIN28*, *OCT4*, *SOX2*, and *NANOG* transcripts at levels comparable to WT-hESC (**Fig. 4.1B**) (n = 3 passages). Following 21 days of differentiation, PCR analysis confirmed that SCA3-hESC derived embryoid bodies express lineage markers *AFP* (endoderm), *BRACHYURY* (mesoderm), and *TUBB3* (ectoderm) (**Fig. 4.1C**). G-banded cytogenetic analysis of SCA3-hESC identified a normal 46,XY karyotype with no chromosomal abnormalities (**Fig. 4.1D**). A previous study showed that the WT-hESC line used here also has a normal 46,XY karyotype with no chromosomal abnormalities[22].

Immunoblot analysis of WT- and SCA3-hESC protein extracts using monoclonal antibody 1C2, which recognizes expanded polyQ, revealed a band of ~60 kDa in SCA3-hESC that is not present in WT-hESC, indicating expression of a polyQ-expanded protein in SCA3-hESC (**Fig. 4.1E**). Anti-ATXN3 immunoblot analysis identified a doublet

of ~42-44 kDa in WT-hESC consistent with normal repeat length polymorphism in *ATXN3*, whereas ATXN3 bands of ~42kDa and ~60kDa were observed in SCA3-hESC, corresponding to wild type ATXN3 (wtATXN3) and polyQ-expanded mutant ATXN3 (mutATXN3), respectively (**Fig. 4.1F**). Subsequent gene fragmentation analysis performed on early passages of both lines confirmed that SCA3-hESC is heterozygous for one pathogenic and one normal *ATXN3* allele encoding ATXN3 polyQ expansions of 70Q and 13Q, respectively, compared to non-pathogenic WT-hESC polyQ lengths of 22Q and 13Q (**Fig. 4.1G**).

4.3.2 Undifferentiated SCA3-hESC exhibit ATXN3 aggregation and nuclear sequestration

Misfolding of expanded polyQ proteins and subsequent accumulation as high molecular weight oligomers and aggregates is a key pathological feature of polyQ diseases[4,23,24]. SCA3 post-mortem patient brains and transgenic mouse models of SCA3 exhibit widespread neuronal intranuclear and cytosolic inclusions of ATXN3 in brain regions affected in disease[24-28]. Aggregation of polyQ-expanded mutATXN3 has been detected in cellular models, but to our knowledge only with the aid of genetic or environmental manipulations, such as overexpression of highly aggregate-prone ATXN3 fragments[29-31] or stress induction through proteasomal inhibition or excitotoxicity[12,32]. A human cell model showing spontaneous aggregation of mutATXN3 expressed at endogenous levels in the absence of exogenous stressors would be an excellent tool for advancing our understanding of the role of native ATXN3 misfolding and aggregation in SCA3 pathogenesis.

We first sought to determine whether SCA3-hESC recapitulated mutATXN3 misfolding and aggregation under normal culture conditions. Anti-ATXN3 immunoblot analysis of undifferentiated WT- and SCA3-hESC protein lysates demonstrated accumulation of high molecular weight (HMW) ATXN3 species in SCA3-hESC that was largely absent in WT-hESC (**Fig. 4.2A**). Quantification confirmed an 80% ± 21% increase in HMW ATXN3 species >100kDa in SCA3-hESC relative to WT-hESC (p = 0.02, n = 3 passages) (**Fig. 4.2B**). Anti-ATXN3 immunocytochemistry (ICC) with DAPI co-staining revealed striking intranuclear and cytoplasmic ATXN3-positive puncta of variable sizes and shapes in SCA3-hESC (**Fig. 4.2C**). Though rare puncta were

observed in WT-hESC, SCA3-hESC formed significantly more puncta, averaging ~1 per cell with many cells containing multiple puncta (SCA3-hESC = 0.93 ± 0.12 ATXN3 puncta/cell, WT-hESC = 0.04 ± 0.01 ATXN3 puncta/cell, p<0.0001, n = 3-4 passages, 3-5 confocal images/passage) (**Fig. 4.2C,D**).

Abnormal sequestration of ATXN3 into neuronal nuclei is also a prominent pathological feature of SCA3 human disease[24,33-35]. Possessing both nuclear export and nuclear localization sequences, non-pathogenic ATXN3 is normally diffusely localized throughout the cytosol and nucleus[35], but undergoes rapid nuclear translocation following induction of proteotoxic stress[32]. Though it remains unclear why polyQ-expanded mutATXN3 becomes sequestered in neuronal nuclei, preventing or decreasing nuclear import of mutATXN3 rescues disease in SCA3 transgenic mouse models, suggesting that nuclear localization of mutATXN3 is a necessary step in disease pathogenesis[33]. To determine whether SCA3-hESC replicate this key pathological hallmark of disease, we quantified mean ATXN3 nuclear integrated density in undifferentiated WT- and SCA3-hESC, employing anti-ATXN3 and DAPI co-stained confocal imaging. Subsequent ImageJ analysis revealed an over 25% increase in mean ATXN3 nuclear integrated density in SCA3-hESC relative to WT-hESC (p < 0.0001) (**Fig. 4.2C,E**). Thus, in contrast to previously reported SCA3 *in vitro* models[12,29-32], SCA3-hESC endogenously form nuclear and cytoplasmic ATXN3 inclusions and exhibit enhanced nuclear sequestration of ATXN3 under normal, unstressed culture conditions.

4.3.3 Large ATXN3 aggregates localize to p62-positive aggresomes in SCA3-hESC

To further characterize observed ATXN3$^+$ puncta, we investigated whether proteins typically co-localizing with aggregates in SCA3 patient brains similarly co-localize in SCA3-hESC. The ubiquitin-binding shuttle protein p62 is found in ubiquitinated protein aggregates in many neurodegenerative diseases[36], including ATXN3 aggregates in SCA3 patient post-mortem brains[26,37,38]. Confocal imaging was performed on undifferentiated WT- and SCA3-hESC following anti-p62 and anti-ATXN3 immunofluorescence and DAPI staining (**Fig. 4.2C**). Unlike WT-hESC, in which p62 was more diffuse throughout cells and formed few p62+ puncta, SCA3-hESC formed large, juxtanuclear p62$^+$ puncta: SCA3-hESC = 0.72 ± 0.13 p62 puncta/cell; WT-hESC = 0.10

± 0.02 p62 puncta/cell ($p < 0.0001$) (**Fig. 4.2C,F)**. Large p62$^+$ structures always co-localized with large ATXN3$^+$ puncta (**Fig. 4.2C**), although many ATXN3$^+$ puncta lacked p62-staining suggesting there are two or more ATXN3 inclusion states in SCA3-hESC. In addition, p62 exhibited significantly increased localization to the nucleus in SCA3-hESC (mean p62 nuclear integrated density: SCA3-hESC = 58065 ± 1141; WT-hESC = 45332 ± 743, p <0.0001). Previous studies have shown that inhibiting autophagy induces p62 nuclear sequestration, thus enhanced nuclear p62 may indicate autophagic impairment in SCA3-hESC[39].

Notably, p62 promotes the formation of mutATXN3 aggresomes in cell-based overexpression model systems[40]. Aggresomes are dynamic pericentriolar structures consisting of a condensed protein aggregate core contained within an intermediate filament vimentin cage that function as a cellular pathway to consolidate misfolded protein aggregates[41]. Anti-vimentin and anti-ATXN3 ICC was performed on WT- and SCA3-hESC to investigate the possibility of aggresome formation in SCA3-hESC. SCA3-hESC formed distinct vimentin$^+$ puncta that consistently coincided with large ATXN3$^+$ puncta (**Fig. 4.2G**). Like p62, vimentin$^+$ puncta were rarely observed in WT-hESC, and when present did not preferentially co-localize with ATXN3 (data not shown). Further ICC investigations revealed that the 26S proteasome subunit PSMD11 also selectively localized to ATXN3 puncta in SCA3-hESC, demonstrating that components of the ubiquitin-dependent protein quality control machinery are also being sequestered into aggregates in SCA3-hESC (**Fig. 4.2H**). Together, these results suggest SCA3-hESC, but not WT-hESC, form ATXN3 aggregates, the majority of which are consolidated into p62$^+$ aggresomes.

4.3.4 Altered expression of key protein clearance pathway proteins in SCA3-hESC

Aggresome formation suggests a failure of canonical degradation pathways to dispose of misfolded proteins[41]. To determine which pathways may contribute to aggresome formation in SCA3-hESC, we evaluated key proteins involved in protein homeostasis including markers for autophagy, ubiquitin-dependent proteasomal degradation and protein folding. The autophagy-linked protein p62 is selectively degraded through autophagic clearance and thus increased levels of p62 may indicate

autophagic inhibition[42]. Immunoblot analysis showed that p62 levels were increased by 80% ± 24% in SCA3-hESC compared to WT-hESC (p = 0.008, n = 3 passages per line, 2-3 replicates per passage) (**Fig. 4.3A,B**). HMW p62, which is presumably aggregated, also accumulated in SCA3-hESC protein lysates, likely corresponding to p62 interactions with insoluble aggresome complexes formed by mutATXN3 (**Fig. 4.3A,B**). The expression of autophagy-related proteins Beclin1 and LC3-II was also compared in WT- and SCA3-hESC protein lysates (**Fig. 4.3C**). Though variable, LC3-II protein levels were significantly decreased by 64% ± 26% in SCA3-hESC relative to WT-hESC (p = 0.037), whereas Beclin1 levels did not statistically differ (p = 0.57) (n = 3 passages per line, 2-3 replicates per passage) (**Fig. 4.3D**).

Increased levels of ubiquitinated substrates have been observed in human SCA3 brain tissue and mouse models of SCA3, possibly reflecting altered mutATXN3 deubiquitinase activity[43] and downstream impairment in proteolytic clearance pathways[44,45]. Using a pan-ubiquitin antibody, we found that poly-ubiquitinated protein levels were slightly but significantly increased by 17% ± 4% in SCA3-hESC relative to WT-hESC (p = 0.015, n = 3 passages per line) (**Fig. 4.3E,F**), suggesting impairment in ubiquitin-dependent proteasomal clearance. Heat shock proteins Hsp40, Hsp70, and Hsp90β, which play important roles in maintaining protein homeostasis in cells[46], are also altered in SCA3 post-mortem brains and disease model systems[46-49]. Immunoblot analysis revealed Hsp40 and Hsp70 to be significantly decreased by 50% ± 21% (p = 0.037) and 42% ± 18% (p = 0.039), respectively, in SCA3-hESC relative to WT-hESC (n = 3 passages per line, 2-3 replicates per passage) (**Fig. 4.3G,H**). SCA3-hESC also consistently exhibited a doublet band for Hsp70 that was absent from WT-hESC, which could indicate altered post-translational modifications, splicing, or protein-protein interactions of Hsp70 in SCA3-hESC. Hsp90β also trended towards decreased levels in SCA3-hESC, but failed to reach statistical significance (p = 0.054) (**Fig. 4.3G,H**). Though further analysis is required to determine the extent and exact nature of autophagic and proteasomal dysfunction in SCA3-hESC, the altered levels of key regulators of protein quality control spanning autophagy, ubiquitin-dependent proteasomal degradation and protein folding machinery suggest widespread disruption of protein clearance in SCA3-hESC, a characteristic feature of SCA3 pathogenesis[1].

4.3.5 ASO-mediated ATXN3 reduction rescues aggresome formation in SCA3-hESC

To assess the potential of SCA3-hESC as a cellular model for preclinical therapeutic testing, we investigated whether delivery of an anti-*ATXN3* antisense oligonucleotide (ASO) recently validated in preclinical studies[20,21] could rescue molecular phenotypes in SCA3-hESC. ASOs are short, chemically modified nucleotide sequences that, when bound to sequence-specific target mRNA, activate RNaseH-mediated degradation of the targeted mRNA thereby reducing expression of the encoded protein[50]. In preclinical studies, we recently demonstrated that a single intracerebroventricular injection of an anti-*ATXN3* ASO into a transgenic mouse model of SCA3 suppressed expression of mutATXN3, reduced neuronal nuclear ATXN3 accumulation, and rescued several molecular, electrophysiological, and behavioral phenotypes in SCA3 mice[20,21].

WT- and SCA3-hESC were transfected with 100 nM or 500 nM anti-*ATXN3* ASO (referred to previously as ASO-5[20,21]), a non-specific ASO control (ASO-Ctrl) or PBS vehicle, then harvested three or four days later for RNA and protein analysis, respectively. Immunoblot analysis identified a significant decrease in both wtATXN3 and mutATXN3 protein levels in SCA3-hESC transfected with 100 nM and 500 nM compared to vehicle-treated or ASO-Ctrl treated SCA3-hESC groups [500 nM: wtATXN3 = 63% ± 8%, (p = 0.0003); mutATXN3 = 70% ± 7% (p = 0.0015)], normalized to vehicle-treated SCA3-hESC set at 100%, n = 6 replicates per treatment group] (**Fig. 4.4A**). qRT-PCR analysis confirmed an approximately 75% reduction in total *ATXN3* transcript levels in SCA3-hESC transfected with 500 nM ASO relative to vehicle-treated SCA3-hESC (p = 0.03, n = 3) (**Fig. 4.4B**). SCA3-hESC transfected with 100 nM ASO trended towards decreased *ATXN3* expression levels at 72 hours, but failed to reach significance (p = 0.09, n = 3 replicates per treatment group) (**Fig. 4.4B**).

To determine whether ASO treatment rescued ATXN3 aggregation and $p62^{+}$ aggresome formation, we performed anti-ATXN3 and anti-p62 ICC on SCA3-hESC transfected with 500 nM ASO compared to vehicle-treated WT- and SCA3-hESC (**Fig. 4.4C**). Four days after transfection, diffuse and punctate ATXN3 fluorescence was visibly reduced in ASO-treated SCA3-hESC relative to vehicle-treated SCA3-hESC

(**Fig. 4.4C**). Importantly, ASO-mediated reduction in ATXN3 markedly reduced ATXN3 puncta per cell in SCA3-hESC to levels non-statistically different from that of WT-hESC (vehicle-treated WT-hESC = 0.21 ± 0.07 ATXN3 puncta/cell, vehicle-treated SCA3-hESC = 1.28 ± 0.33 ATXN3 puncta/cell, ASO-treated SCA3-hESC = 0.43 ± 0.15 ATXN3 puncta/cell, n = 3 replicates per treatment group, 2-3 confocal images per replicate) (**Fig. 4.4C,D**). Similarly, ASO treatment led to visibly reduced diffuse p62 and completely rescued mean p62 puncta per cell four days after ASO transfection (vehicle-treated WT-hESC = 0.05 ± 0.02 p62 puncta/cell, vehicle-treated SCA3-hESC = 0.85 ± 0.12 p62 puncta/cell, ASO-treated SCA3-hESC = 0.30 ± 0.09 p62 puncta/cell, $p<0.0001$, n = 3 replicates per treatment group, 2-3 confocal images per replicate) (**Fig. 4.4C,E**).

In summary, non-allele specific suppression of ATXN3 with an anti-*ATXN3* ASO rescued ATXN3 aggregation and $p62^{+}$ aggresome formation in SCA3-hESC despite achieving a relatively modest 30% reduction in soluble mutATXN3 protein. These findings support the view that these disease-relevant molecular phenotypes are caused by expression of the pathogenic disease protein and do not reflect non-specific hESC line variations between WT- and SCA3-hESC. The identification of aggresome formation as a disease-dependent, reversible molecular phenotype bolsters its potential as a disease biomarker and the potential utility of this line for therapeutic preclinical testing for SCA3.

4.3.6 SCA3-hESC can be differentiated into neural progenitor cells and MAP2-positive cortical neurons

As a degenerative brain disease[1], SCA3 is thought principally to involve neurons. Thus, studying the disease in human neuronal cultures harboring the endogenous causative mutation should provide biologically relevant insights into disease. WT- and SCA3-hESC were differentiated into neural progenitor cells (NPC) and cortical neurons (CN) at similar efficiencies using a previously described protocol[49]. qRT-PCR analysis confirmed loss of pluripotency marker *OCT4* and gain of neural lineage marker *NESTIN* in derived NPC and 30-days post-differentiation (Day 30) CN, with similar *NESTIN* transcript levels achieved in both WT- and SCA3-NPC (**Fig. 4.5A,B**). In addition, differentiated WT- and SCA3-CN expressed the mature neuronal marker *MAP2* at

similar levels 30-days post-differentiation (**Fig. 4.5C**). ICC analysis confirmed expression of the neural lineage marker NESTIN in derived SCA3-NPC (**Fig. 4.5D**) and the mature neuronal marker MAP2 in differentiated SCA3-CN (**Fig. 4.5E**).

To further characterize neuronal maturation, we performed whole-cell electrophysiological recordings of Day 30 WT- and SCA3-CN. In current clamp mode, we observed spontaneous neuronal firing with characteristic action potential shape in SCA3-CN 30-days post-differentiation (**Fig. 4.5F**). Voltage-clamp recordings of WT- and SCA3-CN indicated both inward and outward currents in response to depolarizing voltage steps with no statistical difference between WT- and SCA3-CN peak inward current [$F(1,14)=0.19$, $p=0.67$] or peak outward current [$F(1,14)=0.66$, $p=0.43$] (**Fig. 4.5G-I**). These data suggest proper maturation of derived WT- and SCA3-CN into MAP2-positive neurons that exhibit firing properties, with no indication of impaired neuronal differentiation of SCA3-hESC.

4.3.7 Robust ATXN3 aggregation in SCA3-hESC derived neural progenitor cells and cortical neurons

After confirming NPC and CN differentiation, we evaluated ATXN3 expression and aggregation propensity in derived SCA3-NPC and SCA3-CN. Soluble wtATXN3 and mutATXN3 were expressed in differentiated SCA3-NPC and Day 30 SCA3-CN at the expected molecular weights (**Fig. 4.6A,C**). Similar to SCA3-hESC, SCA3-NPC and SCA3-CN exhibited markedly increased accumulation of HMW ATXN3. Quantified HMW ATXN3 levels were about 2.5 times greater in SCA3-NPC relative to WT-NPC ($p < 0.001$) (**Fig. 4.6A,B**) and 1.7 times greater in SCA3-CNs relative to WT-CNs ($p = 0.003$) (**Fig. 4.6C,D**).

We then performed anti-ATXN3 ICC with DAPI counter-stain on NPC and Day 30 CN differentiated from WT- and SCA3-hESC. Whereas ATXN3 was diffusely expressed throughout the nucleus and cytoplasm in WT-NPC, ATXN3 in SCA3-NPC localized to numerous cytoplasmic aggregates that varied in size, shape, number and location (**Fig. 4.6E**). Differentiated SCA3-CN also exhibited robust ATXN3 inclusion formation, with individual neurons frequently forming one or more large, round, juxtanuclear ATXN3-positive inclusions as well as occasional round inclusions in distal processes (**Fig. 4.6F**). By contrast, inclusions were rarely observed in WT-NPC or WT-CN. Unlike the

case in SCA3-hESC, enhanced nuclear accumulation of ATXN3 was not observed in SCA3-NPC or SCA3-CN. These data demonstrate robust aggregation when mutATXN3 is expressed in SCA3-hESC, -NPC, and -CN under normal culture conditions in the absence of applied stressors, which has not been described in any other SCA3 disease-specific iPSC or hESC line.

4.3.8 Altered expression of key protein clearance pathway proteins in SCA3-CN

We also analyzed whether the dysregulation of components of the protein homeostasis machinery observed in undifferentiated SCA3-hESC persisted in Day 30 SCA3-CN. WT- and SCA3-CN were fractionated into Triton-X100 soluble and insoluble protein extracts which were then subjected to immunoblot analysis. Soluble p62 levels were significantly increased by 69 ± 21% in SCA3-CN relative to WT-CN ($p = 0.03$), and the ratio of insoluble to soluble p62 protein was more than doubled in SCA3-CN ($p = 0.02$) (**Fig. 4.7A,B**). Thus, similar to SCA3-hESC, SCA3-CN exhibit increased p62 expression with some of it likely sequestered into insoluble ATXN3^{+} aggregates. Immunoblot analysis of the autophagy proteins Beclin1 and LC3 was also performed on unfractionated protein lysates from WT- and SCA3-CN. Beclin1 levels trended towards decreased levels but failed to reach statistical significance ($p = 0.07$), and LC3-II levels were unchanged in SCA3-CN relative to WT-CN ($p = 0.72$) (**Fig. 4.7C,D**). Therefore, while SCA3-hESC and SCA3-CN both exhibit markers suggesting impaired autophagy, the observed differences suggest mutATXN3 may interact and interfere with autophagic pathways differently in undifferentiated hESC versus differentiated neurons.

Additional components of the protein homeostasis machinery were evaluated in SCA3- versus WT-CN. Anti-ubiquitin immunoblot analysis revealed no difference in total soluble or insoluble poly-ubiquitinated substrates in protein extracts from the two lines (**Fig. 4.7C,D**). There was, however, a significant increase in the level of short ubiquitin chains [$(Ub)_{2-4}$] partitioning in the insoluble fraction in SCA3-CN: a 54% ± 20% increase relative to WT-CN ($p = 0.05$) (**Fig. 4.7E,F**). As in SCA3-hESC, Hsp70 levels were significantly decreased in unfractionated SCA3-CN relative to WT-CN (decreased by 44% ± 15%; $p = 0.048$) (**Fig. 4.7G,H**). In contrast, Hsp40 and Hsp90β levels did not statistically differ between the two lines ($p = 0.32$ and $p = 0.60$, respectively) (**Fig. 4.7G,H**). Overall, SCA3-CN exhibited significant changes in several markers of

autophagy, ubiquitin-dependent proteasomal clearance, and protein folding. Several disease-specific changes in SCA3-CN mirrored those seen in undifferentiated SCA3-hESC while others did not, suggesting cell-type specific differences in the interaction of mutATXN3 with components of protein homeostasis.

4.4 Discussion

We present here a new SCA3 hESC line with the potential to improve our understanding of this complex, fatal neurodegenerative disease. Despite over 20 years of research since the identification of the disease mutation, limited understanding of SCA3 disease mechanisms and the absence of effective therapeutic interventions point to the need for improved humanized disease model systems[1]. Here we developed and characterized SCA3-hESC, a significant cell line partly because it is the only NIH-approved hESC line harboring a SCA mutation. More importantly, SCA3-hESC represents the first hPSC or cell model of any kind that displays disease-relevant molecular phenotypes, including robust aggregation of the endogenous human disease gene product, without the need for genetic or environmental manipulations[12,29-32].

We observed multiple molecular phenotypes at the undifferentiated hESC stage, including the formation of p62-positive aggresomes containing the disease protein ATXN3 and altered expression of key regulators of protein homeostasis. These findings were unexpected as SCA3 typically presents later in life with selective neuronal vulnerability[1,4,5]. The presence of disease phenotypes in undifferentiated cells could point to early developmental changes that are as yet unappreciated in SCA3, and is reminiscent of recent findings in HD, another adult-onset polyQ disorder[52]. Cellular properties of pluripotent stem cells, notably their heavy reliance on autophagy-dependent protein clearance and rapid rate of division, may also provide insights into polyQ expansion-driven changes in ATXN3 function. Identification of disease protein aggregation and altered protein clearance pathways in SCA3-hESC are also notable since no similar disease-relevant phenotypes have been observed in other published SCA3 iPSC lines without application of cellular stressors[12]. The apparent lack of robust phenotypes in SCA3 iPSC lines could arise from the reprogramming process from a differentiated cell, which can cause unpredictable changes in epigenetic patterning, transcriptional regulation, pluripotent potential, and vulnerability to early senescence[53].

Regardless, our findings bolster support for the development of more SCA3 hESC lines in addition to patient-derived iPSC lines to improve our understanding of SCA3 pathogenesis.

SCA3-hESC presumably can express all ATXN3 isoforms generated from the endogenous human disease gene and, as demonstrated here, recapitulates aggregation and nuclear sequestration of mutATXN3. Thus, SCA3-hESC is well suited to assess compounds aimed at reducing mutATXN3 protein, preventing aggregation, or altering subcellular localization of mutATXN3. Here we performed a proof-of-concept assessment of a previously validated gene silencing therapy[20,21]; specifically, we demonstrated that ASO-mediated reduction of ATXN3 mitigates aggresome formation in SCA3-hESC. The ability to use tools such as ASOs to modify disease-relevant phenotypes supports the hypothesis that at least some of the observed molecular phenotypes are directly attributable to mutATXN3 expression, and could enable future mechanistic studies of disrupted pathways in SCA3. However, we cannot rule out the possibility that some of the observed molecular phenotypes in SCA3-hESC and differentiated cell types are due to cell line-specific variations not directly resulting from expression of mutATXN3. Future studies using this novel cell line would benefit from development of genetically corrected isogenic control lines from SCA3-hESC, such as those that have been developed from Huntington's disease iPSC lines[54]. In addition, the SCA3 field would benefit from the creation of more SCA3 hESC lines, which may occur due to increased numbers of patients choosing in vitro fertilization with preimplantation genetic testing for monogenic and repeat expansion disorders.

We also observed the formation of high molecular weight ATXN3 aggregates throughout neuronal differentiation, including in derived SCA3-NPC and mature SCA3-CN. Though there is evidence for involvement of the frontal, parietal, temporal, occipital and limbic lobes in SCA3[55,56], the degree of neuronal loss in these regions is significantly less severe than in brainstem and cerebellar nuclei[57]. Because cortical regions likely play less of a role in the progressive deterioration of motor control in SCA3 patients, differentiated forebrain cortical neurons may not be the best cellular model in which to study SCA3 disease processes. Dopaminergic neurons in the substantia nigra, however, are highly affected and exhibit significant degeneration in

SCA3 human brains. Future studies could take advantage of the wealth of improved dopaminergic differentiation protocols[58] to assess specific differences in pathology and neuronal vulnerability in disease-affected dopaminergic versus disease-spared cortical neuronal populations. In addition, SCA3 research to date has been neuron-centric, meaning that little is known about glial involvement in disease progression. Recent studies demonstrating significant transcriptional and protein expression changes in glial-enriched genes[59-61]and altered glial morphology and density in affected brain regions with disease progression[4,62] point to the need for glial-focused investigations in SCA3. The pluripotent potential of SCA3-hESC in combination with the detection of native mutATXN3 aggregation demonstrated here, could prove invaluable for future studies of cell-type specific differences in ATXN3 function, aggregation propensity and vulnerability to aggregation-induced cellular insults.

In conclusion, here we have presented a novel hESC line that expresses the endogenous SCA3 human disease protein. We have verified the pluripotent potential of the SCA3-hESC line, and that it can be directed to differentiated into mature, electrophysiologically active neurons. Most importantly, we have identified robust, well-established and mutATXN3-dependent pathogenic features of SCA3 human disease in undifferentiated stem cells and throughout neuronal differentiation. Based on these studies, we believe the SCA3-hESC line holds strong promise to advance our understanding of SCA3 disease mechanisms, enable future investigations into cell-type specific contributions to disease and improve preclinical development of SCA3 therapies.

4.5 Methods

4.5.1 hESC Line Derivation and Characterization

Human embryos were originally created by assistive reproductive technologies for the purpose of procreation and donated to the University of Michigan under MStem Cell Laboratory's Institutional Review Board (IRB) approved study *"Derivation of human Embryonic Stem Cells"* (HUM00028742). Written informed consent was obtained for all embryo donations. Donation and derivation of NIH-approved, unaffected hESC line UM4-6 (Registration # -0147, referred to here as WT-hESC) was reported previously[22]. The SCA3-affected embryo was donated to the

University of Michigan following single gene preimplantation genetic testing identified the embryo as heterozygous for a pathogenic *CAG*-repeat expansion in *ATXN3.* Derived UM134-1 hESC line (referred to here as SCA3-hESC) was accepted to the NIH registry of approved hESC lines on September 29, 2014 (Registration # -0286).

Derivation of UM134-1 and derivatives were performed with non-federal funds prior to acceptance to the NIH registry. Prior to NIH approval, Cell Line DNA Fingerprinting and cytogenetic analysis were performed on passage 6 SCA3-hESC (Cell Line Genetics, Madison, Wisconsin). The resulting DNA STR profile of SCA3-hESC confirmed the presence of a single cell line that's unique from lines published in the ATCC, NIH, or DSMZ websites. Cytogenetic analysis was performed on 20 G-banded metaphase cells. Seventeen cells demonstrated an apparently normal male 46,XY karyotype, while three cells demonstrated non-clonal aberrations ruled as most likely artifacts of culture. To determine *ATXN3* CAG-trinucleotide repeat length in WT- and SCA3-hESC, 10-50 µL of at least 10 ng/µL DNA were analyzed by gene fragmentation analysis (Laragen Inc., Culver City) using primer sequences *ATXN3* (5'-ACAGCAGCAAAAGCAGCAA-3' and 5'- CCAAGTGCTCCTGAACTGGT -3'). Repeat length was calculated as (amplicon fragment size – 66) / 3.

4.5.2 Culture and ASO Transfection of hESC.

Undifferentiated pluripotent hESC were cultured in mTeSR1 media (Stem Cell Technology) on Matrigel-coated plates with daily media changes and passaged using L7 passaging media (Lonza) or ReLeSR passaging media (Stem Cell Technology). The anti-ATXN3 ASO and scrambled control ASO (ASO-Ctrl) used for hESC transfections are 18 nucleotides in length with a mixed phosphodiester and phosphorothioate backbone and five MOE-modified nucleotides on each of the 5' and 3' termini. ASO nucleotide sequences were as follows: anti-*ATXN3* ASO (5'-GCATCTTTTCATACTGGC-3'), ASO-Ctrl (5'-GTTTTCAAATACACCTTC-3'). Oligonucleotides were synthesized as described previously[63,64]. ASOs were solubilized in PBS (without Ca^{2+} or Mg^{2+}). For ASO transfections, undifferentiated hESC were plated on Matrigel-coated plates in mTeSR1 media supplemented with 10 µM Rock Inhibitor and grown overnight. Media was replaced with mTeSR1 the next day and cells were allowed to recover for at least 4 hours. Transfections were performed using

TransIT LT1 transfection reagent (Mirus Bio) according to the manufacturer's protocol. ASO concentration. Cells were cultured with daily media changes and harvested 3 days after transfection for RNA isolation or 4 days after transfection for Western blot analysis or immunocytochemical analysis.

4.5.3 Differentiation and Culture of NPCs and Forebrain CNs

Directed differentiation of hESC to NPCs and CNs was performed as described by Shi *et al.* (*Nature* 2012) with some modifications[49]. Briefly, undifferentiated hESC were cultured to confluency in mTeSR1 media (Stem Cell Technology) on Matrigel-coated plates. Neural differentiation was induced using neural maintenance media supplemented with 1 μM Dorsomorphin and 10 μM SB431542. Cells were cultured for approximately 12 days with daily media changes. Neuroepithelial cells were passaged onto Matrigel-coated plates using Dispase passaging reagent and were maintained in neural maintenance media containing 20 ng/ml FGF2 with daily media changes. Once neural rosettes were visible, NPCs were either collected for experimentation or cultured in neural expansion media supplemented with 20 ng/ml FGF and 20 ng/ml EGF and passaged as needed with Accutase passaging reagent. For forebrain CN differentiation, NPCs were plated onto PLO-Laminin coated plates or coverslips with neural expansion media for 24 hours, and then maintained in neural maintenance for 30 days with media changes every other day.

4.5.4 RNA Isolation Quantitative PCR.

Total RNA was isolated from cell lysates using Trizol reagent according to the manufacturer's protocol (Invitrogen, Carlsbad, CA). Reverse transcription was performed on 0.5-1μg of total RNA using the iScript cDNA synthesis kit according to the manufacturer's instructions (Bio-Rad, Hercules, CA). The cDNA was diluted 1:10 in nuclease-free water. iQ SYBR green quantitative polymerase chain reaction (qPCR) was performed on the diluted cDNA following the manufacturer's protocol (Bio-Rad). Average-adjusted relative quantification analysis was performed using the following human primers: *LIN28 (*5'-AGCCATATGGTAGCCTCATGTCCGC-3' and 5'-TCAATTCTGTGCCTCCGGGAGCAGGGTAGG-3'), *OCT4* (5'-CCCCAGGGCCCCATTTTGGTACC-3' and 5'-ACCTCAGTTTGAATGCATGGGAGAGC-3'), *SOX2* (5'-

TTCACATGTCCCAGCACTACCAGA-3' and 5'-TCACATGTGTGAGAGGGGCAGTGTGC-3'), *NANOG* (5'-TTGGGACTGGTGGAAGAACC-3' and 5'-GATTTGTGGGCCTGAAGAAA-3'), *AFP* (5'-AAACTATTGGCCTGTGGCGA-3' and 5'- GGCCAACACCAGGGTTTACT-3'), *TUJ-1* (5'-ATGCGGGAGATCGTGCACAT-3' and 5'- CCCTGAGCGGACACTGT-3'), *BRACHYURY* (5'-ACCCAGTTCATAGCGGTGAC-3' and 5'-GGATTGGGAGTACCCAGGTT-3'), *ATXN3* (5'-GGAACAATGCGTCGGTTG-3' and 5'-GCCCTAACTTTAGACATGTTAC-3'), *NES* (5'-GGGAAGAGGTGATGGAACCA-3' and 5'-AAGCCCTGAACCCTCTTTGC-3'), *MAP2* (5'-TTGGTGCCGAGTGAGAAGA-3' and 5'-GTCTGGCAGTGGTTGGTTAA-3'), *HPRT* (5'-GGACCTCTCGAAGTGTTGGATA-3' and 5'-ACGTGATTCAAATCCCTGAAGT-3').

4.5.5 Immunoblotting

Cell protein extracts were prepared from cells using two protocols. For immunoblot analysis of total protein extracts, cells were washed with cold PBS and lysed on ice with RIPA buffer containing complete mini protease inhibitor cocktail (Roche), followed by bath ultrasonication in chill water and centrifugation for total protein extract. For immunoblot analysis on soluble versus insoluble protein extracts, cells were washed and collected in PBS, bath ultrasonicated in chill water, centrifuged, and supernatants were collected (soluble fraction). Remaining pellets were washed with PBS and resuspended in 1% sarkosyl in PBS containing complete mini protease inhibitor cocktail (Roche), vortexed for 30 sec and incubated at room temperature for 1 hr. Samples were bath ultrasonicated again for 5 min, centrifuged, and supernatants were collected (insoluble fraction). Total protein concentrations were determined using the bicinchoninic acid (BCA) method (Pierce) and stored at −80°C. A total of 5 or 10 µg protein lysates were resolved in Novex 4-20% Tris-Glycine polyacrylamide electrophoresis gels (XP04205BOX; Invitrogen, Carlsbad, CA) and transferred to polyvinylidene difluoride (PVDF) membranes. Membranes were incubated overnight at 4°C with various antibodies: mouse anti-1C2 (1:1000, MAB1574; Millipore, Billerica, MA), rabbit anti-Ubiquitin (1:2000, #3933S; Cell Signaling Technology, Danvers, MA), rabbit anti-LC3B (1:1000, PM036; MBL International Corporation, Woburn, MA), rabbit anti-Hsp40 (1:1000, #4868; Cell Signaling Technology, Danvers, MA), mouse anti-

Hsp70 (1:1000, ab5439; Abcam, Cambridge, UK), mouse anti-Hsp90β (K3705) (1:5000, ADI-SPA-842-F; Enzo Life Sciences, New York, NY), mouse anti-ATXN3 (1H9; 1:1000, MAB5360; Millipore, Billerica, MA), mouse anti-p62 (1:1000, ADI-SPA-902-D; Enzo Life Sciences, New York, NY), rabbit anti-BECLIN1 (1:1000, ab207612; Abcam, Cambridge, UK), mouse anti-GAPDH (1:5000, MAB374; Millipore, Billerica, MA), and rabbit anti–α-Tubulin (1:5000, #S2144; Cell Signaling Technology, Danvers, MA). Bound primary antibodies were visualized by incubation with peroxidase-conjugated anti-mouse or anti-rabbit secondary antibody (1:10000; Jackson ImmunoResearch Laboratories, West Grove, PA) followed by treatment with the ECL-plus reagent (Western Lighting; PerkinElmer, Waltham, MA) and exposure to autoradiography films. Band intensities were quantified using ImageJ analysis software (NIH, Bethesda, MD). Band intensities for proteins of interest were divided by GAPDH or α-Tubulin band intensity, averaged, normalized to the mean control value indicated for each experiment, and expressed as % indicated control.

4.5.6 Immunocytochemistry and image analysis

Cells were cultured on Poly-D-Lysine/Matrigel-coated coverslips. Cells were washed with cold PBS and then fixed with 4% paraformaldehyde (PFA) solution for 15 min on ice. Cells were permeabilized with 0.1% Triton X-100 for 5 min at room temperature then blocked in a 5% Normal Goat Serum solution for 1 hr at room temperature. Cells were blocked in various primary antibodies overnight at 4°C. Primary antibodies assessed include: rabbit anti-OCT4 (1:1000, #2750; Cell Signaling Technology, Danvers, MA), rabbit anti-SOX2 (1:1000, #3579; Cell Signaling Technology, Danvers, MA), rabbit anti-NANOG (1:1000, #4903; Cell Signaling Technology, Danvers, MA), mouse anti-vimentin (1:1000, MA3-745; Invitrogen, Carlsbad, CA), goat anti-PSMD11 (1:1000, sc-79275; Santa Cruz Biotechnology, Dallas, TX), mouse anti-NESTIN (1:1000, #33475; Cell Signaling Technology, Danvers, MA), rabbit anti-MAP2 (1:2000, #4542; Cell Signaling Technology, Danvers, MA), mouse anti-ATXN3 (1H9; 1:1000, MAB5360, Millipore), mouse anti-p62 (1:1,000, ADI-SPA-902-D, Enzo Life Sciences). The cells were then immunostained with species-specific secondary antibodies conjugated to Alexa 488 or 568 fluorophores and mounted using Prolong Gold. Imaging was performed using an IX71 Olympus inverted

microscope (Melville, NY) or Nikon-A1 confocal microscope (Melville, NY). All image analysis was performed using ImageJ analysis software (NIH, Bethesda, MD).

4.5.7 Electrophysiology

Electrophysiological recordings were performed on WT- and SCA3-CN plated on laminin-coated coverslips at 30-days post-differentiation. Cultured WT- or SCA3-CN were placed into a bath of room temperature Tyrode's solution[65] containing the following (in mmol/L): 82 Na_2SO_4, 30 K_2SO_4, 5 $MgCl_2$, 10 HEPES, 10 glucose, at pH 7.4. Cells were slowly perfused with room-temperature Tyrode's solution bubbled with 5% CO_2 and 95% O_2 (carbogen) during recordings. Patch-clamp recordings were performed with borosilicate glass pipettes of 4-5 mΩ resistance which contained an internal solution containing the following (in mmol/L): 119 K-gluconate, 2 Na-gluconate, 6 NaCl, 2 $MgCl_2$, 0.9 EGTA, 10 HEPES, 14 Tris-phosphocreatine, 4 MgATP, 0.3 tris-GTP, at pH 7.3 and osmolarity 287 mOsm. An agarose bridge (1% in Tyrode's solution) was used to shield cells from the AgCl bath electrode during recordings. Patch-clamp recordings were performed using an Axopatch 200B amplifier, Digidata 1440A interface, and pClamp-10 software (MDS Analytical Technologies, Sunnyvale, CA). Data were acquired at 100 kHz in the fast-current clamp mode of the amplifier and filtered at 2 kHz. Spontaneous neuronal activity was recorded in whole-cell current clamp mode to observe characteristic action potential shape. Whole-cell voltage clamp recordings were used in order measure currents. WT- and SCA3-CN were held at -80 mV, and peak inward and outward currents were quantified in response to depolarizing current steps from -90 mV to +10 mV in +10 mV increments. Series resistance was compensated up to 40%. Cells were included if series resistance remained under 30 MΩ for the duration of the recording.

4.5.8 Statistics

All statistical analyses were performed using Prism (7.0; Graph-Pad Software, La Jolla, CA). Quantified data represent the findings of three or more independent experiments. The statistical tests used are described in each figure legend. All error bars indicate variability about the mean expressed as standard error of the mean. Quantification of qRT-PCR transcript levels is normalized to mean WT-hESC, WT-NPC, or WT-CN transcript levels set at 1. Quantification of immunoblotted protein expression

is normalized to mean WT-hESC, WT-NPC or WT-CN protein levels set at 100%. All tests set the level of significance at $p < 0.05$.

4.6 Acknowledgements and author contributions:

We thank Ionis Pharmaceuticals for generating and providing the anti-ATXN3 ASO. This work was supported in part by a Michigan Brain Initiative Predoctoral Fellowship for Neuroscience (to L.R.M.), the University of Michigan Neuroscience Graduate Program (to L.R.M.), the SCA3 Ataxia Research Fund provided in part by the SCA Network and NIH grant funding (R01-NS038712 to PI Dr. Henry L. Paulson). Lauren Moore, Dr. Gary D. Smith and Dr. Henry L. Paulson conceived and designed the study. Laura Keller and Dr. Smith generated the SCA3-hESC line from the donated human embryo. Lauren Moore, Laura Keller, Dr. Dave D. Bushart, Rodrigo Delatorre, Dorcas Li, Dr. Maria do Carmo Costa, and Dr. Hayley S. McLoughlin performed the experiments. Lauren Moore performed the experiments and analyzed the data. Dr. Vikram G. Shakkottai, Dr. Smith, and Dr. Paulson provided supervision for experimentation and data analysis.

4.7 References

1 Costa Mdo, C. & Paulson, H. L. Toward understanding Machado-Joseph disease. *Progress in neurobiology* **97**, 239-257, doi:10.1016/j.pneurobio.2011.11.006 (2012).
2 Paulson, H. L., Shakkottai, V. G., Clark, H. B. & Orr, H. T. Polyglutamine spinocerebellar ataxias - from genes to potential treatments. *Nature reviews. Neuroscience* **18**, 613-626, doi:10.1038/nrn.2017.92 (2017).
3 Kawaguchi, Y. *et al.* CAG expansions in a novel gene for Machado-Joseph disease at chromosome 14q32.1. *Nature genetics* **8**, 221-228, doi:10.1038/ng1194-221 (1994).
4 Rub, U. *et al.* Clinical features, neurogenetics and neuropathology of the polyglutamine spinocerebellar ataxias type 1, 2, 3, 6 and 7. *Progress in neurobiology* **104**, 38-66, doi:10.1016/j.pneurobio.2013.01.001 (2013).
5 Rosenberg, R. N. Machado-Joseph disease: an autosomal dominant motor system degeneration. *Movement disorders : official journal of the Movement Disorder Society* **7**, 193-203, doi:10.1002/mds.870070302 (1992).
6 Hargus, G., Ehrlich, M., Hallmann, A. L. & Kuhlmann, T. Human stem cell models of neurodegeneration: a novel approach to study mechanisms of disease development. *Acta neuropathologica* **127**, 151-173, doi:10.1007/s00401-013-1222-6 (2014).
7 Siska, E. K., Koliakos, G. & Petrakis, S. Stem cell models of polyglutamine diseases and their use in cell-based therapies. *Frontiers in neuroscience* **9**, 247, doi:10.3389/fnins.2015.00247 (2015).
8 Hansen, S. K. *et al.* Generation of spinocerebellar ataxia type 3 patient-derived induced pluripotent stem cell line SCA3.B11. *Stem cell research* **16**, 589-592, doi:10.1016/j.scr.2016.02.042 (2016).

9 Hansen, S. K. *et al.* Generation of spinocerebellar ataxia type 3 patient-derived induced pluripotent stem cell line SCA3.A11. *Stem cell research* **16**, 553-556, doi:10.1016/j.scr.2016.02.040 (2016).
10 Hansen, S. K. *et al.* Induced pluripotent stem cell - derived neurons for the study of spinocerebellar ataxia type 3. *Stem cell research* **17**, 306-317, doi:10.1016/j.scr.2016.07.004 (2016).
11 Hayer, S. N. *et al.* Generation of an induced pluripotent stem cell line from a patient with spinocerebellar ataxia type 3 (SCA3): HIHCNi002-A. *Stem cell research* **30**, 171-174, doi:10.1016/j.scr.2018.06.006 (2018).
12 Koch, P. *et al.* Excitation-induced ataxin-3 aggregation in neurons from patients with Machado-Joseph disease. *Nature* **480**, 543-546, doi:10.1038/nature10671 (2011).
13 Ou, Z. *et al.* Autophagy Promoted the Degradation of Mutant ATXN3 in Neurally Differentiated Spinocerebellar Ataxia-3 Human Induced Pluripotent Stem Cells. *BioMed research international* **2016**, 6701793, doi:10.1155/2016/6701793 (2016).
14 Ouyang, S. *et al.* CRISPR/Cas9-Targeted Deletion of Polyglutamine in Spinocerebellar Ataxia Type 3-Derived Induced Pluripotent Stem Cells. *Stem cells and development* **27**, 756-770, doi:10.1089/scd.2017.0209 (2018).
15 Ritthaphai, A. *et al.* Derivation of an induced pluripotent stem cell line (MUSIi004-A) from dermal fibroblasts of a 48-year-old spinocerebellar ataxia type 3 patient. *Stem cell research* **30**, 113-116, doi:10.1016/j.scr.2018.05.012 (2018).
16 Soong, B. W. *et al.* Generation of induced pluripotent stem cells from a patient with spinocerebellar ataxia type 3. *Stem cell research* **18**, 29-32, doi:10.1016/j.scr.2016.12.017 (2017).
17 Wang, Y. *et al.* Generation of induced pluripotent stem cell line (ZZUi004-A) from urine sample of a patient with spinocerebellar ataxia type 3. *Stem cell research* **28**, 71-74, doi:10.1016/j.scr.2018.01.027 (2018).
18 Chuang, C. Y. *et al.* Modeling spinocerebellar ataxias 2 and 3 with iPSCs reveals a role for glutamate in disease pathology. *Scientific reports* **9**, 1166, doi:10.1038/s41598-018-37774-2 (2019).
19 Liu, L. *et al.* Generation of human embryonic stem cell line chHES-472 from abnormal embryos diagnosed with Spinocerebellar ataxia type 3. *Stem cell research* **17**, 584-586, doi:10.1016/j.scr.2016.10.001 (2016).
20 McLoughlin, H. S. *et al.* Oligonucleotide therapy mitigates disease in spinocerebellar ataxia type 3 mice. *Annals of neurology* **84**, 64-77, doi:10.1002/ana.25264 (2018).
21 Moore, L. R. *et al.* Evaluation of Antisense Oligonucleotides Targeting ATXN3 in SCA3 Mouse Models. *Molecular therapy. Nucleic acids* **7**, 200-210, doi:10.1016/j.omtn.2017.04.005 (2017).
22 Haenfler, J. M. *et al.* Targeted Reactivation of FMR1 Transcription in Fragile X Syndrome Embryonic Stem Cells. *Frontiers in molecular neuroscience* **11**, 282, doi:10.3389/fnmol.2018.00282 (2018).
23 Yamada, M., Sato, T., Tsuji, S. & Takahashi, H. CAG repeat disorder models and human neuropathology: similarities and differences. *Acta neuropathologica* **115**, 71-86, doi:10.1007/s00401-007-0287-5 (2008).
24 Paulson, H. L. *et al.* Intranuclear inclusions of expanded polyglutamine protein in spinocerebellar ataxia type 3. *Neuron* **19**, 333-344 (1997).
25 Costa Mdo, C. *et al.* Toward RNAi therapy for the polyglutamine disease Machado-Joseph disease. *Molecular therapy : the journal of the American Society of Gene Therapy* **21**, 1898-1908, doi:10.1038/mt.2013.144 (2013).

26 Seidel, K. *et al.* On the distribution of intranuclear and cytoplasmic aggregates in the brainstem of patients with spinocerebellar ataxia type 2 and 3. *Brain pathology (Zurich, Switzerland)* **27**, 345-355, doi:10.1111/bpa.12412 (2017).
27 Ramani, B. *et al.* A knockin mouse model of spinocerebellar ataxia type 3 exhibits prominent aggregate pathology and aberrant splicing of the disease gene transcript. *Human molecular genetics* **24**, 1211-1224, doi:10.1093/hmg/ddu532 (2015).
28 Hayashi, M., Kobayashi, K. & Furuta, H. Immunohistochemical study of neuronal intranuclear and cytoplasmic inclusions in Machado-Joseph disease. *Psychiatry and clinical neurosciences* **57**, 205-213, doi:10.1046/j.1440-1819.2003.01102.x (2003).
29 Yoshizawa, T., Yoshida, H. & Shoji, S. Differential susceptibility of cultured cell lines to aggregate formation and cell death produced by the truncated Machado-Joseph disease gene product with an expanded polyglutamine stretch. *Brain research bulletin* **56**, 349-352 (2001).
30 Colomer Gould, V. F. *et al.* A mutant ataxin-3 fragment results from processing at a site N-terminal to amino acid 190 in brain of Machado-Joseph disease-like transgenic mice. *Neurobiology of disease* **27**, 362-369, doi:10.1016/j.nbd.2007.06.005 (2007).
31 Haacke, A. *et al.* Proteolytic cleavage of polyglutamine-expanded ataxin-3 is critical for aggregation and sequestration of non-expanded ataxin-3. *Human molecular genetics* **15**, 555-568, doi:10.1093/hmg/ddi472 (2006).
32 Reina, C. P., Zhong, X. & Pittman, R. N. Proteotoxic stress increases nuclear localization of ataxin-3. *Human molecular genetics* **19**, 235-249, doi:10.1093/hmg/ddp482 (2010).
33 Bichelmeier, U. *et al.* Nuclear localization of ataxin-3 is required for the manifestation of symptoms in SCA3: in vivo evidence. *The Journal of neuroscience : the official journal of the Society for Neuroscience* **27**, 7418-7428, doi:10.1523/jneurosci.4540-06.2007 (2007).
34 Fujigasaki, H. *et al.* Ataxin-3 is translocated into the nucleus for the formation of intranuclear inclusions in normal and Machado-Joseph disease brains. *Experimental neurology* **165**, 248-256, doi:10.1006/exnr.2000.7479 (2000).
35 Macedo-Ribeiro, S., Cortes, L., Maciel, P. & Carvalho, A. L. Nucleocytoplasmic shuttling activity of ataxin-3. *PloS one* **4**, e5834, doi:10.1371/journal.pone.0005834 (2009).
36 Mori, F. *et al.* Autophagy-related proteins (p62, NBR1 and LC3) in intranuclear inclusions in neurodegenerative diseases. *Neuroscience letters* **522**, 134-138, doi:10.1016/j.neulet.2012.06.026 (2012).
37 Seidel, K. *et al.* Axonal inclusions in spinocerebellar ataxia type 3. *Acta neuropathologica* **120**, 449-460, doi:10.1007/s00401-010-0717-7 (2010).
38 Sittler, A. *et al.* Deregulation of autophagy in postmortem brains of Machado-Joseph disease patients. *Neuropathology : official journal of the Japanese Society of Neuropathology* **38**, 113-124, doi:10.1111/neup.12433 (2018).
39 Wang, Y. *et al.* Autophagy Regulates Chromatin Ubiquitination in DNA Damage Response through Elimination of SQSTM1/p62. *Molecular cell* **63**, 34-48, doi:10.1016/j.molcel.2016.05.027 (2016).
40 Zhou, L. *et al.* p62/sequestosome 1 regulates aggresome formation of pathogenic ataxin-3 with expanded polyglutamine. *International journal of molecular sciences* **15**, 14997-15010, doi:10.3390/ijms150914997 (2014).
41 Johnston, J. A., Ward, C. L. & Kopito, R. R. Aggresomes: a cellular response to misfolded proteins. *The Journal of cell biology* **143**, 1883-1898 (1998).
42 Korolchuk, V. I., Mansilla, A., Menzies, F. M. & Rubinsztein, D. C. Autophagy inhibition compromises degradation of ubiquitin-proteasome pathway substrates. *Molecular cell* **33**, 517-527, doi:10.1016/j.molcel.2009.01.021 (2009).

43 Neves-Carvalho, A. *et al.* Dominant negative effect of polyglutamine expansion perturbs normal function of ataxin-3 in neuronal cells. *Human molecular genetics* **24**, 100-117, doi:10.1093/hmg/ddu422 (2015).
44 Chai, Y., Koppenhafer, S. L., Shoesmith, S. J., Perez, M. K. & Paulson, H. L. Evidence for proteasome involvement in polyglutamine disease: localization to nuclear inclusions in SCA3/MJD and suppression of polyglutamine aggregation in vitro. *Human molecular genetics* **8**, 673-682 (1999).
45 Ashkenazi, A. *et al.* Polyglutamine tracts regulate beclin 1-dependent autophagy. *Nature* **545**, 108-111, doi:10.1038/nature22078 (2017).
46 Arawaka, S., Machiya, Y. & Kato, T. Heat shock proteins as suppressors of accumulation of toxic prefibrillar intermediates and misfolded proteins in neurodegenerative diseases. *Current pharmaceutical biotechnology* **11**, 158-166 (2010).
47 Chai, Y., Koppenhafer, S. L., Bonini, N. M. & Paulson, H. L. Analysis of the role of heat shock protein (Hsp) molecular chaperones in polyglutamine disease. *The Journal of neuroscience : the official journal of the Society for Neuroscience* **19**, 10338-10347 (1999).
48 Bennett, C. F. & Swayze, E. E. RNA targeting therapeutics: molecular mechanisms of antisense oligonucleotides as a therapeutic platform. *Annual review of pharmacology and toxicology* **50**, 259-293, doi:10.1146/annurev.pharmtox.010909.105654 (2010).
49 Shi, Y., Kirwan, P. & Livesey, F. J. Directed differentiation of human pluripotent stem cells to cerebral cortex neurons and neural networks. *Nature protocols* **7**, 1836-1846, doi:10.1038/nprot.2012.116 (2012).
50 Developmental alterations in Huntington's disease neural cells and pharmacological rescue in cells and mice. *Nature neuroscience* **20**, 648-660, doi:10.1038/nn.4532 (2017).
51 Narsinh, K. H., Plews, J. & Wu, J. C. Comparison of human induced pluripotent and embryonic stem cells: fraternal or identical twins? *Molecular therapy : the journal of the American Society of Gene Therapy* **19**, 635-638, doi:10.1038/mt.2011.41 (2011).
52 Xu, X. *et al.* Reversal of Phenotypic Abnormalities by CRISPR/Cas9-Mediated Gene Correction in Huntington Disease Patient-Derived Induced Pluripotent Stem Cells. *Stem cell reports* **8**, 619-633, doi:10.1016/j.stemcr.2017.01.022 (2017).
53 de Oliveira, M. S. *et al.* MRI-texture analysis of corpus callosum, thalamus, putamen, and caudate in Machado-Joseph disease. *Journal of neuroimaging : official journal of the American Society of Neuroimaging* **22**, 46-52, doi:10.1111/j.1552-6569.2010.00553.x (2012).
54 D'Abreu, A. *et al.* Neocortical atrophy in Machado-Joseph disease: a longitudinal neuroimaging study. *Journal of neuroimaging : official journal of the American Society of Neuroimaging* **22**, 285-291, doi:10.1111/j.1552-6569.2011.00614.x (2012).
55 Camargos, S. T., Marques, W., Jr. & Santos, A. C. Brain stem and cerebellum volumetric analysis of Machado Joseph disease patients. *Arquivos de neuro-psiquiatria* **69**, 292-296 (2011).
56 Zhang, P., Xia, N. & Reijo Pera, R. A. Directed dopaminergic neuron differentiation from human pluripotent stem cells. *Journal of visualized experiments : JoVE*, 51737, doi:10.3791/51737 (2014).
57 Ramani, B. *et al.* Comparison of spinocerebellar ataxia type 3 mouse models identifies early gain-of-function, cell-autonomous transcriptional changes in oligodendrocytes. *Human molecular genetics* **26**, 3362-3374, doi:10.1093/hmg/ddx224 (2017).
58 Li, Y. X., Sibon, O. C. M. & Dijkers, P. F. Inhibition of NF-kappaB in astrocytes is sufficient to delay neurodegeneration induced by proteotoxicity in neurons. **15**, 261, doi:10.1186/s12974-018-1278-2 (2018).

59 Evert, B. O. *et al.* Inflammatory genes are upregulated in expanded ataxin-3-expressing cell lines and spinocerebellar ataxia type 3 brains. *The Journal of neuroscience : the official journal of the Society for Neuroscience* **21**, 5389-5396 (2001).
60 Switonski, P. M., Szlachcic, W. J., Krzyzosiak, W. J. & Figiel, M. A new humanized ataxin-3 knock-in mouse model combines the genetic features, pathogenesis of neurons and glia and late disease onset of SCA3/MJD. *Neurobiology of disease* **73**, 174-188, doi:10.1016/j.nbd.2014.09.020 (2015).
61 Cheruvallath, Z. S., Kumar, R. K., Rentel, C., Cole, D. L. & Ravikumar, V. T. Solid phase synthesis of phosphorothioate oligonucleotides utilizing diethyldithiocarbonate disulfide (DDD) as an efficient sulfur transfer reagent. *Nucleosides, nucleotides & nucleic acids* **22**, 461-468, doi:10.1081/ncn-120022050 (2003).
62 McKay, R. A. *et al.* Characterization of a potent and specific class of antisense oligonucleotide inhibitor of human protein kinase C-alpha expression. *The Journal of biological chemistry* **274**, 1715-1722 (1999).
63 Raman, I. M. & Bean, B. P. Resurgent sodium current and action potential formation in dissociated cerebellar Purkinje neurons. *The Journal of neuroscience : the official journal of the Society for Neuroscience* **17**, 4517-4526 (1997).

4.8 Figures

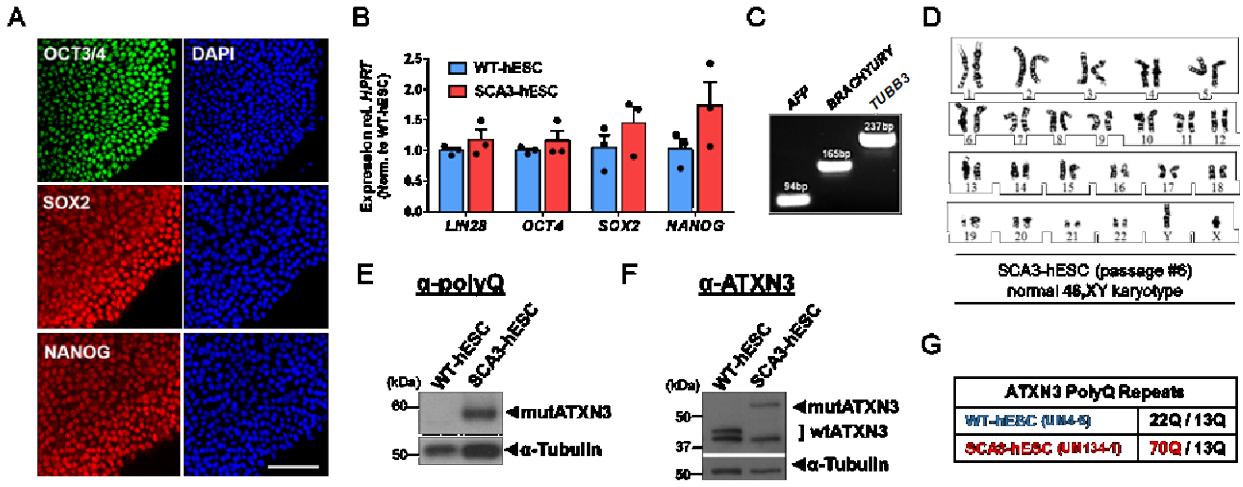

Figure 4.1. SCA3-hESC line UM134-1 is pluripotent, possesses a normal karyotype, and expresses pathogenic polyglutamine-expanded mutant ATXN3. (A) Immunocytochemical analysis with DAPI co-stain of SCA3-hESC revealed expression of pluripotency markers OCT3/4, SOX2, and NANOG. Scale bar = 200 μm. (B) Undifferentiated WT-hESC (blue) and SCA3-hESC (red) expressed pluripotency markers *LIN28*, *OCT4*, *SOX2* and *NANOG* as assessed by qRT-PCR analysis. Data are represented as mean of three replicates ± SEM. (C) SCA3-hESC were differentiated into embryoid bodies for 21 days in culture. Differentiated SCA3-embryoid bodies expressed lineage markers of endodermal [*α-fetoprotein* (*AFP*)], mesodermal [*Brachyury*], and ectodermal tissue [*neuron-specific class III beta-tubulin* (*TUBB3*)]. Electrophoresis demonstrated anticipated amplicon size for each lineage marker PCR primer set. (D) G-banded karyotype analysis of passage 6 undifferentiated SCA3-hESC showed a normal 46,XY karyotype. (E) Representative anti-polyQ expansion and (F) anti-ATXN3 Western blot of undifferentiated WT- and SCA3-hESC revealed heterozygous expression of polyQ-expanded ATXN3 protein in SCA3-hESC within the pathogenic range for SCA3. (G) Anticipated ATXN3 polyQ repeat lengths in WT- and SCA3-hESC lines as determined by gene fragmentation analysis. Mutant polyQ-expanded repeat length is highlighted in red. (mutATXN3 = mutant ATXN3; wtATXN3 = wild type ATXN3).

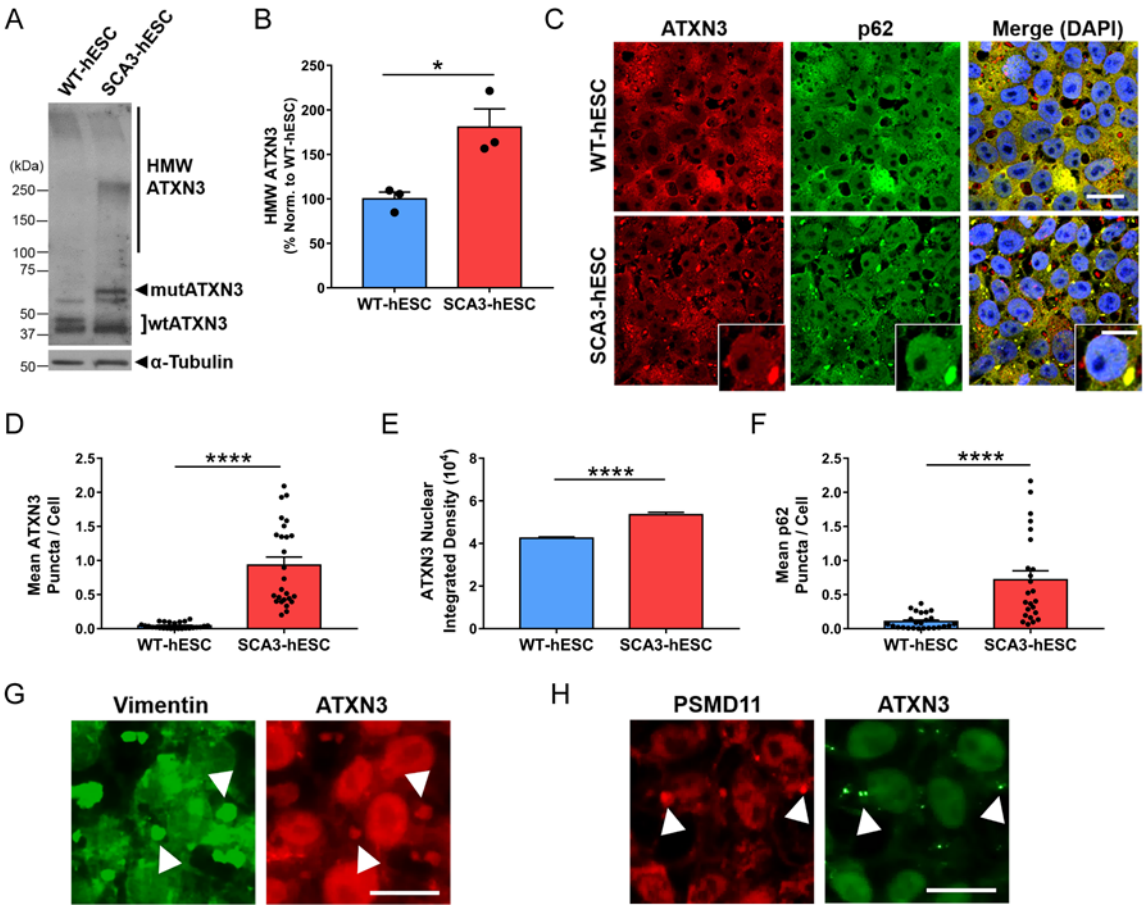

Figure 4.2. SCA3-hESC form high molecular weight ATXN3 aggregates that localize to p62-positive aggresomes and exhibit enhanced nuclear sequestration of ATXN3. (A) Representative anti-ATXN3 Western blot and (B) quantification of high molecular weight (HMW) ATXN3 species in undifferentiated WT-hESC (blue) and SCA3-hESC (red). Data (mean of three replicates ± SEM) are reported normalized to WT-hESC set to 100%. (C) Immunocytochemistry of undifferentiated WT- and SCA3-hESC showing single channel anti-ATXN3 (red) and anti-p62 (green) immunofluorescence merged with DAPI co-stain (blue). Scale bar = 25 μm. Inset scale bar = 10 μm. (D) Mean ATXN3 puncta per cell, (E) ATXN3 nuclear integrated density, and (F) p62 puncta per cell in WT- and SCA3-hESC. (G) Anti-vimentin (green) and anti-ATXN3 (red) immunofluorescence in undifferentiated SCA3-hESC. Scale bar = 20 μm. (H) Anti-PSMD11 (red) and anti-ATXN3 (green) immunofluorescence in undifferentiated SCA3-hESC. White arrowheads indicate co-localization of vimentin$^+$ or PSMD11$^+$ and ATXN3$^+$ puncta. Scale bar = 20 μm. Data (mean ± SEM) are reported (n = 3-5 confocal images per 3-4 independent replicates). Data points in (D) and (F) represent individual confocal images, while mean nuclear integrated density in (E) was calculated by averaging across imaged nuclei. Unpaired two-tailed t test (*p<0.05, **p<0.01, ***p<0.001, ****p<0.0001). (mutATXN3 = mutant ATXN3; wtATXN3 = wild type ATXN3; PSMD11 = proteasome 26S subunit, non-ATPase 11).

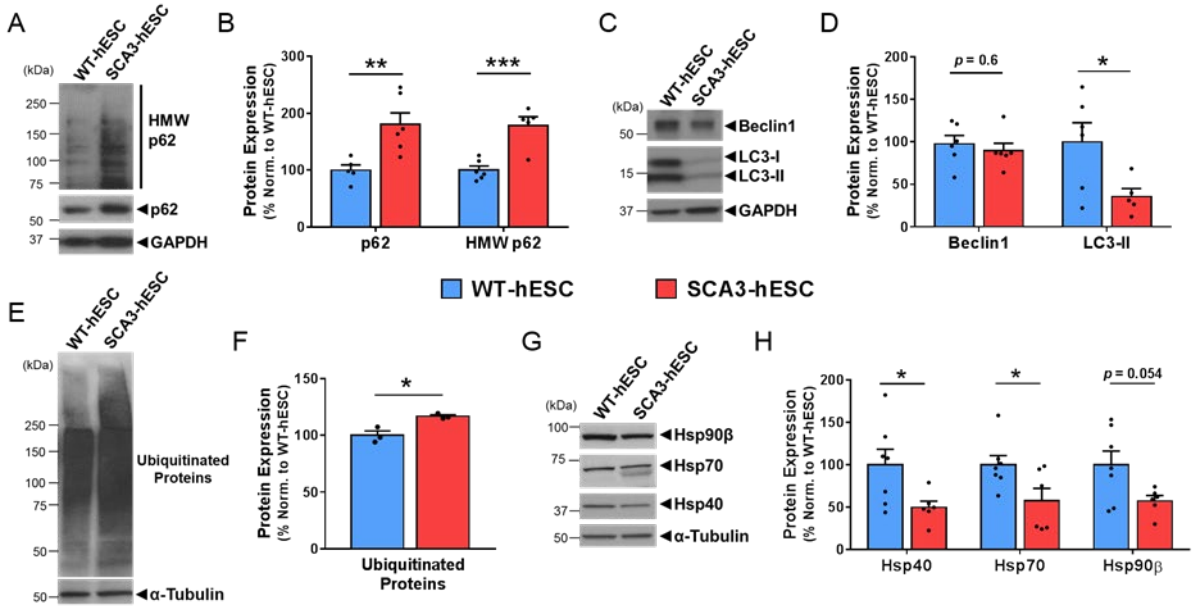

Figure 4.3. SCA3-hESC exhibit altered expression of key regulators of protein homeostasis. (A) Representative anti-p62 Western blot and (B) quantification of monomeric and high molecular weight (HMW) p62 in undifferentiated WT-hESC (blue) and SCA3-hESC (red) (n = 6). (C) Representative anti-Beclin1 and anti-LC3B Western blot and (D) quantification in undifferentiated WT- and SCA3-hESC (n = 6). (E) Representative anti-ubiquitin western blot and (F) quantification of ubiquitinated proteins in WT- and SCA3-hESC (n = 3). (G) Anti-Hsp40, anti-Hsp70, and anti-Hsp90β Western blots and (H) quantification in WT- and SCA3-hESC (n = 6). Data (mean of 3-6 independent replicates ± SEM) are reported relative to WT-hESC set to 100%. Unpaired two-tailed t test (*p<0.05, **p<0.01, ***p<0.001). (GAPDH = glyceraldehyde-3-phosphate dehydrogenase).

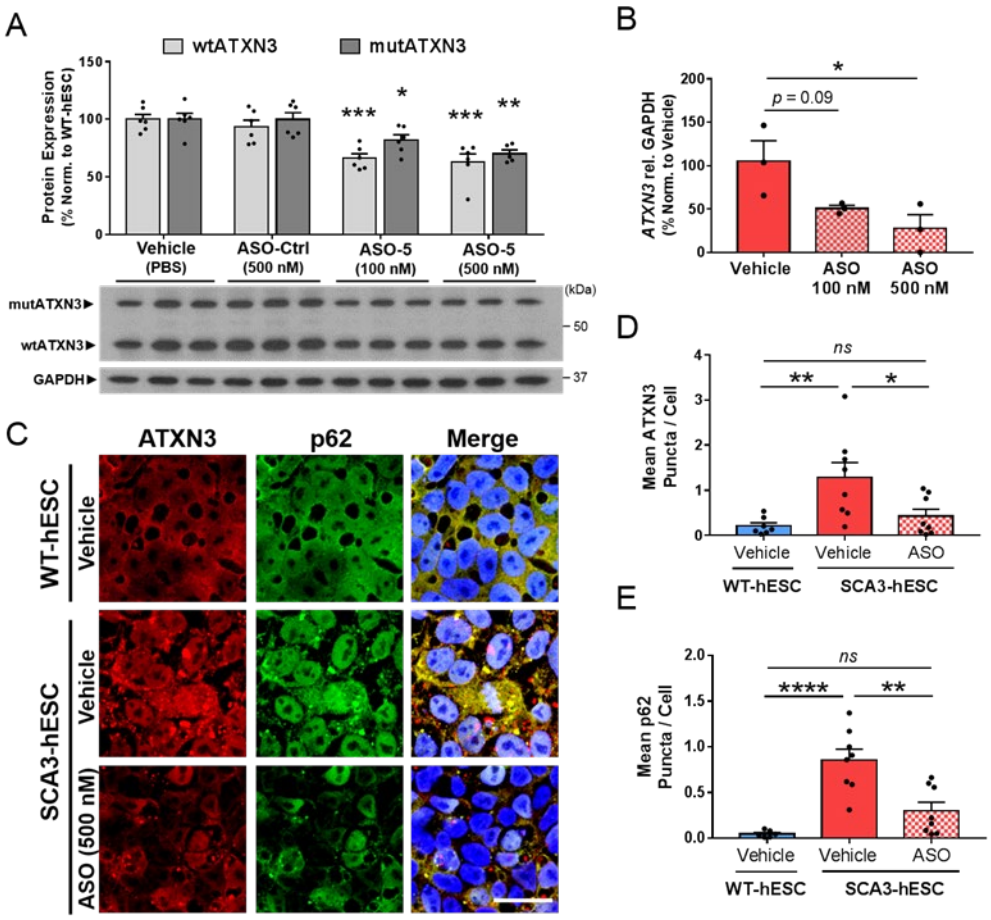

Figure 4.4. Anti-*ATXN3* antisense oligonucleotide-mediated reduction of ATXN3 rescues ATXN3 aggregation and aggresome formation in SCA3-hESC.
(A) Representative anti-ATXN3 Western blot and quantification of mutant ATXN3 (mutATXN3, dark gray) and wild type ATXN3 (wtATXN3, light gray) in SCA3-hESC protein lysates four days after transfection with PBS vehicle, 500 nM of scrambled antisense oligonucleotide control (ASO-Ctrl), and 100 nM or 500 nM of an anti-*ATXN3* antisense oligonucleotide (ASO) (n = 6 replicates). (B) qRT-PCR analysis of total *ATXN3* transcript levels in SCA3-hESC three days after transfection vehicle, 100 nM or 500 nM of ASO (n = 3 replicates). (C) Anti-ATXN3 (red) and anti-p62 (green) immunofluorescence and DAPI co-stain (blue) merged images in vehicle-treated WT-hESC, vehicle-treated SCA3-hESC, and SCA3-hESC transfected with 500 nM ASO. Cells were fixed four days following transfection of vehicle or ASO. Scale bar = 25 μm. (D) Quantification of mean ATXN3 puncta per cell and (E) mean p62 puncta per cell in WT-hESC (blue) and SCA3-hESC (red) transfected with vehicle, and SCA3-hESC transfected with 500 nM anti-ATXN3 ASO (red/white checkered) (n = 2-3 images quantified from 3 experimental replicates). Data (mean ± SEM) are reported. One-way ANOVA performed with the post-hoc Tukey test. (*p<0.05, **p<0.01, ****p<0.0001). (GAPDH = glyceraldehyde-3-phosphate dehydrogenase; *ns* = not significant).

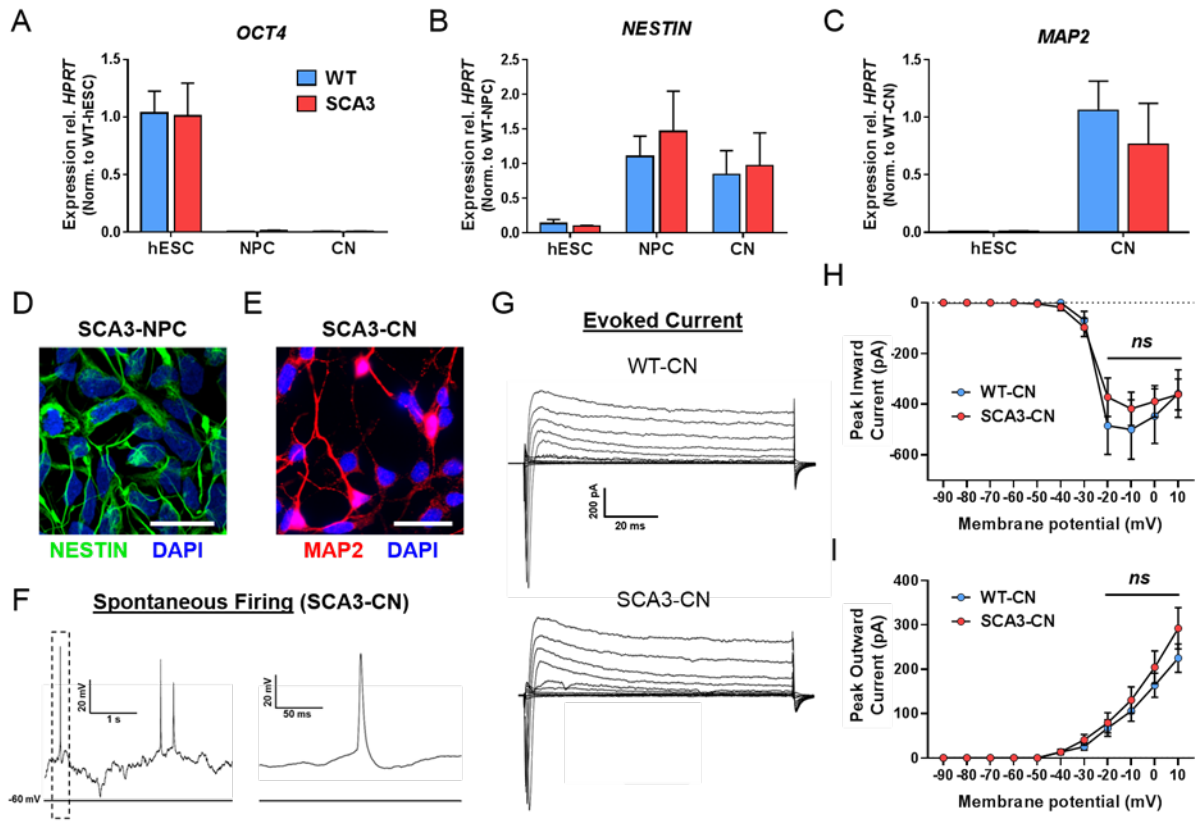

Figure 4.5. SCA3-hES can be differentiated into NESTIN$^+$ neural progenitor cells and MAP2$^+$ forebrain cortical neurons that exhibit spontaneous firing activity. (A) qRT-PCR analysis for pluripotency marker *OCT4*, (B) neural stem cell marker *NESTIN*, and (C) mature neural lineage marker *MAP2* in undifferentiated WT- (blue) and SCA3-hESC (red) and differentiated neural progenitor cells (NPC) and cortical neurons (CN). Data (mean ± SEM) are reported normalized to WT-hESC, WT-NPC, or WT-CN as indicated in graph (n = 3 replicates). (D) NPCs derived from SCA3-hESC immunostained for neural stem cell marker NESTIN (green) and DAPI (blue). Scale bar = 50 µm. (E) Neurons derived from SCA3-hESC immunostained with mature neuronal marker MAP2 (red) and DAPI (blue). Scale bar = 25 µm. (F) Representative whole-cell current-clamp electrophysiological recording and enlarged inset of SCA3-CN showing spontaneous action potentials. (G) Representative whole-cell voltage-clamp recordings of WT- and SCA3-CN indicating evoked inward and outward currents in response to depolarizing voltage steps. (H) Quantification of peak inward currents in response to depolarizing voltage steps in WT- (n = 7 cells) and SCA3-CN (n = 9 cells). (I) Quantification of peak outward currents in response to depolarizing voltage steps in WT- (n=7 cells) and SCA3-CN (n = 9 cells). Data (mean ± SEM) are reported. Two-way ANOVA performed with Holm Sidak correction for multiple comparisons.

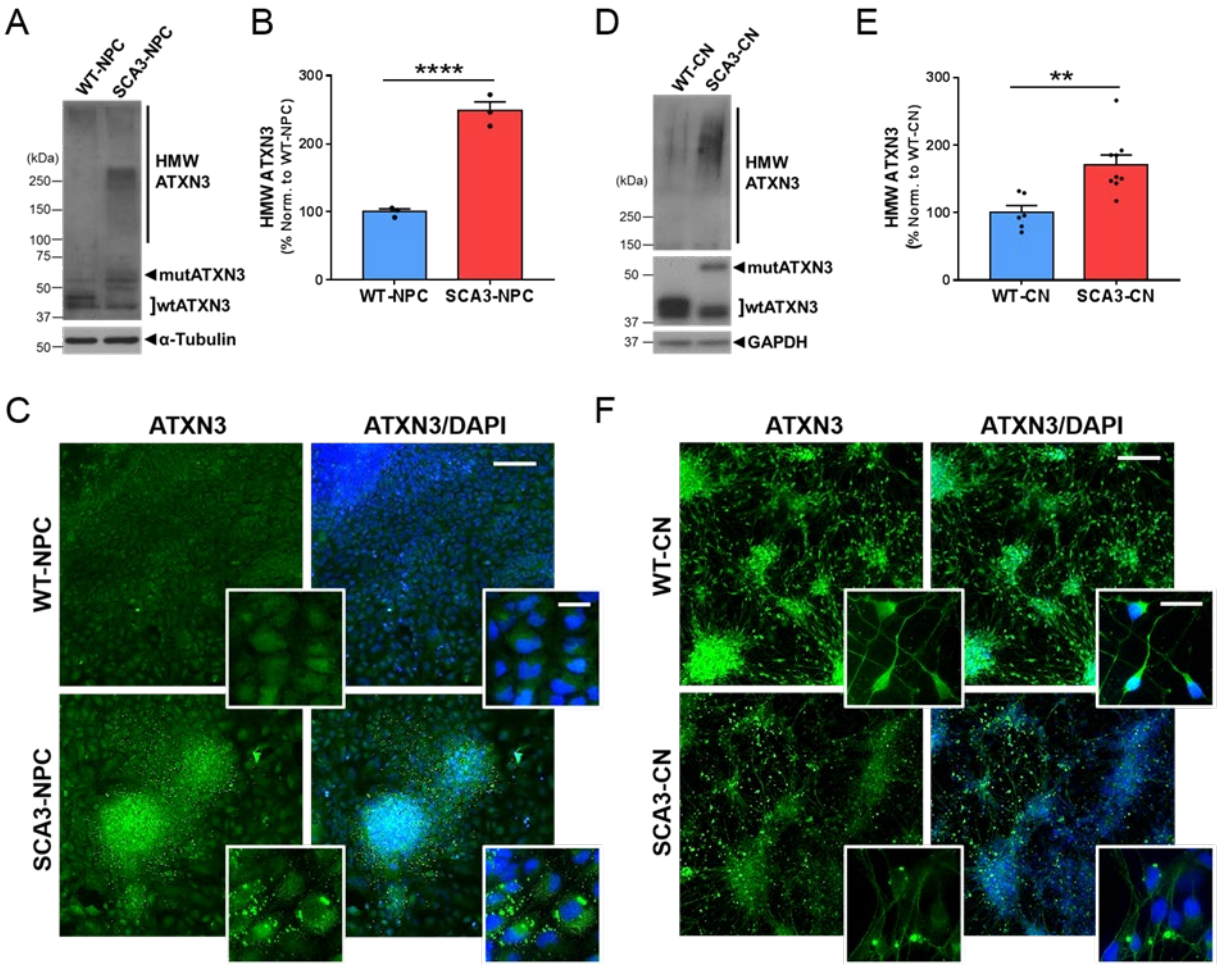

Figure 4.6. SCA3-hESC derived neural progenitor cells and cortical neurons express polyglutamine-expanded mutant ATXN3 and accumulate high molecular weight ATXN3 aggregates. (A) Representative anti-ATXN3 Western blot and (B) quantification of high molecular weight (HMW) ATXN3 levels in neural progenitor cells (NPC) derived from WT-hESC (WT-NPC, blue) and SCA3-hESC (SCA3-NPC, red). Data (mean ± SEM) are reported relative to mean WT-NPC set to 100% (n=3 replicates). (C) WT- and SCA3-NPC immunostained for ATXN3 (green) and DAPI (blue). (D) Representative anti-ATXN3 Western blot and (E) quantification of HMW ATXN3 levels in cortical neurons (CN) derived from WT-hESC (WT-CN, blue) and SCA3-hESC (SCA3-CN, red). Data (mean ± SEM) are reported relative to mean WT-CN set to 100% (n=3 replicates). (F) WT-CN and SCA3-CN shown with anti-ATXN3 (green) and DAPI (blue) immunostaining. Scale bar = 200 μm. Inset scale bar = 25 μm. Unpaired two-tailed t test (**p<0.01, ****p<0.0001).

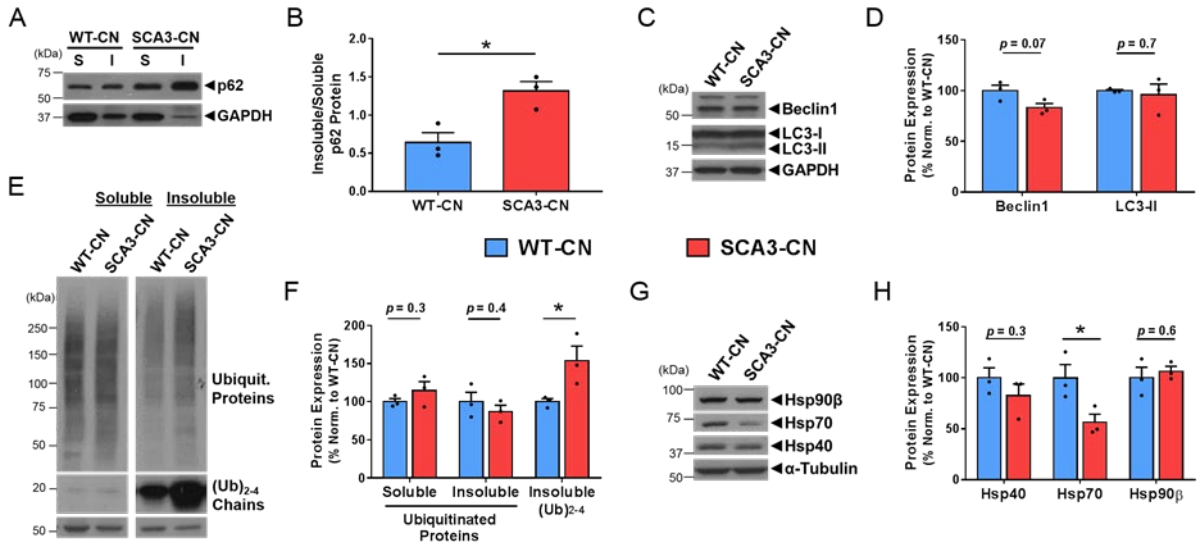

Figure 4.7. SCA3-hESC derived cortical neurons exhibit altered expression of key regulators of protein homeostasis. (A) Representative anti-p62 Western blot of soluble (S) and insoluble (I) protein fractions from WT-CN (blue) and SCA3-CN (red). (B) Ratio of insoluble/soluble p62 protein in WT-CN and SCA3-CN. (C) Representative anti-Beclin1 and anti-LC3B Western blots and (D) quantification in RIPA-lysed WT-CN and SCA3-CN. (E) Representative anti-ubiquitin Western blot of soluble and insoluble protein fractions from WT-CN and SCA3-CN. (F) Quantification of soluble ubiquitinated and insoluble ubiquitinated proteins, and insoluble small ubiquitin chains [$(Ub)_{2-4}$] in WT-CN and SCA3-CN. (G) Representative anti-Hsp40, -Hsp70, and -Hsp90β Western blot and (H) quantification in RIPA-lysed WT-CN and SCA3-CN. Data (mean of 3 replicates ± SEM) are reported relative to mean WT-CN set to 100%. Unpaired two-tailed t test (*p<0.05). (Ubiquit. = ubiquitinated; GAPDH = glyceraldehyde-3-phosphate dehydrogenase).

CHAPTER 5
Evidence of Nucleocytoplasmic Transport Dysfunction and Compromised Nuclear Integrity in SCA3

5.1 Abstract

The most common autosomal dominant ataxia worldwide, spinocerebellar ataxia type 3 (SCA3) is a late-onset neurological disorder caused by a *CAG*-repeat expansion encoding a long, aggregate-prone polyglutamine sequence in the deubiquitinase ATXN3. Abnormal nuclear sequestration of mutant ATXN3 (mutATXN3) is a prominent pathological feature of SCA3 human disease, and is likely a necessary step in disease as preventing mutATXN3 nuclear import rescues disease features in SCA3 mice. Though it remains unclear why mutATXN3 becomes sequestered in neuronal nuclei, identifying mechanisms that contribute to its nuclear localization may reveal novel therapeutic targets for SCA3. Impaired nucleocytoplasmic transport (NCT) has also emerged as a common disease mechanism in several neurodegenerative disorders, including amyotrophic lateral sclerosis, Alzheimer's disease, and Huntington's disease. However, whether overall NCT is impaired in SCA3, and contributes to mutATXN3 nuclear localization and neuronal dysfunction, is unknown. In this chapter, we complete the first descriptive study of NCT function and nuclear integrity in cellular and transgenic mouse models of SCA3. Active NCT of most proteins depends on a highly regulated asymmetric distribution of the nucleotide-bound GTPase Ran. We identified a striking decrease in the nuclear/cytoplasmic ratio of Ran in disease-vulnerable brain regions in (YAC)MJD-Q84.2 and (CMV)MJD-Q135 SCA3 transgenic mice that was completely rescued by antisense oligonucleotide-mediated reduction of mutATXN3 in (YAC)MJD-Q84.2 mice. Interestingly, a subset of neurons in SCA3 mice exhibited a severe, essentially complete loss of nuclear Ran that directly correlated with a loss of nuclear

mutATXN3 and was associated with formation of cytoplasmic puncta containing the NCT proteins Ran, components of nuclear pore complexes, and RanGAP1. We also identified evidence for impaired nuclear integrity in SCA3 mice, indicated by increased DNA damage and folding or blebbing of the nuclear envelope. Overall, these studies point to global impairments in active NCT in SCA3, and add SCA3 to the growing list of neurodegenerative diseases characterized by dysfunction in nuclear trafficking and perturbations in nuclear integrity.

5.2 Introduction

Spinocerebellar ataxia type 3 (SCA3) is an adult-onset, fatal neurodegenerative disorder characterized by progressive degeneration of selective neuronal nuclei spanning the brainstem, cerebellum, striatum, and spinal cord[1]. SCA3 is caused by a *CAG* repeat expansion in *ATXN3* leading to an abnormally long polyglutamine (polyQ) sequence in the encoded disease protein ATXN3[2]. ATXN3 is a ubiquitously expressed deubiquitinating enzyme involved in ubiquitin-dependent proteolysis pathways, macroautophagy, transcriptional regulation, and DNA damage repair[3,4]. Complex changes in all of these cellular pathways have been observed in the SCA3 disease brain, but the underlying mechanism by which mutant ATXN3 (mutATXN3) expression triggers selective neuronal dysfunction and loss in SCA3 patients is unclear[3]. PolyQ-expanded ATXN3 exhibits altered protein-protein interactions, subcellular localization, enzymatic activity, and a high propensity to misfold and aggregate within neuronal nuclei[2,3]. Notably, nuclear localization of mutATXN3 is required for full disease features to manifest in SCA3 mice, suggesting that mislocalization of mutATXN3 proteins plays a key role in SCA3 pathogenesis[5].

Bidirectional trafficking of macromolecules across the nuclear membrane underlies cellular homeostatic processes and is essential to rapid cellular responses to environmental changes or stress, such as oxidative stress and heat shock[6,7]. Nucleocytoplasmic transport (NCT) of RNA and proteins >40 kDa occurs through a highly regulated and energetic process. Movement of macromolecules across the nuclear membrane takes place through large nuclear pore complexes (NPCs) that span the nuclear envelope[8]. Transport of protein cargo through NPCs is facilitated by numerous nuclear transport receptors, often referred to as importins and exportins, that

selectively bind to nuclear localization sequences (NLS) or nuclear export sequences (NES) on cargo, respectively, triggering its NCT[9]. Nuclear transport receptor binding and release of protein cargo before and after facilitated NCT is energetically driven by hydrolysis of the small GTPase Ras-related nuclear protein (Ran)[9]. In the cytoplasm, Ran-GTP is converted to Ran-GDP by Ran GTPase activating protein 1 (RanGAP1), whereas in the nucleus Ran-GDP is converted to Ran-GTP by Ran guanine exchange factor (RanGEF)[10]. The symmetric distribution of nucleotide-bound Ran, with relatively high Ran-GDP concentrations in the cytoplasm and high Ran-GTP concentrations in the nucleus, underlies the directionality of NCT[10]. The overall distribution of Ran is also maintained at higher concentrations in the nucleus, as cytoplasmic Ran-GDP is rapidly imported into the nucleus by nuclear transport factor 2 (NTF2)[11].

Chronic perturbations to neuronal nuclear trafficking and nuclear integrity are hallmarks of physiological aging, but have also recently emerged as mechanisms contributing to several neurodegenerative proteinopathies including amyotrophic lateral sclerosis (ALS), frontotemporal dementia (FTD), Alzheimer's diseases (AD), and Huntington's disease (HD)[12-18]. Despite significant clinical differences, all of these diseases share key neuropathological features: subcellular mislocalization and aggregation of disease-associated proteins in affected neurons that exacerbates with time. Growing evidence suggests that impairments in NCT may help drive mislocalization of disease-associated proteins in neurodegenerative disease[19,20]. In addition, aberrant behavior and/or aggregation of the disease proteins appears to directly contribute to NCT dysfunction. For example, RanGAP1 and a number of NUPs are sequestered into stress granules or protein aggregates in ALS, AD, and HD patient brains and model systems[13,16,17,21,22]. Protein aggregation and abnormal nuclear localization of mutATXN3 are characteristic of SCA3, but whether these features may be indicative of, or driven by, impairments in nuclear trafficking has not yet been examined. Here, we investigate whether NCT dysfunction occurs in cellular and mouse models of SCA3, and if so, if reducing levels of mutATXN3 rescue NCT deficits in SCA3 mice.

5.3 Results

5.3.1 Perturbations to normal Ran distribution in 293 cells expressing polyQ-expanded ATXN3 and in (CMV)MJD-Q135 SCA3 transgenic mice.

Decreased Ran nuclear to cytoplasmic (N/C) distribution indicative of NCT dysfunction has been observed in several neurodegenerative diseases including ALS[23] and HD[13], but has not been examined in SCA3. We began by investigating whether exogenous expression of mutATXN3 alters normal Ran distribution *in vitro* using HEK293 cells stably expressing FLAG-tagged human ATXN3 with 80 *CAG* repeats [ATXN3(Q80)] or FLAG-tagged FLP recombinase target (FRT). We performed anti-Ran immunocytochemistry (ICC) with DAPI staining on FRT and ATXN3(Q80) 293 cells, and quantified integrated density of Ran within nuclei using ImageJ analysis software (n=3 experimental replicates per line).

As shown in **Fig. 5.1A,** FRT-expressing 293 cells exhibited a uniform Ran distribution pattern, with high nuclear/low cytoplasmic Ran levels apparent in all cells. In ATXN3(Q80)-expressing 293 cells, however, two distinct Ran distribution patterns were observed. Approximately 60-80% of ATXN3(Q80) cells exhibited overall decreased total Ran intensity and a “leveling” of Ran cellular distribution relative to FRT 293 cells, with only slightly increased or equivalent Ran intensities observed in nuclei relative to the cytoplasmic compartment. The remaining 20-40% of ATXN3(Q80) cells demonstrated high total cell Ran intensities, but a reversal in Ran cellular distribution, with abnormally high Ran levels in the cytoplasm relative to nuclei. The mean integrated density of nuclear Ran across all ATXN3(Q80)-expressing cells was significantly reduced by approximately 35% relative to FRT-expressing cells (p<0.0001) (**Fig. 5.1B**).

Next, we investigated whether Ran distribution is affected by mutATXN3 expression *in vivo,* by comparing the Ran N/C ratios of neurons in disease-vulnerable brain regions in wild type (WT) versus (CMV)MJD-Q135 (Q135) hemizygous mice. Q135 mice ubiquitously express a human *ATXN3* cDNA isoform from the CMV promoter and form ATXN3 aggregates in brainstem and cerebellar nuclei by 6-8wks of age[24]. Anti-Ran and anti-NeuN immunohistochemistry (IHC) with DAPI stain was performed on 16wk old sex-matched Q135 and WT littermates (n=4 mice per genotype).

Ran nuclear and cytoplasmic integrated densities were then calculated in NeuN-positive neurons within deep cerebellar nuclei (DCN) and pontine gray nuclei (pons), two brain regions that are highly affected in SCA3 patients (**Fig. 5.2A-B**) (NeuN staining data not shown).

Neurons in WT mice exhibited overall higher Ran concentrations in nuclei relative to cytoplasm, as demonstrated by a mean Ran N/C>1 in both pontine and DCN neurons. WT DCN and pontine neurons also displayed strong Ran immunolabeling of the nuclear membrane, illustrated by the distinct Ran-positive rings in WT neurons in **Fig. 5.2A-B**. In contrast, Q135 mice exhibited significantly reduced Ran N/C ratios in DCN and pontine neurons, with mean Ran N/C ratios <1 in both regions ($p<0.0001$) (**Fig. 5.2C-D)**. Though the overall mean Ran N/C was only decreased by 10-20% in DCN and pons of Q135 mice compared to WT mice, the variability in Ran distribution across individual neurons was much greater in Q135 than WT mice. About a third of Q135 pontine neurons exhibited Ran N/C<0.5 suggesting a complete reversal in Ran distribution. About 10% of Q135 neurons exhibited severe, complete clearance of intranuclear and nuclear membrane-localized Ran that often coincided with the formation of abnormal cytoplasmic Ran puncta. Examples of mild and severe Ran distribution and puncta formation phenotypes in Q135 DCN neurons are shown in **Fig. 5.2E**.

5.3.2 Knockdown of ATXN3 rescues abnormal Ran N/C distribution in homozygous (YAC)MJD.Q84.2 transgenic mice.

We next investigated features of Ran-dependent NCT in a second complementary SCA3 transgenic mouse model: homozygous (YAC)MJD.Q84.2 (Q84) mice expressing the full-length human *ATXN3* disease gene. By 6 weeks of age, Q84 mice present with robust accumulation of high molecular weight (HMW) ATXN3 aggregates and abnormal nuclear ATXN3 localization in DCN and pontine neurons[25,26]. In a recently published preclinical study (also presented in Chapter 3 of this dissertation), we demonstrated that a single intracerebroventricular (ICV) injection of an anti-*ATXN3* antisense oligonucleotide (ASO) into 8wk old homozygous Q84 mice led to sustained suppression of soluble mutATXN3 and HMW ATXN3 oligomers, and rescued abnormal nuclear ATXN3 sequestration in DCN and pontine nuclei at 16 weeks of age

(i.e. 8 weeks after injection)[27,28]. Importantly, the ~50% reduction in soluble mutATXN3 and clearance of nuclear mutATXN3 was sufficient to rescue motor and electrophysiological phenotypes in Q84 mice. Here, we employed the same injection protocol as previously described[27] to evaluate Ran N/C distribution in sex-matched vehicle-treated WT, vehicle-treated Q84, and ASO-treated Q84 (Q84-ASO) mice (n=4 mice per treatment group)(**Fig. 5.3A**).

First, anti-ATXN3 immunoblot analysis of brainstem lysates confirmed ASO-mediated knockdown of soluble mutATXN3 and HMW ATXN3 in Q84-ASO mice to levels similar to that achieved in our previous study[27] (**Fig. 5.3B**). IHC analysis and subsequent quantification revealed significantly reduced mean neuronal Ran N/C in Q84 DCN (p<0.0001) and pontine neurons (p<0.001) relative to WT littermates (**Fig. 5.3C-F**). Notably, a single ICV injection of the anti-*ATXN3* ASO at 8 weeks of age significantly rescued this aberrant Ran distribution in 16-week-old Q84-ASO mice: mean Ran N/C measured from Q84-ASO DCN neurons was significantly increased relative to vehicle-treated Q84 mice (p<0.001), though still significantly reduced compared to vehicle-treated WT mice (p<0.01) (**Fig. 5.3E**). In contrast, ASO-mediated reduction of mutATXN3 fully rescued neuronal Ran distribution in pontine neurons of Q84 mice relative to levels seen in WT mice (**Fig. 5.3F**).

As in Q135 mice, individual neurons in vehicle-treated Q84 DCN and pons displayed high heterogeneity in Ran distribution, with calculated Ran N/C ratios ranging from close to 0 (i.e. complete loss of nuclear Ran) to within normal Ran N/C levels of >1 (**Fig. 5.3E,F**). Examples of mild and severe Ran neuronal phenotypes in Q84 DCN and pontine neurons are shown in **Fig. 5.3G.** As in Q135 mice, large cytoplasmic Ran puncta were observed in a subset of Q84 DCN and pontine neurons. Q84 neurons containing numerous Ran puncta also typically exhibited a Ran N/C ratio of <1, loss of Ran from the nuclear membrane, and abnormal or distorted nuclear shape.

Thus, mutATXN3 expression resulted in overall decreased Ran N/C distribution in *in vitro* studies and in two complementary SCA3 mouse models. HEK293 cells and SCA3 mouse neurons expressing mutATXN3 exhibited heterogeneity in Ran localization that ranged from severely abnormal depletion of nuclear Ran to relatively normal Ran distribution. In addition, clearance of nuclear Ran in Q135 and Q84 neurons

appeared to coincide with the formation of multiple Ran cytoplasmic puncta and perturbations to nuclear membrane shape and Ran immunolabeling. However, further analysis is required to conclude a positive correlation between nuclear Ran clearance and the formation of cytoplasmic Ran puncta. Nevertheless, Ran mislocalization was rescued by ASO-mediated reduction in ATXN3 levels in Q84 mice. In this study, ASOs achieved about a 50% knockdown of soluble mutATXN3 levels and a 75% reduction in HMW ATXN3 in brainstem lysates, suggesting that Ran subcellular localization is sensitive to changes in neuronal levels of either soluble mutATXN3, oligomeric mutATXN3, or both.

5.3.3 Nuclear Ran positively correlates with nuclear ATXN3 in WT and Q84 mice.

Because nuclear accumulation of mutATXN3 is a major driver of neuronal dysfunction in SCA3, we investigated whether increased nuclear mutATXN3 levels directly correlated with reversal of Ran N/C distribution in ATXN3(Q80)-expressing HEK293 cells and Q84 neurons. To investigate the relationship between Ran and ATXN3 localization *in vitro*, we performed anti-Ran and anti-ATXN3 ICC on FRT and ATXN3(Q80)-stably expressing HEK293 cells (**Fig. 5.4A**). As expected, endogenous non-expanded ATXN3 appeared diffusely localized throughout both nuclear and cytoplasmic compartments in FRT cells. ATXN3(Q80) cells exhibited much more complex and irregular patterns of expression and distribution of ATXN3 and Ran: cells expressing very high levels of overall Ran and Ran N/C <1 tended to exhibit low levels of nuclear ATXN3, whereas cells showing more normal Ran N/C distributions exhibited higher levels of nuclear ATXN3.

Next, we quantified and plotted the nuclear integrated densities of Ran versus ATXN3 within individual ATXN3(Q80) and FRT nuclei and performed Pearson correlation analysis of nuclear Ran versus nuclear Ran (**Fig. 5.4B**). Surprisingly, both FRT and ATXN3(Q80) cells exhibited a significant linear positive correlation between nuclear Ran and ATXN3 integrated densities ($p<0.0001$). FRT-expressing 293 cells exhibited a more highly correlated linear relationship between nuclear ATXN3 and nuclear Ran ($R^2 = 0.83$). Though statistically significant, a much lower positive correlation between nuclear ATXN3 and nuclear Ran was found in ATXN3(Q80)-

expressing cells (R^2 =0.30), reflecting the high variability in observed phenotypes in these cells.

Anti-Ran, -ATXN3, and -NeuN immunofluorescence analysis also revealed an intriguing, but surprising relationship between neuronal nuclear ATXN3 and Ran levels in sex-matched 16wk old WT and Q84 mice (n=4 mice per genotype) (**Fig. 5.4C-F**). Endogenous ATXN3 appeared diffusely localized predominantly in the cytoplasm, but also was present in nuclear compartments in WT DCN and pontine neurons (**Fig. 5.4C,E**). However, quantification of neuronal nuclear Ran and ATXN3 revealed an almost perfect linear relationship between nuclear Ran and nuclear ATXN3 mean nuclear integrated densities in WT DCN (p<0.0001; R^2 = 0.95) and pons (p<0.0001; R^2 = 0.96) (**Fig. 5.4D,F**). This positive correlation between Ran and ATXN3 nuclear intensity was also apparent in Q84 neurons. Quantification of neuronal nuclear Ran and ATXN3 confirmed a significant positive correlation in both DCN neurons (p<0.0001; R^2 = 0.86) and pontine neurons (p<0.0001; R^2 = 0.82) of Q84 mice. Q84 DCN and pontine neurons exhibiting little to no nuclear Ran were similarly cleared of nuclear ATXN3, while neurons exhibiting a more normal Ran N/C distribution had exceedingly high levels of nuclear ATXN3.

The positive correlation between nuclear Ran and nuclear ATXN3 levels in both FRT HEK293 cells and WT mice suggests that ATXN3 may normally play a role in Ran-mediated NCT or may directly interact with Ran. The fact that this linear relationship between ATXN3 and Ran is largely maintained in SCA3 model systems suggests that mutATXN3 may also deregulate Ran subcellular localization through a direct mechanism of action. However, why neurons with the most severe changes in Ran distribution appear to have the most “normal” ATXN3 distribution while neurons with the most severe nuclear ATXN3 accumulation appear to have “normal” Ran distribution, is unclear.

5.3.4 Distorted nuclear membrane shape and sequestration of key NCT proteins into cytoplasmic puncta in Q84 DCN and pontine neurons.

Disturbances to nuclear membrane structure are characteristic of aging neurons and have also been described in AD[17], HD[13,22], and ALS[18]. Anti-Ran IHC in Q135 and Q84 neurons revealed that loss of nuclear Ran often coincided with abnormally shaped

nuclei with a “ruffled” nuclear membrane appearance. Because Ran staining of the nuclear membrane was heterogeneous in SCA3 mice, we next performed anti-RanGAP1 and anti-NeuN IHC with DAPI staining on 16wk-old WT and Q84 mice to investigate whether Q84 mice indeed exhibit compromised structural integrity of neuronal nuclei. SUMO1-modified RanGAP1 localizes to the cytoplasmic filaments of NPCs where it converts Ran-GTP to Ran-GDP for nuclear import, and thus is a marker for the nuclear membrane outer surface.

As shown in **Fig 5.5A-B**, WT DCN and pontine neuronal nuclei typically displayed distinct, circular or oval-shaped RanGAP1 rings that surrounded neuronal nuclei, with little to no cytoplasmic RanGAP1 detected. RanGAP1 imaging of Q84 mice revealed much more irregular shaped nuclear membranes in Q84 DCN and pontine neurons. Preliminary analysis of RanGAP1-positive nuclear membrane roundness trended towards a decrease in Q84 DCN neurons (n=9-12 neurons imaged from 2 mice per genotype, p=0.08) and was significantly decreased in Q84 pontine neurons (n=36-48 neurons from 3 mice per genotype, p<0.0001), as quantified by ImageJ analysis (**Fig. 5.5C-D**). More extensive imaging and quantification of neuronal nuclear roundness is still ongoing.

Q84 neurons exhibited a variety of RanGAP1 abnormalities: A few Q84 nuclei appeared to have sparse RanGAP1 punctate perinuclear staining rather than a more solid ring (**Fig. 5.5B**, Q84 inset). Some Q84 neurons exhibited invaginations and blebbing of the nuclear membrane leading to a ruffled nuclear appearance (**Fig. 5.5E**). Many Q84 neurons appeared to have invasion of parts of RanGAP1-positive nuclear membrane into the intranuclear compartment (**Fig. 5.5E-F**). Fragmented, punctate DAPI-positive chromatin visibly localized to these intranuclear membrane projections, suggesting that these projections may disturb normal heterochromatin condensation in neuronal nuclei (**Fig. 5.5F**). Other Q84 nuclei appeared to have small ruptures in the nuclear membrane, with cytoplasmic RanGAP1- and DAPI-positive material found adjacent to discontinuous nuclear membrane segments (**Fig. 5.5G**). Observed micronuclei may also be a sign of defective DNA repair processes.

Ran, RanGAP1 and NPC-component proteins, called nucleoporins (NUPs), have previously been shown to accumulate into nuclear or perinuclear aggregates in HD

model systems[13] and into cytoplasmic stress granules and cytoplasmic TDP-43 aggregates in ALS model systems[21,29,30]. Small nuclear ATXN3 aggregates are characteristic of brainstem and cerebellar neurons in Q84 mice. However, no nuclear RanGAP1 puncta were observed in Q84 neurons that would suggest mislocalization of RanGAP1 into ATXN3 aggregates. Instead, higher cytoplasmic RanGAP1 levels were apparent in Q84 pontine and DCN neurons (**Fig 5.5AB)**, with many cells containing large, round RanGAP1 cytoplasmic puncta similar to the Ran-positive cytoplasmic puncta described above in **Fig 5.3G**. To determine whether NUPs were also sequestered into RanGAP1 cytoplasmic puncta in Q84 mice, we performed IHC on 16wk-old WT and Q84 mice using anti-RanGAP1 with the NPC [mAb414] antibody, which recognizes most phenylalanine-glycine repeat-containing NUPs (FG-NUPs) that comprise about half of all mammalian NUPs[31]. Large round cytoplasmic RanGAP1 puncta were consistently positive for NPC [mAb414] staining (**Fig. 5.5H**). Though it is clear that Q84 DCN and pontine neurons aberrantly accumulate Ran, RanGAP1, and NUP-containing cytoplasmic puncta, further assessment is required to determine whether all three of these key NCT proteins colocalize within the same structure, the exact nature of these structures, and whether they are rescued by reducing mutATXN3 protein.

5.3.5 Evidence for compromised genomic integrity in Q84 SCA3 mice

In addition to forming a protective barrier for genomic material, the nuclear membrane, and particularly the nuclear lamina, plays an important role in maintaining genomic integrity through the tethering of chromatin. The appearance of fragmented, punctate chromatin in Q84 neurons and altered nuclear membrane structure may point to compromised genomic integrity in Q84 mice. There is also evidence from the literature that wildtype ATXN3 plays normal roles in regulating DNA repair processes, and that the presence of a polyQ expansion in mutATXN3 leads to less efficient DNA repair. For example, ATXN3 regulates levels of the key DNA repair pathway upstream activator Tumor protein 53 (p53)[32] and the downstream DNA repair kinase polynucleotide kinase phosphatase (PNKP)[33,34] through direct binding and DUB-dependent editing of ubiquitin chains.

To investigate mutATXN3-dependent effects on genomic integrity, we performed immunolabeling for several key markers of DNA damage and activated DNA repair pathways on 16wk old WT, Q84, and Q84-ASO mice (**Fig. 5.6A-C**). Q84 pontine neurons exhibited significantly increased levels of phosphorylated histone 2A family member X (γ-H2AX) (**Fig. 5.6A**) and PNKP (**Fig. 5.6B**), both of which localize to DNA breaks to facilitate DNA repair. High nuclear γ-H2AX and PNKP staining consistently occurred in Q84 pontine neurons expressing high levels of nuclear mutATXN3, and was qualitatively reduced in Q84-ASO pontine neurons in which ATXN3 levels are reduced and redistributed to the cytoplasm. We next assessed whether Q84 neurons exhibited increased p53 activation, as evidenced by enhanced nuclear levels of p53 target proteins p21 and phosphorylated p53 binding protein 1 (p-53BP1) levels in nuclei. Both p21 and p-53BP1 were robustly up-regulated and accumulated in the nuclei of Q84 neurons, and this was again rescued by ASO treatment in Q84-ASO mice (**Fig. 5.6C**). Overall, these data reflect compromised genomic integrity and sustained activation of p53-mediated DNA repair pathways in Q84 mice. Whether loss of genomic integrity in Q84 mice is directly linked to destabilization of nuclear lamina-tethered heterochromatin or instead reflects mutATXN3-dependent dysregulation of the DNA repair pathway itself has yet to be determined.

5.4 Discussion

Using stably expressing HEK293 cell lines and two transgenic mouse models of SCA3, we demonstrate that expression of polyQ-expanded mutATXN3 leads to disruption of NCT, the nuclear membrane, and genomic integrity. First, altered subcellular localization of Ran was identified in a HEK293 SCA3 model and in vulnerable disease brain regions of two complementary mouse models of SCA3. Importantly, reducing mutATXN3 protein rescued Ran distribution in Q84 neurons, suggesting that mislocalization of Ran is sensitive to mutATXN3 expression levels. In a previous study, we showed that ASO-mediated reduction of soluble mutATXN3 levels by ~50% effectively translated to a 100% reduction of nuclear accumulated ATXN3 levels in Q84-ASO mice. Thus, our finding of decreased Ran N/C in Q84 mice suggested that Ran subcellular localization might be specifically tuned to mutATXN3 nuclear accumulation in mice.

Enhancing nuclear import of mutATXN3 aggravates disease while preventing its import mitigates disease features in SCA3 mice, supporting the view that mutATXN3 nuclear localization is an early and critical step in the SCA3 disease brain[5]. Here, we hypothesized that aberrant nuclear localization of mutATXN3 within neuronal nuclei would either induce or be caused by dysregulation of Ran N/C gradient. Unexpectedly, we discovered that abnormal Ran cytoplasmic localization indicative of deregulated NCT correlated with ATXN3 nuclear clearance rather than nuclear accumulation in Q84 neurons. In addition, we observed a highly correlated linear relationship between nuclear Ran and endogenous nuclear ATXN3 levels in WT neurons.

Together, these data suggest several intriguing possibilities. First, both wildtype and mutATXN3 may interact directly with Ran or its many binding partners to regulate Ran levels, stability, or subcellular localization. Close interactions between ATXN3 and Ran are supported by a previous study showing that ATXN3 nuclear import can largely be prevented by knocking down karyopherin-α3 (KPNA3) or by mutating Ran so that it is stuck in the Ran-GTP state, suggesting that KPNA3 and Ran together regulate ATXN3 import[35]. Secondly, our unexpected finding of absence of nuclear ATXN3 in Q84 neurons that exhibit severely abnormal Ran distribution could reflect an alternative pathway in SCA3 for the removal of toxic nuclear mutATXN3, such as nucleophagy. Nucleophagy is an alternative non-canonical degradation pathway in which nuclear waste is packaged into nuclear membrane-bound vesicles that pinch off from the nucleus for autophagic degradation in the cytoplasm. Evidence for nucleophagy has been found in animal and cell models of the polyQ disease Dentatorubral–pallidoluysian atrophy (DRPLA)[36]. The presence of normally nuclear membrane-bound proteins within cytoplasmic puncta of Q84 mice supports this possibility. Future investigations using real-time monitoring of the subcellular localization of mutATXN3, Ran, and other nuclear membrane proteins in cell models of SCA3 could shed light on whether nucleophagy is a protective mechanism for removing nuclear mutATXN3 in SCA3

Nucleophagy is not the only potential explanation for the formation of cytoplasmic puncta enriched in key NCT proteins (i.e. Ran, RanGAP1, and NUPs) in SCA3 mice. Other intriguing possibilities are suggested by recent literature on neurodegenerative diseases that share disease features with SCA3. In two recent HD studies, RanGAP1

and several NUPs selectively localized to intranuclear and perinuclear polyQ-expanded HTT aggregates in *in vitro* and *in vivo* models of HD, as well as in post-mortem HD brains[13,22]. In studies described here, RanGAP1 and FG-NUPs did not appear to preferentially localize within nuclei of Q84 neurons in which small ATXN3 nuclear aggregates had accumulated. Instead, the cytoplasmic puncta containing NCT components that we observed in Q135 and Q84 neurons more closely resemble a phenotype recently described in ALS/FTD model systems[21]. Specifically, expressing mutant TDP-43 or hexanucleotide-expanded C9orf72 protein, or applying specific stressors to human neurons, induced the formation of cytoplasmic stress granules that sequestered key NCT proteins including nuclear transport receptors, Ran, and several NUPs[29]. Stress granule formation has not been previously described in SCA3 model systems. However, ATXN3 directly interacts with stress granule proteins such as ATXN2, and stress granules are a shared feature of several neurodegenerative diseases including two other polyQ diseases, SCA2 and HD[37,38]. Though further studies are required to determine the identity and biological significance of the NCT-enriched cytoplasmic puncta observed here, stress granule assembly and the sequestration of key NCT proteins represent intriguing, unexplored potential disease pathways in SCA3.

Together, these findings point to multiple disruptions in the NCT pathway and nuclear integrity in SCA3 model systems. NCT perturbations observed in Q84 mice may drive nuclear mutATXN3 accumulation and/or be partially caused by mutATXN3-dependent pathogenic processes. Furthermore, proper function of NCT is essential for maintenance of cellular homeostasis, adaptation to cellular stress, and neuronal survival. Thus, the disruptions to NCT described here may contribute to neuronal dysfunction and cell loss in SCA3. In conclusion, we have established that NCT is broadly impaired by expression of mutATXN3. Future investigations are required to understand how and why NCT is deregulated in SCA3, and to determine whether improving NCT may be a viable therapeutic approach to mitigate disease in SCA3.

5.5 Materials and Methods

5.5.1 Cell lines

HEK293 stably expressing cell lines were grown in DMEM supplemented with 10% FBS, 2 mM glutamine and 1% penicillin/streptomycin. Derivation of stably expressing FLAG-ATXN3-Q80 FLAG-FRT 293 cells was previously described[39].

5.5.2 Animals

All animal procedures were approved by the University of Michigan Institutional Animal Care and Use Committee and conducted in accordance with the United States Public Health Service's Policy on Humane Care and Use of Laboratory Animals. Genotyping was performed using tail biopsy DNA isolated prior to weaning and confirmed post mortem, as previously described[28]. Fragment analysis was used to assess the human *ATXN3* repeat expansions (Laragen, San Diego, CA), with only homozygous YACQ84.2 mice expressing human ATXN3 repeat expansions of Q75 or greater included in immunohistochemical and biochemical studies. Animals were sex-, littermate- and age-matched for each study. For biochemical and histological analysis, animals were euthanized at 16 weeks of age after either ASO or PBS vehicle treatment at 8 weeks, and tissue macro-dissected for histology and biochemical assessments, as previously described[28]. All treatment groups were blinded to the experimenter prior to analysis.

5.5.3 Stereotaxic mouse ICV ASO delivery

The anti-*ATXN3* candidate ASO (ASO-5; GCATCTTTTCATTACTGGC) used in this study was previously described[27,28]. Specifically, the anti-*ATXN3* ASO used here targets the 3'UTR of both human and mouse ATXN3. It has a gapmer design[40] with eight unmodified deoxynucleotides with native sugar-phosphate backbone flanked on both sides by five 2'-O-methoxyethylribose modified ribonucleotides with phosphorothioate backbones. Oligonucleotides were synthesized as previously described[41,42] and solubilized in PBS (without Ca2+ or Mg2+). Stereotaxic administration of 700 µg ASO or PBS vehicle into the right lateral ventricle via ICV bolus injection was performed as previously described[27,28]. Following surgery, weight, grooming activity and home cage activity was recorded for up to ten days.

5.5.4 Immunoblotting.

Protein lysates from macro-dissected brainstem and cerebellar tissue were processed as previously described[28] and stored at -80°C. 40 µg total mouse brainstem protein lysate were resolved in 4-20% gradient sodium dodecyl sulfate-polyacrylamide (SDS) electrophoresis gels and transferred to 0.45 µm nitrocellulose membranes. Membranes were incubated overnight at 4°C with various antibodies: mouse anti-ATXN3 (1H9) (1:1000, MAB5360; Millipore, Billerica, MA) and mouse anti-GAPDH (1:5000, MAB374; Millipore, Billerica, MA). Bound primary antibodies were visualized by incubation with peroxidase-conjugated anti-mouse or anti-rabbit secondary antibody (1:10000; Jackson Immuno Research Laboratories, West Grove, PA) followed by treatment with the ECL-plus reagent (Western Lighting; PerkinElmer, Waltham, MA) and exposure to autoradiography films. Band intensities were quantified using ImageJ analysis software (NIH, Bethesda, MD).

5.5.5 Immunocytochemistry, immunohistochemistry, and image analysis

Cells were cultured on Poly-D-Lysine/Matrigel-coated coverslips. Cells were washed with cold PBS and then fixed with 4% paraformaldehyde (PFA) solution for 15 min on ice. Cells were permeabilized with 0.1% Triton X-100 for 5 min at room temperature then blocked in a 5% Normal Goat Serum solution for 1 hr at room temperature. Cells were blocked in primary antibodies overnight at 4°C. Whole brains perfused with PBS were processed as previously described[28]. Primary antibodies assessed include: mouse anti-ATXN3 (1H9) (1:1000, MAB5360; Millipore, Billerica, MA), rabbit anti-NeuN-488 conjugated (1:1000, ABN78A4; Millipore, Billerica, MA), mouse anti-Ran (1:1000, 610340; BD Biosciences, San Jose, CA), rabbit anti-RanGAP1 (1:2000, AB92360; Abcam), rabbit anti-gamma H2A.X (phospho S139) (1:1000, Ab11174; Abcam), mouse anti-p21 (1:1000, sc-6246; Santa Cruz Biotechnology, Santa Cruz, CA), rabbit anti-phospho-53BP1 (Ser1778) (1:1000, 2675; Cell Signaling Technology, Danvers, MA), rabbit anti-PNK (1:1000, Ab17094; Abcam) and mouse anti-NPC[mAb414] (1:1000, AB24609; Abcam). Imaging was performed using an IX71 Olympus inverted microscope (Melville, NY) or Nikon-A1 confocal microscope (Melville, NY) in the basilar pontine nuclei (denoted as pons) and deep cerebellar nuclei (DCN). Nuclear ATXN3 accumulation was quantified as previously described[27,28]. Nuclear

roundness quantification was performed on NeuN-positive neurons using ImageJ analysis.

5.5.6 Statistics.

All statistical analyses were performed using Prism (7.0; GraphPad Software, La Jolla, CA). Variability about the mean is expressed as mean ± standard error of the mean. Quantified data represent the findings of three or more independent experiments or mice. The statistical tests used are described in each figure legend. All error bars indicate variability about the mean expressed as standard error of the mean (SEM). All tests set the level of significance at $p < 0.05$.

5.6 Acknowledgements and Author Contributions

We thank Ionis Pharmaceuticals for generating and providing the anti-***ATXN3*** ASO. This work was supported in part by the SCA3 Ataxia Research Fund provided in part by the SCA Network and NIH grant funding (R01-NS038712 to PI H.L.P.). Dr. Hayley McLoughlin and other members of the Paulson lab contributed to mouse ASO injections, harvesting, and processing of mouse biological tissue.

5.7 References

1 Durr, A. *et al.* Spinocerebellar ataxia 3 and Machado-Joseph disease: clinical, molecular, and neuropathological features. *Annals of neurology* **39**, 490-499, doi:10.1002/ana.410390411 (1996).

2 Paulson, H. L. *et al.* Intranuclear inclusions of expanded polyglutamine protein in spinocerebellar ataxia type 3. *Neuron* **19**, 333-344 (1997).

3 Costa Mdo, C. & Paulson, H. L. Toward understanding Machado-Joseph disease. *Progress in neurobiology* **97**, 239-257, doi:10.1016/j.pneurobio.2011.11.006 (2012).

4 Burnett, B., Li, F. & Pittman, R. N. The polyglutamine neurodegenerative protein ataxin-3 binds polyubiquitylated proteins and has ubiquitin protease activity. *Human molecular genetics* **12**, 3195-3205, doi:10.1093/hmg/ddg344 (2003).

5 Bichelmeier, U. *et al.* Nuclear localization of ataxin-3 is required for the manifestation of symptoms in SCA3: in vivo evidence. *The Journal of neuroscience : the official journal of the Society for Neuroscience* **27**, 7418-7428, doi:10.1523/jneurosci.4540-06.2007 (2007).

6 Kodiha, M. & Stochaj, U. Nuclear transport: a switch for the oxidative stress-signaling circuit? *Journal of signal transduction* **2012**, 208650, doi:10.1155/2012/208650 (2012).

7 Ogawa, Y. & Imamoto, N. Nuclear transport adapts to varying heat stress in a multistep mechanism. *The Journal of cell biology* **217**, 2341-2352, doi:10.1083/jcb.201712042 (2018).

8 Beck, M. & Hurt, E. The nuclear pore complex: understanding its function through structural insight. *Nature reviews. Molecular cell biology* **18**, 73-89, doi:10.1038/nrm.2016.147 (2017).

9 Izaurralde, E. & Adam, S. Transport of macromolecules between the nucleus and the cytoplasm. *RNA (New York, N.Y.)* **4**, 351-364 (1998).

10 Cole, C. N. & Hammell, C. M. Nucleocytoplasmic transport: driving and directing transport. *Current biology : CB* **8**, R368-372 (1998).
11 Ribbeck, K., Lipowsky, G., Kent, H. M., Stewart, M. & Gorlich, D. NTF2 mediates nuclear import of Ran. *The EMBO journal* **17**, 6587-6598, doi:10.1093/emboj/17.22.6587 (1998).
12 Chapple, J. P., Bros-Facer, V., Butler, R. & Gallo, J. M. Focal distortion of the nuclear envelope by huntingtin aggregates revealed by lamin immunostaining. *Neuroscience letters* **447**, 172-174, doi:10.1016/j.neulet.2008.09.075 (2008).
13 Grima, J. C. *et al.* Mutant Huntingtin Disrupts the Nuclear Pore Complex. *Neuron* **94**, 93-107 e106, doi:10.1016/j.neuron.2017.03.023 (2017).
14 Loureiro, J. R., Oliveira, C. L. & Silveira, I. Unstable repeat expansions in neurodegenerative diseases: nucleocytoplasmic transport emerges on the scene. *Neurobiology of aging* **39**, 174-183, doi:10.1016/j.neurobiolaging.2015.12.007 (2016).
15 Zhang, K., Grima, J. C., Rothstein, J. D. & Lloyd, T. E. Nucleocytoplasmic transport in C9orf72-mediated ALS/FTD. *Nucleus (Austin, Tex.)* **7**, 132-137, doi:10.1080/19491034.2016.1172152 (2016).
16 Paonessa, F. *et al.* Microtubules Deform the Nuclear Membrane and Disrupt Nucleocytoplasmic Transport in Tau-Mediated Frontotemporal Dementia. *Cell reports* **26**, 582-593 e585, doi:10.1016/j.celrep.2018.12.085 (2019).
17 Eftekharzadeh, B. *et al.* Tau Protein Disrupts Nucleocytoplasmic Transport in Alzheimer's Disease. *Neuron* **99**, 925-940 e927, doi:10.1016/j.neuron.2018.07.039 (2018).
18 Chou, C. C. *et al.* TDP-43 pathology disrupts nuclear pore complexes and nucleocytoplasmic transport in ALS/FTD. *Nature neuroscience* **21**, 228-239, doi:10.1038/s41593-017-0047-3 (2018).
19 Fahrenkrog, B. & Harel, A. Perturbations in Traffic: Aberrant Nucleocytoplasmic Transport at the Heart of Neurodegeneration. *Cells* **7**, doi:10.3390/cells7120232 (2018).
20 Ferreira, P. A. The coming-of-age of nucleocytoplasmic transport in motor neuron disease and neurodegeneration. *Cellular and molecular life sciences : CMLS*, doi:10.1007/s00018-019-03029-0 (2019).
21 Zhang, K. *et al.* Stress Granule Assembly Disrupts Nucleocytoplasmic Transport. *Cell* **173**, 958-971 e917, doi:10.1016/j.cell.2018.03.025 (2018).
22 Gasset-Rosa, F. *et al.* Polyglutamine-Expanded Huntingtin Exacerbates Age-Related Disruption of Nuclear Integrity and Nucleocytoplasmic Transport. *Neuron* **94**, 48-57 e44, doi:10.1016/j.neuron.2017.03.027 (2017).
23 Zhang, K. *et al.* The C9orf72 repeat expansion disrupts nucleocytoplasmic transport. *Nature* **525**, 56-61, doi:10.1038/nature14973 (2015).
24 Silva-Fernandes, A. *et al.* Motor uncoordination and neuropathology in a transgenic mouse model of Machado-Joseph disease lacking intranuclear inclusions and ataxin-3 cleavage products. *Neurobiology of disease* **40**, 163-176, doi:10.1016/j.nbd.2010.05.021 (2010).
25 Cemal, C. K. *et al.* YAC transgenic mice carrying pathological alleles of the MJD1 locus exhibit a mild and slowly progressive cerebellar deficit. *Human molecular genetics* **11**, 1075-1094 (2002).
26 Costa Mdo, C. *et al.* Toward RNAi therapy for the polyglutamine disease Machado-Joseph disease. *Molecular therapy : the journal of the American Society of Gene Therapy* **21**, 1898-1908, doi:10.1038/mt.2013.144 (2013).
27 McLoughlin, H. S. *et al.* Oligonucleotide therapy mitigates disease in spinocerebellar ataxia type 3 mice. *Annals of neurology* **84**, 64-77, doi:10.1002/ana.25264 (2018).

28 Moore, L. R. *et al.* Evaluation of Antisense Oligonucleotides Targeting ATXN3 in SCA3 Mouse Models. *Molecular therapy. Nucleic acids* **7**, 200-210, doi:10.1016/j.omtn.2017.04.005 (2017).
29 Chew, J. *et al.* Aberrant deposition of stress granule-resident proteins linked to C9orf72-associated TDP-43 proteinopathy. *Molecular neurodegeneration* **14**, 9, doi:10.1186/s13024-019-0310-z (2019).
30 Gasset-Rosa, F. *et al.* Cytoplasmic TDP-43 De-mixing Independent of Stress Granules Drives Inhibition of Nuclear Import, Loss of Nuclear TDP-43, and Cell Death. *Neuron* **102**, 339-357 e337, doi:10.1016/j.neuron.2019.02.038 (2019).
31 Onischenko, E. *et al.* Natively Unfolded FG Repeats Stabilize the Structure of the Nuclear Pore Complex. *Cell* **171**, 904-917 e919, doi:10.1016/j.cell.2017.09.033 (2017).
32 Liu, H. *et al.* The Machado-Joseph Disease Deubiquitinase Ataxin-3 Regulates the Stability and Apoptotic Function of p53. *PLoS biology* **14**, e2000733, doi:10.1371/journal.pbio.2000733 (2016).
33 Gao, R. *et al.* Inactivation of PNKP by mutant ATXN3 triggers apoptosis by activating the DNA damage-response pathway in SCA3. *PLoS genetics* **11**, e1004834, doi:10.1371/journal.pgen.1004834 (2015).
34 Chatterjee, A. *et al.* The role of the mammalian DNA end-processing enzyme polynucleotide kinase 3'-phosphatase in spinocerebellar ataxia type 3 pathogenesis. *PLoS genetics* **11**, e1004749, doi:10.1371/journal.pgen.1004749 (2015).
35 Sowa, A. S. *et al.* Karyopherin alpha-3 is a key protein in the pathogenesis of spinocerebellar ataxia type 3 controlling the nuclear localization of ataxin-3. *Proceedings of the National Academy of Sciences of the United States of America* **115**, E2624-E2633, doi:10.1073/pnas.1716071115 (2018).
36 Baron, O. *et al.* Stall in Canonical Autophagy-Lysosome Pathways Prompts Nucleophagy-Based Nuclear Breakdown in Neurodegeneration. *Current biology : CB* **27**, 3626-3642 e3626, doi:10.1016/j.cub.2017.10.054 (2017).
37 Mahboubi, H. & Stochaj, U. Cytoplasmic stress granules: Dynamic modulators of cell signaling and disease. *Biochimica et biophysica acta. Molecular basis of disease* **1863**, 884-895, doi:10.1016/j.bbadis.2016.12.022 (2017).
38 Nobrega, C. *et al.* Re-establishing ataxin-2 downregulates translation of mutant ataxin-3 and alleviates Machado-Joseph disease. *Brain : a journal of neurology* **138**, 3537-3554, doi:10.1093/brain/awv298 (2015).
39 Winborn, B. J. *et al.* The deubiquitinating enzyme ataxin-3, a polyglutamine disease protein, edits Lys63 linkages in mixed linkage ubiquitin chains. *The Journal of biological chemistry* **283**, 26436-26443, doi:10.1074/jbc.M803692200 (2008).
40 Bennett, C. F. & Swayze, E. E. RNA targeting therapeutics: molecular mechanisms of antisense oligonucleotides as a therapeutic platform. *Annu Rev Pharmacol Toxicol* **50**, 259-293, doi:10.1146/annurev.pharmtox.010909.105654 (2010).
41 Cheruvallath, Z. S., Kumar, R. K., Rentel, C., Cole, D. L. & Ravikumar, V. T. Solid phase synthesis of phosphorothioate oligonucleotides utilizing diethyldithiocarbonate disulfide (DDD) as an efficient sulfur transfer reagent. *Nucleosides, nucleotides & nucleic acids* **22**, 461-468, doi:10.1081/NCN-120022050 (2003).
42 McKay, R. A. *et al.* Characterization of a potent and specific class of antisense oligonucleotide inhibitor of human protein kinase C-alpha expression. *The Journal of biological chemistry* **274**, 1715-1722 (1999).

5.8 Figures

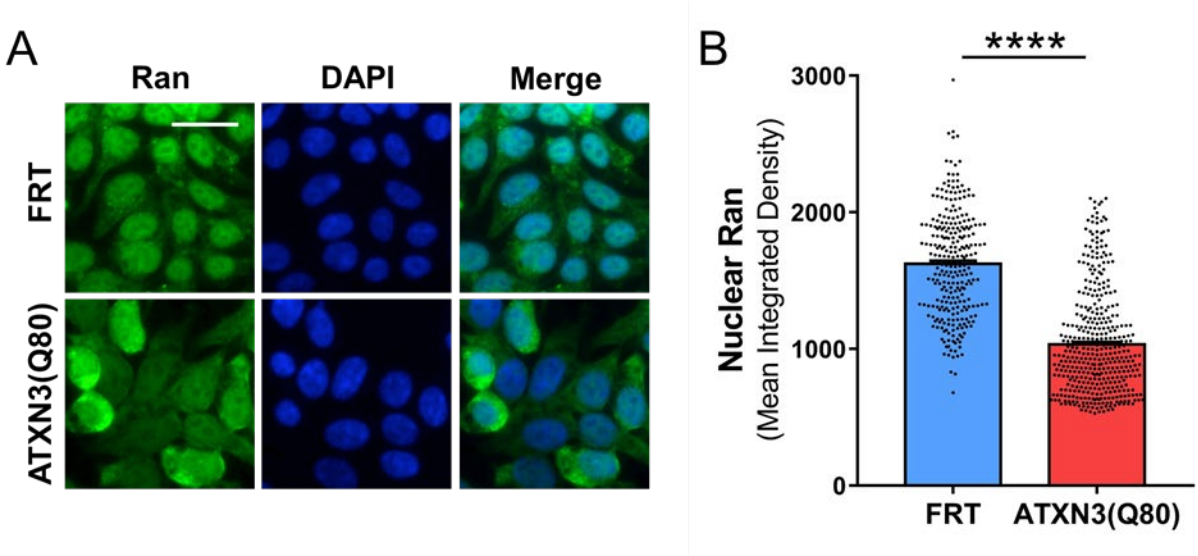

Figure 5.1 Perturbations to Ran GTPase distribution in HEK293 cells stably expressing mutant expanded ATXN3. (A) Anti-Ran immunocytochemistry with DAPI stain of HEK293 cells stably expressing FLAG-tagged FLP recombinase target (FRT) and FLAG-tagged human polyglutamine-expanded ATXN3 with 80 *CAG* repeats [ATXN3(Q80)]. (B) Quantification of nuclear Ran integrated density in FRT versus ATXN3(Q80) stably expressing HEK293 cells. Scatter plot of individual cell intensities with means shown (n = 278-410 cells from 3 experimental replicates). Unpaired two-tailed t test (****p<0.0001). Scale bar = 20 μm.

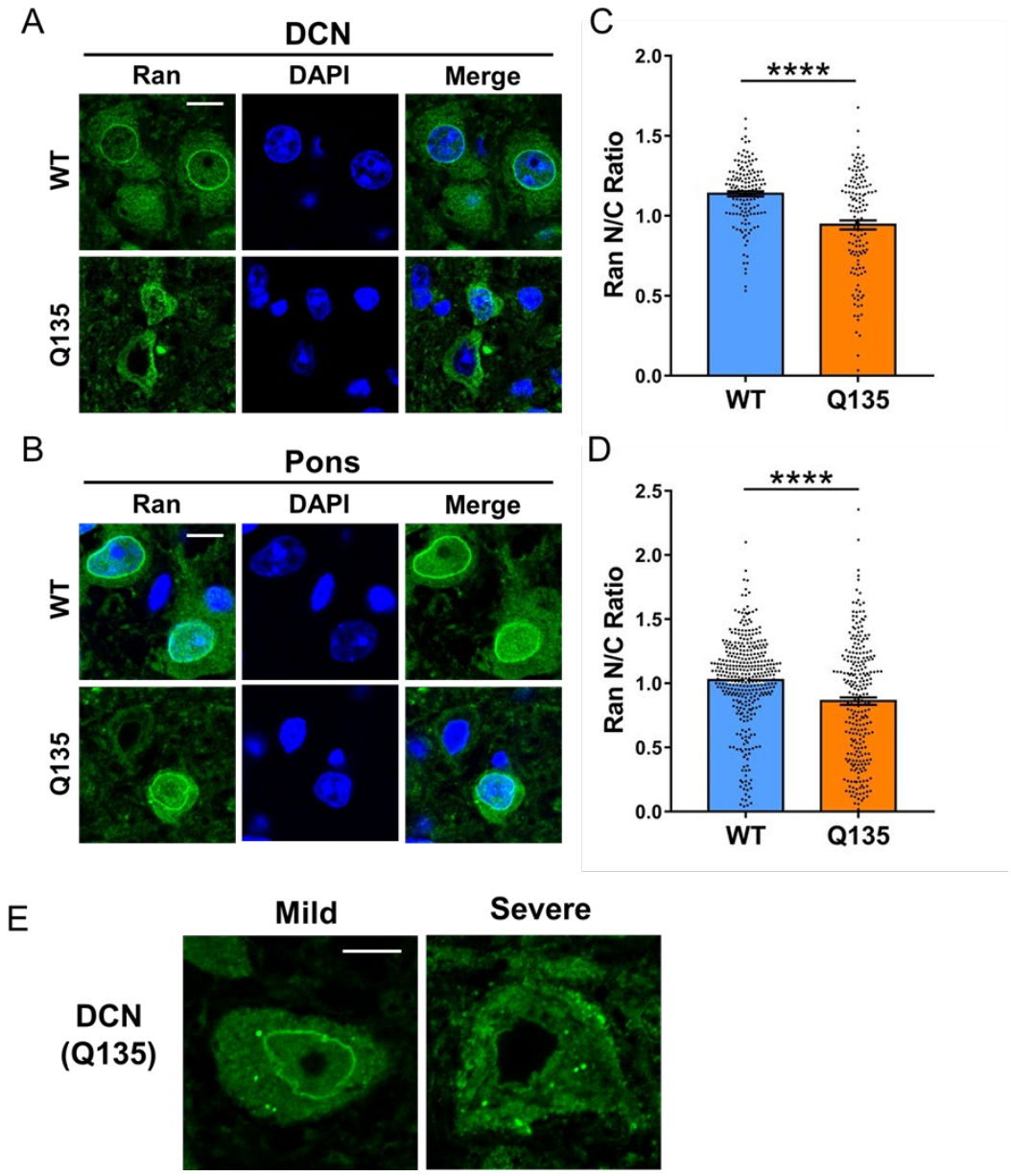

Figure 5.2. Decreased Ran nuclear/cytoplasmic distribution in hemizygous Q135 SCA3 transgenic mice. (A) NeuN-positive deep cerebellar nuclei (DCN) and (B) pontine gray (pons) neurons from 16-wk-old wild type (WT) and hemizygous Q135 SCA3 transgenic co-stained for Ran (green) and DAPI (blue). (C) Ratio of nuclear/cytoplasmic (N/C) Ran integrated densities quantified from DCN and (D) pontine neurons in WT and Q135 mice. Scatter plot of individual neuron ratios with means shown (n = 132-144 DCN neurons; 258-362 pontine neurons from 4 mice per genotype). Unpaired two-tailed t test (****p<0.0001). (E) Examples of mild and severe Ran phenotypes in Q135 DCN neurons. Scale bars = 10 μm.

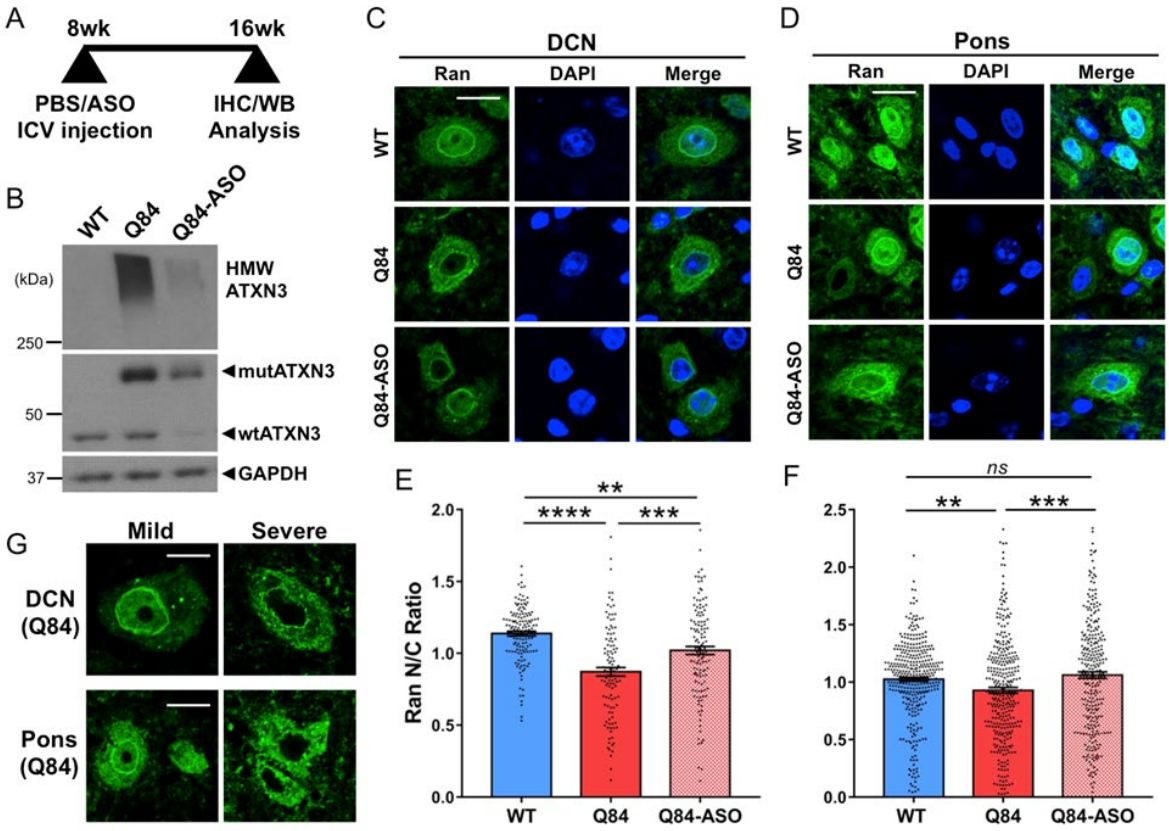

Figure 5.3. ASO-mediated reduction of ATXN3 partially rescues abnormal Ran distribution in homozygous Q84 SCA3 transgenic mice (A) Wild type (WT) and homozygous Q84 mice received a unilateral intracerebroventricular (ICV) injection of PBS vehicle or 700 µg anti-*ATXN3* antisense oligonucleotide (ASO) at 8 weeks of age. Mice were sacrificed at 16 weeks for immunohistochemical (IHC) and western blot (WB) analysis. (B) Representative anti-ATXN3 WB showing ASO-mediated knockdown of mutant ATXN3 (mutATXN3) and high molecular weight (HMW) ATXN3 species in brainstem lysates from ASO-treated Q84 mice (Q84-ASO) at 16wks. (C) Anti-Ran IHC with DAPI co-stain images of NeuN-positive deep cerebellar nuclei (DCN) neurons and (D) pontine gray (pons) neurons from treated WT, Q84, and Q84-ASO mice. (E) Ratio of nuclear/cytoplasmic (N/C) Ran integrated densities quantified from DCN and (F) pontine neurons in WT, Q84, and Q84-ASO mice. (G) Examples of mild and severe Ran distribution phenotypes in Q84 DCN and pontine neurons. Scatter plot of individual neuron ratios with means shown (n = 115-144 DCN neurons; 283-362 pontine neurons from 4 mice per genotype). One-way ANOVA performed with the post-hoc Tukey test. (**p<0.01, ***p<0.001, ****p<0.0001). (wtATXN3 = wild type ATXN3; GAPDH = glyceraldehyde-3-phosphate dehydrogenase; ns = not significant). Scale bars = 20 µm (C,D), 10 µm (G)

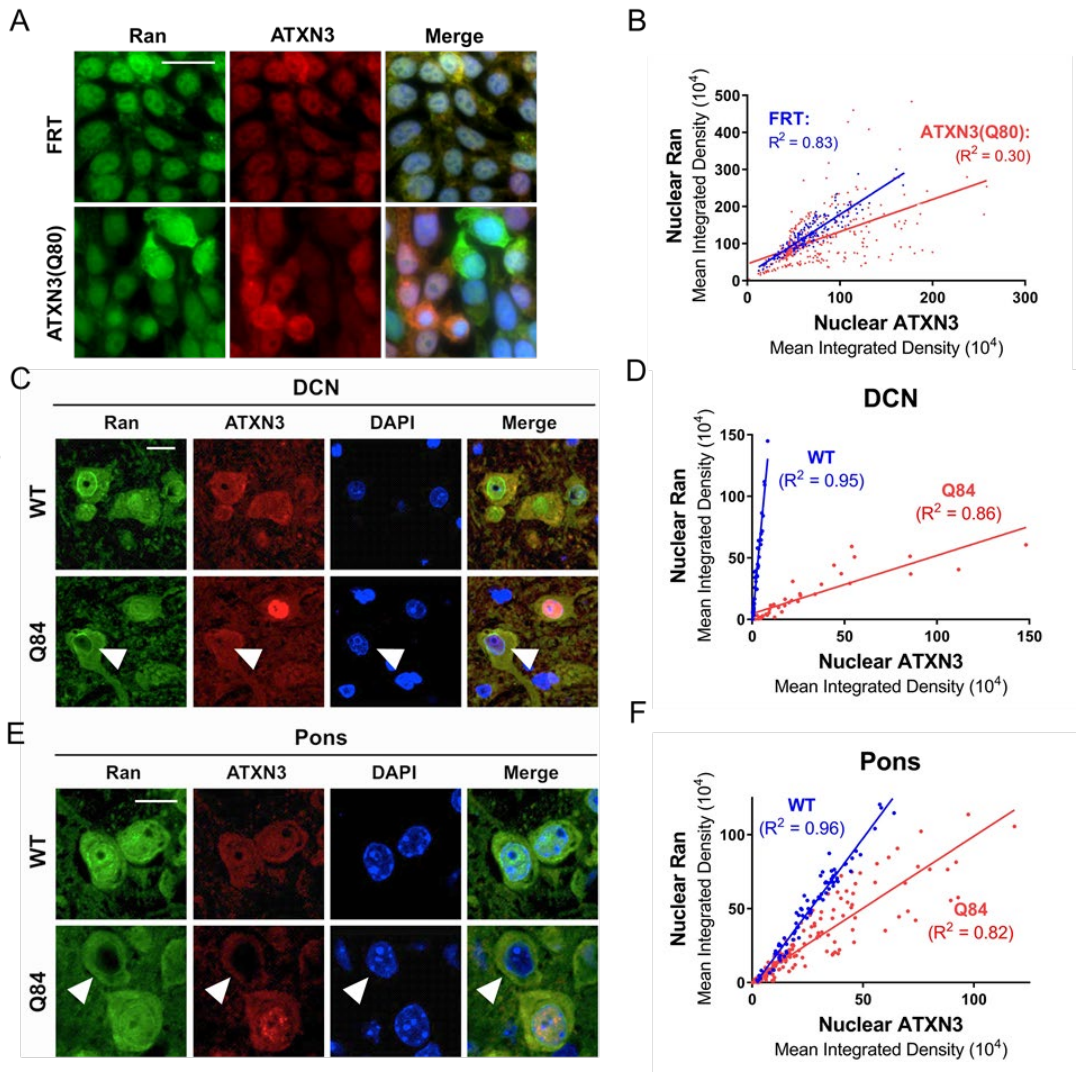

Figure 5.4. Nuclear localization of ATXN3 and Ran GTPase are normally and pathologically correlated. (A) Ran (green) and ATXN3 (red) immunocytochemistry with DAPI co-stain in FRT and ATXN3(Q80) HEK293 cells. (B) Scatter plot of nuclear Ran versus nuclear ATXN3 integrated densities of individual FRT (blue) and ATXN3(Q80) (red) cells. Linear regressions and calculated Pearson correlation R^2 values are shown for both lines (n=167-363 cells). (C-F) Nuclear ATXN3 and nuclear Ran mean integrated densities are positively correlated in 16-week-old wildtype (WT) and homozygous Q84 deep cerebellar nuclei (DCN) and pontine neurons. Representative images of anti-Ran (green) and anti-ATXN3 (green) immunolabeled DCN neurons (C) and pontine neurons (E). Scatter plot of nuclear Ran versus nuclear ATXN3 integrated densities of individual WT (blue) and Q84 (red) DCN neurons (D) and pontine neurons (F). Linear regressions and calculated Pearson correlation R^2 values shown in plots (n=38-43 DCN neurons, 86-175 pontine neurons). Scale bars = 20 μm (A,E), 10 μm (C).

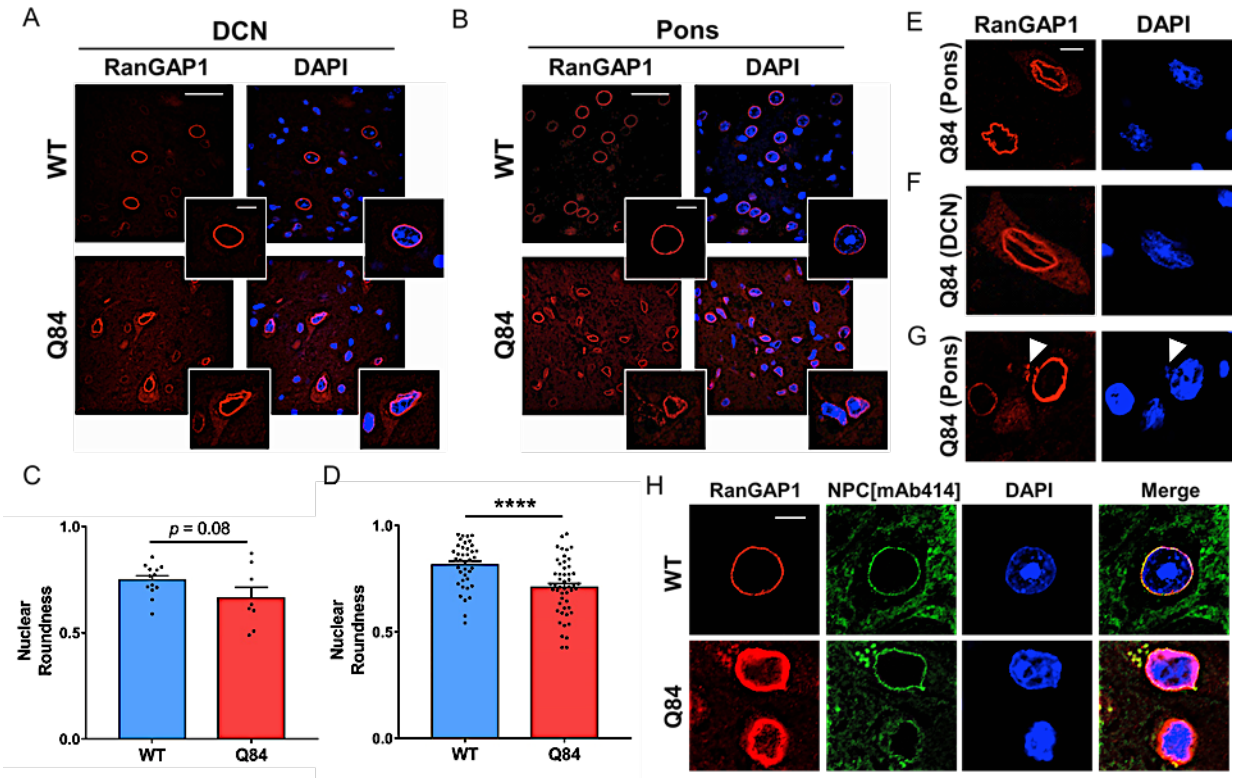

Figure 5.5. Abnormal nuclear shape and formation of cytoplasmic puncta containing key NCT proteins in SCA3 Q84 pontine and DCN neurons. (A) Pontine and (B) deep cerebellar nuclei (DCN) neurons from 16-week-old wild type (WT) and Q84 mice co-stained for RanGAP1 (red) and DAPI (blue). Scale bar = 20 μm, inset scale bar = 10 μm. Calculated nuclear roundness of DCN (C) and pontine neurons (D). (E-G) Examples of RanGAP1 nuclear membrane abnormalities in Q84 pontine neurons, including (E) ruffled nuclear membrane structure, (F) intranuclear projections of the nuclear membrane that co-localize with small punctate heterochromatin, (G) and extranuclear RanGAP1/DAPI cytoplasmic projections (indicated by white arrow head). (H) Anti-RanGAP1 (red) and anti-NPC[mAb414] (green) immunohistochemistry with DAPI co-stain in NeuN-positive pontine neurons of 16-week-old wild type and Q84 mice showing formation of extranuclear punctate structures positive for RanGAP1 and FG-NUPs. Scale bar = 10 μm. Two-tailed t test (****p = 0.0001).

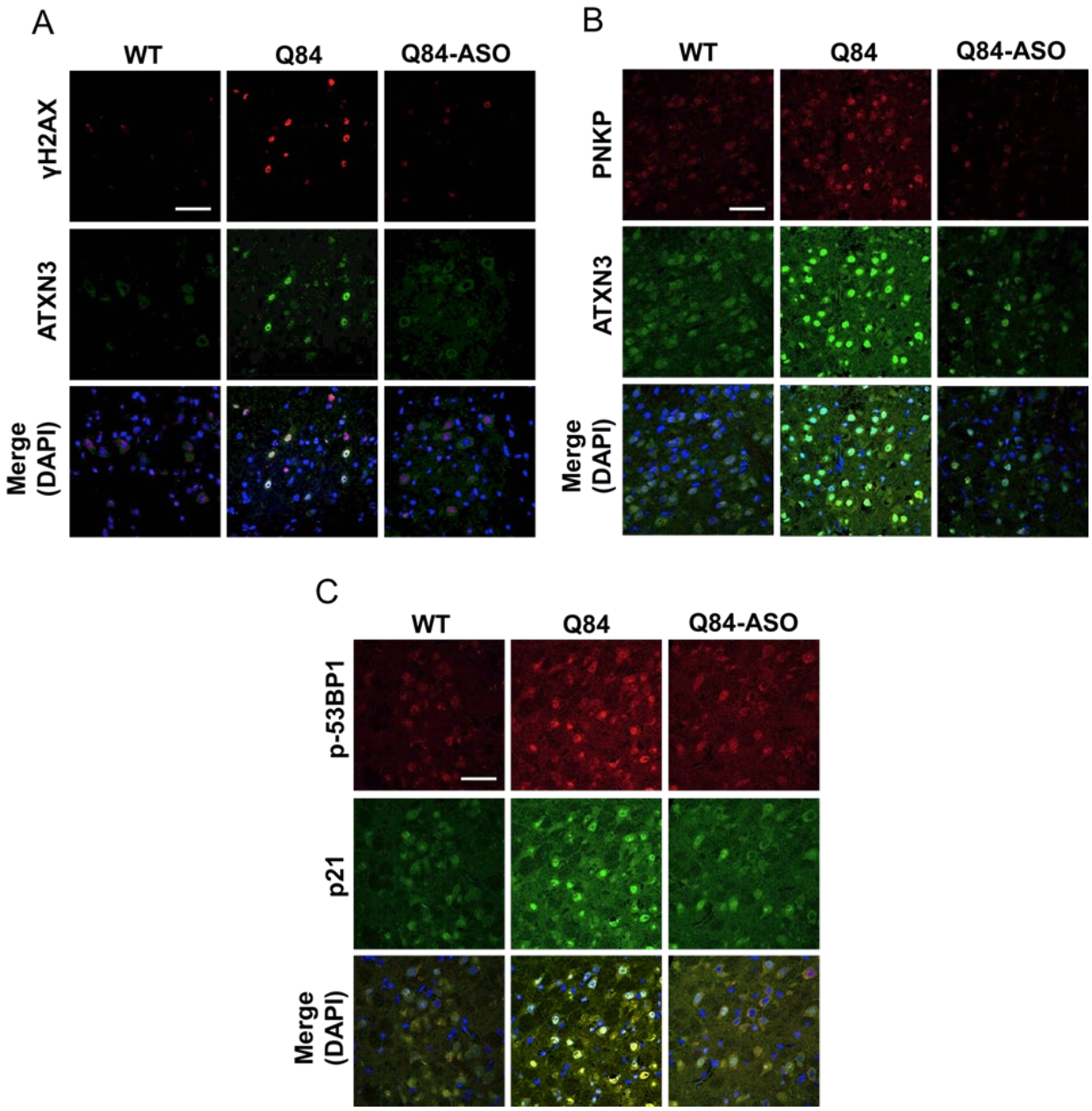

Figure 5.6. Loss of genomic integrity in SCA3 mice is corrected by ASO-mediated knockdown of mutATXN3. Enhanced accumulation of DNA damage markers in 16-week-old Q84 mice is rescued in by anti-*ATXN3* antisense oligonucleotide (ASO) intracerebroventricular injection at 8 weeks. (A-B) Vehicle-treated wildtype (WT), Q84, and ASO-treated Q84 pontine neurons immunolabled for ATXN3 (green) and DNA damage markers phosphorylated histone 2A family member X (γ-H2AX) (A) and polynucleotide kinase phosphatase (PNKP) (B). (C) Increased expression and nuclear localization of p53-target genes phosphorylated p53 binding-protein 1 (p-53BP1) and p21. Scale bars = 50 μm.

CHAPTER 6
Conclusions and Future Directions

6.1 Abstract

The results presented in this dissertation provide support for three main conclusions. First, broad CNS delivery of an anti-*ATXN3* ASO is well tolerated by SCA3 transgenic mice and leads to sustained rescue of neuropathological, motor, and electrophysiological features of disease in Q84/Q84 homozygous mice. Second, the SCA3-hESC line represents a significant novel disease model for the SCA3 field due to its ability to replicate human disease features and its potential to differentiate into disease-relevant human neurons and non-neuronal populations. And finally, in what has become a recurrent theme in neurodegenerative diseases, Ran-mediated nuclear trafficking and nuclear integrity are compromised in cellular and mouse models of SCA3 suggesting a new potential mechanism for toxic nuclear localization of mutATXN3 in the SCA3 brain. Together, these findings further support the view that SCA3 is predominantly caused by a toxic-gain-of-function mechanism requiring nuclear accumulation of mutATXN3. Furthermore, additional results presented in Chapter 5 of this thesis expand beyond this current understanding to suggest that general impairments in neuronal NCT may play an important, yet unappreciated role in driving mutATXN3 nuclear sequestration that inevitably leads to neuronal dysfunction and loss. Nevertheless, there is still much to be learned about ATXN3's function and dysfunction in normal and pathological nuclear states, and about the causes of NCT impairments and if/how they contribute to toxicity in SCA3. There is also still little established evidence to explain why certain neurons are selectively vulnerable to mutATXN3-dependent dysfunction and death. The compelling therapeutic and disease modeling tools developed and presented in this dissertation could provide future opportunities to better understand SCA3 pathogenesis, and most importantly, move the field closer to the ultimate goal of safe and effective disease-modifying therapies for SCA3 patients.

6.2 Moving ASO therapy into clinical trials for SCA3

As presented in Chapters 2 and 3 of the dissertation, the strong safety profile and positive efficacy data from my completed preclinical assessments of anti-*ATXN3* ASO candidates strongly support continued development of ASOs for SCA3 therapy[1,2]. On top of my findings, overwhelmingly positive outcomes reported from completed or ongoing ASO clinical trials for SMA[3-6] and HD[7,8] have led many to anticipate clinical trials of oligonucleotide-based therapies for multiple monogenic neurodegenerative disorders, including SCA3, in the near future. Indeed, the anti-*ATXN3* ASO safety and efficacy preclinical results presented in Chapters 2 and 3 of this dissertation closely mirror those of the murine anti-*HTT* ASO preclinical HD studies published in 2012 that inevitably led to a Phase 1 ASO HD trial which began in August 2015 (NCT02519036)[8].

But several substantial obstacles remain before a potential candidate ASO can advance to human clinical trials for SCA3, the most significant being the lack of sensitive biomarkers for SCA3. As a slowly progressing disease, accurate and timely assessment of any potential disease-modifying therapy will likely require a multi-arm approach that is capable of detecting sensitive molecular and physiological changes that correlate with disease progression and severity in SCA3 patients. The Scale for the Assessment and Rating of Ataxia (SARA) is the most commonly used method to track disease progression in SCA3 patients[9]. It can be performed quickly in the clinic by a trained neurologist and results in an assigned SARA score representative of broad severity of ataxia-related symptoms[9]. However, previous studies have shown that SCA3 patients exhibit an average increase of only 1-2 points in SARA scores per year[10]; Thus, SARA scoring alone would likely not be sensitive enough to detect mild to moderate slowing of disease progression or even an improvement in ataxia symptoms following treatment with a candidate drug within the timescale of early phase clinical trials. Thankfully, published studies that preceded SMA and HD ASO clinical trials provide a blueprint for preclinical biomarker development that still needs to be done in preparation for an ASO clinical trial for SCA3. I will focus here on developed HD biomarkers, as HD disease mechanisms and the anti-*HTT* ASO therapeutic approach being employed in clinical trials closely aligns with those of SCA3.

Arguably the most important biological measurement that enabled the relatively rapid transition of a promising ASO candidate from HD animal models into patients was the ability to detect differences in the concentration of mutant HTT protein in patient cerebrospinal fluid (CSF)[11]. Prior to 2015, there were no available tools capable of measuring the femtomolar concentrations of soluble mutant HTT present in HD patient CSF[11]. The technique that finally enabled adequately sensitive measurements of CSF HTT utilized a single molecule counting (SMC) immunoassay that captured allele-specific mutant HTT protein using a combination of two antibodies: a non-allele specific HTT antibody and the 1C2 antibody that binds to expanded polyQ-repeats[12]. Using variations of this technology, preclinical studies have demonstrated that premanifest and symptomatic HD patients could be distinguished by their CSF concentration of mutant HTT, and importantly that mutant HTT CSF concentration positively correlates with HD clinical severity in longitudinal HD animal and patient CSF studies[12-14].

These key preclinical studies led to the phase 1b/2a clinical trial (NCT02519036) to assess the safety and tolerability of intrathecal delivered anti-*HTT* ASO into HD patients. Though the primary aim of this recently completed study was to evaluate ASO tolerability at effective doses, several outcome measures aimed at investigating ASO clinical efficacy and target-engagement in patients were also included. Two traditional HD biomarker and clinical assessments were included (ventricular volume and Huntington's disease cognitive assessment battery composite score), but for the first time longitudinal CSF HTT protein concentrations assessed before and after treatment were included in patient evaluation. As mutant HTT is both the target of ASO therapy and a correlative measure of disease severity, ASO-mediated decrease in CSF mutant HTT levels detected within a relatively short treatment window enabled this ASO to rapidly progress into ongoing phase 2 and 3 clinical trials.

Significant efforts are currently underway by clinical ataxia researchers and physicians, both in the United States and abroad, that aim to achieve a similar state of clinical trial readiness as the HD field achieved prior to the start of HD ASO clinical trials. Of particular importance is the Clinical Trial Readiness for SCA1 and SCA3 trial (NCT03487367), abbreviated READISCA, which gained NIH approval in 2018 and is currently enrolling patients. READISCA aims to combine cohorts of SCA1 and SCA3

patients in the US and Europe for the largest, multi-approach assessment of disease features in pre-manifest and early symptomatic individuals, including of previously identified magnetic resonance-based biochemical and morphological biomarkers, as well as potential biomarkers in patient blood and CSF. It has yet to be shown that levels of mutATXN3 protein can be detected with high sensitivity in the CSF of persons with SCA3, and if so, whether mutATXN3 protein concentrations significantly correlate with severity of disease. Nevertheless, SCA3 patient natural history and biomarker clinical studies, such as READISCA, are an important and necessary step before the potential promise of ASO therapy can be effectively tested in patients.

6.3 Potential diverse uses of the SCA3-hESC line

Prior to the development of the SCA3-hESC line presented in Chapter 4, there were no NIH-approved hESC models available for SCA3 or any other dominantly inherited ataxias. In addition, there were no identified SCA3 human cell lines that could recapitulate the most well characterized molecular features of SCA3 (i.e. ATXN3 mislocalization and aggregation) without the addition of genetic or environmental stressors[15,16]. The exclusive observation of robust aggregation and aggresome formation in undifferentiated SCA3-hESCs and derived neurons begs the question: What makes this line uniquely capable of replicating key features of the human disease? Perhaps the high division rate and enhanced autophagic activity of pluripotent stem cells contributes to mishandling of mutATXN3 by SCA3-hESCs and increases its aggregation propensity, but the absence of unelicited aggregation in published SCA3 iPSC lines[17-19] suggests that the reasons for the uniquely robust phenotypes in SCA3-hESCs may be more complicated. It is possible that the somatic reprogramming process, incomplete epigenetic reprogramming, or the fact that iPSCs are derived from aged somatic cells could impact mutATXN3 expression, activity, and various disease-relevant pathways in iPSCs. Unfortunately, given that our observations were made in a single SCA3 hESC line, it is impossible to state with certainty that disease-specific hESCs are “better” able to replicate SCA3 human disease processes than iPSCs. This question could be addressed in future studies that directly compare multiple (as yet unavailable) SCA3 hESC lines and SCA3 patient-derived iPSC lines. Without the aid of

these additional studies, we can only speculate as to why disease features that are prominent in the SCA3-hESC line are absent from SCA3 iPSC lines.

As presented in Chapter 4, identification of disease-relevant molecular phenotypes in SCA3-hESC, namely the formation of ATXN3- and p62-positive aggresomes, provided us with an opportunity to confirm that ASO-mediated knockdown of mutATXN3 could rescue disease features in a human cell line expressing endogenous levels of mutATXN3. The robustness of ATXN3 aggregation and p62 aggresome formation observed in SCA3-hESCs makes this line well suited for high-throughput drug or gene modifying screening efforts. The particular phenotypes observed in SCA3-hESCs lend this line to the identification of drugs or genes that improve protein quality control pathways and decrease protein aggregation, enhance degradation of mutATXN3, or alter subcellular localization of mutATXN3. In addition, genetic manipulations of the SCA3-hESC line, such as knocking in a fluorescent tag onto the 3' or 5' end of *ATXN3,* could further improve the utility of the SCA3-hESC line in high-throughput preclinical drug development. For example, knocking in a GFP tag into the *ATXN3* gene could enable the use of automated spectroscopy screens to identify small molecules that reduce total levels of green fluorescently-tagged ATXN3 signal.

The utility of SCA3-hESCs or SCA3-hESC derived neurons in mechanistic disease studies, however, is limited by the fact that this line truly is one of a kind. As the only NIH-approved SCA3 hESC line, it would be difficult to prove that complex molecular differences in SCA3-hESCs or derived cells are uniquely attributable to expression of polyQ-expanded mutATXN3. In the absence of additional SCA3 hESC lines, the ability to delineate mutATXN3-dependent phenotypes could be improved through the derivation of isogenic control hESC lines from SCA3-hESC in which the pathogenic *CAG*-repeat expansion is retracted or removed using CRISPR-mediated homology directed repair approaches. In addition, NIH-approved control hESC lines could be modified by targeted insertion of a pathogenic repeat expansion. Both targeted correction and introduction of polyQ repeat expansions into the endogenous *HTT* gene have been achieved in HD disease-specific iPSCs and hESC lines[10,20]. Taking advantage of these published protocols and continued advancements in precise genetic

engineering approaches should enable the development of multiple SCA3 hESC lines and isogenic control hESC lines for future mechanistic studies.

The characterization of the SCA3-hESC line presented in Chapter 4 of this dissertation is in preparation for publication in the near future. Though the characterization of SCA3-hESC studies and differentiated neurons performed in Chapter 4 did not extend beyond well-established SCA3 molecular phenotypes, completion of these studies was needed in order to confirm the validity of this line as an accurate and relevant model of SCA3 human disease prior to its use in more exploratory, mechanistic studies such as to investigate glial involvement in SCA3 or to explore nucleocytoplasmic transport dysfunction in SCA3-hESC neurons. As an NIH-approved hESC cell line, the SCA3-hESC line is already available for use within any NIH-approved study in the United States. We hope that once our characterization of the line is published, other SCA3 researchers will decide to use this line to supplement mechanistic and translational studies for SCA3.

6.4 Understanding the role of nucleocytoplasmic transport dysfunction in SCA3

Numerous studies have demonstrated that disease features of polyQ diseases, such as aggregation and toxicity, can be modulated by manipulating the nuclear trafficking and subcellular localization of polyQ disease proteins[16,21-24]. But only recently have studies led scientists to recognize that mislocalization of disease proteins in polyQ diseases and other neurodegenerative proteinopathies may indicate a more generalized impairment in nucleocytoplasmic transport (NCT)[25-27]. The work presented in Chapter 5 of this dissertation is the first to show that expression of mutATXN3 is associated with striking changes in the subcellular localization of key proteins involved in nucleocytoplasmic transport in SCA3 cellular and transgenic mouse models. Though these results are novel and build on recent literature associating NCT impairment with neurodegenerative processes, the studies I have completed thus far are mostly descriptive, assessing disease-specific differences at a single time point in model systems. It is also important to note that the disease models tested, including the ATXN3(Q80) HEK293 cell line, and the Q135 and Q84 transgenic mouse models, all express high levels of mutATXN3 protein well above physiological levels. Thus, the

relationship of the observed nuclear trafficking changes in SCA3 models to actual human disease remains to be established.

The obvious next step to determine the broad relevance of NCT dysfunction in SCA3 is to evaluate markers for abnormal NCT (i.e. Ran, RanGAP1, and nucleoporin expression and distribution) in disease-affected brain regions of SCA3 post-mortem brain tissue. These studies are already planned, using fixed SCA3 brain tissue made available through the University of Michigan Brain Bank. If NCT phenotypes, such as Ran cytoplasmic mislocalization and formation of NCT-enriched structures or aggregates, are confirmed in SCA3 post-mortem tissue, it will further support a role for NCT impairment in disease pathogenesis, at least at end-stage disease. Because NCT defects and loss of nuclear structural and genomic integrity are general features of sick, aged, or senescent neurons, their presence in SCA3 atrophic brain tissue still would not answer a central question arising from Chapter 5: Do the observed NCT abnormalities contribute to neuronal dysfunction in SCA3, or are they merely a byproduct of neuronal dysfunction?

One way to begin addressing this question would be to investigate whether abnormal NCT phenotypes arise in early or late stages of the disease process in SCA3 mice. To this end, brains from WT and homozygous Q84/Q84 mice have been collected at several early time points (post-natal days: P0, P3, P7, P21) and at late time points (>1 year). Preliminary IHC and western blot analyses (*data not shown*) demonstrate that ATXN3 nuclear sequestration and accumulation of high molecular weight ATXN3 proteins is apparent by P7, but is not apparent in P3 Q84/Q84 mice. Longitudinal immunohistochemical analysis comparing Ran and ATXN3 expression and subcellular localization in WT versus Q84 homozygous mice at P0, P3, P7 and P21 may answer whether mislocalization of NCT proteins precedes mutATXN3 nuclear sequestration and oligomerization, supporting an early, potentially causal role, or occurs only after nuclear mutATXN3 becomes apparent, suggesting that mutATXN3 expression actually drives Ran mislocalization.

The major Chapter 5 finding that key NCT proteins are mislocalized in SCA3 models suggests, but does not prove, nuclear trafficking deficits in SCA3. Previous literature offers some evidence as to whether nuclear import or nuclear export pathways

play a larger role in modulating mutATXN3 localization, aggregation, and associated toxicity. A study published in 2018 evaluated whether knockdown or over-expression of various importins and exportins affected mutATXN3 aggregation and ATXN3 nuclear localization *in vitro*. This study identified karyopherin-α3 (KPNA3) and to a lesser extent importin-13 (IPO13) as key facilitators of ATXN3 nuclear import, and exportin-1 (aka CRM1) as the key facilitator of ATXN3 nuclear export[28]. Furthermore, knocking down KPNA3 significantly rescued disease features in SCA3 *drosophila* and decreased mutATXN3 aggregation in SCA3 cells, while over-expressing CRM1 only mildly improved disease features in both SCA3 flies and cell model systems, suggesting that enhanced nuclear import of mutATXN3 may play a larger role in disease than diminished export[28,29]. However, these findings haven't been validated in a vertebrate model system nor have studies been performed to assess whether a more generalized dysfunction in nuclear trafficking drives mutATXN3 mislocalization in SCA3.

Ongoing *in vitro* studies aim to determine whether nuclear import, nuclear export, or both are deregulated or inhibited in SCA3 cell lines. Specifically, FRT control, mutant ATXN3(Q80), and wildtype ATXN3(Q22)-expressing HEK293 cells are being transfected with an NES-mCherry-NLS reporter plasmid. This plasmid expresses red fluorescent mCherry protein carrying a strong nuclear export signal and a weak nuclear localization signal. In normal HEK293 cells, the expressed mCherry protein readily traverses the nuclear membrane but predominantly localizes to the cytoplasm. The first aim of ongoing *in vitro* studies is to evaluate whether the N/C distribution of mCherry is altered in the ATXN3(Q80) line, and if so, what is the relationship between mCherry, ATXN3, and Ran distribution in cells. If mCherry predominantly localizes to the nucleus in the ATXN3(Q80) line, it could suggest impairment in nuclear export proteins or enhancement in nuclear import signaling. If no change is observed, I also intend to assess changes in mCherry cellular localization over time following the addition of leptomycin B (LMB) to cell media, followed by washout. LMB is a potent exportin inhibitor that, while present in cell media, transiently enhances mCherry nuclear localization. This study will address whether ATXN3(Q80) expression in HEK293 cells impedes nuclear import (e.g. LMB treatment doesn't enhance nuclear localization of mCherry) or nuclear export (e.g. slower redistribution of mCherry to the cytoplasm

following LMB washout). Pending the results of these studies, I may extend these in vitro experiments to SCA3-hESCs and WT-hESCs and to differentiated neurons, to determine whether nuclear trafficking is impaired in human cells expressing physiological levels of mutATXN3 protein and to define the potential relationship between ATXN3 aggregation and altered nuclear trafficking.

The work presented in this dissertation demonstrates that subcellular localization of Ran is tuned to both expression and subcellular localization of endogenous ATXN3 and mutATXN3 in HEK293 cells and neurons. The positive correlation between nuclear Ran and nuclear ATXN3 levels in both FRT HEK293 cells and WT mice suggests that ATXN3 may play an as yet unidentified function within Ran-mediated NCT pathways. What role might ATNX3 play in Ran-mediated NCT? The localization and activity of proteins within the NCT pathway are primarily co-regulated by ubiquitin and small ubiquitin-like modifier post-translational modifications[17]. ATXN3 can bind both to ubiquitin chains and SUMO modifications, and thus may interact with polyubiquitinated or SUMOylated proteins in the NCT pathway to affect stability or subcellular localization of NCT proteins[30]. Future studies should investigate whether knocking down ATXN3 or expressing polyQ-expanded mutATXN3 alters these key post-translational modifications, expression levels, and subcellular localization of NCT proteins.

6.5 Closing Remarks

There are no effective therapies available for the ~75,000 persons that are affected with SCA3 worldwide. But improvements in our understanding of normal and abnormal functions of the SCA3 disease protein ATXN3, and advances in translational techniques such as the ASO technology used in this dissertation, offer reasons to be hopeful that disease-modifying therapies may be on the horizon for SCA3 patients. On its surface, this dissertation can be separated into distinct sections with distinct goals, namely therapeutic assessment (Chapters 2 and 3), disease model development (Chapter 4), and mechanistic studies of SCA3 pathogenesis (Chapter 5). However, the seemingly distinct studies presented in this dissertation exemplify the synergistic connections between translational and mechanistic studies of disease. For example, ASO development and assessment in Chapters 2 and 3 enabled the validation of mutATXN3-dependent molecular phenotypes in the SCA3-hESC line in Chapter 4.

Furthermore, identification of NCT impairments as a potentially important contributor to neuronal dysfunction in Chapter 5 would not have been possible without the repository of biological material collected in the ASO studies of Chapters 2 and 3. With the still incomplete picture of the critical pathways contributing to neurodegeneration in SCA3, it is imperative that advances in models and therapeutic approaches continue to be combined in order to achieve the ultimate goal: a disease-modifying therapy for SCA3.

6.6 References

1 Moore, L. R. *et al.* Evaluation of Antisense Oligonucleotides Targeting ATXN3 in SCA3 Mouse Models. *Molecular therapy. Nucleic acids* **7**, 200-210, doi:10.1016/j.omtn.2017.04.005 (2017).

2 McLoughlin, H. S. *et al.* Oligonucleotide therapy mitigates disease in spinocerebellar ataxia type 3 mice. *Annals of neurology* **84**, 64-77, doi:10.1002/ana.25264 (2018).

3 Wurster, C. D. *et al.* Intrathecal administration of nusinersen in adolescent and adult SMA type 2 and 3 patients. *Journal of neurology* **266**, 183-194, doi:10.1007/s00415-018-9124-0 (2019).

4 Gidaro, T. & Servais, L. Nusinersen treatment of spinal muscular atrophy: current knowledge and existing gaps. *Developmental medicine and child neurology* **61**, 19-24, doi:10.1111/dmcn.14027 (2019).

5 Wan, L. & Dreyfuss, G. Splicing-Correcting Therapy for SMA. *Cell* **170**, 5, doi:10.1016/j.cell.2017.06.028 (2017).

6 Ottesen, E. W. ISS-N1 makes the First FDA-approved Drug for Spinal Muscular Atrophy. *Translational neuroscience* **8**, 1-6, doi:10.1515/tnsci-2017-0001 (2017).

7 van Roon-Mom, W. M. C., Roos, R. A. C. & de Bot, S. T. Dose-Dependent Lowering of Mutant Huntingtin Using Antisense Oligonucleotides in Huntington Disease Patients. *Nucleic acid therapeutics* **28**, 59-62, doi:10.1089/nat.2018.0720 (2018).

8 Kordasiewicz, H. B. *et al.* Sustained therapeutic reversal of Huntington's disease by transient repression of huntingtin synthesis. *Neuron* **74**, 1031-1044, doi:10.1016/j.neuron.2012.05.009 (2012).

9 Yabe, I., Matsushima, M., Soma, H., Basri, R. & Sasaki, H. Usefulness of the Scale for Assessment and Rating of Ataxia (SARA). *Journal of the neurological sciences* **266**, 164-166, doi:10.1016/j.jns.2007.09.021 (2008).

10 Jacobi, H. *et al.* Long-term disease progression in spinocerebellar ataxia types 1, 2, 3, and 6: a longitudinal cohort study. *The Lancet. Neurology* **14**, 1101-1108, doi:10.1016/s1474-4422(15)00202-1 (2015).

11 Byrne, L. M. & Wild, E. J. Cerebrospinal Fluid Biomarkers for Huntington's Disease. *Journal of Huntington's disease* **5**, 1-13, doi:10.3233/jhd-160196 (2016).

12 Wild, E. J. *et al.* Quantification of mutant huntingtin protein in cerebrospinal fluid from Huntington's disease patients. *The Journal of clinical investigation* **125**, 1979-1986, doi:10.1172/jci80743 (2015).

13 Fodale, V. *et al.* Validation of Ultrasensitive Mutant Huntingtin Detection in Human Cerebrospinal Fluid by Single Molecule Counting Immunoassay. *Journal of Huntington's disease* **6**, 349-361, doi:10.3233/jhd-170269 (2017).
14 Southwell, A. L. *et al.* Ultrasensitive measurement of huntingtin protein in cerebrospinal fluid demonstrates increase with Huntington disease stage and decrease following brain huntingtin suppression. *Scientific reports* **5**, 12166, doi:10.1038/srep12166 (2015).
15 Colomer Gould, V. F. *et al.* A mutant ataxin-3 fragment results from processing at a site N-terminal to amino acid 190 in brain of Machado-Joseph disease-like transgenic mice. *Neurobiology of disease* **27**, 362-369, doi:10.1016/j.nbd.2007.06.005 (2007).
16 Fujigasaki, H. *et al.* Ataxin-3 is translocated into the nucleus for the formation of intranuclear inclusions in normal and Machado-Joseph disease brains. *Experimental neurology* **165**, 248-256, doi:10.1006/exnr.2000.7479 (2000).
17 Rodriguez, J. A. Interplay between nuclear transport and ubiquitin/SUMO modifications in the regulation of cancer-related proteins. *Seminars in cancer biology* **27**, 11-19, doi:10.1016/j.semcancer.2014.03.005 (2014).
18 Siska, E. K., Koliakos, G. & Petrakis, S. Stem cell models of polyglutamine diseases and their use in cell-based therapies. *Frontiers in neuroscience* **9**, 247, doi:10.3389/fnins.2015.00247 (2015).
19 Soong, B. W. *et al.* Generation of induced pluripotent stem cells from a patient with spinocerebellar ataxia type 3. *Stem cell research* **18**, 29-32, doi:10.1016/j.scr.2016.12.017 (2017).
20 Xu, X. *et al.* Reversal of Phenotypic Abnormalities by CRISPR/Cas9-Mediated Gene Correction in Huntington Disease Patient-Derived Induced Pluripotent Stem Cells. *Stem cell reports* **8**, 619-633, doi:10.1016/j.stemcr.2017.01.022 (2017).
21 Macedo-Ribeiro, S., Cortes, L., Maciel, P. & Carvalho, A. L. Nucleocytoplasmic shuttling activity of ataxin-3. *PloS one* **4**, e5834, doi:10.1371/journal.pone.0005834 (2009).
22 Stoyas, C. A. & La Spada, A. R. The CAG-polyglutamine repeat diseases: a clinical, molecular, genetic, and pathophysiologic nosology. *Handbook of clinical neurology* **147**, 143-170, doi:10.1016/b978-0-444-63233-3.00011-7 (2018).
23 Bichelmeier, U. *et al.* Nuclear localization of ataxin-3 is required for the manifestation of symptoms in SCA3: in vivo evidence. *The Journal of neuroscience : the official journal of the Society for Neuroscience* **27**, 7418-7428, doi:10.1523/jneurosci.4540-06.2007 (2007).
24 Fahrenkrog, B. & Harel, A. Perturbations in Traffic: Aberrant Nucleocytoplasmic Transport at the Heart of Neurodegeneration. *Cells* **7**, doi:10.3390/cells7120232 (2018).
25 Gasset-Rosa, F. *et al.* Polyglutamine-Expanded Huntingtin Exacerbates Age-Related Disruption of Nuclear Integrity and Nucleocytoplasmic Transport. *Neuron* **94**, 48-57 e44, doi:10.1016/j.neuron.2017.03.027 (2017).
26 Eftekharzadeh, B. *et al.* Tau Protein Disrupts Nucleocytoplasmic Transport in Alzheimer's Disease. *Neuron* **99**, 925-940 e927, doi:10.1016/j.neuron.2018.07.039 (2018).

27 Zhang, K., Grima, J. C., Rothstein, J. D. & Lloyd, T. E. Nucleocytoplasmic transport in C9orf72-mediated ALS/FTD. *Nucleus (Austin, Tex.)* **7**, 132-137, doi:10.1080/19491034.2016.1172152 (2016).
28 Sowa, A. S. *et al.* Karyopherin alpha-3 is a key protein in the pathogenesis of spinocerebellar ataxia type 3 controlling the nuclear localization of ataxin-3. *Proceedings of the National Academy of Sciences of the United States of America* **115**, E2624-E2633, doi:10.1073/pnas.1716071115 (2018).
29 Tsou, W. L. *et al.* DnaJ-1 and karyopherin alpha3 suppress degeneration in a new Drosophila model of Spinocerebellar Ataxia Type 6. *Human molecular genetics* **24**, 4385-4396, doi:10.1093/hmg/ddv174 (2015).
30 Wan, L., Xu, K., Chen, Z., Tang, B. & Jiang, H. Roles of Post-translational Modifications in Spinocerebellar Ataxias. *Frontiers in cellular neuroscience* **12**, 290, doi:10.3389/fncel.2018.00290 (2018).